Towards Model-independent Predictions for R-parity Violating Supersymmetry

Dissertation
zur
Erlangung des Doktorgrades (Dr. rer. nat.)
der
Mathematisch-Naturwissenschaftlichen Fakultät
der
Rheinischen Friedrich-Wilhelms-Universität Bonn

von
Saurabh Nangia
aus
New Delhi, India

Bonn, Juni 2023

Angefertigt mit Genehmigung der Mathematisch-Naturwissenschaftlichen Fakultät der Rheinischen Friedrich-Wilhelms-Universität Bonn

1. Gutachter:	Prof. Herbert K. Dreiner, Ph.D.
2. Gutachter:	Prof. Dr. Manuel Drees
Tag der Promotion:	02.11.2023
Erscheinungsjahr:	2024

To my family.

Abstract

Extensive searches for supersymmetry (SUSY), over the last four decades, have returned no evidence for it yet. Particularly, with the Large Hadron Collider (LHC) results, this begs the question: "Is it time to give up on the idea of SUSY at energy scales accessible to us, or are there still potential gaps in our coverage that need to be explored?" In this thesis, we advocate the latter view. In particular, we consider the R-parity violating Minimal Supersymmetric Standard Model (RPV-MSSM). We argue that this setup is as well-motivated as the MSSM. On the other hand, the phenomenological space is vastly more complex; this creates potential for gaps in our SUSY coverage. In this thesis, we identify and focus on four such gaps in our current studies:

(i) There is no systematic classification of the RPV-MSSM signatures at colliders. In particular, there could be signatures we may have missed in our coverage.

(ii) Lepton parton distribution functions (PDFs) can initiate resonant squark production in the RPV-MSSM at the LHC, resulting in a clean final state consisting of a single charged lepton, no/low missing energy, and either one or a few jets. This can be a sensitive probe to SUSY that has not been covered at the LHC yet.

(iii) The RPV-MSSM can accommodate massive neutrinos. However, the implications of the precisely measured neutrino oscillation data have not been analyzed for the most general RPV-MSSM setup.

(iv) The mass of the lightest neutralino – if bino-like – is still completely unconstrained in the RPV-MSSM.

On the flip side, we argue that, with recent and upcoming developments in the field, each of the above offers an exciting new opportunity to find SUSY. We explicitly demonstrate this by implementing studies that take steps towards covering the above gaps. Our results show that, in this way, there is still significant potential to discover SUSY in the near future. Our approach, throughout, will emphasize model-independence.

Acknowledgments

I owe gratitude to several, many people who have contributed to this thesis either directly or indirectly; I value each of you. If I forget any names, please find the strength to forgive a slightly sleep-deprived human.

I want to first express how grateful I am that I got to work under Herbi. He gave me all the freedom and independence I needed to pursue questions that interested me. And, yet, he has always had my back. I have also always admired his intuition when it comes to explaining physics. But, best of all, he has this ability to switch quickly from being a serious boss to being a guy who makes dad jokes; from being someone giving me life advice to being a bully making fun of how I pronounce 'v'; from being my cricket buddy to being the guy who disses the Indian cricket team. However, whatever role he dons, he manages to charm you with his humor and his kindness. Truly, I do not think I will find a better boss. I would also like to thank Manuel for agreeing to be the second reviewer for this thesis. He is one of the people I have looked up to the most, ever since my first days at the BCTP. However, I think this experience is common. You sit with Manuel for one conversation and you are in awe of how smart and witty he is. I have particularly enjoyed my journal club presentations with all of Manuel's questions. Finally, I wish to thank the other members of my doctoral committee for kindly accepting my invitation and giving me their valuable time. Finally, I would also like to thank the BCGS for all their support over the years. They are the reason I am in Bonn. I will miss this place.

Next, I wish to acknowledge the members of the BCTP – both current and former – who made office life so much more fun. In no particular order: Andi T., Christoph L., Bardia, Annika, Stefano, Manuel K., Yashasvee, Florian D., Max, Julian G., Rhitaja, Rhorry, Joshua, Paarth, Chenhuan, Wenbin, Urmi, Thorsten, Christoph N., Fabian F., Cesar. And our beloved support system, without whom the BCTP would never work: Christa, Petra, Patricia, Lora, Andreas W., and Oliver.

I would also like to thank all my collaborators who might or might not have frustrated me at times, but also whom I definitely frustrated a lot more in return: Simon W., Martin, Víctor, Toby, Sheng, Javier, Nadja, Apoorva, and most importantly Dommy who has been my work twin for the whole PhD – I am sorry I asked you to make those annoying plots so many times.

Next on the list are all my amazing friends: Jimstah, Thodoris, Simon H., Jonathan, Lorenz, Janin, Fabian B., Rahul, Mr. Xu, Armando, Niko, Apoorva, Dommy. And, of course, Juhi and Janak – whom I miss having in Bonn so dearly. Also, my X-C gang: Jum, Aru, Diya, Gaurav, Samridhi, Vanika, Geetu, Nikita, Raghav, Anjali, Sambhavi, Sparsh, Jvalin, Dhruv, Kartik, Iqbal, Prateek, Vanisha – always miss you guys! And finally, my Venky people: Ambar, Anuj and Shishir – so glad we got to do Amsterdam 2 weeks before my thesis submission!

Finally, I want to mention my whole family. Dadi, Nani, Mamu, Mami, Maasi, Maansi, all my aunts, uncles, and cousins.

And, most importantly, Pops, Ma, Nikhil, Tommy and Shivani – everything that I am is because of you guys.

List of Publications

[1] H. K. Dreiner, V. M. Lozano, S. Nangia, and T. Opferkuch,
Lepton PDFs and multipurpose single-lepton searches at the LHC,
Published in Phys. Rev. D 107 (2023) 3, 035011,
DOI: https://doi.org/10.1103/PhysRevD.107.035011.

[2] J. L. Feng et al.,
The Forward Physics Facility at the High-Luminosity LHC,
Published in J. Phys. G 50 (2023) 3, 030501,
DOI:https://doi.org/10.1088/1361-6471/ac865e.

[3] H. K. Dreiner, D. Köhler, S. Nangia, and Z. S. Wang,
Searching for a single photon from lightest neutralino decays in R-parity-violating supersymmetry at FASER,
Published in JHEP 02 (2023) 120,
DOI: https://doi.org/10.1007/JHEP02(2023)120.

[4] H. K. Dreiner, D. Köhler, and S. Nangia,
*A ν approach to analyzing neutrino data in the **R**-parity-violating MSSM*,
Published in Eur. Phys. J. C 83 (2023) 1, 44,
DOI: https://doi.org/10.1140/epjc/s10052-022-11161-8.

[5] H. K. Dreiner, Y. S. Koay, D. Köhler, V. M. Lozano, J. M. Berlingen, S. Nangia, and N. Strobbe,
The ABC of RPV: classification of R-parity violating signatures at the LHC for small couplings,
Published in JHEP 07 (2023) 215,
DOI: https://doi.org/10.1007/JHEP07(2023)215.

[6] H. K. Dreiner, D. Köhler, S. Nangia, M. Schürmann, and Z. S. Wang,
Recasting bounds on long-lived heavy neutral leptons in terms of a light supersymmetric R-parity violating neutralino,
Published in JHEP 08 (2023) 058,
DOI: https://doi.org/10.1007/JHEP08(2023)058.

[7] H. K. Dreiner, D. Köhler, S. Nangia, and A. Shah,
A novel proton decay signature at DUNE, JUNO and Hyper-K,
In preparation.

The contents of this thesis are based on publications [1] and [3-6].

Contents

"karmaṇy-evādhikāras te mā phaleṣhu kadāchana
mā karma-phala-hetur bhūr mā te saṅgo 'stvakarmaṇi"
- Bhagavad Gita: Chapter 2, Verse 47

1 Introduction

This thesis is dedicated to a study of supersymmetry (SUSY), and various aspects of its phenomenology in the context of particle physics. SUSY has been one of the mainstays of the field for the large part of the last few decades, with extensive experimental and theoretical effort devoted to its discovery – unfortunately, without success so far. Given this, it is valid to wonder what motivates yet another dedicated study. In this chapter, we outline the main arguments for why we believe there are still gaps and opportunities in the quest for SUSY, and discuss how recent and upcoming developments are promising to provide insights into these. Before delving into details, however, we begin with a brief overview of the current status of particle physics.

1.1 Particle Physics, Today

Our current understanding of physics at the smallest scales is described by the Standard Model (SM) of particle physics. Broadly speaking, the framework combines insights from three advances made over the last century: the advent of relativity, the discovery of quantum effects, and the realization that symmetries play a pivotal role in Nature. More precisely, the SM is a quantum field theory that describes the known particles as excitations of fields. The propagation, and interactions of these fields with themselves, and each other, are dictated by symmetries – transformations that leave the physics unchanged. In the SM, these symmetries are of two kinds: external transformations acting on spacetime, as described by the (restricted) Poincaré group; and gauged ones acting on the fields embedded in spacetime, locally, as described by the group $\mathrm{SU}(3)_C \times \mathrm{SU}(2)_L \times \mathrm{U}(1)_Y$. Here, C: color, L: left, Y: hypercharge are traditional labels.

We summarize the building blocks of the SM in Table 1.1; shown are the field content, and the transformation properties of each field under the above groups. The three known generations for the leptons (electron, muon, tau); up-type quarks (up, charm, top); and down-type quarks (down, strange, bottom) are denoted by $i = 1, 2, 3$. The components corresponding to the $\mathrm{SU}(2)_L$ multiplets are shown explicitly, while those corresponding to $\mathrm{SU}(3)_C$ are not.

Name	Particle Symbol	Spin	$SU(3)_C$	$SU(2)_L$	$U(1)_Y$
Left-handed quarks	$q_i = (u_L, d_L)_i$	$\frac{1}{2}$	**3**	**2**	$\frac{1}{3}$
Right-handed up quark	$(u_R)_i$	$\frac{1}{2}$	**3**	**1**	$\frac{4}{3}$
Right-handed down quark	$(d_R)_i$	$\frac{1}{2}$	**3**	**1**	$\frac{-2}{3}$
Left-handed leptons	$l_i = (\nu_L, e_L)_i$	$\frac{1}{2}$	**1**	**2**	-1
Right-handed lepton	$(e_R)_i$	$\frac{1}{2}$	**1**	**1**	-2
Higgs field	$(\phi^0, \phi^\pm)$	0	**1**	**2**	1
Weak hypercharge	B	1	**1**	**1**	0
Weak isospin	$W = (W_1, W_2, W_3)$	1	**1**	**3**	0
Gluon	g	1	**8**	**1**	0

Table 1.1: The first two columns list the field content of the SM and the symbols we employ for the corresponding particles, with $i \in \{1, 2, 3\}$ labeling the three generations. The second column depicts the spin quantum number which (along with the mass) determines the representation the particle transforms in under the Poincaré group; while the last three columns depict the representation under the gauge group. See, for instance, Refs. [1, 2] for specifics on how to interpret these transformation properties.

Thus, given the field content and the corresponding transformation rules of Table 1.1, one can write all the renormalizable terms that leave the Lagrangian invariant under the considered symmetries, and calculate predictions. The technical details are not relevant here; rather, we wish to emphasize the elegance of the symmetry framework. As it turns out, the framework is also extremely successful. The Standard Model provides a remarkably accurate description of three of the four known fundamental forces (excluding gravity), and is consistent with all experimentally measured particle properties till date (except neutrino masses, as we discuss below). Since its formulation, it has held up against increasingly scrutinizing precision tests – see, for instance, Ref. [3] for a review. It further predicted the existence and properties of several particles before their discoveries, *e.g.*, $W^\pm$ boson [4, 5], Z boson [6, 7], top quark [8, 9], most recently the Higgs boson [10, 11], etc.[1]

Despite the above, the SM is incomplete, and there are several motivations to expect new physics to eventually show up. We highlight a few important ones:

- Conclusive evidence comes from the neutrino sector. Precise measurements of neutrino oscillations [12] have established that at least two of the three neutrino species need to be massive. With the particle content of Table 1.1, one cannot write down a mass term that satisfies the SM symmetries. While, in principle, one can easily extend the particle content to include a right-handed partner for the neutrino, allowing – as for the other fermions – a Dirac mass term to be written, no such particle has been discovered yet. Further, the neutrino mass scale is at least five orders of magnitude lower than that of any other SM fermion, as indicated by indirect bounds $\left(\sum m_{\nu_i} < 0.12\,\text{eV}\right)$ from cosmology [13], or direct bounds $\left(m_\nu < 0.8\,\text{eV}\right)$ at the `KATRIN` experiment [14]; this might require an explanation.

- As mentioned above, the SM does not include gravity. More generally, we do not have an established theoretical framework for combining quantum effects with our understanding of

[1] The fact that this thesis – being written in 2023 – as well as most of particle physics research today focuses on finding new physics rather than explaining a definitive discrepancy in our extensive searches is in itself testimony to the success of the SM.

gravity.

- At the largest scales, the SM seems to explain only about 5% of the mass-energy content of the universe. Astrophysical and cosmological observations imply that about one-fourth of the energy consists of dark matter. There are no suitable candidates in the SM that can explain properties of this form of matter. Similarly, more than two-thirds of the remaining content is in the form of dark energy, which is also unexplained in the SM.
- The SM cannot account for the prevalence of matter over antimatter in the observable universe [15, 16].
- While the SM remains a consistent framework, it has some features that are theoretically unappealing, *e.g.*, the various naturalness and fine-tuning problems related to the smallness of certain parameters (discussed below in more detail); or the inability to unify the three gauge groups at high energies.
- Finally, while not definitive so far, there are discrepancies between measured data and the SM predictions at certain particle physics experiments. These include the flavor anomalies measured in B-meson decays [17], and the anomalous magnetic moment of the muon [18].

With the above context, we now turn our attention to supersymmetry and see how it addresses some of the above concerns.

1.2 SUSY in the ϕ with Answers?

One of the main original motivations for supersymmetry was that it provided an elegant solution to a specific naturalness problem: the so-called hierarchy problem concerning the Higgs boson mass. We now briefly introduce this; our discussion is based on Ref. [19].

The issue is that the quantum corrections to the Higgs mass-squared (δm_ϕ^2) show an extreme sensitivity to any high mass scale where potential new physics (interacting with the Higgs) lies. In particular, treating the SM as an effective theory with a cutoff at the scale of the new physics, Λ, one finds,

$$\delta m_\phi^2 = a\Lambda^2 + \dots , \tag{1.1}$$

with a some constant and the ellipsis representing other contributions that grow at most logarithmically with Λ. Both of these depend on the details of the calculation that will not be relevant to us.

The crucial part in Eq. (1.1), however, is the quadratic dependence of the Higgs mass-squared on Λ. The hierarchy problem, then, is the puzzle that the experimentally measured value of m_ϕ is only $O(100\,\text{GeV})$, while, from Eq. (1.1), it "naturally" receives corrections of $O(\Lambda)$. These corrections can, as usual, be absorbed by appropriately chosen counter-terms. However, the fine-tuning required to cancel two large numbers precisely to obtain a small one is theoretically unsatisfactory.

A few things are worth stressing here. First, although we have chosen a simple cutoff-based approach for demonstration above, the hierarchy problem persists regardless of which renormalization procedure one chooses; see, for instance, Ref. [19]. Second, the problem persists even if the new physics at Λ (a new heavy particle, for instance) only couples indirectly to the Higgs through its interactions with other SM particles. And third, the above problem does not arise for the other SM bosons or fermions. One can understand this intuitively from the symmetry picture again. The masses of the other bosons

are protected by the gauge symmetries, and are exactly zero at all orders; while corrections to the fermion masses are protected by an approximate chiral symmetry that becomes exact as $m_f \to 0$. On the other hand, there is no such symmetry that protects a scalar field's mass.

Thus, we are faced with three possibilities: (i) the scale of any new physics Λ is not too far from $O(100\,\text{GeV})$, or (ii) any new physics at very high scales does not interact at all with the SM content, or (iii) we accept the precise cancellations of the large corrections as a feature of Nature.[2] While the first two options could certainly be true, we have not found any evidence yet. However, from our discussion about symmetries so far, one may wonder if the third option could perhaps originate from some symmetry reasoning. This is where supersymmetry comes into the picture.

SUSY extends the group of spacetime symmetries of a quantum field theory to include transformations that turn bosons into fermions, and vice versa. The components that transform into one another form a *supermultiplet* that transforms under irreducible representations of the SUSY algebra. One can easily show that the number of bosonic and fermionic components of a supermultiplet are equal. Moreover, in unbroken SUSY, all members of a supermultiplet share the same mass and gauge transformation properties. Using just this simple idea is sufficient to solve the hierarchy problem. This is because the quadratic term of Eq. (1.1) has a relative negative sign for contributions from bosonic degrees of freedom, compared to fermionic ones. Thus, the two contributions, when added up together, exactly cancel! Thus, SUSY is able to explain the precise cancellation needed to generate the right Higgs mass without the need for any fine-tuning: the Higgs mass is "only" $O(100\,\text{GeV})$ because supersymmetry protects it from large quantum corrections. We can understand why this works out from the symmetry picture again: under unbroken SUSY, the Higgs and its fermionic partner are constrained to have the same mass. As we mentioned above, the mass of fermions is protected by the chiral symmetry. Thus, the mass of the Higgs boson is also protected, by extension.

Supersymmetry has several more appealing features. From a theoretical perspective, the SUSY algebra is unique since it represents the only way to non-trivially extend the group of spacetime symmetries [21, 22]. Further, it allows for the unification of the gauge couplings at high energies, which could provide a framework for unifying the three SM gauge groups. From a phenomenological perspective, SUSY – depending on model details – provides candidates for dark matter, as well as possible explanations for neutrino masses, the matter-antimatter asymmetry, and the muon and flavor anomalies. We will discuss a couple of these in the sections to follow. Finally, we note that SUSY is also an important ingredient for string theory – a proposed framework for including quantum gravity effects in our description.

1.3 The Minimal Supersymmetric Standard Model

We can construct a minimal, phenomenologically viable supersymmetric version of the SM by extending its algebra by one set of SUSY generators; this is referred to as $N = 1$ SUSY. We also need to double its particle content by adding fermionic partners for all bosons, and scalar partners for all the fermions. Further, for consistency and completeness, we also need to add an extra Higgs scalar and a corresponding fermionic partner. This field content is summarized in Table 1.2. As mentioned, the gauge transformation properties of the new fields are the same as those of their partners, *cf.* Table 1.1 (H_u transforms as the SM Higgs field, while H_d transforms as $(\mathbf{1}, \mathbf{2}, -\mathbf{1})$).

[2] One more option we will not be interested in here would be to modify the Higgs field such that it is no longer a fundamental scalar field; see, for instance, Ref. [20] for a review.

Supermultiplet	Boson	Fermion
Q_i	$\tilde{q}_i = (\tilde{u}_L, \tilde{d}_L)_i$	$q_i = (u_L, d_L)_i$
$\bar{U}_i$	$(\tilde{u}_R)_i^\dagger$	$(u_R)_i^*$
$\bar{D}_i$	$(\tilde{d}_R)_i^\dagger$	$(d_R)_i^*$
L_i	$\tilde{l}_i = (\tilde{\nu}_L, \tilde{e}_L)_i$	$l_i = (\nu_L, e_L)_i$
$\bar{E}_i$	$(\tilde{e}_R)_i^\dagger$	$(e_R)_i^*$
H_u	$(H_u^\pm, H_u^0)$	$(\tilde{H}_u^\pm, \tilde{H}_u^0)$
H_d	$(H_d^0, H_d^\pm)$	$(\tilde{H}_d^0, \tilde{H}_d^\pm)$
B	B	$\tilde{B}$
W	(W_1, W_2, W_3)	$(\tilde{W}^\pm, \tilde{W}^0)$
G	g	$\tilde{g}$

Table 1.2: Field content of the Minimal Supersymmetric Standard Model. The first column depicts the supermulitplets; the second and third ones list the components of these explicitly. The scalar partners to quarks (leptons) are conventionally referred to as squarks (sleptons), while the new fermionic degrees of freedom are called the Higgsinos, bino, winos, and gluino, respectively. Daggers and asterisks denote antiparticles; they transform in the conjugate represntations of the particles.

With the above setup, we can then write all renormalizable (and holomorphic) interactions allowed by the symmetries (this time including SUSY), as before. Explicitly, we have,

$$W = W_{\text{MSSM}} + W_{\text{LNV}} + W_{\text{BNV}}\,, \tag{1.2}$$

with,

$$\begin{aligned} W_{\text{MSSM}} &= h_e^{ij} H_d L_i \bar{E}_j + h_d^{ij} H_d Q_i \bar{D}_j + h_u^{ij} Q_i H_u \bar{U}_j + \mu H_u H_d\,, \\ W_{\text{LNV}} &= \frac{1}{2}\lambda^{ijk} L_i L_j \bar{E}_k + \lambda'^{ijk} L_i Q_j \bar{D}_k + \kappa^i H_u L_i\,, \\ W_{\text{BNV}} &= \frac{1}{2}\lambda''^{ijk} \bar{U}_i \bar{D}_j \bar{D}_k\,. \end{aligned} \tag{1.3}$$

Here, W represents the superpotential of the theory, an economical way of writing out the non-gauge interactions in the Lagrangian. In the above, we have suppressed all the gauge indices while the generational ones have been retained explicitly: $i, j, k \in \{1, 2, 3\}$, with a summation implied over repeated indices. The λs, hs, μ, and κs represent undetermined parameters of the model, to be fixed by experiment.

In addition to the terms of Eq. (1.2), there are also gauge interactions (and of course, kinetic terms) present. SUSY ensures that, for the new particles, these are identical to those of the SM partners (which remain unchanged from before). Further, we have mentioned that unbroken SUSY also requires the masses of the new SUSY particles (sparticles) to be the same as their SM partners. This, obviously, cannot hold true since otherwise these new partners would have been discovered by our experiments long ago. Thus, SUSY must necessarily be broken. At the same time, the breaking should be achieved in a way that we do not lose desirable features that help solve the hierarchy problem. This can be achieved by adding terms that break SUSY *softly* [19]; this includes extra mass terms for the sparticles that allows them to be heavier than their SM partners, as desired. With this, the complete Lagrangian

is specified.

The reason for splitting the terms in Eq. (1.2) is that $W_{\rm LNV}$ ($W_{\rm BNV}$) violates lepton-number, L (baryon-number, B), while $W_{\rm MSSM}$ conserves both.[3] In the SM, these quantities are only violated through small non-perturbative effects [23–26] but are "accidentally" conserved at the perturbative level. Accidental here means there is no explicit symmetry protecting L and B but the most general interactions one can write with the SM symmetry group automatically conserve them. Experimentally, no processes that violate L or B have ever been observed, putting strict constraints on the couplings corresponding to the $W_{\rm LNV}$ and $W_{\rm BNV}$ operators of Eq. (1.2). For instance, with simultaneous $L_1 Q_1 \bar{D}_i$ and $\bar{U}_1 \bar{D}_1 \bar{D}_i$ operators (with $i \in \{2, 3\}$), the proton can decay into a pion and a positron (or a neutrino); we will discuss this in more detail in Section 1.4. Experiments have obtained strong limits on such decays, *e.g.*, $\tau(p \to \pi^0 + e^+) > 1.6 \times 10^{34}$ yrs [27]. One can estimate that this implies the strict bound,

$$|\lambda'_{11i}\lambda''_{11i}| \lesssim \mathcal{O}(10^{-27})\,, \tag{1.4}$$

if the virtual squarks mediating the decay are assumed to have a mass $\sim \mathcal{O}(1\,\text{TeV})$. Note that the indices written in subscript here compared to superscript in Eq. (1.3) is irrelevant, and we will freely use both notations to denote the same couplings.

In the minimal model that has traditionally received the most amount of phenomenological and experimental attention – the *Minimal Supersymmetric Standard Model* (MSSM) – only the $W_{\rm MSSM}$ term in Eq. (1.2) is retained, while the other two are set to zero. This is achieved by imposing a discrete $\mathbb{Z}_2$ symmetry, called R-parity, defined as,

$$R_p = (-1)^{3(B-L)+2s}\,, \tag{1.5}$$

where L, B and s are the lepton-number, baryon-number, and spin of a given field. With the assignments $L = +1(-1)$ for $L_i(\bar{E}_i)$, and $B = +1/3(-1/3)$ for $Q_i(\bar{U}_i, \bar{D}_i)$, one can easily check that all interactions contained in $W_{\rm MSSM}$ preserve the above symmetry, while those in $W_{\rm LNV} + W_{\rm BNV}$ violate it. For this reason, the latter terms are referred to as R-parity violating (RPV) terms. Similarly, RPV interactions in the soft-breaking sector are also forbidden by the above symmetry in the MSSM.

One dramatic consequence of forbidding RPV interactions is that only vertices with an even number of sparticles are allowed in the MSSM. An easy way to see this is by realizing that Eq. (1.5) assigns even R-parity to all SM particles and the Higgs bosons, and odd R-parity to all the remaining SUSY particles. This has two important implications. First, it implies that SUSY particles can only be produced from SM-only initial states in pairs. Moreover, it guarantees that the lightest supersymmetric particle (LSP) is absolutely stable in the MSSM since it has no odd R-parity states to decay into. There are severe constraints on such a stable particle if it is charged or colored [28, 29]. Thus, in most viable scenarios, the neutralino (admixture of the bino, wino and Higgsinos after electroweak symmetry breaking) is the most attractive candidate to be the LSP; an added advantage here is that it is also a good candidate for dark matter [30, 31].[4]

While, in general, getting predictions in the MSSM is complicated by the fact that the model contains several unknown parameters – particularly in the soft-breaking sector which includes mass terms for all the SUSY particles – we know what typical signature to expect in our searches: large amounts of

[3] L (B) is just a quantum number that takes non-zero values for leptons (quarks) and zero for other fields.

[4] We note that the gravitino in SUSY models including gravity and sneutrinos are also electrically neutral and uncolored LSP candidates, but they are less favored by dark matter constraints [29].

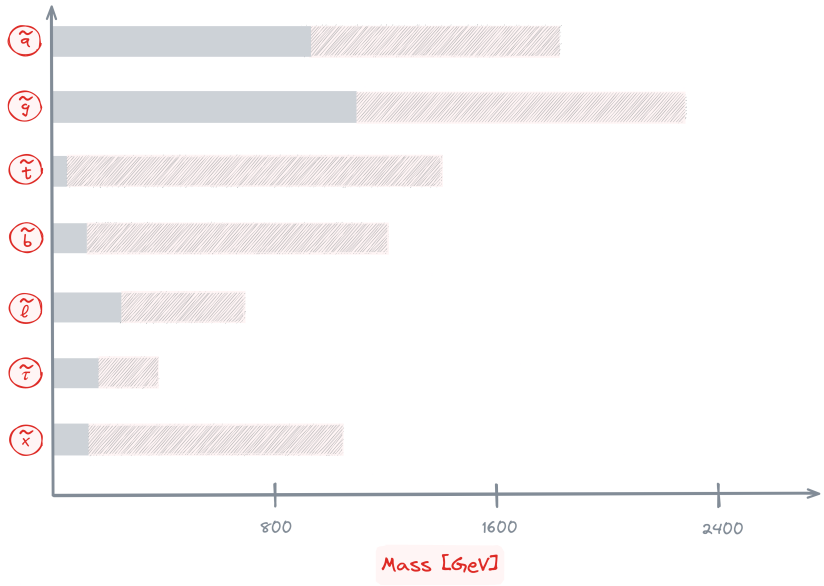

Figure 1.1: Exclusion limits on masses of various sparticles, adapted from Ref. [32]. The derived limits depend on model assumptions (see the reference for details): here, the right edge of the solid (hatched) bar represents the minimum (maximum) quoted exclusion limit for each sparticle. Note that $\tilde{q}$ $(\tilde{t}, \tilde{b})$ is shorthand for *all* light-flavor (heavy-flavor) squarks; $\tilde{l}$ for *all* charged sleptons; $\tilde{\chi}$ for *all* electroweakinos.

transverse missing energy (E_T^{miss}). This can be understood from the above. At experiments such as the Large Hadron Collider (LHC), where beams of protons are collided, SUSY particles are expected to be produced in pairs (typically two in a collision). The expectation then is for these to decay promptly via gauge couplings down to the LSP which – being stable and only weakly interacting – escapes the detector as missing energy. Extensive searches looking for such E_T^{miss} signals have been carried out over the last couple of decades, with the LHC pushing at the multi-TeV energy frontier. However, we have not found any evidence for supersymmetry yet. Sparticles upto masses of $O(1-2\text{ TeV})$ for the colored sector, and $O(100-1000\text{ GeV})$ for the electroweak sector have now been excluded [32], with some dependence on the model parameters. We summarize the exclusion limits in Fig. 1.1.

1.4 The RPV-MSSM

Given that our searches have returned null results so far, it is reasonable to question our assumption of R-parity conservation above.[5] While the constraints coming from experiments looking for L and B violation are stringent, setting all terms in $W_{\text{RPV}} \equiv W_{\text{LNV}} + W_{\text{BNV}}$ to zero is excessive. For instance, the proton can be protected from decaying by imposing alternate symmetries that still allow for some RPV terms. One example is a $\mathbb{Z}_3$ symmetry called Baryon triality, B_3, which forbids all the terms in W_{BNV}, while allowing the W_{LNV} (and W_{MSSM}) ones [35]. Similarly other phenomenological constraints can be

[5] Of course, it is also possible that SUSY simply lies at higher energies currently inaccessible to us. While less appealing from the perspective of the hierarchy problem, heavy-scale SUSY still retains many of the other desirable features we mentioned [33, 34]. Nevertheless, with no major energy upgrades available at our collider experiments in the near future, we focus on "low-scale" SUSY here.

satisfied while still allowing for small RPV couplings; see Ref. [29] for a consolidated list of the bounds implied on the RPV couplings. In fact, allowing for baryon-number violating interactions in the theory may even be necessary to explain the matter-antimatter asymmetry problem mentioned before [36]. Even in the MSSM (and in the SM as mentioned already), B and L are not exactly conserved with higher dimensional operators violating them. All such models, where the particle content is the same as that of the MSSM, and any of the interactions contained in W_{RPV} are non-vanishing, will be generically referred to as the *RPV-MSSM* in this thesis.

We can consider some theoretical perspectives too, as summarized in Ref. [37]. Here, the idea is that a more complete theory – such as string theory which describes gravity, or a Grand Unified Theory (GUT) which unifies the gauge groups – would need to be adopted at higher energies. Then, our current description (whether the SM, the MSSM, or the RPV-MSSM) should be recovered in the low-energy limit of the ultraviolet (UV) complete theory. Thus, we can ask if such theories show a preference for RPC or RPV models. In string theory frameworks, this does not seem to be the case, and both RPC and RPV models have been constructed (for instance, see Refs. [38, 39] for explicit examples of RPV models). Within GUTs, however, RPV models might naively seem to be disfavored. This is because GUTs typically treat quarks and leptons in a unified way while RPV symmetries that protect the proton – such as B_3 – typically do not. Nevertheless, explicit models have been constructed for both RPC and RPV cases, showing that, here too, there is no clear reason to prefer one over the other; see, for instance, Refs. [29, 37, 40] and the references therein for explicit examples. Finally, general arguments in quantum gravity frameworks show that any discrete symmetry that does not arise from a gauged one at a higher energy is maximally violated by gravity effects [41, 42]. Requiring the corresponding gauge symmetry to be anomaly-free translates into severe constraints on the allowed form of the low-energy symmetries. For instance, it has been shown [35, 43, 44] that out of all possible $\mathbb{Z}_2$ and $\mathbb{Z}_3$ symmetries, only two – R-parity and baryon triality – can satisfy the above criterion. The important thing to note is that, once again, both RPC and RPV models can be obtained.

From the above, we can see that there is no clear motivation to choose RPC models over RPV ones. Importantly, allowing for even a small amount of R-parity violation in the theory can dramatically change the phenomenology. As we had discussed, in the MSSM, sparticles can only be produced in even numbers, and the LSP is absolutely stable. With R-parity violated, this is no longer the case. Thus, at colliders, we can have single production of sparticles, significantly extending the kinematic reach of the experiment. Moreover, the characteristic E_T^{miss} signature of the MSSM is now replaced by whatever SM objects the LSP decays into. Further, with the LSP no longer a stable particle, the constraints we had mentioned before do not necessarily apply. Hence, the LSP is not restricted to be electrically neutral and uncolored anymore; it can be any sparticle. Finally, the explicit lepton-number and/or baryon-number violation present in RPV models can lead to striking signatures as well.

Thus, the RPV-MSSM significantly extends the phenomenological space relative to the MSSM. Before we really dismiss SUSY altogether, it is imperative to ensure we have explored this landscape thoroughly. In the following paragraphs, we explore some of the features of RPV phenomenology in more detail, with a particular focus on the new opportunities that these offer for discovering SUSY in the context of recent and upcoming developments in the field.

Before concluding this section, however, we note one final important change in the RPV-MSSM. With the LSP no longer stable – unless the RPV couplings are tiny – there is no natural dark matter candidate.[6] This might be seen as an advantage of the RPC-MSSM; on the other hand, the RPV-MSSM

[6] In more extended RPV models describing SUSY breaking, the gravitino may still be a dark matter candidate, but this

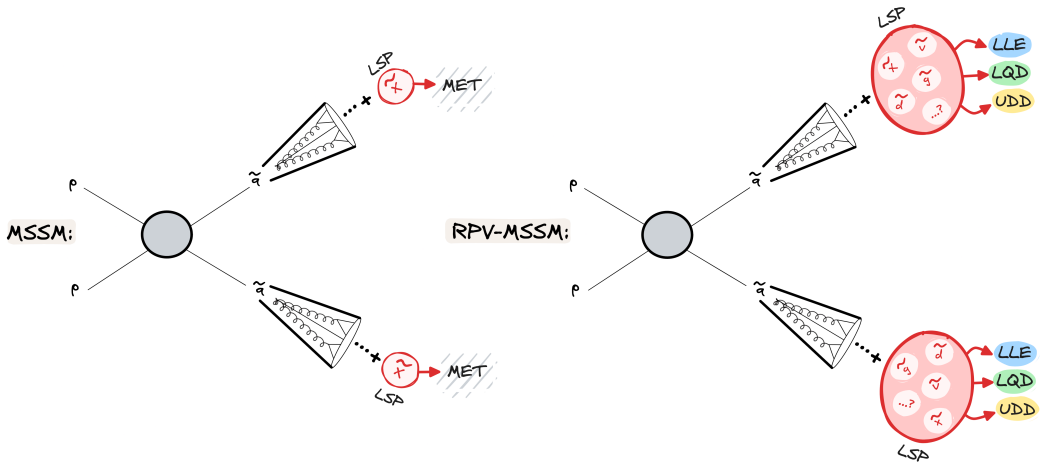

Figure 1.2: Schematic representation of the changes in RPV-MSSM phenomenology compared to the MSSM at the LHC. We depict squark pair production, followed by decay down to the LSP. For the RPV case, only some LSP possibilities, and only the trilinear couplings are shown. MET indicates E_T^{miss}.

allows for massive neutrinos without adding any new particles (as we shall discuss below) – this feature is not present in the RPC version.

1.4.1 The RPV Landscape

One can immediately see that collider searches for the RPV-MSSM require more detailed consideration than those for the MSSM. As discussed, the latter predicts E_T^{miss} signatures at colliders, arising from neutralino LSPs escaping the detector unobserved. Let us consider the RPV-MSSM instead. Since the bounds on RPV operators are typically rather strict, we focus on small couplings for now, and come back to the large-coupling case shortly. Then, the production of sparticles and their cascade decays down to the LSP are expected to remain unchanged from the MSSM case. However, now the LSP can be any sparticle, and can itself decay into SM objects inside the detector. Thus, the characteristic E_T^{miss} signal of the MSSM is depleted, or even completely absent. The final state depends on both the LSP-type, and the dominant RPV coupling. Considering the $3 + 9 + 27 + 9 = 48$ ($\kappa^i, \lambda^{ijk}, \lambda'^{ijk}, \lambda''^{ijk}$) RPV couplings that the superpotential of Eq. (1.2) introduces,[7] and the possible LSP types (*cf.* Table 1.2), the number of possibilities for the final state is truly immense! This is depicted schematically in Fig. 1.2; we will discuss the point more explicitly in Chapter 2.

Thus, the RPV-MSSM offers challenges for our experimental search strategy. While several searches have explicitly looked for specific RPV scenarios (see, for instance, Refs. [29, 32, 45], and references therein for summaries), it is not clear if the assumptions or simplified frameworks employed in such searches allow us to definitively exclude the entire RPV-MSSM landscape.

requires one to carefully ensure that the relic density does not overclose the universe [29].

[7] Gauge invariance requires the λs (λ''s) to be antisymmetric in the first two (last two) indices; this is hidden in the gauge indices which have been suppressed in Eq. (1.3).

On the other hand, this also means that there may be unidentified gaps in our strategies which could offer new opportunities to probe SUSY. Thus, it is crucial that we systematically categorize the potential RPV-MSSM signatures and analyze their coverage. This has already been achieved for the MSSM in Ref. [46], where it was concluded that almost all SUSY models with gluinos lighter than about 1 TeV were already ruled out after LHC Run 1. While several studies have classified signatures for various simplified versions of the RPV-MSSM (see, for instance, Refs. [45, 47, 48]) – as we shall discuss in more detail in Chapter 2 – there is no model-independent treatment of the most general setup in the literature.

This brings us to the first opportunity that we shall address in this thesis:

> ***Opportunity I****: The RPV-MSSM landscape is vast and there is no systematic classification of the possible signatures in the most general setup. Thus, the current status of its coverage is ambiguous. In particular, it is important to check for any potential gaps in our search strategies, which typically constrain only simplified scenarios.*

1.4.2 Single Production at the HL-LHC

So far we have only considered RPV effects in the decay of the LSP. However, for RPV couplings that are not too tiny, the production of the sparticles and their decay chains down to the LSP can also be affected. Most interestingly, as noted, the possibility of single sparticle production opens up, significantly extending the kinematic reach of our colliders. Such signals have been studied extensively in the literature, and searched for at colliders such as LEP, HERA, Tevatron, as well as the LHC; see, for instance, Ref. [29] for a review.

Although these channels are expected to have small cross-sections (given the bounds on the RPV couplings), they can receive a significant boost if they proceed via an s-channel resonance. At the LHC, typically, analyses looking for resonant production of sparticles focus either on dijet final states (arising from $LQ\bar{D}$ or $\bar{U}\bar{D}\bar{D}$ operators) which have to contend with a high SM background, or on scenarios with two RPV couplings.

However, there is another possibility not considered so far: a squark can be resonantly produced at the LHC through a single $LQ\bar{D}$ operator via the leptonic content of the proton parton distribution function (PDF). This results in a clean lepton-number violating final state consisting of a jet and a charged lepton ("single-lepton channel"), which suffers from very low background. Although the lepton PDFs are expected to be tiny, Ref. [49] recently demonstrated that the above channel, also proceeding via lepton PDFs in an analogous way, provides sensitivity to large parts of the leptoquark parameter space that are currently unexplored. The kinematic advantage of single production, the boost from resonance, and the clean final state help the single-lepton channel overcomes the suppression from the PDFs.

Thus, studying the above single production mode in the RPV-MSSM context may be worthwhile. One complication that can arise here, compared to the leptoquark case, is that the squark may also have cascade decay modes into other sparticles available, possibly eroding the single-lepton signal. However, as we will show in Chapter 3, in most cases, one still obtains a generalized version of the single-lepton channel, independent of model details.

Studying such a production mode is particularly relevant now as we prepare to gear up for the High-Luminosity LHC (HL-LHC) upgrade, where increased luminosity could shed light on rare

signatures that we may have considered unimportant so far. This brings us to our next opportunity:

> ***Opportunity II****: The lepton PDFs of the proton offer an exciting opportunity to explore new single production modes for squarks in the RPV-MSSM, particularly in the context of the HL-LHC. It is worthwhile that we explore the resulting signals.*

1.4.3 Striking Low-energy Signatures from LNV and BNV

SUSY may also manifest itself indirectly in our low-energy experiments, where we usually have precise measurements. This may provide us with a sensitive probe, complementary to our high-energy collider experiments. In particular, the lepton- and baryon-number violating interactions present in the RPV-MSSM can lead to particularly interesting effects. Let us discuss two important cases.

Neutrino Masses: As discussed Section 1.1, neutrino masses (and their smallness) need to be explained in any extension of the SM. The RPV-MSSM provides a natural setting for this. To understand how, consider Table 1.2; we see that the neutral down-type Higgsino has identical quantum numbers to the three neutrinos.[8] Thus, after electroweak symmetry breaking, the latter mix with the four massive neutralino eigenstates, obtaining mass terms that are naturally suppressed by the heavy SUSY masses (via a see-saw mechanism).

While neutrino oscillation experiments provide precise measurements of the neutrino mixing parameters, the interpretation of this data in the RPV-MSSM is complicated. As we shall show in Chapter 4, the RPV-MSSM prediction for the neutrino mass matrix gets contributions from all the lepton-number violating couplings contained in Eq. (1.2), and depends on several undetermined SUSY mass scales. Thus, all existing studies in the literature only interpret the neutrino data in specific RPV scenarios. A more general, model-independent treatment studying the implications of the neutrino data for the RPV-MSSM is missing.

Proton Decay: While proton decay has never been observed, it may directly be linked to the fundamental puzzle regarding the baryon asymmetry. The latter can be explained, if baryon number is violated,[9] through the mechanism of baryogenesis [36]. This BNV can then also cause the proton to become unstable [54–57].

Proton decay in the RPV-MSSM context has been studied extensively in the literature; see, *e.g.*, Refs. [29, 58–60]. The canonical scenario allows for decay via simultaneous LNV and BNV couplings. We show an example diagram for decay into a meson and a lepton via squark exchange, involving $LQ\bar{D}$ and $\bar{U}\bar{D}\bar{D}$ operators, in Fig. 1.3(a). Typically, current constraints lead to very stringent bounds on the products of the involved couplings, *cf.* Eq. (1.4).

There is another possibility to consider. As we shall discuss in the following section, the lightest neutralino, if bino-like, is still allowed to be arbitrarily light – even massless. Then, the decay mode, $p \to K^+ + \tilde{B}$, can proceed via a single $\bar{U}\bar{D}\bar{D}$ coupling [60], if kinematically open. We show an example Feynman diagram for this process in Fig. 1.3(b). Such decay modes for the proton into a SUSY particle have received only limited attention in the literature [61–64]. The signature in the

[8] This is prevented in the MSSM by R-parity, which assigns different quantum numbers to the fields.

[9] The BNV, through non-perturbative effects, in the SM is not sufficient to account for the observed asymmetry [50–53].

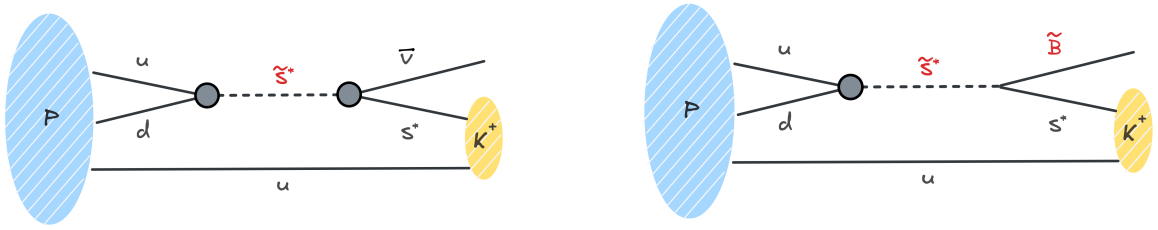

(a) The canonical decay involving two RPV couplings, $LQ\bar{D}$ and $\bar{U}\bar{D}\bar{D}$.

(b) The decay mode that opens up for a light bino, involving only one $U\bar{D}\bar{D}$ coupling.

Figure 1.3: Schematic Feynman diagrams for proton decay in the RPV-MSSM. The RPV vertices are denoted by the bubbles.

detector depends on the lifetime of the neutralino. It may be long-lived, in which case the signature would be similar to the two-coupling mode, $p \to K^+ + \bar{\nu}$, which has been searched for at experiments such as `Super-Kamiokande` [65]. The neutralino mass can lead to different kinematics, however. On the other hand, the neutralino may also decay inside the detector, leading to a unique striking signature. The sensitivities of current and upcoming proton decay facilities to both possibilities need to be determined.

Thus, we can identify another opportunity for RPV-MSSM studies:

> ***Opportunity III****: The lepton- and baryon-number violating interactions in the RPV-MSSM may address fundamental puzzles such as the origin of neutrino masses, or the matter-antimatter asymmetry, and lead to prominent effects in low-energy phenomena. However, some effort is needed to explore the phenomenological space in this context more thoroughly.*

This is particularly relevant as neutrino oscillation data gets ever more precise, and with several upcoming next-generation detectors looking for proton decay, such as `DUNE` [66–69], `JUNO` [70, 71], and `Hyper-K` [72]. In this thesis, we will focus on the neutrino aspect; the study on proton decay is currently in preparation.

1.4.4 Light SUSY

Apart from the indirect ways in which SUSY may show up in low-energy experiments that we have considered above, there is also the intriguing possibility that such experiments directly detect it. Although exclusion limits for most of the sparticle spectrum of Table 1.2 are robust up to at least $O(100\,\text{GeV})$ or so, a bino-like neutralino ($\tilde{B}$) is an exception.

Indeed, there is no mass limit coming from colliders that applies to binos [73, 74]. From the cosmology side, dark matter constraints can become important if the neutralino is stable. For instance, the Lee-Weinberg bound then requires, $m_{\tilde{B}} \gtrsim O(10\,\text{GeV})$ [74–82]. This would be the case in the MSSM. However, in RPV models, the neutralino can decay, even if it is the LSP. Thus, the above bound does not apply. Further, astrophysical constraints are also consistent with light neutralinos, provided the sfermions are heavy enough to satisfy constraints from white dwarf cooling [79, 83,

84]. Thus, $\tilde{B}$ is still allowed to be very light in the RPV-MSSM (in principle, even massless) by all experimental constraints.

Scenarios with such light neutralinos represent an important potential opportunity to discover SUSY at energy scales accessible to us. It is conceivable that the remaining spectrum is too heavy to be easily accessible at current experiments. On the other hand, as we shall discuss in Part IV of this thesis, the RPV-MSSM predicts that light neutralinos ($m_{\tilde{B}} \lesssim O(5\,\text{GeV})$) can still be produced in abundance at colliders through the decays of mesons via $LQ\bar{D}$ operators, leptons via $LL\bar{E}$ ones, or even Z bosons via the RPC gauge couplings. Since these neutralinos are expected to be long-lived – owing to the small masses, and the small RPV couplings responsible for their decays – they would travel a macroscopic distance in the detector before decaying. At the LHC, for instance, neutralinos with a proper decay length greater than $O(5\,\text{m})$ would decay outside the main detector. Further, if these neutralinos come from the decays of light mesons or leptons, they would be produced dominantly in the far-forward direction, and the associated E_T^{miss} signal would be insignificant. Thus, they would have escaped all our current searches at the LHC.[10]

On the other hand, there are several long-lived particles with similar properties that have been considered in other contexts in the literature for quite some time now. These are usually proposed to explain the neutrino masses, or dark matter. Examples include sterile neutrinos, axion-like particles (ALPs), dark scalars, etc. Several experimental searches have already looked for such particles, resulting in stringent exclusion limits. Further, many present and upcoming experiments – including the new dedicated far-detector at the LHC, FASER [85, 86] – will further provide improved sensitivity. These experiments could also offer us an opportunity to probe the light bino.

Indeed, several recent studies have calculated the sensitivities of the above experiments to the light-bino scenario; see, for instance, Refs. [87–94]. However, since the RPV-MSSM landscape is large, there are still some gaps. In particular, we identify two important ones:

- There are several RPV couplings (or coupling combinations) that are not covered by the existing studies. As we will show in Chapter 5, the extensive analyses in the literature for heavy neutral leptons (HNLs) can be especially relevant in addressing this, since light HNLs have a very similar phenomenology to the light bino.[11] Thus, recasting these analyses allows us to probe a very wide range of possible RPV scenarios.

- The existing studies have focused on tree-level decays of the bino. However, for very light binos, the loop-decay into one photon and a neutrino can be dominant. As we will discuss in Chapter 6, this mode can be a sensitive probe of SUSY at FASER in certain RPV scenarios.

This brings us to the final opportunity we shall be addressing in this thesis:

> ***Opportunity IV**: Scenarios involving long-lived binos lighter than $O(5\,\text{GeV})$ represent a gap in the current LHC coverage of the RPV-MSSM. However, several past and upcoming experiments offer the opportunity to bridge this gap. The landscape of possible signatures needs to be analyzed to ensure complete coverage.*

[10] In comparison, light neutralinos in the MSSM would still be expected to be produced with a significant amount of E_T^{miss}, since they can only be produced in the decays of the heavier (s)particles.

[11] This can naively be understood from the fact that the bino and an HNL have the same quantum numbers under the SM symmetry group after electroweak symmetry breaking.

1.5 Thesis Roadmap

The rest of this thesis is organized into four parts, each tackling some aspects of the four opportunities we have identified, followed by a conclusion.

In Part I, we begin exploring the RPV-MSSM landscape. Restricting ourselves to the case of small RPV couplings, we will systematically analyze the final states that can arise in the general setup, relying only on minimal assumptions about the model (mass-spectrum) details. Our objective will be to organize the vast number of possibilities into a more manageable, minimal set of signatures that provides complete coverage of the model space. We can then analyze the current experimental coverage of this set and identify any potential gaps in it, directly addressing the first opportunity we had identified.

In Part II, we will explore the second opportunity we had identified: the possibility of single squark production via lepton PDFs of the proton. Our objective will be to show how the single-lepton channel can be generalized to be a sensitive probe for kinematically accessible squarks in the RPV-MSSM, in a largely model-independent way.

In Part III, we will study neutrino-mass generation in the context of the RPV-MSSM. We will demonstrate – as noted in the third opportunity we identified – the difficulty of making predictions in the most general framework, where the neutrino-mass matrix gets a whole host of contributions involving several undetermined RPV-MSSM parameters. We will then implement a new framework that will allow us to tackle this problem. Using this framework, we will be able to study the implications of the neutrino oscillation data for a large class of RPV-MSSM models in a unified, model-independent manner.

Finally, in Part IV, we will consider the possibility of very light binos in the RPV-MSSM, as identified in the fourth opportunity we mentioned. First, in Chapter 5, we will demonstrate that the phenomenology of a light HNL is very similar to that of a light bino. This will allow us to find sensitivity limits for the RPV-MSSM across a very wide range of scenarios. Next, in Chapter 6, we will demonstrate how the radiative decay mode of the light bino can become dominant in certain scenarios. We will then compute its ability to probe the RPV-MSSM at FASER.

Part I

Aikyam

2

The ABC of RPV: Small Couplings

2.0 Preface

The contents of this chapter and the supplementary material presented in Appendix A have already been published:

- H. K. Dreiner, Y. S. Koay, D. Köhler, V. M. Lozano, J. M. Berlingen, S. Nangia, and N. Strobbe, *The ABC of RPV: Classification of R-Parity Violating Signatures at the LHC for Small Couplings*, `arXiv:2306.07317 [hep-ph]`.

2.0.1 Overview

In this chapter, we set out to address the first opportunity identified in Chapter 1. One of the central themes that we are interested in exploring in this thesis is the broad question: *are existing mass limits on supersymmetric models robust, or does our current coverage still have gaps or loopholes that could hide SUSY at energy scales accessible to us?*

As discussed in Chapter 1, the above consideration is particularly interesting in the context of RPV-SUSY. For R-parity conserving frameworks such as the MSSM, since the LSP – expected to be the neutralino – is stable, we expect a characteristic E_T^{miss} signature which has been searched for extensively at colliders such as the LHC. Ref. [46] has shown that even in scenarios where the E_T^{miss} signal is diluted – for instance, due to a hidden sector, or a compressed spectrum – the MSSM final states can still be simply classified: we should expect to get final states containing either a high multiplicity of objects (≥ 8), or a large number of top quarks. Thus, just five search regions, identified in the above reference, are sufficient to exclude almost all RPC-SUSY models with gluinos lighter than 1 TeV, after LHC Run 1 data. On the other hand, we will show that this is not the case with the RPV-MSSM, where final states not satisfying any of the above criteria can be obtained. While several searches have looked for RPV scenarios relying on specific assumptions about the model spectrum, it is not clear (i) how the derived exclusion limits generalize to RPV-MSSM scenarios not explicitly covered by these searches, and (ii) more pertinently, if the entire RPV-MSSM model space is covered.

In order to remedy the above, we provide a simple scheme to classify all possible topologies that can arise in the most general RPV-MSSM setup in this chapter. Using this, we are able to identify – for the case of small RPV couplings – a minimal set comprising of just 17 final state signatures that provides complete coverage to the RPV-MSSM, irrespective of LSP type, and other mass-spectrum details: 6 for scenarios with $LL\bar{E}$ operators, 6 for the $LQ\bar{D}$ case, and 5 for the $\bar{U}\bar{D}\bar{D}$ case. This allows us to gauge the coverage of the RPV-MSSM in a reasonably model-independent way, analogous to the MSSM case above. The entire framework is presented by considering only one non-vanishing RPV

operator at a time. However, generalization to the case with multiple RPV couplings contributing is easily possible.

Confronting the 17 final states with existing ATLAS and CMS searches, we find that all signatures have been covered at the LHC (even if indirectly), at least at the level of topologies. However, increased sensitivity is needed in order to probe certain LSP direct production scenarios that we identify. Further, we use our framework and the software, CheckMATE, to reinterpret the existing searches and derive current exclusion limits on the RPV-MSSM for scenarios involving a dominant $LL\bar{E}$ operator; we find the limits to be comparable to or better than the R-parity conserving case. By considering a wide range of benchmark scenarios, we show that these limits are robust across the model space.

This work can be straightforwardly extended to calculate the limits on RPV-MSSM scenarios involving $LQ\bar{D}$ or $\bar{U}\bar{D}\bar{D}$ operators. Further, an analogous systematic classification of signatures for the case of large RPV couplings would also be interesting; work is already being pursued in this direction.

2.0.2 Contributions of the Author

The author of this thesis developed the framework to classify the topologies of the RPV-MSSM in a model-independent way after being inspired by the approach taken in Ref. [48] (which in turn was stimulated by Ref. [95]), as well as through discussions with Herbi Dreiner. All the signature tables presented in this chapter and in Appendix A, and the consolidated list of 17 topologies have been compiled by the author. Further, all benchmarks considered in the study, and the corresponding MadGraph5_aMC@NLO and CheckMATE simulations (except for simulations involving a gluino LSP, wino LSPs, and direct LSP production) were provided by the author.

2.1 Introduction

Supersymmetry (SUSY) [96–99] is a well-motivated extension of the Standard Model (SM). It uniquely extends the SM algebra [21, 22], addresses the 'naturalness problem' of the Higgs boson [100, 101], and has many further appealing features, as reviewed in Refs. [19, 102, 103]. Extensive experimental effort has been devoted in its search, particularly at the Large Hadron Collider (LHC) by the ATLAS and CMS Collaborations. However, no evidence for SUSY has been found so far with lower mass bounds reaching $O(1-2\text{ TeV})$ for the colored sector [32, 104–126], and $O(100-1000\text{ GeV})$ for the electroweak sector [32, 108, 110, 111, 127–142], with some dependence on the model details.

As we prepare for more data through Run 3 at the LHC, and especially in the high-luminosity era, it is an excellent opportunity to assess the current status of supersymmetric searches and gain insight into how we should proceed. An interesting question is: *Are the above bounds robust, or are there gaps/loopholes that could still allow LHC-scale SUSY to be hiding?* Typically, ATLAS and CMS derive these limits within the framework of various simplified models or a limited number of complete models such as the Constrained Minimal Supersymmetric Standard Model (CMSSM); it is not clear whether these results can be used to conclude that low-scale SUSY has been definitively excluded.

The above question was first addressed in Ref. [143], and – after LHC Run 1 – in Ref. [46], in more detail. In the latter, it was argued that any 'natural' SUSY model[1] with kinematically accessible gluinos – independent of model details – results in final states containing at least one of the following ingredients: large missing transverse momentum $\left(E_{\mathrm{T}}^{\mathrm{miss}}\right)$, high multiplicity of objects (≥ 8), or a significant number of top quarks. Using this, the authors showed that combining just five existing ATLAS and CMS searches, and one newly proposed search [144] excludes almost any 'natural' SUSY model containing gluinos lighter than 1 TeV. Of course, using current data and a similar strategy should yield a higher mass bound. Nevertheless, the demonstration that a minimal set of searches can target almost any SUSY setup, independent of details concerning the model, mass spectrum, UV-completion, etc., is noteworthy. Such an approach is desirable, especially since it informs us about potential gaps that may exist in our SUSY coverage. For instance, the search proposed by Ref. [144] represented a real gap that has since been filled by ATLAS and CMS in Refs. [145, 146].

In this work, we wish to consider the same question but with two important differences. First, beyond assuming the MSSM particle content, we remain completely blind to the particle-spectrum details. In particular, we do not require that the gluinos are kinematically accessible. With the LHC transitioning from an era of energy upgrades to one of increasing luminosity, we should seriously entertain the possibility that the colored sector may be heavy, while a focus on rarer production channels may yield fruit. We also do not make any 'naturalness' requirements in the sense of Ref. [46].

Second, our focus will be on the R-parity Violating MSSM (RPV-MSSM). The most general, renormalizable superpotential with the MSSM particle content includes lepton- and baryon-number violating operators, together referred to as RPV terms [19, 29, 37, 54]. These are usually set to zero by imposing a discrete $\mathbb{Z}_2$-symmetry called R-parity as they can lead to proton decay [60, 147] at rates in excess of the strict experimental bound [13]. However, the proton-decay problem can be averted without removing all RPV terms [43, 44, 148]; in general, there is no theoretical or phenomenological reason to consider the MSSM without RPV terms [37]. On the other hand, as we demonstrate in Section 2.2, the different configurations of couplings and types of the lightest SUSY particle (LSP) in the RPV-MSSM lead to a bewildering number of possible signatures. In particular, with the

[1] The 'naturalness' criterion in Ref. [46] requires the Higgsinos and stops to be light.

requirements on gluino and higgsino masses absent, a large number of these signatures do not possess any of the characteristics listed in Ref. [46]. In comparison, the 'vanilla' MSSM is less interesting as it tends to retain its characteristic significant E_T^{miss} signal, irrespective of spectrum details.[2] This makes a systematic treatment and classification particularly crucial in the case of the RPV-MSSM.

To summarize, we study the coverage of the most general RPV-MSSM setup at the LHC, without making any assumptions about the particle-spectrum details. We seek a minimal set of searches that would provide complete coverage; this will allow us to identify any potential gaps in our current searches. We will restrict ourselves to the case of small RPV couplings in this work, leaving the large-coupling case for a dedicated study in the future. Thus, the production of sparticles is unchanged from the MSSM case and we only need to consider pair-production channels. The final state signatures will be altered, however, due to the RPV couplings affecting decays.

The paper is organized as follows. In Section 2.2, we set notation and state the assumptions of our framework. Further, we explicitly describe the vast phenomenology of the RPV-MSSM, in order to demonstrate our point about the need for a systematic method of classification. In Section 2.3, we provide such a systematic classification by grouping signatures in a meaningful way, according to the coupling and nature of the LSP. Our approach allows us to identify a minimal set of searches that would provide complete RPV-MSSM coverage at the LHC, and discuss the current status of such a program. Then, in Section 2.4, we demonstrate applications of our framework – as a first study – for the case of a dominant $LL\bar{E}$ RPV-operator. We consider several benchmark scenarios with such lepton-number violating operators, involving the full range of LSP types, and derive exclusion limits. Our results demonstrate that, irrespective of model details, the minimal set of searches proposed in this work can be used to derive strong limits. Finally, we conclude and discuss the implications and limitations of our work, and provide an outlook in Section 2.5. Additionally, we provide a set of appendices containing supplementary details about our simulation procedure (Appendix A.1), information that can be used to optimize future searches (Appendix A.2), and an introduction to `abc-rpv` (Appendix A.3), an accompanying RPV Python library[3] that can be used to generate all the signature tables in this paper.

2.2 Framework

2.2.1 Conventions and Assumptions

With the MSSM particle content and the $N = 1$ supersymmetry algebra, the most general $\mathrm{SU}(3)_C \times \mathrm{SU}(2)_L \times \mathrm{U}(1)_Y$-invariant, renormalizable superpotential is,

$$W = W_{\text{MSSM}} + W_{\text{LNV}} + W_{\text{BNV}}\,, \tag{2.1}$$

[2] We note that the E_T^{miss} signature can be diluted even in the case of the MSSM through scenarios with a compressed spectrum or a 'Hidden Valley'; see, for instance, Refs. [46, 149] for details. Despite the varied phenomenology offered by these models, we believe that it is more efficient to thoroughly explore the minimal setup provided by the RPV-MSSM before adding further complexities.

[3] Available at: `https://github.com/kys-sheng/abc-rpv.git`

where $W_{\rm MSSM}$ is the usual MSSM superpotential – see, for instance, Ref. [40] – while,

$$W_{\rm LNV} = \frac{1}{2}\lambda^{ijk} L_i L_j \bar{E}_k + \lambda'^{ijk} L_i Q_j \bar{D}_k + \kappa^i H_u L_i \,, \qquad W_{\rm BNV} = \frac{1}{2}\lambda''^{ijk} \bar{U}_i \bar{D}_j \bar{D}_k \,, \tag{2.2}$$

violate lepton- and baryon-number, respectively. Together, $W_{\rm RPV} \equiv W_{\rm LNV} + W_{\rm BNV}$, are called the RPV superpotential terms. In our notation, L ($\bar{E}$) and Q ($\bar{U}$, $\bar{D}$) are the MSSM lepton- and quark-doublet (-singlet) chiral superfields, respectively, while H_u labels the (up-type) $\mathrm{SU}(2)_L$-doublet Higgs chiral superfield. We do not write gauge indices explicitly but retain the generational ones: $i, j, k \in \{1, 2, 3\}$ with a summation implied over repeated indices. The λ's and the κ's are the trilinear and bilinear couplings, respectively.

We shall employ the particle content of the MSSM and the superpotential of Eq. (2.1) as the basis for this study. As mentioned in the Introduction, some terms in the superpotential can lead to rapid proton decay. In general, this requires combinations of certain $LQ\bar{D}$ and $\bar{U}\bar{D}\bar{D}$ operators.[4] As long as these combinations are kept small, the proton's lifetime remains consistent with the bounds. Indeed, there are symmetries that can achieve this – see, for instance, Refs. [43, 44, 148]. In this study, we will not bother with the details of how this is done; our focus will be on classifying all possible collider signatures coming from the various couplings. We will, however, ignore the bilinear couplings. These are severely constrained by neutrino mass data [40] and are expected to be relevant for colliders only in limited contexts [29, 150]. Furthermore, at a fixed energy scale they can be rotated away [61, 151].

The optimal search strategy for RPV-MSSM scenarios at colliders depends on the magnitude of the RPV couplings. We will restrict ourselves to the case where these couplings are small enough such that the production of sparticles and their cascade decays down to the LSP remain unchanged from the MSSM case, but large enough so that the LSP decays promptly in the detector (we also require the cascade decays of the other sparticles to be prompt). While the exact magnitudes depend on the spectrum details, we can estimate it to roughly mean the range,

$$\sqrt{\frac{(\beta\gamma)\, 10^{-12}\,\mathrm{GeV}}{m_{\rm LSP}}} \lesssim \lambda \ll g \,, \tag{2.3}$$

where λ is the relevant RPV coupling, g is a gauge coupling, $m_{\rm LSP}$ is the mass of some LSP that has a two body-decay via the RPV coupling, and β and γ are its velocity and Lorentz factor, respectively. The left condition is derived from the requirement that the LSP has a decay length of about 1 cm in the lab frame.[5] For an LSP mass of 1 TeV, Eq. (2.3) implies the range $O(10^{-7}) \lesssim \lambda \ll O(10^{-1})$. Considering λ values smaller or larger than the above range leads to unique features that require separate studies. The former can lead to new kinds of signals such as displaced vertices or long-lived particles, and both topics have received some attention in recent times [152–163]. The latter also leads to interesting features; in particular, single production of sparticles [47, 164–167], and RPV effects in cascade chains can lead to phenomenological changes requiring a dedicated study that we shall pursue in the future, as a continuation of this work.

[4] One exception is if the lightest neutralino is lighter than the proton in which case the decay can occur via $\bar{U}\bar{D}\bar{D}$ operators alone [60].

[5] We have considered a two-body decay here. For comparison, a similar estimate for an LSP with mass 500 GeV undergoing a three-body decay via a virtual sfermion of mass 1 TeV (this is how a neutralino decays, for instance) gives the range $O(10^{-5}) \lesssim \lambda \ll O(10^{-1})$. We note that, in some cases, four-body decays are also possible, *e.g.*, a slepton LSP decaying via λ'' couplings.

One assumption, related to the above point, that we will need to make in this work is that the LSP is not too light, *i.e.*, $m_{\rm LSP} > O(200\,{\rm GeV})$. While current mass bounds on most SUSY particles place them well above this limit, a bino-like neutralino is still allowed to be massless [74, 79]. Requiring the above condition ensures that the decay of the LSP can be prompt without requiring the RPV couplings to be too large. Further, it allows the LSP to decay into all SM fermions (except for, perhaps, the top quark).[6] Dedicated LHC studies for a very light neutralino can be found in, for instance, Refs. [87, 92, 168].

Table 2.1: Summary of notation for labeling the RPV-MSSM particle content used in this work. For the particles not mentioned in the table, we use standard notation.

Symbol	Particles
ℓ	e/μ
L	ℓ/τ
j_l	$u/d/c/s$ jets
j_3	t/b jets
j	j_l/j_3 jets
V	$W/Z/h$
$\tilde{\ell}(\tilde{\nu})$	$\tilde{e}_L(\tilde{\nu}_e)/\tilde{\mu}_L(\tilde{\nu}_\mu)$
$\tilde{e}$	$\tilde{e}_R/\tilde{\mu}_R$
$\tilde{q}$	$\tilde{u}_L/\tilde{d}_L/\tilde{c}_L/\tilde{s}_L$
$\tilde{u}$	$\tilde{u}_R/\tilde{c}_R$
$\tilde{d}$	$\tilde{d}_R/\tilde{s}_R$
$\tilde{q}_3$	$\tilde{t}_L/\tilde{b}_L$
$\tilde{t}$	$\tilde{t}_R$
$\tilde{b}$	$\tilde{b}_R$
$\tilde{B}$	Bino
$\tilde{W}$	Winos (charged/neutral)
$\tilde{H}$	Higgsinos (charged/neutral)

Finally, before concluding this subsection, we introduce our notation for labeling the particle content in Table 2.1. We will find the groupings we define useful in presenting our results later. For simplicity, we will also assume all SUSY particles belonging to a particular grouping are mass degenerate – *i.e.*, we treat mass splittings between components of the same doublet (for instance, $\tilde{H}^\pm$ and $\tilde{H}^0$), as well as between first and second generation sparticles as negligible. The former assumption holds true to a very good approximation [19]. The latter is not essential for our framework but allows us to be concise; generalization is straightforward.

2.2.2 The RPV Landscape

The presence of even small RPV couplings can drastically change collider phenomenology compared to the MSSM. In the latter case, SUSY particles are pair-produced at colliders and undergo gauge-cascade

[6] Note that, throughout this work, we will neglect all SM Yukawas, except for that of the top quark.

decays into the LSP – typically the neutralino[7] – which then escapes the detector unobserved, giving the characteristic E_T^{miss} signature. The presence of RPV couplings changes this simple picture in two main ways. First, the LSP is no longer constrained to be the neutralino but can be any SUSY particle [45, 169]. Second, the RPV couplings make the LSP unstable; the E_T^{miss} signature is now replaced (diluted, or even completely absent) by the objects arising in this decay, which are determined by the dominant RPV coupling. The total number of possible signatures for the RPV-MSSM at a hadron collider can be summarized as (adapted from Ref. [45], see also Ref. [48]):

$$\text{RPV signature} = \begin{pmatrix} \tilde{g}\tilde{g} \\ \tilde{g}\tilde{q}, \tilde{g}\tilde{u}\ldots \\ \tilde{q}\tilde{q}, \tilde{q}_3\tilde{q}_3, \tilde{q}\tilde{u}\ldots \\ \tilde{\ell}\tilde{\ell}, \tilde{\tau}_L\tilde{\tau}_L, \tilde{\ell}\tilde{\nu}\ldots \\ \tilde{H}\tilde{H} \\ \tilde{W}\tilde{W} \\ \tilde{B}\tilde{B} \end{pmatrix}_{\substack{\text{Production} \\ \text{Channels}}} \otimes \begin{pmatrix} \tilde{B} \\ \tilde{H} \\ \tilde{W} \\ \tilde{\ell}(\tilde{\nu}) \\ \tilde{\tau}_L(\tilde{\nu}_\tau) \\ \tilde{e} \\ \tilde{\tau}_R \\ \tilde{q} \\ \tilde{u} \\ \tilde{d} \\ \tilde{q}_3 \\ \tilde{t} \\ \tilde{b} \\ \tilde{g} \end{pmatrix}_{\substack{\text{Possible} \\ \text{LSPs}}} \otimes \begin{pmatrix} L_1L_2\bar{E}_1 \\ \ldots \\ L_1Q_1\bar{D}_1 \\ \ldots \\ \bar{U}_3\bar{D}_2\bar{D}_3 \end{pmatrix}_{\substack{\text{LSP} \\ \text{Decay}}} \tag{2.4}$$

There are 45 different RPV trilinear couplings to consider above. Further, the final state will depend on the details of the cascade decays which, in turn, are determined by the mass orderings in the SUSY spectrum: the total number of possibilities is immense! The first systematic analysis of these signatures was performed in Ref. [47], for the particular case of a neutralino LSP. A more general classification, allowing for all possible LSPs, has been presented in Ref. [48] (see also Ref. [95]). However, the study assumes that the lightest colored particle is kinematically accessible at the collider. In this work, we extend this by also including the possibility that the colored sector lies beyond LHC energies. More importantly, the emphasis in Ref. [48] was on finding signatures arising most frequently from Eq. (2.4), when one considers the space of all possible mass orderings of the SUSY spectrum. Our approach here is different: we wish to create a minimal set of signatures that provides complete coverage for the space of RPV-MSSM models, irrespective of how frequently an individual signature may arise. Furthermore, we will concretely tie this to the LHC search program, discussing the current experimental coverage and identifying possible gaps; this aspect is absent in Ref. [48]. Ref. [45] has studied it for the case of the RPV-CMSSM, but a more general model-independent treatment is missing in the literature.

[7] The nature of the LSP in the MSSM follows from the strict constraints on charged or colored stable particles [28, 29].

2.3 Classification of Signatures: The RPV Dictionary

We now describe our approach for classifying the most general RPV-MSSM signatures. Since we assume the RPV couplings are small, sparticles are pair-produced at the LHC via gauge interactions, as in the MSSM. The production channels that we consider are listed in Eq. (2.4) on the left; the mass spectrum determines which of these are kinematically accessible. The produced sparticles – if not the LSP – will then cascade-decay via gauge interactions until the LSP is reached with the details of the cascade also depending on the model (*i.e.*, the spectrum). The LSP, once produced, decays promptly via the relevant RPV coupling.

In our model-independent approach, we target the last step above: the LSP decay. The essential features of the signatures can be characterized by specifying the nature of the LSP and the RPV coupling, independent of any spectrum-specific details such as the exact chain leading to the LSP production, the mass hierarchies, etc. This is obviously true when the LSP couples directly to the relevant RPV decay operator, leading to a two-body decay. However, it is also true more generally. To illustrate this point, we consider a scenario with a $\tilde{q}$ LSP (first or second generation squark doublet, *cf.* Table 2.1), with λ''_{312} the only non-zero RPV coupling. In this case, there is no direct two-body decay available for $\tilde{q}$. Instead, it must decay via a virtual $\tilde{t}$ or $\tilde{d}$; some of the paths it can take are depicted in Fig. 2.1. Without specifying the model spectrum, it is impossible to state which path will be favored. However, note that in each case we end up with the final state $t + 3j_l + X$.[8] This is a general feature, independent of the path it actually takes. Thus, any model with a $\tilde{q}$ LSP and a dominant λ''_{312} operator has a characteristic $t + 3j_l$ signature, irrespective of any other spectrum details. We can target all such scenarios with a single search – this observation is the most crucial aspect of this work.

Using the above approach, we can compile the characteristic signatures arising from each LSP and dominant RPV coupling combination, in order to arrive at a minimal set of searches that would provide complete coverage for the RPV-MSSM, in a model-independent way. We present this set in the form of tables below. We will also compare it to what has been covered by the vast program of BSM searches by the ATLAS and CMS collaborations. Although only a small subset of these searches provides an explicit interpretation in terms of RPV-SUSY models, the wide range of final states considered covers the majority of signatures expected from RPV decays. Thus, appropriately reinterpreted, they could be used to restrict the RPV parameter space.

In order to facilitate a systematic exploration of the RPV-MSSM landscape with our approach, we have developed an RPV Python library called `abc-rpv`. This library provides a powerful toolkit containing a range of features for analyzing the characteristic signatures arising from various RPV scenarios. The main functionalities include identifying signatures and decay chains for any LSP and RPV coupling combination, as well as going in the other direction: identifying potential RPV scenarios leading to a user-given final state. Using this library, one can reproduce all signature tables in this paper – for instance, (Tables 2.2-2.11) shown below, as well as Table A.1 in Appendix A.2. The information in Fig. 2.1 (possible decay chains for a given LSP) can also be generated easily up to a fixed number of vertices. An introduction to the `abc-rpv` library, including a quick user manual is provided in Appendix A.3.

We note that one downside of our approach is that only final state objects arising in the LSP decay are targeted, and all objects arising in the cascade decays are neglected. In specific models –

[8] There is one subtlety here: the $\tilde{H}$ path in Fig. 2.1 leads to a b-jet instead of t if it proceeds via $\tilde{H}^{\pm}$. However, since we assume $\tilde{H}^{\pm}$ and $\tilde{H}^{0}$ are mass-degenerate, the corresponding path via $\tilde{H}^{0}$ is always equally likely.

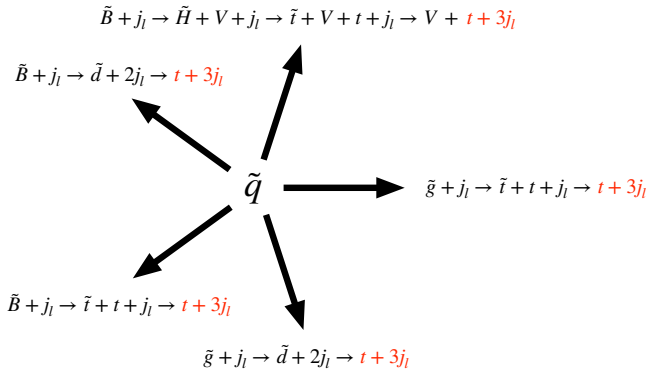

Figure 2.1: Some possible paths a $\tilde{q}$ LSP can take while decaying through λ''_{312}. Since $\tilde{q}$ is the LSP here, all the intermediate sparticles are virtual. See Table 2.1 for the notation employed.

for instance, one with squark pair-production and a neutralino LSP – one could certainly optimize by targeting the additional jets arising in the cascade decays of the parent squarks, thus improving the search sensitivity. However, in order to analyze the status of complete coverage while being model-independent, our approach is necessary. For completeness, we compile a list of additional objects that can arise in cascade decays for various production channels in Table A.1 in Appendix A.2. That table may be used to optimize the searches compiled below for particular scenarios when the model details are known. Further, it can help understand the loss in sensitivity for searches that veto additional objects to help with background suppression.

2.3.1 LLE Tables

We depict the signatures corresponding to the decay of a pair of LSPs for the $LL\bar{E}$ operators of Eq. (2.2) in Tables 2.2 and 2.3. The tables have been written assuming that LSPs are gauge eigenstates, and the pair decays via the same coupling. However, if one is interested in scenarios where the mass eigenstates have significant mixing, or where several dominant RPV couplings contribute, the results can be generalized by considering linear combinations of the table entries.

The tables show the LSP in the first column. The second and third columns depict the resulting signature depending on the generation structure of the $LL\bar{E}$ operator responsible for decay; we employ the compact notation of Table 2.1. Note that, to be concise, we assume all RPV operators within a given category are non-zero, *e.g.*, both $L_1L_2\bar{E}_1$ and $L_1L_2\bar{E}_2$ are non-zero for the category $LL\bar{E}$. Otherwise, more objects may arise, *e.g.*, with a $\tilde{\mu}_R$ LSP and a non-zero $L_1L_2\bar{E}_1$ operator, the smuon would first need to transition into $\tilde{\ell}(\tilde{\nu})$ or $\tilde{e}_R$ leading to two extra muons; the extension is straightforward. In some cases, there is more than one signature possible. If two signatures are

Table 2.2: Characteristic signatures arising from LSP decays for $L_iL_j\bar{E}_k$ operators. The first column depicts the LSPs. The second and third columns represent the signatures for pair production of LSPs for the cases where the indices $i, j, k \in \{1, 2\}$, and where the indices $i, k \in \{1, 2\}$ and $j = 3$, respectively. Color-coding has been introduced to improve the readability of the table; see the main text for details.

LSP	LLE	LL_3E
$\tilde{\ell}\,(\tilde{\nu})$	$3\ell + E_T^{\text{miss}}/4\ell$	$2\ell + \tau + E_T^{\text{miss}}/2\ell + 2\tau$
$\tilde{e}$	$2\ell + E_T^{\text{miss}}$	$2\ell + E_T^{\text{miss}}/\ell + \tau + E_T^{\text{miss}}$
$\tilde{\tau}_L\,(\tilde{\nu}_\tau)$	$4\ell + 2\tau + E_T^{\text{miss}}/4\ell + \tau + E_T^{\text{miss}}$	$3\ell + E_T^{\text{miss}}/4\ell$
$\tilde{\tau}_R$	$4\ell + 2\tau + E_T^{\text{miss}}$	$4\ell + 2\tau + E_T^{\text{miss}}/3\ell + 3\tau + E_T^{\text{miss}}$
$\tilde{g}$	$4\ell + 4j + E_T^{\text{miss}}$	$4\ell + 4j + E_T^{\text{miss}}/3\ell + \tau + 4j + E_T^{\text{miss}}$
$\tilde{q},\ \tilde{u},\ \tilde{d}$	$4\ell + 2j_l + E_T^{\text{miss}}$	$4\ell + 2j_l + E_T^{\text{miss}}/3\ell + \tau + 2j_l + E_T^{\text{miss}}$
$\tilde{t}_L(\tilde{b}_L)$	$4\ell + 2j_3 + E_T^{\text{miss}}$	$4\ell + 2j_3 + E_T^{\text{miss}}/3\ell + \tau + 2j_3 + E_T^{\text{miss}}$
$\tilde{t}_R$	$4\ell + 2t + E_T^{\text{miss}}$	$4\ell + 2t + E_T^{\text{miss}}/3\ell + \tau + 2t + E_T^{\text{miss}}$
$\tilde{b}_R$	$4\ell + 2b + E_T^{\text{miss}}$	$4\ell + 2b + E_T^{\text{miss}}/3\ell + \tau + 2b + E_T^{\text{miss}}$
$\tilde{B},\ \tilde{W},\ \tilde{H}$	$4\ell + E_T^{\text{miss}}$	$4\ell + E_T^{\text{miss}}/3\ell + \tau + E_T^{\text{miss}}$

equally likely, we have listed the one that contains more electrons or muons, since we expect it to be more readily observable. In cases where a signature with fewer e/μ can have a higher cross-section, we have retained both separated by a '/'. For instance, in the case of a $\tilde{\ell}(\tilde{\nu})$ LSP (we assume mass degeneracy of $\text{SU}(2)_L$-doublets, *cf.* Table 2.1) decaying via λ_{121}, the $\tilde{\ell}$ decays into one charged lepton and one neutrino, while the $\tilde{\nu}$ decays into two charged leptons. Thus, the possible signatures from pair production are: 4ℓ, $3\ell + E_T^{\text{miss}}$, $2\ell + E_T^{\text{miss}}$. In the table, we retain the first and second signatures: the former because it has the highest number of charged leptons, and the latter because it has the highest cross-section.

From the tables, we see that the $LL\bar{E}$ case can be completely covered through the following six searches:

1. $2L + E_T^{\text{miss}}$
2. $3L + E_T^{\text{miss}}$
3. $4L$
4. $4L + (0-4)j + E_T^{\text{miss}}$
5. $5L + E_T^{\text{miss}}$
6. $6L + E_T^{\text{miss}}$

Table 2.3: Same as Table 2.2 but for $L_iL_j\bar{E}_k$ operators with $i, j \in \{1, 2\}$ and $k = 3$ (second column), and $j, k = 3$ and $i \in \{1, 2\}$ (third column).

LSP	$\mathbf{LLE_3}$	$\mathbf{LL_3E_3}$
$\tilde{\ell}\,(\tilde{\nu})$	$\ell + 2\tau + E_T^{\text{miss}}/2\ell + 2\tau$	$3\tau + E_T^{\text{miss}}/4\tau$
$\tilde{e}$	$4\ell + 2\tau + E_T^{\text{miss}}$	$4\ell + 2\tau + E_T^{\text{miss}}/3\ell + 3\tau + E_T^{\text{miss}}$
$\tilde{\tau}_L\,(\tilde{\nu}_\tau)$	$2\ell + 4\tau + E_T^{\text{miss}}/2\ell + 3\tau + E_T^{\text{miss}}$	$2\ell + 2\tau/\ell + 2\tau + E_T^{\text{miss}}$
$\tilde{\tau}_R$	$2\ell + E_T^{\text{miss}}$	$2\ell + E_T^{\text{miss}}/\ell + \tau + E_T^{\text{miss}}$
$\tilde{g}$	$2\ell + 2\tau + 4j + E_T^{\text{miss}}$	$2\ell + 2\tau + 4j + E_T^{\text{miss}}/\ell + 3\tau + 4j + E_T^{\text{miss}}$
$\tilde{q},\ \tilde{u},\ \tilde{d}$	$2\ell + 2\tau + 2j_l + E_T^{\text{miss}}$	$2\ell + 2\tau + 2j_l + E_T^{\text{miss}}/\ell + 3\tau + 2j_l + E_T^{\text{miss}}$
$\tilde{t}_L(\tilde{b}_L),$	$2\ell + 2\tau + 2j_3 + E_T^{\text{miss}}$	$2\ell + 2\tau + 2j_3 + E_T^{\text{miss}}/\ell + 3\tau + 2j_3 + E_T^{\text{miss}}$
$\tilde{t}_R$	$2\ell + 2\tau + 2t + E_T^{\text{miss}}$	$2\ell + 2\tau + 2t + E_T^{\text{miss}}/\ell + 3\tau + 2t + E_T^{\text{miss}}$
$\tilde{b}_R$	$2\ell + 2\tau + 2b + E_T^{\text{miss}}$	$2\ell + 2\tau + 2b + E_T^{\text{miss}}/\ell + 3\tau + 2b + E_T^{\text{miss}}$
$\tilde{B},\ \tilde{W},\ \tilde{H}$	$2\ell + 2\tau + E_T^{\text{miss}}$	$2\ell + 2\tau + E_T^{\text{miss}}/\ell + 3\tau + E_T^{\text{miss}}$

To improve the readability of the table, we have introduced a color scheme based on the number of charged leptons in the search region: red (two), blue (three), yellow (four without missing energy), green (four with missing energy), purple (five), and gray (six).

Thus, indeed – in spite of the large number of possibilities that RPV offers – it is possible to organize experimental searches into a small, workable set. The identification of these minimal signatures and the corresponding experimental coverage is one of the main results of this paper. We stress that this is more than just a convenient notational scheme. As will be shown, all signatures that we will classify in our tables – except for one – are experimentally covered by ATLAS and CMS in one form or another, although in some cases strong improvements in sensitivity are required to reach the electroweak production cross-sections. In Section 2.4, we will further apply these to see how the same small set of searches provides exclusion limits across a broad class of RPV models.

One point to note is that, in the above, we have only classified the total number of leptons in each search. However, often it may be useful to know the flavor/sign combinations of these leptons. While we do not employ them in our numerical studies, we provide tables in Appendix A.2 that explicitly show these configurations. These may be useful in developing more sensitive search regions, in case one wishes to target specific scenarios.

We now discuss the experimental coverage of the above signatures. The six final states identified include multiple leptons, may include additional jets, and may come with or without E_T^{miss}. Searches for R-parity Conserving SUSY (RPC-SUSY) typically have good coverage for signatures with E_T^{miss} or with at least three leptons (or two with the same charge), with several of these searches providing some interpretations in RPV-SUSY models as well. Other searches sensitive to the $LL\bar{E}$ case include analyses targeting heavy leptons or additional Higgs bosons. LHC searches relevant for the $LL\bar{E}$ coupling broadly span the final states of (1.) $2\ell + E_T^{\text{miss}}$ [110–112, 130, 131, 136, 141, 170, 171], (2.) $3\ell + E_T^{\text{miss}}$ [110, 112, 127, 138, 172, 173], (3.) 4ℓ [127, 174–178], and (4., 5., 6.) $\geq 4\ell + E_T^{\text{miss}}$ [112,

127, 173, 179]. Searches with four leptons are typically inclusive and include events with more than four leptons, therefore covering also the $5L$ and $6L$ categories.

2.3.2 UDD Tables

Next, we show analogous results for the $\bar{U}\bar{D}\bar{D}$ case in Tables 2.4 and 2.5. The comments from before apply here too. These scenarios can be completely covered through the following five searches:

1. $4j$
2. $2j_l + 4j$
3. $2j_l + 6j$
4. $1L + 2j_l + 4j + E_T^{\text{miss}}$
5. $2L + 2j_l + 4j$

The color scheme is based on the number of jets and charged leptons: red (four jets), blue (six jets, no leptons), yellow (eight jets), green (six jets, one lepton), and purple (six jets, two leptons).

One interesting point worth noting is that we write j_3 and not t in Table 2.5 for the non-colored LSPs (j_3 indicates that the jet could be t/b, *cf.* Table 2.1). This is to account for the possibility that kinematic suppression may lead to the decay into a b (via a virtual chargino) to be preferred over the decay into a t (via a neutralino). Generally, in all tables to follow, we will take this consideration into account for all the non-colored LSPs.

Three of the five $U\bar{D}\bar{D}$ final states listed above contain only jets and correspond to the largest fraction of the possible LSP decays. However, up to two of the jets listed could be top quarks in certain configurations. This would result in additional final state jets or leptons which can be used as experimental handles to improve sensitivity. The last two signatures listed arise from slepton LSPs and always include leptons and/or E_T^{miss} in the final state. `ATLAS` and `CMS` have covered the signatures of (1.) 4 jets [180–182], (2.) 6 jets [183, 184], (3.) 8 jets [146, 178, 185–187], (4.) 1 lepton plus at least 6 jets [115, 145, 146, 188, 189], and (5.) 2 leptons plus 6 jets [112, 189, 190].

Some of these searches explicitly require a minimum number of b-tagged jets, whereas others are more inclusive. The searches considering leptons typically only consider electrons or muons, which reduces the sensitivity to scenarios featuring tau leptons. Additionally, while some final states are nominally covered, the large difference in production cross-sections leads to exclusion limits being available for some production modes (*e.g.*, $\tilde{g} \to 3j_l$) but still requiring orders of magnitude of improvement to reach others (*e.g.*, $\tilde{H} \to 3j_l$).

2.3.3 LQD Tables

Lastly, we show the results for the $LQ\bar{D}$ case in Tables 2.6-2.11. The comments from before apply here. Analyzing the tables, we see that the $LQ\bar{D}$ scenarios can be completely covered through the following six searches:

1. $4j$
2. $2b + 2j + E_T^{\text{miss}}$

3. $1L + (2-6)j + E_T^{\text{miss}}$
4. $2L + (2-6)j + (E_T^{\text{miss}})$
5. $3L + 4j + E_T^{\text{miss}}$
6. $4L + 4j$

The color scheme is based on the number of charged leptons and jets: red (no charged leptons, four jets, without missing energy), blue (no charged leptons, four jets, with missing energy), yellow (one charged lepton), green (two charged leptons), purple (three charged leptons), and gray (four charged leptons).

As can be seen from the tables, $LQ\bar{D}$ operators result in a wide range of possible final states, typically including at least one lepton and several jets. Therefore, searches targeting a wide range of BSM models beyond RPV-SUSY can be sensitive, *e.g.*, searches for RPC-SUSY, leptoquarks, etc. It is important to consider whether one of the generation indices of the $L_i Q_j \bar{D}_k$ operator is 3 since this changes the experimental signature significantly. For example, searches explicitly requiring b-tagged jets typically are the most sensitive for $j, k = 3$. An operator with $i = 3$ requires searches

Table 2.4: Characteristic signatures arising from LSP decays for $\bar{U}_i \bar{D}_j \bar{D}_k$ operators. The first column depicts the LSPs. The second and third columns represent the signatures for pair production of LSPs for the cases where the indices $i, j, k \in \{1, 2\}$, and where the indices $i, k \in \{1, 2\}$ and $j = 3$, respectively. Color-coding has been introduced to improve the readability of the table; see the main text for details.

LSP	**UDD**	**UD$_3$D**
$\tilde{\ell}\,(\tilde{\nu})$	$2\ell + 6j_l / \ell + 6j_l + E_T^{\text{miss}}$	$2\ell + 2b + 4j_l / \ell + 2b + 4j_l + E_T^{\text{miss}}$
$\tilde{e}$	$2\ell + 6j_l$	$2\ell + 2b + 4j_l$
$\tilde{\tau}_L\,(\tilde{\nu}_\tau)$	$2\tau + 6j_l / \tau + 6j_l + E_T^{\text{miss}}$	$2\tau + 2b + 4j_l / \tau + 2b + 4j_l + E_T^{\text{miss}}$
$\tilde{\tau}_R$	$2\tau + 6j_l$	$2\tau + 2b + 4j_l$
$\tilde{g}$	$6j_l$	$2b + 4j_l$
$\tilde{q}$	$8j_l$	$2b + 6j_l$
$\tilde{u}$	$4j_l$	$2b + 2j_l$
$\tilde{d}$	$4j_l$	$2b + 2j_l$
$\tilde{t}_L(\tilde{b}_L)$	$6j_l + 2j_3$	$2b + 4j_l + 2j_3$
$\tilde{t}_R$	$2t + 6j_l$	$2t + 2b + 4j_l$
$\tilde{b}_R$	$2b + 6j_l$	$4j_l$
$\tilde{B},\ \tilde{W},\ \tilde{H}$	$6j_l$	$2b + 4j_l$

Table 2.5: Same as Table 2.4 but for $\bar{U}_i\bar{D}_j\bar{D}_k$ operators with $j,k \in \{1,2\}$ and $i = 3$ (second column), and $i,j = 3$ and $k \in \{1,2\}$ (third column).

LSP	U_3DD	U_3D_3D
$\tilde{\ell}\,(\tilde{\nu})$	$2\ell + 4j_l + 2j_3/\ell + 4j_l + 2j_3 + E_T^{\text{miss}}$	$2\ell + 2b + 2j_l + 2j_3/\ell + 2b + 2j_l + 2j_3 + E_T^{\text{miss}}$
$\tilde{e}$	$2\ell + 4j_l + 2j_3$	$2\ell + 2b + 2j_l + 2j_3$
$\tilde{\tau}_L\,(\tilde{\nu}_\tau)$	$2\tau + 4j_l + 2j_3/\tau + 4j_l + 2j_3 + E_T^{\text{miss}}$	$2\tau + 2b + 2j_l + 2j_3/\tau + 2b + 2j_l + 2j_3 + E_T^{\text{miss}}$
$\tilde{\tau}_R$	$2\tau + 4j_l + 2j_3$	$2\tau + 2b + 2j_l + 2j_3$
$\tilde{g}$	$2t + 4j_l$	$2t + 2b + 2j_l$
$\tilde{q}$	$2t + 6j_l$	$2t + 2b + 4j_l$
$\tilde{u}$	$2t + 6j_l$	$2t + 2b + 4j_l$
$\tilde{d}$	$2t + 2j_l$	$2t + 2b$
$\tilde{t}_L(\tilde{b}_L)$	$4j_l + 4j_3$	$2b + 2j_l + 4j_3$
$\tilde{t}_R$	$4j_l$	$2b + 2j_l$
$\tilde{b}_R$	$2t + 2b + 4j_l$	$2t + 2j_l$
$\tilde{B},\ \tilde{W},\ \tilde{H}$	$4j_l + 2j_3$	$2b + 2j_l + 2j_3$

exploiting final states with τ leptons. The relevant existing searches for the $LQ\bar{D}$ coupling cover the final states of (1.) 4 jets [180–182], (2.) ≥ 4 jets (including b-tags) plus E_T^{miss} [117, 118], (3.) 1ℓ plus 2 jets [191, 192] or 1ℓ plus 6 jets [109, 119, 145, 146, 188, 189], (4.) 2ℓ-same-sign plus 2 jets [193], or 2ℓ-same-sign plus 6 jets [106, 112], or 2ℓ-opposite-sign plus 2 or more jets [105, 111, 116, 123, 189, 194–197], (5.) 3ℓ plus 4 jets [112, 127, 198], and (6.) 4ℓ plus 4 jets [127, 179].

It is important to note that for signatures 1. ($4j$) and 2. ($2b + 2j + E_T^{\text{miss}}$), the relevant searches target strong production cross-sections. As seen from Tables 2.7 to 2.11, these signatures arise from the decays $\tilde{\ell} \to jj$ and $\tilde{\chi}_1^0 \to \nu jb$ respectively. While the latter is experimentally less sensitive than the competing $\tilde{\chi}_1^0 \to \ell jt$ decay, phase-space effects due to the top-quark mass can lead to a strong suppression of channels involving t. In both cases, the existing analyses target strong production, via $\tilde{q} \to jj$ and $\tilde{g} \to bj\tilde{\chi}_1^0$, respectively,[9] and have no sensitivity to low masses and electroweak cross sections. We do note the special case of $\tilde{\chi}_1^0 \to \nu bb$, leading to the $4b$+E_T^{miss} final state which has already been explored for Higgsino production [199, 200]. However, crucially, the searches require an intermediate Higgs resonance which is not present in the RPV case.

[9] The scenario with an almost massless neutralino matches the $LQ\bar{D}$ signature of $\tilde{g} \to bj\nu$.

Table 2.6: Characteristic signatures arising from LSP decays for $L_iQ_j\bar{D}_k$ operators. The first column depicts the LSPs. The second and third columns represent the signatures for pair production of LSPs for the cases where the indices $i, j, k \in \{1, 2\}$, and where the indices $i, j \in \{1, 2\}$ and $k = 3$, respectively. Color-coding has been introduced to improve the readability of the table; see the main text for details.

LSP	LQD	LQD_3
$\tilde{\ell}\,(\tilde{\nu})$	$4j_l$	$2b + 2j_l$
$\tilde{e}$	$4\ell + 4j_l / 3\ell + 4j_l + E_T^{\text{miss}}$	$4\ell + 2b + 2j_l / 3\ell + 2b + 2j_l + E_T^{\text{miss}}$
$\tilde{\tau}_L\,(\tilde{\nu}_\tau)$	$2\ell + 2\tau + 4j_l / \ell + 2\tau + 4j_l + E_T^{\text{miss}} /$ $2\ell + \tau + 4j_l + E_T^{\text{miss}} / \ell + \tau + 4j_l + E_T^{\text{miss}}$	$2\ell + 2\tau + 2b + 2j_l / \ell + 2\tau + 2b + 2j_l + E_T^{\text{miss}} /$ $2\ell + \tau + 2b + 2j_l + E_T^{\text{miss}} / \ell + \tau + 2b + 2j_l + E_T^{\text{miss}}$
$\tilde{\tau}_R$	$2\ell + 2\tau + 4j_l / \ell + 2\tau + 4j_l + E_T^{\text{miss}}$	$2\ell + 2\tau + 2b + 2j_l / \ell + 2\tau + 2b + 2j_l + E_T^{\text{miss}}$
$\tilde{g}$	$2\ell + 4j_l / \ell + 4j_l + E_T^{\text{miss}}$	$2\ell + 2b + 2j_l / \ell + 2b + 2j_l + E_T^{\text{miss}}$
$\tilde{q}$	$2\ell + 2j_l$	$2\ell + 2b$
$\tilde{u}$	$2\ell + 6j_l / \ell + 6j_l + E_T^{\text{miss}}$	$2\ell + 2b + 4j_l / \ell + 2b + 4j_l + E_T^{\text{miss}}$
$\tilde{d}$	$2\ell + 2j_l / \ell + 2j_l + E_T^{\text{miss}}$	$2\ell + 2b + 4j_l / \ell + 2b + 4j_l + E_T^{\text{miss}}$
$\tilde{t}_L(\tilde{b}_L)$	$2\ell + 4j_l + 2j_3 / \ell + 4j_l + 2j_3 + E_T^{\text{miss}}$	$2\ell + 2b + 2j_l + 2j_3 / \ell + 2b + 2j_l + 2j_3 + E_T^{\text{miss}}$
$\tilde{t}_R$	$2\ell + 2t + 4j_l / \ell + 2t + 4j_l + E_T^{\text{miss}}$	$2\ell + 2t + 2b + 2j_l / \ell + 2t + 2b + 2j_l + E_T^{\text{miss}}$
$\tilde{b}_R$	$2\ell + 2b + 4j_l / \ell + 2b + 4j_l + E_T^{\text{miss}}$	$2\ell + 2j_l / \ell + 2j_l + E_T^{\text{miss}}$
$\tilde{B},\ \tilde{W},\ \tilde{H}$	$2\ell + 4j_l / \ell + 4j_l + E_T^{\text{miss}}$	$2\ell + 2b + 2j_l / \ell + 2b + 2j_l + E_T^{\text{miss}}$

Table 2.7: Same as Table 2.6 but for $L_iQ_j\bar{D}_k$ operators with $i, k \in \{1, 2\}$ and $j = 3$.

LSP	LQ_3D
$\tilde{\ell}\,(\tilde{\nu})$	$2j_l + 2j_3$
$\tilde{e}$	$4\ell + 2t + 2j_l / 3\ell + t + b + 2j_l + E_T^{\text{miss}} / 2\ell + 2b + 2j_l + E_T^{\text{miss}}$
$\tilde{\tau}_L\,(\tilde{\nu}_\tau)$	$2\ell + 2\tau + 2t + 2j_l / \ell + 2\tau + t + b + 2j_l + E_T^{\text{miss}} / 2\tau + 2b + 2j_l + E_T^{\text{miss}} / 2\ell + \tau + 2t + 2j_l + E_T^{\text{miss}} /$ $\ell + \tau + t + b + 2j_l + E_T^{\text{miss}} / \tau + 2b + 2j_l + E_T^{\text{miss}}$
$\tilde{\tau}_R$	$2\ell + 2\tau + 2t + 2j_l / \ell + 2\tau + t + b + 2j_l + E_T^{\text{miss}} / 2\tau + 2b + 2j_l + E_T^{\text{miss}}$
$\tilde{g}$	$2\ell + 2t + 2j_l / \ell + t + b + 2j_l + E_T^{\text{miss}}$
$\tilde{q}$	$2\ell + 2t + 4j_l / \ell + t + b + 4j_l + E_T^{\text{miss}}$
$\tilde{u}$	$2\ell + 2t + 4j_l / \ell + t + b + 4j_l + E_T^{\text{miss}}$
$\tilde{d}$	$2\ell + 2t / \ell + t + b + E_T^{\text{miss}}$
$\tilde{t}_L(\tilde{b}_L)$	$2\ell + 2j_l$
$\tilde{t}_R$	$2\ell + 4t + 2j_l / \ell + 3t + b + 2j_l + E_T^{\text{miss}}$
$\tilde{b}_R$	$2\ell + 2t + 2b + 2j_l / \ell + t + 3b + 2j_l + E_T^{\text{miss}}$
$\tilde{B},\ \tilde{W},\ \tilde{H}$	$2\ell + 2j_l + 2j_3 / \ell + 2j_l + 2j_3 + E_T^{\text{miss}} / 2b + 2j_l + E_T^{\text{miss}}$

Table 2.8: Same as Table 2.6 but for $L_i Q_j \bar{D}_k$ operators with $j, k = 3$ and $i \in \{1, 2\}$.

LSP	$\mathbf{LQ_3D_3}$
$\tilde{\ell}\,(\tilde{\nu})$	$2b + 2j_3$
$\tilde{e}$	$4\ell + 2t + 2b / 3\ell + t + 3b + E_T^{\text{miss}} / 2\ell + 4b + E_T^{\text{miss}}$
$\tilde{\tau}_L\,(\tilde{\nu}_\tau)$	$2\ell + 2\tau + 2t + 2b / \ell + 2\tau + t + 3b + E_T^{\text{miss}} / 2\tau + 4b + E_T^{\text{miss}} / 2\ell + \tau + 2t + 2b + E_T^{\text{miss}} / \ell + \tau + t + 3b + E_T^{\text{miss}} / \tau + 4b + E_T^{\text{miss}}$
$\tilde{\tau}_R$	$2\ell + 2\tau + 2t + 2b / \ell + 2\tau + t + 3b + E_T^{\text{miss}} / 2\tau + 4b + E_T^{\text{miss}}$
$\tilde{g}$	$2\ell + 2t + 2b / \ell + t + 3b + E_T^{\text{miss}}$
$\tilde{q}$	$2\ell + 2t + 2b + 2j_l / \ell + t + 3b + 2j_l + E_T^{\text{miss}}$
$\tilde{u}$	$2\ell + 2t + 2b + 2j_l / \ell + t + 3b + 2j_l + E_T^{\text{miss}}$
$\tilde{d}$	$2\ell + 2t + 2b + 2j_l / \ell + t + 3b + 2j_l + E_T^{\text{miss}}$
$\tilde{t}_L(\tilde{b}_L)$	$2\ell + 2b$
$\tilde{t}_R$	$2\ell + 4t + 2b / \ell + 3t + 3b + E_T^{\text{miss}}$
$\tilde{b}_R$	$2\ell + 2t / \ell + t + b + E_T^{\text{miss}}$
$\tilde{B},\ \tilde{W},\ \tilde{H}$	$2\ell + 2b + 2j_3 / \ell + 2b + 2j_3 + E_T^{\text{miss}} / 4b + E_T^{\text{miss}}$

Table 2.9: Same as Table 2.6 but for $L_i Q_j \bar{D}_k$ operators with $j, k \in \{1, 2\}$ and $i = 3$ (second column), and $i, k = 3$ and $j \in \{1, 2\}$ (third column).

LSP	$\mathbf{L_3QD}$	$\mathbf{L_3QD_3}$
$\tilde{\ell}\,(\tilde{\nu})$	$2\ell + 2\tau + 4j_l / 2\ell + \tau + 4j_l + E_T^{\text{miss}} / \ell + 2\tau + 4j_l + E_T^{\text{miss}} / \ell + \tau + 4j_l + E_T^{\text{miss}}$	$2\ell + 2\tau + 2b + 2j_l / 2\ell + \tau + 2b + 2j_l + E_T^{\text{miss}} / \ell + 2\tau + 2b + 2j_l + E_T^{\text{miss}} / \ell + \tau + 2b + 2j_l + E_T^{\text{miss}}$
$\tilde{e}$	$2\ell + 2\tau + 4j_l / 2\ell + \tau + 4j_l + E_T^{\text{miss}}$	$2\ell + 2\tau + 2b + 2j_l / 2\ell + \tau + 2b + 2j_l + E_T^{\text{miss}}$
$\tilde{\tau}_L\,(\tilde{\nu}_\tau)$	$4j_l$	$2b + 2j_l$
$\tilde{\tau}_R$	$4\tau + 4j_l / 3\tau + 4j_l + E_T^{\text{miss}}$	$4\tau + 2b + 2j_l / 3\tau + 2b + 2j_l + E_T^{\text{miss}}$
$\tilde{g}$	$2\tau + 4j_l / \tau + 4j_l + E_T^{\text{miss}}$	$2\tau + 2b + 2j_l / \tau + 2b + 2j_l + E_T^{\text{miss}}$
$\tilde{q}$	$2\tau + 2j_l$	$2\tau + 2b$
$\tilde{u}$	$2\tau + 6j_l / \tau + 6j_l + E_T^{\text{miss}}$	$2\tau + 2b + 4j_l / \tau + 2b + 4j_l + E_T^{\text{miss}}$
$\tilde{d}$	$2\tau + 2j_l / \tau + 2j_l + E_T^{\text{miss}}$	$2\tau + 2b + 4j_l / \tau + 2b + 4j_l + E_T^{\text{miss}}$
$\tilde{t}_L(\tilde{b}_L)$	$2\tau + 4j_l + 2j_3 / \tau + 4j_l + 2j_3 + E_T^{\text{miss}}$	$2\tau + 2b + 2j_l + 2j_3 / \tau + 2b + 2j_l + 2j_3 + E_T^{\text{miss}}$
$\tilde{t}_R$	$2\tau + 2t + 4j_l / \tau + 2t + 4j_l + E_T^{\text{miss}}$	$2\tau + 2t + 2b + 2j_l / \tau + 2t + 2b + 2j_l + E_T^{\text{miss}}$
$\tilde{b}_R$	$2\tau + 2b + 4j_l / \tau + 2b + 4j_l + E_T^{\text{miss}}$	$2\tau + 2j_l / \tau + 2j_l + E_T^{\text{miss}}$
$\tilde{B},\ \tilde{W},\ \tilde{H}$	$2\tau + 4j_l / \tau + 4j_l + E_T^{\text{miss}}$	$2\tau + 2b + 2j_l / \tau + 2b + 2j_l + E_T^{\text{miss}}$

Table 2.10: Same as Table 2.6 but for $L_i Q_j \bar{D}_k$ operators with $i, j = 3$ and $k \in \{1, 2\}$.

LSP	$\mathbf{L_3Q_3D}$
$\tilde{\ell}\,(\tilde{\nu})$	$2\ell + 2\tau + 2t + 2j_l / 2\ell + \tau + t + b + 2j_l + E_T^{\text{miss}} / 2\ell + 2b + 2j_l + E_T^{\text{miss}} / \ell + 2\tau + 2t + 2j_l + E_T^{\text{miss}} /$ $\ell + \tau + t + b + 2j_l + E_T^{\text{miss}} / \ell + 2b + 2j_l + E_T^{\text{miss}}$
$\tilde{e}$	$2\ell + 2\tau + 2t + 2j_l / 2\ell + \tau + t + b + 2j_l + E_T^{\text{miss}} / 2\ell + 2b + 2j_l + E_T^{\text{miss}}$
$\tilde{\tau}_L\,(\tilde{\nu}_\tau)$	$2j_l + 2j_3$
$\tilde{\tau}_R$	$4\tau + 2t + 2j_l / 3\tau + t + b + 2j_l + E_T^{\text{miss}} / 2\tau + 2b + 2j_l + E_T^{\text{miss}}$
$\tilde{g}$	$2\tau + 2t + 2j_l / \tau + t + b + 2j_l + E_T^{\text{miss}}$
$\tilde{q}$	$2\tau + 2t + 4j_l / \tau + t + b + 4j_l + E_T^{\text{miss}}$
$\tilde{u}$	$2\tau + 2t + 4j_l / \tau + t + b + 4j_l + E_T^{\text{miss}}$
$\tilde{d}$	$2\tau + 2t / \tau + t + b + E_T^{\text{miss}}$
$\tilde{t}_L(\tilde{b}_L)$	$2\tau + 2j_l$
$\tilde{t}_R$	$2\tau + 4t + 2j_l / \tau + 3t + b + 2j_l + E_T^{\text{miss}}$
$\tilde{b}_R$	$2\tau + 2t + 2b + 2j_l / \tau + t + 3b + 2j_l + E_T^{\text{miss}}$
$\tilde{B},\ \tilde{W},\ \tilde{H}$	$2\tau + 2j_l + 2j_3 / \tau + 2j_l + 2j_3 + E_T^{\text{miss}} / 2b + 2j_l + E_T^{\text{miss}}$

Table 2.11: Same as Table 2.6 but for $L_i Q_j \bar{D}_k$ operators with $i, j, k = 3$.

LSP	$\mathbf{L_3Q_3D_3}$
$\tilde{\ell}\,(\tilde{\nu})$	$2\ell + 2\tau + 2t + 2b / 2\ell + \tau + t + 3b + E_T^{\text{miss}} / 2\ell + 4b + E_T^{\text{miss}} / \ell + 2\tau + 2t + 2b + E_T^{\text{miss}} /$ $\ell + \tau + t + 3b + E_T^{\text{miss}} / \ell + 4b + E_T^{\text{miss}}$
$\tilde{e}$	$2\ell + 2\tau + 2t + 2b / 2\ell + \tau + t + 3b + E_T^{\text{miss}} / 2\ell + 4b + E_T^{\text{miss}}$
$\tilde{\tau}_L\,(\tilde{\nu}_\tau)$	$2b + 2j_3$
$\tilde{\tau}_R$	$4\tau + 2t + 2b / 3\tau + t + 3b + E_T^{\text{miss}} / 2\tau + 4b + E_T^{\text{miss}}$
$\tilde{g}$	$2\tau + 2t + 2b / \tau + t + 3b + E_T^{\text{miss}}$
$\tilde{q}$	$2\tau + 2t + 2b + 2j_l / \tau + t + 3b + 2j_l + E_T^{\text{miss}}$
$\tilde{u}$	$2\tau + 2t + 2b + 2j_l / \tau + t + 3b + 2j_l + E_T^{\text{miss}}$
$\tilde{d}$	$2\tau + 2t + 2b + 2j_l / \tau + t + 3b + 2j_l + E_T^{\text{miss}}$
$\tilde{t}_L(\tilde{b}_L)$	$2\tau + 2b$
$\tilde{t}_R$	$2\tau + 4t + 2b / \tau + 3t + 3b + E_T^{\text{miss}}$
$\tilde{b}_R$	$2\tau + 2t / \tau + t + b + E_T^{\text{miss}}$
$\tilde{B},\ \tilde{W},\ \tilde{H}$	$2\tau + 2b + 2j_3 / \tau + 2b + 2j_3 + E_T^{\text{miss}} / 4b + E_T^{\text{miss}}$

2.4 Sample Application of the Framework: LLE Couplings

2.4.1 Benchmark Scenarios

We now demonstrate the practical application of our framework by using it to calculate mass bounds on SUSY particles in a wide range of RPV scenarios. Throughout this section, for simplicity, we assume that the only non-zero RPV coupling corresponds to a single $LL\bar{E}$ operator, although – as mentioned – generalization to several non-zero RPV couplings is possible by combining the different rows of our signature tables. Further, we assume all mass eigenstates are aligned with the gauge eigenstates, except for the neutral Higgsinos which are assumed to be maximally mixed.

As discussed in Section 2.3, the signatures in our 'RPV Dictionary' have significant coverage through existing ATLAS and CMS searches, even if only indirectly. We can, therefore, reinterpret these searches in the context of RPV scenarios to set limits on the latter. In the $LL\bar{E}$ scenario, these can be comparable to or even more constraining than the MSSM limits.

In order to calculate the mass limits, we have simulated SUSY processes at leading order using the program MadGraph5_aMC@NLO [201] linked to PYTHIA 8.2 [202]. We have employed the UFO RPV-MSSM model file available at Ref. [203]. The decays are computed under the narrow-width approximation. The branching ratios for two-body decays are computed by MadGraph5_aMC@NLO, while for higher-multiplicity decays – to save computational time – we set them by hand; the details of how we do this are given in Appendix A.1. The width is always set by hand to a small arbitrary value (smaller than the experimental resolution) such that the decay of the LSP remains prompt; under the narrow-width approximation, the results are independent of the number. PYTHIA 8.2 then produces the final decayed and showered event samples. These are passed through CheckMATE 2 [204–208] which uses a database of several existing ATLAS and CMS analyses in order to determine whether the RPV-MSSM parameter point used to generate the event sample can be excluded or not.[10] Detector effects have been accounted for through the DELPHES 3 [210] detector simulation module linked with CheckMATE 2.

We now describe the various benchmark scenarios we study. These have been designed to cover what, we believe, should be all relevant possibilities for the $LL\bar{E}$ case, subject to our minimal assumptions.

Gluino LSP: The first set of scenarios we consider is with a gluino LSP. It is sufficient to consider only direct gluino-pair production since the cross-section is higher than any channel where the gluino LSP is produced in cascade decays (see discussion in Appendix A.2). Thus, in our simulation, we consider the rest of the spectrum to be decoupled; this gives us the most conservative, model-independent exclusion limits. However, we assume that, despite this decoupling, the gluino LSP still decays promptly; see Appendix A.1 for details on the specific decay modes chosen in the simulation. In the first three scenarios, we consider λ_{121} to be the only non-zero RPV operator. The characteristic signature for the gluino decay is $2\ell + 2j + E_T^{\text{miss}}$, *cf.* Table 2.2. Here j can be a light, top, or bottom jet depending on the nature of the virtual squark involved in the decay; the three scenarios target the possible dependence of the coverage on this choice. Next, to study how the results are affected if the RPV operator leads to more muons or taus instead of electrons, we consider three more scenarios

[10] We note that we limit ourselves to the analyses already implemented in CheckMATE 2 as of December 2022; the list of implemented analyses can be found at Ref. [209]. Some analyses explicitly targeting $LL\bar{E}$ models such as the most relevant SRs from Ref. [179] are not implemented. Despite this, we observe excellent coverage.

corresponding to $\lambda_{122}, \lambda_{311}$, and λ_{313}, respectively, being the sole non-zero RPV couplings. The details of all gluino benchmarks have been summarized in Table 2.12.

Table 2.12: Details of our benchmarks: the first two columns depict the LSP and the production mode considered, respectively; the RPV coupling assumed to be non-zero is shown in the third column; the fourth column represents the possible decays of the LSP (these are split into two columns for better readability); the last column shows the notation we use for labeling the scenario.

LSP	**Production**	**Coupling**		LSP Decay	**Label**
$\tilde{g}$	Direct	λ_{121}	$2e + 2j_l + \nu_\mu$	$e + \mu + 2j_l + \nu_e$	$\mathrm{D}_{\tilde{g}}^{e\mu e}$
	Direct	λ_{121}	$2e + 2b + \nu_\mu$	$e + \mu + 2b + \nu_e$	$\mathrm{D}_{\tilde{g}}^{e\mu e-b}$
	Direct	λ_{121}	$2e + 2t + \nu_\mu$	$e + \mu + 2t + \nu_e$	$\mathrm{D}_{\tilde{g}}^{e\mu e-t}$
	Direct	λ_{122}	$2\mu + 2j_l + \nu_e$	$e + \mu + 2j_l + \nu_\mu$	$\mathrm{D}_{\tilde{g}}^{e\mu\mu}$
	Direct	λ_{311}	$2e + 2j_l + \nu_\tau$	$e + \tau + 2j_l + \nu_e$	$\mathrm{D}_{\tilde{g}}^{\tau ee}$
	Direct	λ_{313}	$2\tau + 2j_l + \nu_e$	$e + \tau + 2j_l + \nu_\tau$	$\mathrm{D}_{\tilde{g}}^{\tau e\tau}$

Squark LSPs: Similar to above, for squark LSP scenarios, we first consider only direct pair production with the other sparticles decoupled. Thus, we have selected two scenarios each for the light-flavor squarks ($\tilde{q},\ \tilde{u},\ \tilde{d}$), and the heavy-flavor ones ($\tilde{q}_3,\ \tilde{t},\ \tilde{b}$), corresponding to the couplings λ_{121} and λ_{313}.[11] All squarks within a particular scenario are considered mass-degenerate for simplicity.

For the squarks, cascade decays involving gluino production channels (pair as well as associated) can also be relevant since these can have a higher cross-section than the direct production channels, *cf.* the discussion in Appendix A.2. Thus, we include four more scenarios – covering the two couplings for each of the two squark groups – where the gluino and squarks are both kinematically accessible, while the rest of the spectrum is decoupled (again, in a way that the squarks still decay promptly according to branching ratios described in Appendix A.1). The corresponding results are presented as two-dimensional plots in the gluino mass vs. squark mass plane. The details of all the squark benchmarks have been summarized in Table 2.13.

Electroweakino LSPs: For the electroweakinos, we study three sets of scenarios corresponding to the winos ($\tilde{W}$), the Higgsinos ($\tilde{H}$), or the bino ($\tilde{B}$) being the LSP(s), respectively.

For the winos and the higgsinos, as before, we look at scenarios focusing on the direct modes, as well as the relevant indirect modes mentioned in Appendix A.2. For winos, the latter includes production of gluinos, light-flavor squarks, or heavy-flavor squarks. However, the latter two scenarios have similar features, so we only focus on the light-flavor squarks. For the higgsinos, we include only production of gluinos and the heavy-flavor squarks since their coupling to the light-flavor squarks is suppressed.

[11] These couplings correspond to the two extreme cases: maximum and minimum number of light leptons in the final state. For the remaining scenarios we will only consider these cases; the results for the other coupling configurations can be interpolated from the gluino LSP results.

Table 2.13: As in Table 2.12 but for the squark LSP benchmarks.

LSP	Production	Coupling		LSP Decay	Label
$\tilde{q}/\tilde{u}/\tilde{d}$	Direct $\tilde{g}$	λ_{121}	$2e + j_l + \nu_\mu$	$e + \mu + j_l + \nu_e$	$\mathrm{D}^{e\mu e}_{\tilde{q}}$ $\mathrm{I}^{e\mu e}_{\tilde{g}\to\tilde{q}}$
	Direct $\tilde{g}$	λ_{313}	$2\tau + j_l + \nu_e$	$e + \tau + j_l + \nu_\tau$	$\mathrm{D}^{\tau e\tau}_{\tilde{q}}$ $\mathrm{I}^{\tau e\tau}_{\tilde{g}\to\tilde{q}}$
$\tilde{q}_3/\tilde{t}/\tilde{b}$	Direct $\tilde{g}$	λ_{121}	$2e + j_3 + \nu_\mu$	$e + \mu + j_3 + \nu_e$	$\mathrm{D}^{e\mu e}_{\tilde{q}_3}$ $\mathrm{I}^{e\mu e}_{\tilde{g}\to\tilde{q}_3}$
	Direct $\tilde{g}$	λ_{313}	$2\tau + j_3 + \nu_e$	$e + \tau + j_3 + \nu_\tau$	$\mathrm{D}^{\tau e\tau}_{\tilde{q}_3}$ $\mathrm{I}^{\tau e\tau}_{\tilde{g}\to\tilde{q}_3}$

For the bino, direct production is not relevant due to the small cross-section, and thus we only study indirect modes. This time, we need to consider the possibility of each of the other SUSY particles being the parent: this includes the colored sector, the winos, the Higgsinos, and the sleptons.

As before, apart from the LSP(s) and the relevant parent sparticle(s), all other SUSY fields are considered decoupled, in a way that the LSP decay remains prompt. We study scenarios corresponding to both λ_{121} and λ_{313}. The details for all benchmarks corresponding to electroweakino LSPs have been summarized in Table 2.14.

Slepton LSPs: Finally, we have the slepton LSP scenarios. For each case – light-flavor sleptons ($\tilde{\ell}/\tilde{\nu}/\tilde{e}$), and heavy-flavor sleptons ($\tilde{\tau}_L/\tilde{\nu}_\tau/\tilde{\tau}_R$) – we study direct and indirect production, once again for the couplings λ_{121} and λ_{313}. The relevant indirect modes include every sparticle except the Bino, *cf.* discussion in Appendix A.2. We only study scenarios with $\tilde{g}$ or $\tilde{W}$ parents; results for other colored sparticles or electroweakinos can be interpolated.

Unlike sparticles considered so far, sleptons can couple directly to the $LL\bar{E}$ operators, depending on the flavor configuration. This can significantly affect the decay modes for a given slepton. To study this effect, we also include scenarios with non-zero λ_{122} and λ_{311} for both slepton classes. The details of the slepton benchmarks are summarized in Table 2.15.

Table 2.14: As in Table 2.12 but for the electroweakino LSP benchmarks.

LSP	Production	Coupling		LSP Decay	Label
$\tilde{W}$	Direct	λ_{121}	$2e+\nu_\mu/2e+\mu$	$e+\mu+\nu_e/e+\nu_e+\nu_\mu$	$\mathrm{D}^{e\mu e}_{\tilde{W}}$
	$\tilde{g}$				$\mathrm{I}^{e\mu e}_{\tilde{g}\to\tilde{W}}$
	$\tilde{q}/\tilde{u}/\tilde{d}$				$\mathrm{I}^{e\mu e}_{\tilde{q}\to\tilde{W}}$
	Direct	λ_{313}	$2\tau+\nu_e/e+2\tau$	$e+\tau+\nu_\tau/\tau+\nu_e+\nu_\tau$	$\mathrm{D}^{\tau e\tau}_{\tilde{W}}$
	$\tilde{g}$				$\mathrm{I}^{\tau e\tau}_{\tilde{g}\to\tilde{W}}$
	$\tilde{q}/\tilde{u}/\tilde{d}$				$\mathrm{I}^{\tau e\tau}_{\tilde{q}\to\tilde{W}}$
$\tilde{H}$	Direct	λ_{121}	$2e+V+\nu_\mu$	$e+\mu+V+\nu_e$	$\mathrm{D}^{e\mu e}_{\tilde{H}}$
	$\tilde{g}$				$\mathrm{I}^{e\mu e}_{\tilde{g}\to\tilde{H}}$
	$\tilde{q}_3/\tilde{t}/\tilde{b}$				$\mathrm{I}^{e\mu e}_{\tilde{q}_3\to\tilde{H}}$
	Direct	λ_{313}	$2\tau+V+\nu_e$	$e+\tau+V+\nu_\tau$	$\mathrm{D}^{\tau e\tau}_{\tilde{H}}$
	$\tilde{g}$				$\mathrm{I}^{\tau e\tau}_{\tilde{g}\to\tilde{H}}$
	$\tilde{q}_3/\tilde{t}/\tilde{b}$				$\mathrm{I}^{\tau e\tau}_{\tilde{q}_3\to\tilde{H}}$
$\tilde{B}$	$\tilde{g}$	λ_{121}	$2e+\nu_\mu$	$e+\mu+\nu_e$	$\mathrm{I}^{e\mu e}_{\tilde{g}\to\tilde{B}}$
	$\tilde{q}/\tilde{u}/\tilde{d}$				$\mathrm{I}^{e\mu e}_{\tilde{q}\to\tilde{B}}$
	$\tilde{q}_3/\tilde{t}/\tilde{b}$				$\mathrm{I}^{e\mu e}_{\tilde{q}_3\to\tilde{B}}$
	$\tilde{\ell}/\tilde{\nu}/\tilde{e}$				$\mathrm{I}^{e\mu e}_{\tilde{\ell}\to\tilde{B}}$
	$\tilde{\tau}_L/\tilde{\nu}_\tau/\tilde{\tau}_R$				$\mathrm{I}^{e\mu e}_{\tilde{\tau}\to\tilde{B}}$
	$\tilde{W}$				$\mathrm{I}^{e\mu e}_{\tilde{W}\to\tilde{B}}$
	$\tilde{H}$				$\mathrm{I}^{e\mu e}_{\tilde{H}\to\tilde{B}}$
	$\tilde{g}$	λ_{313}	$2\tau+\nu_e$	$e+\tau+\nu_\tau$	$\mathrm{I}^{\tau e\tau}_{\tilde{g}\to\tilde{B}}$
	$\tilde{q}/\tilde{u}/\tilde{d}$				$\mathrm{I}^{\tau e\tau}_{\tilde{q}\to\tilde{B}}$
	$\tilde{q}_3/\tilde{t}/\tilde{b}$				$\mathrm{I}^{\tau e\tau}_{\tilde{q}_3\to\tilde{B}}$
	$\tilde{\ell}/\tilde{\nu}/\tilde{e}$				$\mathrm{I}^{\tau e\tau}_{\tilde{\ell}\to\tilde{B}}$
	$\tilde{\tau}_L/\tilde{\nu}_\tau/\tilde{\tau}_R$				$\mathrm{I}^{\tau e\tau}_{\tilde{\tau}\to\tilde{B}}$
	$\tilde{W}$				$\mathrm{I}^{\tau e\tau}_{\tilde{W}\to\tilde{B}}$
	$\tilde{H}$				$\mathrm{I}^{\tau e\tau}_{\tilde{H}\to\tilde{B}}$

Table 2.15: As in Table 2.12 but for the slepton LSP benchmarks. For brevity, we skip showing decay modes explicitly (indicated by $*$) for some sleptons that do not couple directly to the relevant RPV operator (*e.g.*, $\tilde{\mu}_R$ LSP with λ_{121}). However, the details of how we include these modes in our simulations can be found in Appendix A.1.

LSP	**Production**	**Coupling**	LSP Decay		**Label**
$\tilde{\ell}/\tilde{\nu}/\tilde{e}$	Direct	λ_{121}	$2e/e+\mu$	$e+\nu_e/e+\nu_\mu$	$\mathrm{D}^{e\mu e}_{\tilde{\ell}}$
	$\tilde{g}$				$\mathrm{I}^{e\mu e}_{\tilde{g}\to\tilde{\ell}}$
	$\tilde{W}$		$\mu+\nu_e$	$*$	$\mathrm{I}^{e\mu e}_{\tilde{W}\to\tilde{\ell}}$
	Direct	λ_{313}	$2\tau/\tau+\nu_\tau$	$*$	$\mathrm{D}^{\tau e\tau}_{\tilde{\ell}}$
	$\tilde{g}$				$\mathrm{I}^{\tau e\tau}_{\tilde{g}\to\tilde{\ell}}$
	$\tilde{W}$				$\mathrm{I}^{\tau e\tau}_{\tilde{W}\to\tilde{\ell}}$
	Direct	λ_{122}	$2\mu/e+\mu/e+\nu_\mu$	$\mu+\nu_e/\mu+\nu_\mu/*$	$\mathrm{D}^{e\mu\mu}_{\tilde{\ell}}$
	Direct	λ_{311}	$e+\tau/e+\nu_\tau$	$\tau+\nu_e/*$	$\mathrm{D}^{\tau ee}_{\tilde{\ell}}$
$\tilde{\tau}_L/\tilde{\nu}_\tau/\tilde{\tau}_R$	Direct	λ_{121}	$2e+\tau+\nu_\mu$	$2e+\nu_\mu+\nu_\tau$	$\mathrm{D}^{e\mu e}_{\tilde{\tau}}$
	$\tilde{g}$				$\mathrm{I}^{e\mu e}_{\tilde{g}\to\tilde{\tau}}$
	$\tilde{W}$		$e+\mu+\tau+\nu_e$	$e+\mu+\nu_e+\nu_\tau$	$\mathrm{I}^{e\mu e}_{\tilde{W}\to\tilde{\tau}}$
	Direct	λ_{313}	$e+\tau/e+\nu_\tau$	$\tau+\nu_e$	$\mathrm{D}^{\tau e\tau}_{\tilde{\tau}}$
	$\tilde{g}$				$\mathrm{I}^{\tau e\tau}_{\tilde{g}\to\tilde{\tau}}$
	$\tilde{W}$				$\mathrm{I}^{\tau e\tau}_{\tilde{W}\to\tilde{\tau}}$
	Direct	λ_{122}	$2\mu+\tau+\nu_e/e+\mu+\tau+\nu_\mu$	$2\mu+\nu_e+\nu_\tau/e+\mu+\nu_\mu+\nu_\tau$	$\mathrm{D}^{e\mu\mu}_{\tilde{\tau}}$
	Direct	λ_{311}	$2e/e+\nu_e$	$2e+\tau+\nu_\tau/e+2\tau+\nu_e$	$\mathrm{D}^{\tau ee}_{\tilde{\tau}}$

2.4.2 Results

Before presenting the numerical results of our simulations, we stress one important detail: even though our benchmarks correspond to simple scenarios where only the LSP (and NLSP) are decoupled, we expect our results to be more general. Since the characteristic signature from the LSP decay – which provides the exclusion, as we show below – is independent of the spectrum details, the sensitivity should only be slightly modified for scenarios with arbitrary sparticle mass spectra, as long as the objects in the characteristic topology do not become too soft.

We now discuss our results. All relevant details for the ATLAS and CMS searches implemented in CheckMATE 2 that show sensitivity to our scenarios have been summarized in Table 2.16 for reference. This list is merely meant to illustrate the searches with the strongest sensitivity and is not exhaustive. When there are multiple overlapping searches offering comparable sensitivity, we have omitted some of them.

Table 2.16: Summary of the most sensitive searches in our numerical simulations. The first column lists existing ATLAS and CMS searches providing sensitivity and our shorthand notation for each; the second column summarizes the relevant cuts; and the last column refers to the scenario labels presented in Tables 2.12-2.15. We have color-coded the labels according to the final state topologies of Section 2.3: $3L+E_T^{\rm miss}$, $4L+(0-4)j+E_T^{\rm miss}$, and $5L+E_T^{\rm miss}$. The same searches also constrain the $\mathrm{I}_{\tilde{x}\to\tilde{p}}$ scenarios (not shown here).

Reference and search region	Representative cuts	Most sensitive for
CMS-ewk-4ℓ [128] SR **G05**	$\geq 4\ell, 0b, E_T^{\rm miss}$	$D^{e\mu e}_{\tilde{g}}, D^{e\mu\mu}_{\tilde{g}}, D^{e\mu e}_{\tilde{q},\tilde{W},\tilde{H}}, D^{\tau ee}_{\tilde{\ell}}, D^{e\mu e}_{\tilde{\tau}}, D^{e\mu\mu}_{\tilde{\tau}}$
ATLAS-gluino-SS/3ℓ [106] SR **Rpv2L**	$\geq 2\ell, \geq 6j$	$D^{e\mu e}_{\tilde{g}}, D^{e\mu\mu}_{\tilde{g}}, D^{e\mu e-b}_{\tilde{g}}, D^{e\mu e-t}_{\tilde{g}}, D^{\tau ee}_{\tilde{g}}, D^{e\mu e}_{\tilde{q}_3}$
ATLAS-RPV-1ℓ/SS [145] SR **SS-6j100-0b**	$\geq 2\ell, \geq 6j, 0b$	$D^{\tau ee}_{\tilde{g}}, D^{\tau e\tau}_{\tilde{g}}, D^{\tau e\tau}_{\tilde{q}}$
ATLAS-gluino-SS/3ℓ-1b [211] SR **Rpc3L1bH**	$\geq 3\ell, \geq 4j, \geq 1b, E_T^{\rm miss}$	$D^{e\mu e}_{\tilde{q}_3}, D^{\tau e\tau}_{\tilde{q}_3}$
CMS-ewk-2τ2ℓ [128] SR **K03**	$2\ell, 2\tau, E_T^{\rm miss}$	$D^{\tau e\tau}_{\tilde{W}}, D^{\tau e\tau}_{\tilde{H}}$
CMS-ewk-3ℓ [128] SR **A44**	$3\ell, E_T^{\rm miss}$	$D^{e\mu e}_{\tilde{\ell}}, D^{e\mu\mu}_{\tilde{\ell}}, D^{\tau ee}_{\tilde{\tau}}$
CMS-ewk-1τ3ℓ [128] SR **I04**	$3\ell, 1\tau, E_T^{\rm miss}$	$D^{\tau e\tau}_{\tilde{\ell}}$
CMS-ewk-2τ1ℓ [128] SR **F12**	$1\ell, 2\tau, E_T^{\rm miss}$	$D^{\tau e\tau}_{\tilde{\tau}}$

Direct Production

Fig. 2.2 shows a summary of the mass limits corresponding to 95% confidence level for the direct-production scenarios, *i.e.*, all the $\mathrm{D}_{\tilde{p}}$ scenarios from Tables 2.12-2.15, where $\tilde{p}$ stands for the relevant LSP. The rest of the spectrum is assumed to be decoupled in these benchmarks, while the LSP decays remain prompt. We see that the exclusion limits are comparable to the current mass bounds corresponding to the regular MSSM (see, for instance, Ref. [32]). We now discuss the results in more detail in the following paragraphs.

The $\tilde{g}$-LSP scenarios can be ruled out up to about $m_{\tilde{g}} \sim 2.1 - 2.4\,\mathrm{TeV}$, with the weaker limits corresponding to cases where the λ_{ijk} coupling involves third-generation indices. The strongest limit is achieved for scenarios involving couplings to light leptons and decay via off-shell top squarks. The signature from pair production for the gluino benchmarks is $4L + 4j + E_T^{\rm miss}$. In general, the strongest sensitivity comes, as expected, from multilepton searches, especially CMS-ewk-4ℓ and ATLAS-gluino-SS/3ℓ.[12] In scenarios with heavy-flavor squarks, $\mathrm{D}^{e\mu e-b}_{\tilde{g}}$ and $\mathrm{D}^{e\mu e-t}_{\tilde{g}}$, CMS-ewk-4$\ell$

[12] See Table 2.16 for the notation we employ for searches.

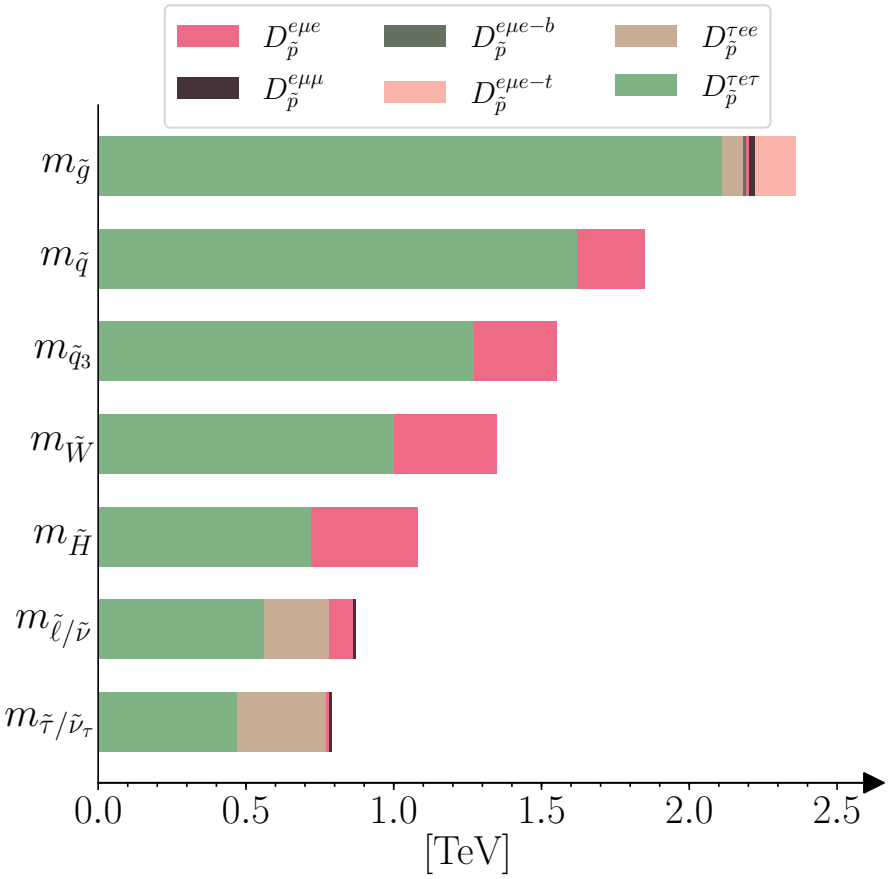

Figure 2.2: 95% confidence-level mass-exclusion limits for various LSPs corresponding to direct pair production. In each scenario, all sparticles other than the LSP(s) ($\tilde{p}$) are assumed to be decoupled, while the LSP decays are still prompt.

shows a weaker sensitivity due to the veto of b-jets. Finally, for couplings that involve τ leptons, $\mathrm{D}_{\tilde{g}}^{\tau ee}$ and $\mathrm{D}_{\tilde{g}}^{\tau e\tau}$, the most relevant analyses are `ATLAS-gluino-SS/3`ℓ and `ATLAS-RPV-1`ℓ`/SS`. Both searches offer sensitivity despite the fact that they focus only on light leptons. This is due to the fraction of gluino decays into electrons (*cf.* Table 2.12), and the leptonic decay of taus. The hadronic decays of taus are reconstructed as additional jets which satisfy the jet multiplicity requirement of both searches. None of the searches are optimized for our signal but they still provide great sensitivity.

For the squarks and the electroweakinos, the final states are similar to the gluino case, albeit with fewer jets: $4L + (0-2)j + E_T^{\mathrm{miss}}$. The most stringent limits for the $\mathrm{D}_{\tilde{p}}^{e\mu e}$ scenarios are provided by `CMS-ewk-4`ℓ: $m_{\tilde{q}} \gtrsim 1.85\,\mathrm{TeV}$, $m_{\tilde{W}} \gtrsim 1.35\,\mathrm{TeV}$, $m_{\tilde{H}} \gtrsim 1.1\,\mathrm{TeV}$. The reduced jet multiplicity limits the sensitivity of `ATLAS-gluino-SS/3`ℓ and `ATLAS-RPV-1`ℓ`/SS`. The $\mathrm{D}_{\tilde{W}}^{\tau e\tau}$ and $\mathrm{D}_{\tilde{H}}^{\tau e\tau}$ scenarios are now instead covered by `CMS-ewk-2`τ`2`ℓ, a search explicitly targeting two hadronic taus, leading to the limits, $m_{\tilde{W}} \gtrsim 1\,\mathrm{TeV}$ and $m_{\tilde{H}} \gtrsim 720\,\mathrm{GeV}$. However, similar to the gluino case, `ATLAS-RPV-1`ℓ`/SS` is the most sensitive for $\mathrm{D}_{\tilde{q}}^{\tau e\tau}$ and rules out this scenario up to $m_{\tilde{q}} \approx 1.6\,\mathrm{TeV}$.

The production of stops and sbottoms is special due to the presence of additional b jets, which are vetoed by `CMS-ewk-4`ℓ and `ATLAS-RPV-1`ℓ`/SS`. Thus, the best limits in this case come from

ATLAS-gluino-SS/3ℓ-1b and ATLAS-gluino-SS/3ℓ for $\mathrm{D}^{e\mu e}_{\tilde{q}_3}$ ($m_{\tilde{q}_3} \gtrsim 1.55$ TeV) and $\mathrm{D}^{\tau e\tau}_{\tilde{q}_3}$ ($m_{\tilde{q}_3} \gtrsim 1.3$ TeV).

Finally, we have the slepton-LSP scenarios. For $\tilde{\ell}/\tilde{\nu}/\tilde{e}$, the exclusion limits lie in the broad range $m_{\tilde{\ell}} \sim 560 - 860$ GeV. The most constraining search for scenarios $D^{e\mu e}_{\tilde{\ell}}$ and $D^{e\mu\mu}_{\tilde{\ell}}$ turns out to be CMS-ewk-3ℓ. This search matches the $3L + E_T^{\mathrm{miss}}$ topology from $\tilde{\ell}\tilde{\nu}$ production, as listed in Table 2.2. For scenarios $D^{\tau ee}_{\tilde{\ell}}$ and $D^{\tau e\tau}_{\tilde{\ell}}$, the most relevant searches are CMS-ewk-4ℓ and CMS-ewk-1τ3ℓ, respectively. The latter needs at least three light leptons and at least one hadronic tau.

In the case of $\tilde{\tau}_L/\tilde{\nu}_\tau/\tilde{\tau}_R$, a large gap in sensitivity is observed between scenarios $D^{e\mu e}_{\tilde{\tau}}$, $D^{e\mu\mu}_{\tilde{\tau}}$, and $D^{\tau ee}_{\tilde{\tau}}$ which are excluded up to $m_{\tilde{\tau}} \sim 780 - 790$ GeV; and the $D^{\tau e\tau}_{\tilde{\tau}}$ scenario with a reach of just $m_{\tilde{\tau}} \gtrsim 470$ GeV. The former are covered by CMS-ewk-4ℓ and CMS-ewk-3ℓ, while the latter is targeted by CMS-ewk-2τ1ℓ. The topologies targeted by all the above search regions match those in Tables 2.2-2.3.

Cascade Decays

We next look at the results for the indirect-production/cascade-decay scenarios, *i.e.*, all the $\mathrm{I}_{\tilde{x}\to\tilde{p}}$ benchmarks from Tables 2.12-2.15, where $\tilde{p}$ is the LSP and $\tilde{x}$ denotes the directly produced parent particle decaying into the LSP. Cascade decays are especially important for scenarios with a bino LSP, where direct production is irrelevant. For all other LSP types, the limits from direct LSP production (corresponding to $D_{\tilde{p}}$) are also taken into account.

In general, exclusion limits are mostly independent of the LSP mass (with a few exceptions) as the signal regions have high acceptance and the limit is driven by the production cross-section. A loss in sensitivity is observed in regions with small mass splittings only for models where the most sensitive signal region requires additional jets. In the bino scenarios, a loss in sensitivity is also observed for low LSP masses as its decay products carry energies that are too low to survive the search region cuts. This effect is not observed for other scenarios as the direct production of LSP becomes dominant for lower masses.

Squark LSPs: In Fig. 2.3, we show the exclusion limits for $\tilde{q}/\tilde{u}/\tilde{d}$-LSPs (Fig. 2.3(a)) and $\tilde{q}_3/\tilde{t}/\tilde{b}$-LSPs (Fig. 2.3(b)) for a non-decoupled gluino. The relevant production processes are gluino-gluino, squark-squark, and associated gluino-squark production, followed by the decay of the gluino into the squark LSP(s) and a jet, and finally the LSP decay via the RPV operator into $2L + j + E_T^{\mathrm{miss}}$.[13] The phase-space region $m_{\tilde{g}} < m_{\tilde{q}}$ ($m_{\tilde{g}} < m_{\tilde{q}_3} + m_t$) is kinematically disallowed[14] in the light-flavor (heavy-flavor) scenario, where we have neglected the masses of all SM fermions except the top quark. These regions are depicted in gray in the plot.

From Fig. 2.3(a), we see that $I_{\tilde{g}\to\tilde{q}}$ can be excluded roughly up to the kinematic limit as long as we are below the threshold for $\tilde{g}\tilde{g}$ production, *cf.* Fig. 2.2. However, even above this threshold, we can exclude large regions of the parameter space that lie beyond the bounds from direct squark-pair production with a decoupled gluino. For instance, we see that even with $m_{\tilde{g}} \sim 8$ TeV, we get higher exclusion in the squark mass compared to the limit coming from $D_{\tilde{q}}$ (shown in red in the figure). This is due to two reasons. First, the associated-production channel (involving a single gluino) can stay

[13] See Appendix A.1 for a detailed discussion on the specific decay modes we pick for each simulation.

[14] Technically, for the heavy-flavor scenario, the region $m_{\tilde{q}_3} \leq m_{\tilde{g}} < m_{\tilde{q}_3} + m_t$ lets the gluino decay into a sbottom (ignoring the b-quark mass), and is allowed. However, for simplicity, we will ignore this here.

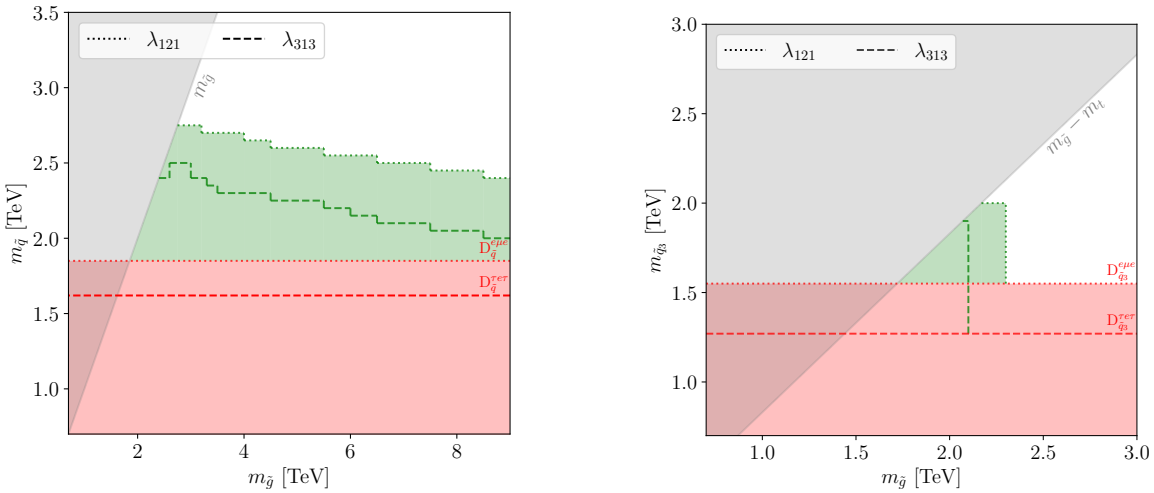

(a) $\tilde{q}/\tilde{u}/\tilde{d}$-LSPs with non-decoupled $\tilde{g}$.

(b) $\tilde{q}_3/\tilde{t}/\tilde{b}$-LSPs with non-decoupled $\tilde{g}$.

Figure 2.3: Exclusion regions (in green) corresponding to 95% confidence level for the $I_{\tilde{g}\to\tilde{q}}$ (left) and $I_{\tilde{g}\to\tilde{q}_3}$ (right) scenarios. The bounds of Fig. 2.2 from direct squark production also apply to the scenario and are shown in red. The gray region is kinematically disallowed in the scenario. The dotted (dashed) contours correspond to coupling λ_{121} (λ_{313}).

kinematically accessible for longer. More importantly, a non-decoupled gluino significantly boosts direct squark-pair production cross-sections through its t-channel contributions [212]. For very high masses, the gluino is essentially decoupled and the limits start converging, *i.e.*, the scenarios reduce to the $D_{\tilde{q}}$ cases.

For Fig. 2.3(b), the exclusion limits behave differently. For both couplings, roughly all kinematically viable regions can be excluded up to the corresponding $m_{\tilde{g}}$ limits of Fig. 2.2. However, the limits reduce sharply to the $D_{\tilde{q}_3}$ bounds beyond this. For third-generation squarks, associated production as well as the boost in squark-squark cross-sections due to non-decoupled gluinos are suppressed by the small parton distribution functions (PDFs) for the heavy quarks inside the proton. Thus, as soon as gluino-pair production becomes kinematically inaccessible, the scenarios reduce to the $D_{\tilde{q}_3}$ cases.

Electroweakino LSPs: We next show the results for wino-LSP production with a non-decoupled gluino in Fig. 2.4(a) and non-decoupled light-flavor squarks in Fig. 2.4(b).

For the gluino case, we see features similar to Fig. 2.3(b). For both couplings, all phase-space regions almost up to the gluino-pair production threshold can be ruled out. Beyond this, the results from $D_{\tilde{W}}$ apply. One interesting feature is the flattening of the exclusion contour for λ_{313} at $m_{\tilde{W}} \sim 1.7\,\text{TeV}$ for gluino masses, $m_{\tilde{g}} \sim 1.7 - 2\,\text{TeV}$. This reduction in sensitivity occurs because the cuts in `ATLAS-RPV-1`ℓ`/SS` place a high demand on the transverse momentum of the six required jets, $p_{\text{T}} > 100\,\text{GeV}$. If the wino and gluino are too close in mass, the jets produced in the gauge decay of the latter may not pass these requirements.

Fig. 2.4(b) is more interesting. We again see that the parameter space roughly up to the squark-production thresholds can be ruled out and we observe the flattening effect mentioned above. However, we also see a new effect. The exclusion limit slightly weakens as we move lower in wino mass. This is

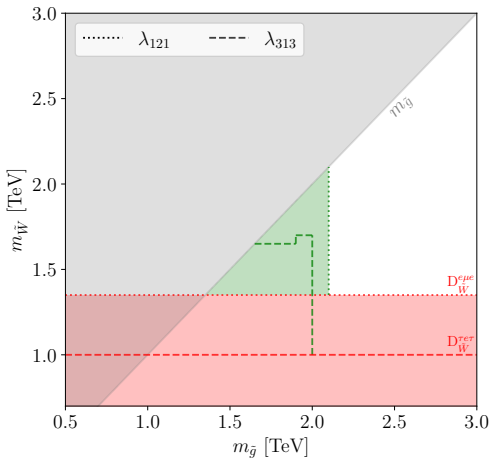

(a) $\tilde{W}$ LSP with non-decoupled $\tilde{g}$.

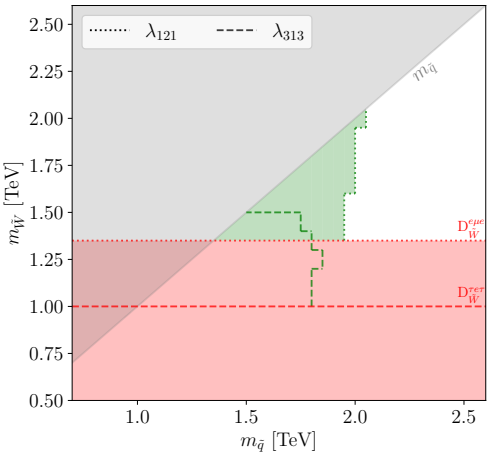

(b) $\tilde{W}$ LSP with non-decoupled $\tilde{q}/\tilde{u}/\tilde{d}$.

Figure 2.4: As in Fig. 2.3 but for the $I_{\tilde{g}\to\tilde{W}}$ (left) and $I_{\tilde{q}\to\tilde{W}}$ (right) scenarios.

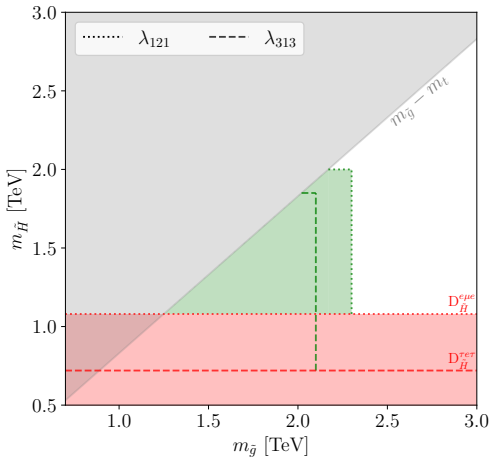

(a) $\tilde{H}$ LSP with non-decoupled $\tilde{g}$.

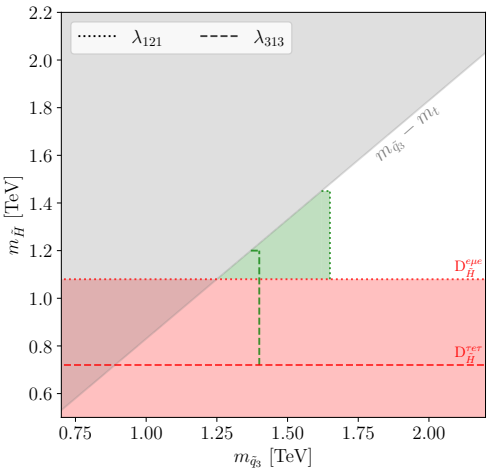

(b) $\tilde{H}$ LSP with non-decoupled $\tilde{q}_3/\tilde{t}/\tilde{b}$.

Figure 2.5: As in Fig. 2.3 but for the $I_{\tilde{g}\to\tilde{H}}$ (left) and $I_{\tilde{q}_3\to\tilde{H}}$ (right) scenarios.

clearly seen for the λ_{121} case but the reduction in sensitivity occurs for both couplings throughout the phase space. This is because squark-pair production can also occur via t-channel wino exchange which can interfere negatively with the QCD contribution [213]; this interference term is bigger for lighter winos.

Next, we show the Higgsino-LSP results for non-decoupled gluinos and non-decoupled third-generation squarks in Fig. 2.5(a) and Fig. 2.5(b), respectively. The exclusion limits show features similar to the earlier cases and are straightforward to interpret. Beyond the pair-production thresholds for the parents, the benchmarks reduce to the respective $D_{\tilde{H}}$ scenarios.

The bino-LSP results are depicted in Fig. 2.6: these correspond to scenarios with gluinos (Fig. 2.6(a)), light-flavor squarks (Fig. 2.6(b)), heavy-flavor squarks (Fig. 2.6(c)), winos (Fig. 2.6(d)), Higgsinos

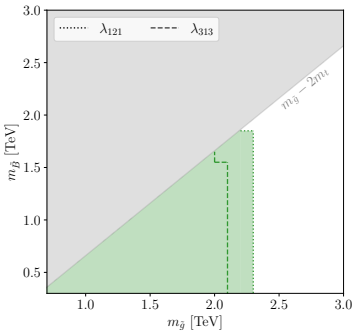

(a) $\tilde{B}$ LSP with non-decoupled $\tilde{g}$.

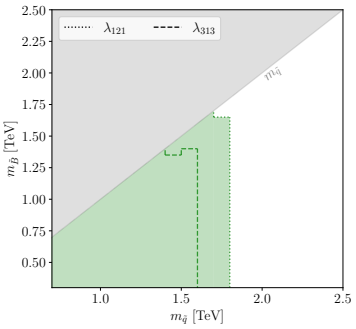

(b) $\tilde{B}$ LSP with non-decoupled $\tilde{q}/\tilde{u}/\tilde{d}$.

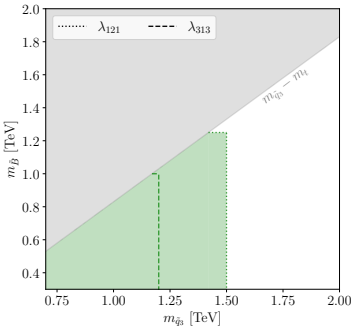

(c) $\tilde{B}$ LSP with non-decoupled $\tilde{q}_3/\tilde{t}/\tilde{b}$.

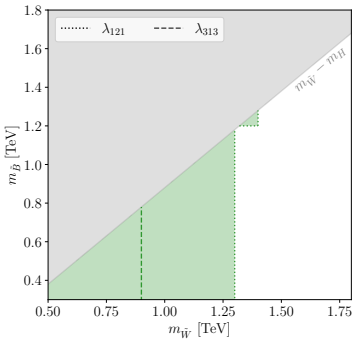

(d) $\tilde{B}$ LSP with non-decoupled $\tilde{W}$.

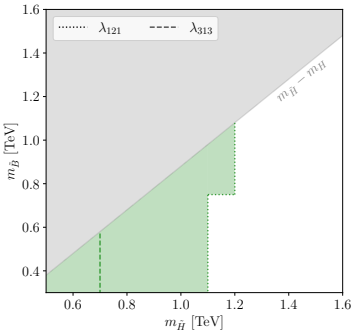

(e) $\tilde{B}$ LSP with non-decoupled $\tilde{H}$.

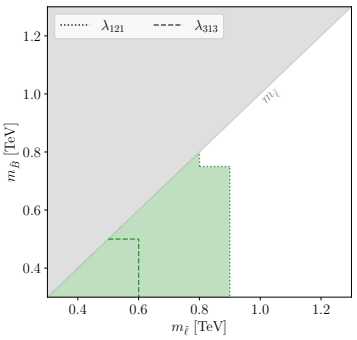

(f) $\tilde{B}$ LSP with non-decoupled $\tilde{\ell}/\tilde{\nu}/\tilde{e}$.

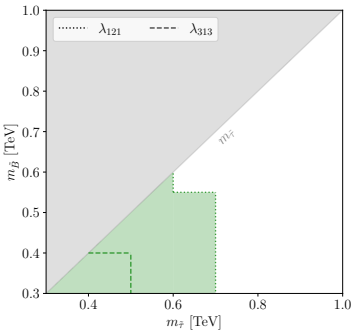

(g) $\tilde{B}$ LSP with non-decoupled $\tilde{\tau}_L/\tilde{\nu}_\tau/\tilde{\tau}_R$.

Figure 2.6: As in Fig. 2.3 but for the $I_{\tilde{x}\to\tilde{B}}$ scenarios.

(Fig. 2.6(e)), light-flavor sleptons (Fig. 2.6(f)), and third-generation sleptons (Fig. 2.6(g)). Generally, the exclusion limits cover almost the whole phase-space region up to the kinematic thresholds for the pair-production of the parents. However, there are a couple of features worth mentioning. First, we see the flattening effect, that we had described for Fig. 2.4, in scenarios $I^{\tau e\tau}_{\tilde{x}\to\tilde{B}}$ with $\tilde{x} = \tilde{q}, \tilde{\ell}, \tilde{\tau}$. The other interesting effect is the slight increase in sensitivity as the $\tilde{B}$ mass increases from very low masses to higher values. This effect can be most clearly seen in Fig. 2.6(e) but is a general feature in the other $\tilde{B}$ plots too. This happens due to the reason mentioned at the beginning of this subsection: for very low bino masses, the decay products are not energetic enough to pass the cuts of the analyses. We did not

encounter it in the case of the other LSPs since the mass scales there were higher.

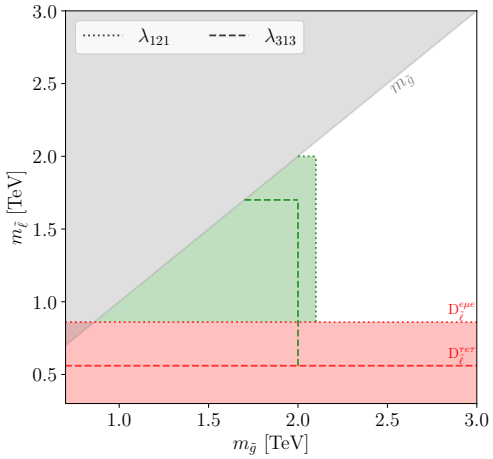

(a) $\tilde{\ell}/\tilde{\nu}/\tilde{e}$ LSPs with non-decoupled $\tilde{g}$.

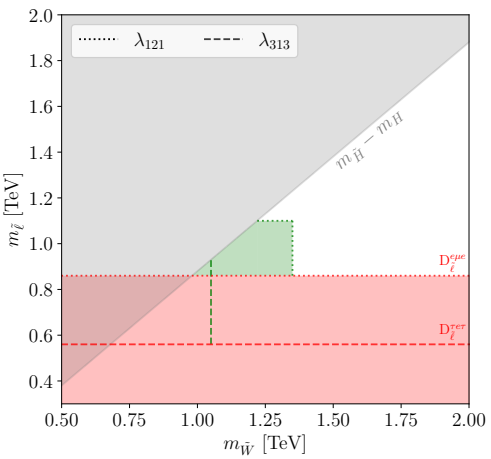

(b) $\tilde{\ell}/\tilde{\nu}/\tilde{e}$ LSPs with non-decoupled $\tilde{W}$.

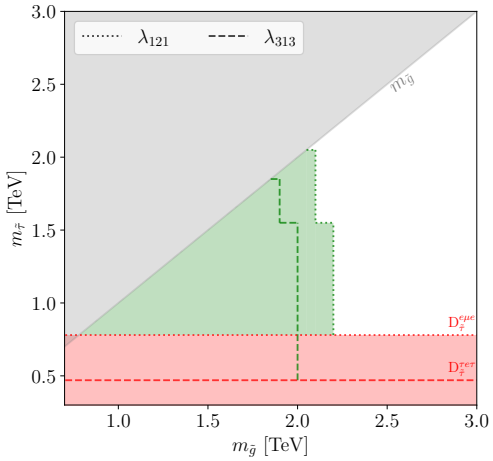

(c) $\tilde{\tau}_L/\tilde{\nu}_\tau/\tilde{\tau}_R$ LSPs with non-decoupled $\tilde{g}$.

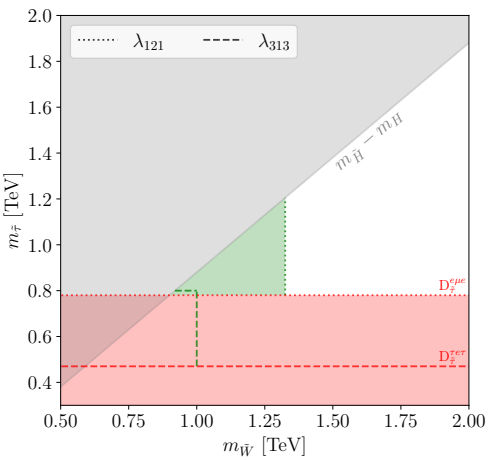

(d) $\tilde{\tau}_L/\tilde{\nu}_\tau/\tilde{\tau}_R$ LSPs with non-decoupled $\tilde{W}$.

Figure 2.7: As in Fig. 2.3 but for the $I_{\tilde{x}\to\tilde{\ell}/\tilde{\tau}}$ scenarios.

Slepton LSPs: Finally, we show the slepton-LSP results in Fig. 2.7. The exclusion limits can extend significantly in the cascade decay due to the much higher production cross-sections of other parent particles compared to direct slepton production.

LSP summary: To summarize, we collect, in Fig. 2.8, the minimum excluded mass for each sparticle, $\tilde{p}$, undergoing a cascade decay (*i.e.*, the minimum limits obtained for each of the $\mathrm{I}_{\tilde{p}\to\tilde{x}}$ scenarios with $\tilde{x}$ the various LSPs), and compare it to the limit obtained from direct production of the sparticle when it is the LSP (*i.e.*, the corresponding $\mathrm{D}_{\tilde{p}}$ scenarios). It is interesting to note that, although cascade decays generally lead to final states with more visible objects, the sensitivity can be both degraded or improved. The reduction in E_T^{miss} and the distribution of energy across more

decay products can reduce the sensitivity. For example, the decay to a slepton or bino LSP yields in most cases the worst limits given that intermediate particles in the decay chain can become soft for compressed spectra, *e.g.*, $\tilde{g} \to 2j + \ell + \tilde{\ell}(\to \ell\nu)$. However, changes in the decay modes due to the varying nature of the LSP can also lead to a higher number of leptons or third-generation quarks which leads to an improvement in the limits. It is worth highlighting that the degradation is around 20% at maximum, and the exclusion limits remain for all sparticles under all variations of LSP hypotheses, LSP masses, and coupling choice.

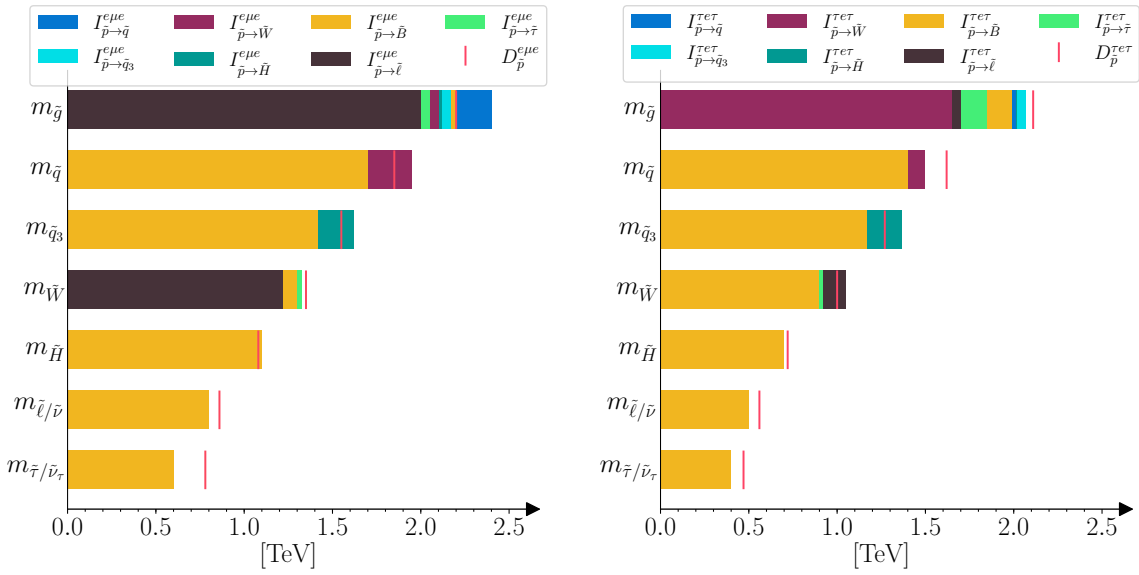

(a) λ_{121}. (b) λ_{313}.

Figure 2.8: Summary of minimum mass bounds on sparticle $\tilde{p}$ across the various $\mathrm{I}_{\tilde{p}\to\tilde{x}}$ benchmarks considered, where $\tilde{x}$ corresponds to the LSPs. The vertical red line represents the direct production mass bound when $\tilde{p}$ is the LSP, *i.e.*, the limit corresponding to $\mathrm{D}_{\tilde{p}}$.

2.5 Conclusions and Outlook

In this paper, we have systematically analyzed the RPV-MSSM and classified the possible signatures at the LHC with the goal of compiling a minimal set of experimental searches that provides complete coverage. Our study provides, for the first time, a completely general and model-independent treatment of the phenomenology, for the case of small RPV couplings. We briefly summarize the central results of the paper:

- As demonstrated, the phenomenological space for the most general RPV-MSSM setup is vast and complicated. Nevertheless, we have shown that just 17 final state topologies (six for $LL\bar{E}$, five for $\bar{U}\bar{D}\bar{D}$, and six for $LQ\bar{D}$) are sufficient to provide complete coverage for the RPV-MSSM at the LHC; we call this the 'RPV Dictionary'. Our signature tables can be generated by using the accompanying `abc-rpv` Python library, described in Appendix A.3.

- Using the 'RPV Dictionary', we have analyzed the current coverage of the RPV-MSSM at the

LHC. In general, we find that even though most RPV scenarios have not been searched for directly, the vast landscape of searches implemented by ATLAS and CMS provides full coverage of the possible RPV-MSSM signatures.

- However, we do point out the need for strong experimental improvements in some of the final states in order to achieve sensitivity to electroweak production cross-sections. Some examples are found for $LQ\bar{D}$ and $U\bar{D}\bar{D}$ decays, such as $\tilde{\ell} \to jj$, $\tilde{\chi}_1^0 \to jb\nu$, and $\tilde{\chi}_1^0 \to jjj$.

- As an application of our framework, and in order to demonstrate the second point above, we have performed numerical simulations specifically for the case of a dominant $LL\bar{E}$ operator (single non-zero coupling at a time), in order to quantitively assess the coverage. We have derived mass bounds on SUSY particles within several RPV benchmark models corresponding to all relevant LSPs. We find that strong exclusion limits comparable to, or even better than, the RPC-MSSM are obtained, and these are robust across the wide range of models. Apart from clarifying the current status of several of these scenarios for which there are no explicit exclusion limits in the literature, our numerical examples demonstrate that our approach of using just a few characteristic topologies to cover the most general RPV-MSSM setting is not merely a reductionist fantasy, but can indeed offer a viable, model-independent search strategy. We have left the detailed analyses of the $LQ\bar{D}$ and $\bar{U}\bar{D}\bar{D}$ cases for future work.

We stress that there are a couple of limitations of our framework. As mentioned in the main body, we require that all decays in the cascade chain are prompt, including that of the LSP. Furthermore, we require that the final state decay products of the LSP are not too soft to be detected. This assumption is crucial and restricts us to scenarios with $m_{\text{LSP}} > O(200\,\text{GeV})$. Further, while we require the RPV coupling to be large enough to cause the LSP to decay promptly, it cannot be too large, as that would modify the pattern of the cascade decays. Similarly, adding exotic particles to the MSSM spectrum that can modify the sparticle decay chains also affects our analysis. In such cases, our classification may not apply anymore. The most important restriction is that our approach – in prioritizing model independence – compromises on search sensitivity for certain scenarios. For example, if the colored sector is always kinematically accessible at the LHC, stricter bounds can be obtained by including the cascade decay products in the search signature, whereas, in our approach, we only target decay products from the LSP. The former approach is usually adopted by ATLAS and CMS in their searches for specific RPV-SUSY scenarios.

On the other hand, we believe our unbiased approach is highly relevant, given that no supersymmetry has yet been discovered at the LHC, and with the HL-LHC era just around the corner. Nevertheless, we have compiled auxiliary tables in Appendix A.2 that can help in designing optimized search strategies in exchange for some model-independence.

As a continuation of this work, we shall pursue a detailed numerical treatment of the $LQ\bar{D}$ and $\bar{U}\bar{D}\bar{D}$ scenarios analogous to the $LL\bar{E}$ case considered in this paper. In those cases, present coverage is less comprehensive and it is important to identify potential gaps. Furthermore, we would like to extend the present work to a systematic study of the large RPV coupling case, affecting both production and decay.

Part II

Prakāśa

3

Lepton PDFs and Multipurpose Single-Lepton Searches at the LHC

3.0 Preface

The contents of this chapter have already been published:

- H. K. Dreiner, V. M. Lozano, S. Nangia, and T. Opferkuch,
  Lepton PDFs and multipurpose single-lepton searches at the LHC,
  Published in Phys. Rev. D 107 (2023) 3, 035011, arXiv:2112.12755 [hep-ph].

3.0.1 Overview

In this chapter, we analyze the potential of discovering RPV-SUSY via resonant squark production at the LHC, initiated by the leptonic content of the proton – the second of the opportunities we had identified in Chapter 1.

As we had discussed in Chapter 1, the naive expectation of this production mechanism being too suppressed to be relevant does not hold. The suppression coming from the smallness of the RPV coupling involved in prodution, and the lepton parton distribution functions (PDFs) can be overcome by the kinematic advantage of single production, the boost in cross-section from resonance, and the clean final state signature. This was demonstrated explicitly in Ref. [49] for the case of leptoquarks, where the production mechanism is analogous to that for squarks. Their results show that the single production mode complements other production channels such as pair production and Drell-Yan by probing large regions of the leptoquark parameter space that are currently unconstrained.

In this chapter, we wish to consider, analogously, the RPV-MSSM case. Once resonantly produced through an initial state lepton and quark via an $LQ\bar{D}$ operator, the squark may decay directly via the same operator, leading to a final state of one lepton and one jet. This is completely analogous to the leptoquark case above, and was the search channel proposed in Ref. [49]. However, depending on the mass-spectrum details, the squark may also have additional decay modes involving complicated cascades down to other sparticles. The cascade mode competes with the direct one and can thus dilute the sensitivity of the one lepton plus one jet channel. However, as we will show in this chapter, even in the case of cascade decays, the RPV-MSSM, largely model-independently, predicts a final state with a single lepton and at least three jets; this retains the quality of being a clean probe of new physics, relatively free from SM background.

Thus, we propose a more generalized "single-lepton channel" with two bins containing: (i) 1 lepton and 1 jet, and (ii) 1 lepton and at least 3 jets. Such a channel, as we shall argue, can be a sensitive probe for new physics, in general, even beyond supersymmetry. However, it has not been searched for

at the LHC, yet. In this chapter, we explicitly demonstrate its ability to probe kinematically accessible squarks in the RPV-MSSM in a largely model-independent way. Through numerical simulations, we find that it has sensitivity to large regions of the RPV-MSSM model space beyond existing bounds coming from pair-production, Drell-Yan, and other existing low-energy experiments. As an example, we find that at the High-Luminosity LHC, the channel will allow us to probe squarks as heavy as $O(3.5\,\text{TeV})$ for an RPV coupling of $\lambda' \approx 0.6$.

In this work, we will restrict ourselves to the case of light leptons and light jets. A dedicated study is required for scenarios involving third generation particles (and squarks) which have very distinct signatures at colliders.

3.0.2 Contributions of the Author

The idea to consider the lepton PDFs in the context of the RPV-MSSM was jointly developed by Herbi Dreiner and Toby Opferkuch, after the latter came across the work in Ref. [49]. The idea to generalize the single-lepton channel to include a mode targeting final states with at least three jets was given by the author of this thesis, after he realized that it allows one to probe the cascade decays in a rather model-independent manner. The cuts in the analysis corresponding to the one lepton plus at least three jets search region were designed and implemented on `CheckMATE 2` by the author. Further, all numerical results, including the simulations of signal and background on `MadGraph5_aMC@NLO`, and the relevant sensitivity limits of the search regions, were provided by the author. The corresponding plots, however, were compiled by Toby Opferkuch, while the existing limits shown in the plots were provided jointly by Víctor Martín Lozano (pair production) and Toby Opferkuch (Drell-Yan and charged current universality).

3.1 Introduction

With the High-Luminosity (HL) era almost upon us, the Large Hadron Collider (LHC) is gearing up for a paradigm shift: A transition from energy upgrades to a focus on increased luminosity. The LHC has already accumulated close to 200 fb^{-1} of data [214]. This will be surpassed in just a single year of HL-LHC runtime, which by its conclusion will increase the total integrated luminosity by a factor 15 overall [215].

Given the breadth of possible observables, such a drastic increase in integrated luminosity places a renewed importance in exploring the question, "Where should we look for new physics?". In contrast to an increase in energy, increases in luminosity do not typically yield dramatic improvements in reach when considering resonantly produced new physics. On the other hand, rare processes, indirect searches, and new trigger techniques – to which the experiments are currently insensitive with the data on tape – can offer promising avenues to explore; current examples include Refs. [216–221]. Such strategies can be more powerful than one may expect. In this work we demonstrate this point explicitly by making the case for a specific example of an unusual signal at the LHC: One light charged lepton, one light jet, and no missing energy – what we will call the *single-lepton channel*.

We mention that an interesting aspect of the kind of lepton-number violating searches we discuss is the fact that they could also be relevant to current topics of interest such as the B-anomalies [222, 223], and the muon $(g-2)$ [224–227]; the variety of models that produce signals of interest to us may also explain these anomalies (see for example Refs. [228–232]).

The outline of this paper is as follows. In Section 3.2, we discuss the single-lepton channel in detail, and argue that it can be applied to a wide range of models with lepton number violating interactions. Section 3.3 discusses its application to the specific context of RPV-SUSY. In Section 3.4, we demonstrate how such a search for RPV-SUSY may be implemented at the LHC. In Section 3.5, we present and discuss our numerical results. We conclude in Section 3.6.

3.2 The Single-Lepton Channel

The final state we are interested in has exactly one energetic[1] first or second generation charged lepton (ℓ), at least one energetic light jet (j), and little or no missing transverse energy ($E_{\text{T}}^{\text{miss}}$). In what follows we refer to this as the single-lepton channel for short.

At first glance this channel is forbidden at hadron colliders in the limit $E_{\text{T}}^{\text{miss}} \to 0$ as the final state is odd in lepton number (discounting the possibility of additional un-tagged soft leptons). Such a channel could still be populated if at least one of the following ingredients is present:

1. Sizeable lepton number violating interactions.

2. A hard process that is initiated by the leptonic content of the proton.

However, the first is bounded by strict low-energy constraints; see, for instance, Refs. [29, 37]. For the second, the leptonic parton distribution functions (PDFs) are suppressed compared to quark or gluon initiated processes as they rely on the splitting function of the photon. The photon density in the proton is low and the splitting adds one more power of the fine-structure constant, α_{EM}. Early work on

[1] There can be additional soft objects from the showering but they will not affect the analysis.

lepton PDFs can be found in Refs. [233, 234]. A higher order calculation has recently been performed in Ref. [235].

Before turning to the details of the proposed search, we first discuss existing single-lepton searches in the literature. Among early experimental work, the only potentially sensitive searches are those by CMS and ATLAS for quantum black holes, such as Refs. [236, 237]. However, these searches require very high multiplicity final states producing a large overall scalar sum $\sum p_T \gtrsim 2\,\text{TeV}$, have no upper limit on $E_{\text{T}}^{\text{miss}}$, and allow for more than 1 charged lepton. In Refs. [238, 239], attempts were made at model-independent searches by considering several hundreds of signal topologies including the ones we are studying here. However, since the datasets considered correspond to small integrated luminosities, and the analyses are not designed to optimally target the single-lepton final state, we expect low sensitivity to our rare signals.

Another related channel was proposed in Ref. [144] (and searched for at the LHC in Refs. [145, 146, 188, 240]) involving a single lepton with high jet multiplicity ($1\ell + nj$, n large) but no $E_{\text{T}}^{\text{miss}}$ cut. This was constructed to be sensitive to several new physics scenarios which may escape high $E_{\text{T}}^{\text{miss}}$ searches. These include lepton number conserving models, in which case the possibly present $E_{\text{T}}^{\text{miss}}$ from neutrinos is diluted due the large number of final state objects. In later work, Ref. [46] demonstrated how such a channel can play a pivotal role in closing the last remaining gaps in natural supersymmetric theories. But the channel is sensitive to more generic models of new physics as well, *e.g.*, composite Higgs models, models producing top-rich final states, or even more exotic phenomena involving high-scale non-perturbative effects.

We propose to go beyond this earlier work by focusing on the related but orthogonal final state: $1\ell + nj$, *n small*. The main difference is that we allow for a significantly lower multiplicity in the final state. The low $E_{\text{T}}^{\text{miss}}$ in such scenarios is not due to dilution as above, but due to lepton number violating processes and/or lepton PDFs. Thus, unlike above, we require a strict upper limit on $E_{\text{T}}^{\text{miss}}$. In Section 3.4, we define two separate search regions to cover what we think are the most relevant scenarios missed so far.

Very recently, Ref. [49] demonstrated that a specific example of the above – a final state with one energetic charged lepton, low $E_{\text{T}}^{\text{miss}}$, and exactly one energetic jet – may probe large unexplored regions of the leptoquark parameter space at the LHC.[2] The s-channel leptoquark resonance is produced via the leptonic PDFs of the proton, mimicking the production at HERA [242–244]. While the result may seem surprising at first due to the suppressed lepton PDFs, the point is that the s-channel resonance has double the kinematic reach compared to leptoquark pair production, and smaller suppression from the leptoquark coupling compared to the Drell-Yan mode. Thus, it can complement these modes [245] by probing regimes where the leptoquark mass is beyond the pair production threshold, while the leptoquark coupling is not large enough for Drell-Yan to be effective. Further, it has a far cleaner signature and a dynamic boost compared to other single production modes. This idea forms the basis for the work that follows: How can these single-lepton searches be generalized to exploit a wide range of new physics appearing in s-channel resonances.

Searches for $1\ell + nj$ with n small are yet to be performed. These would not only target leptoquarks but more generally theories that contain lepton number violation, or even some new interaction between leptons and quarks, such as a heavy partially leptophillic Z' [246]. As an example of the former we will consider R-parity Violating SUSY in what follows.

[2] Also see Ref. [241] for a generalization to the case of third-generation leptons and jets.

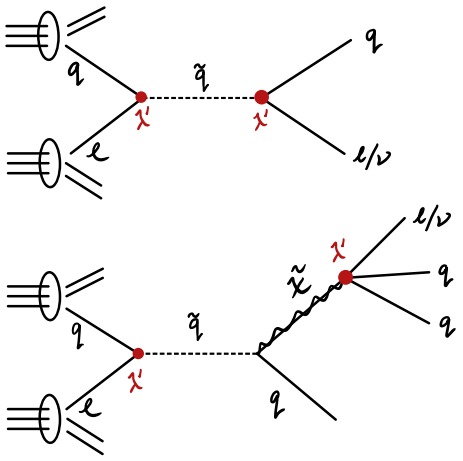

Figure 3.1: Resonant squark produced via the $\lambda'_{ijk} L_i Q_j \bar{D}_k$ operator at the LHC followed by its direct decay mode (top) and decay via an example of a gauge-cascade mode (bottom). Here $\tilde{\chi}$ denotes a chargino or neutralino, lighter than the squark.

3.3 An Application to R-parity Violating Supersymmetry

RPV is the most general realization of the minimal supersymmetric Standard Model (MSSM) where, with the minimal field content, all renormalizable operators allowed under the Standard Model (SM) gauge symmetries are permitted [54]. This has immediate phenomenological consequences, allowing for lepton- and baryon number violating operators. However, a subset must be prohibited (for example, through a discrete symmetry) to ensure the stability of the proton [35, 37, 40, 44, 148, 247, 248]. In the MSSM, the imposed discrete symmetries [147, 249] – *e.g.* R-parity – prohibit the entire set of lepton- and baryon number violating operators.

Allowing some of the RPV terms changes the phenomenology compared to the MSSM in two drastic ways: (a) The lightest supersymmetric particle (LSP) is unstable, and (b) Single production of supersymmetric particles is possible. The latter not only improves our kinematic reach but also provides a mechanism for overcoming the suppression from the lepton PDFs.

The complete superpotential for the RPV-MSSM is given by,

$$W = W_{\text{MSSM}} + W_{\text{LNV}} + W_{\text{BNV}}\,, \tag{3.1}$$

where W_{MSSM} is the usual MSSM superpotential – for details see Ref. [40] – and

$$W_{\text{LNV}} = \frac{1}{2}\lambda_{ijk} L_i L_j \overline{E}_k + \lambda'_{ijk} L_i Q_j \overline{D}_k + \kappa_i H_u L_i\,, \tag{3.2}$$

$$W_{\text{BNV}} = \frac{1}{2}\lambda''_{ijk} \overline{U}_i \overline{D}_j \overline{D}_k\,, \tag{3.3}$$

are the new interactions that explicitly violate R-parity. In the above, $L\,(Q)$ and $\bar{E}\,(\bar{U}, \bar{D})$ refer to the lepton (quark) $\text{SU}(2)_L$ doublet and singlet chiral superfields from the MSSM, respectively, while H_u, H_d label the $\text{SU}(2)_L$ doublet Higgs chiral superfields. The λ's, are dimensionless coupling constants; the κ's are dimension-one mass parameters. All gauge indices are suppressed but we

Cascade End	**Example Decay Chain**	**Final State Signature**
Bino ($\widetilde{B}$)	$\tilde{d}_R \to \tilde{B} + 1j$	$1\ell + 3j$
Wino ($\widetilde{W}$)	$\tilde{d}_R \to \tilde{g}^{(*)} + 1j \to \tilde{q}_L^{(*)} + 2j \to \widetilde{W}^0/\widetilde{W}^\pm + 3j$	$1\ell + 5j$
Gluino ($\tilde{g}$)	$\tilde{d}_R \to \tilde{g} + 1j$	$1\ell + 3j$
Doublet squark ($\tilde{q}_L$)	$\tilde{d}_R \to \tilde{g}^{(*)} + 1j \to \tilde{q}_L + 2j$	$1\ell + 3j$
Up-type singlet squark ($\tilde{u}_R$)	$\tilde{d}_R \to \tilde{g}^{(*)} + 1j \to \tilde{u}_R + 2j$	$1\ell + 5j$
Doublet charged slepton ($\tilde{e}_L$)	$\tilde{d}_R \to \tilde{g}^{(*)} + 1j \to \tilde{q}_L^{(*)} + 2j \to \widetilde{W}^{0(*)} + 3j \to \tilde{e}_L + 1\ell + 3j$	$1\ell + 5j$
Sneutrino ($\tilde{\nu}_L$)	$\tilde{d}_R \to \tilde{g}^{(*)} + 1j \to \tilde{q}_L^{(*)} + 2j \to \widetilde{W}^{\pm(*)} + 3j \to \tilde{\nu}_L + 1\ell + 3j$	$1\ell + 5j$
Singlet charged slepton ($\tilde{e}_R$)	$\tilde{d}_R \to \widetilde{B}^{(*)} + 1j \to \tilde{e}_R + 1\ell + 1j$	$3\ell + 3j$

Table 3.1: Decay chains and final state signatures resulting from a resonantly produced down-type squark ($\tilde{d}_R$) in the case of $\lambda' \neq 0$. The first column indicates the supersymmetric particle involved in the final step of the decay chain, which is typically the LSP. We give a representative decay chain for each case that populates the single-lepton channel, as well as the total signature in the final column. $(*)$ indicates possibly off-shell.

explicitly write the generational ones: $i, j, k = 1, 2, 3$, with a summation implied over repeated labels.

Consider just a single LQD operator in the superpotential, *e.g.*, $\lambda'_{111} L_1 Q_1 \bar{D}_1$. The simplest possibility leading to a single-lepton signal via this operator requires a spectrum with only a light squark, $\tilde{d}_R$ or $\tilde{u}_L$. Given no other supersymmetric particles lighter than the squark, and taking into account the lepton PDFs, the dominant process is an s-channel squark resonance, illustrated in the top diagram of Fig. 3.1. Here the squark decays back to the initial state, as it is the LSP. This is analogous to the scalar leptoquark scenarios considered in Ref. [49], leading to a final state comprised of a single lepton plus one jet. In contrast to leptoquark models, supersymmetry typically predicts new states lying below the squark masses [250, 251], such that the squark would cascade via gauge couplings, typically all the way down to the LSP. In Table 3.1 we list possible final state signatures for $\tilde{d}_R$ as a function of the particular state lying below the squark mass. The branching ratios into these final states is determined via the relative size of the RPV coupling versus the gauge couplings, as well as details of the mass spectrum, see Refs. [45, 47, 48]. A canonical example is an LSP bino-like neutralino [74] giving rise to the extended decay chain depicted in the bottom diagram of Fig. 3.1. Upon its production from the squark, the bino-like neutralino decays via the RPV operator resulting in a final signature with three jets plus the desired single lepton.

Surveying the final states in the last column of Table 3.1, we observe that the single-lepton channel can be populated irrespective of the supersymmetric particle involved in the final step of the decay cascade. The only exception is a decay chain featuring a light charged slepton $\tilde{e}_R$, where two additional charged leptons result.[3] There are however limitations to this analysis. As stated above the cascade details depend sensitively on the mass spectrum, as well as the size of the RPV coupling, λ', relative to the gauge couplings [48]. Fortunately, the latter does not modify the above conclusions. The large value of the strong coupling means that additional steps in the decay chains typically only increase jet multiplicity. Therefore, the single-lepton channel provides a sensitive probe irrespective of the model details, allowing us to implement a largely model-independent search strategy. We now turn to the details of how such a strategy can be implemented at the LHC.

[3] The case of additional leptons is more constrained by existing searches, see Ref. [46].

3.4 Implementation

We first organize the framework of our analysis in a way that allows us to be model independent. We then discuss our analysis strategy in detail, describing the signal regions and the main backgrounds involved.

3.4.1 Framework

In order to probe the RPV model, and other new physics scenarios that populate the single-lepton channel, it is useful to separate it into two distinct signatures: (a) $1\ell + 1j$ (SR_ej), and $1\ell + (\geq 3j)$ (SR_e3j). The branching ratios satisfy:

$$\mathrm{BR}\,(1\ell + 1j) + \mathrm{BR}\,(1\ell + \geq 3j) + \mathrm{BR}\,(\text{other}) = 1\,. \tag{3.4}$$

Here, BR(X) refers to the branching ratio for the resonantly produced squark to decay into the final state X. $\ell = e$ or μ, and j is any (light) SM jet. Direct decays of the squark via an LQD coupling contribute to BR($1\ell + 1j$), just like a leptoquark. From Table 3.1, we see that the BR($1\ell + \geq 3j$) channel gives us almost complete coverage of the possible cascade modes. BR (other) takes into account the squark decays *not* covered by the single-lepton channel, *e.g.*, as in the last line of Table 3.1.[4] The separation as in Eq. (3.4) allows us to experimentally distinguish between pure scalar leptoquark theory and a more complicated spectrum and decay pattern as for example in RPV superymmetry.

Analytic expressions exist for the RPV-SUSY 2- or 3-body final states contributing to the branching ratios appearing in Eq. (3.4) [253]. For the more complicated decay chains, numerical methods are necessary, see for example the tools HERWIG [254, 255], SPheno [256] and MadGraph5_aMC@NLO [201]. The analytic branching ratios even for the simpler decay chains are complicated expressions of the relevant supersymmetric parameters. Thus, we take the branching ratios in Eq. (3.4) as our free parameters. This also underlines our model-independent approach, as these branching ratios could easily be computed in any other model leading to the cascade decay of a resonance.

We now discuss the specifics of the search strategy, targeting the two signal regions $1\ell + 1j$ (SR_ej) and $1\ell + (\geq 3j)$ (SR_e3j).

3.4.2 Signal Region: SR_ej

The $1\ell + 1j$ mode for a squark corresponds exactly to a decaying single leptoquark, as investigated in Ref. [49]. We briefly review this, and implement it analogously. We require one negatively charged electron or muon,[5] and one light jet and label the signature as SR_ej. Since we expect the mass of the squark decaying into the lepton and jet to be $O(1\,\mathrm{TeV})$, we impose rather strict requirements on the transverse momentum of both objects:

$$p_{\mathrm{T}}(\ell),\ p_{\mathrm{T}}^{\mathrm{jet}} > 500\,\mathrm{GeV}\,, \tag{3.5}$$

[4] An extended RPV sector with multiple non-zero couplings could lead to further squark decays, possibly contributing to BR (other). However, note the strict bounds on products of couplings from flavor changing neutral currents [29, 252] and from proton decay [58, 60].

[5] The positively charged lepton mode is slightly PDF suppressed, by the different luminosities of u- and d-quarks in the proton. Of course, at high energies, one must also consider how well charge identification can perform but we consider 100% efficiency here.

with a pseudorapidity cut, $|\eta| < 2.5$. Z-boson, top quark, and QCD backgrounds are reduced by imposing a veto on events with an extra lepton with $p_T > 7\,\text{GeV}$ (and $|\eta| < 2.5$), or an extra jet with $p_T > 30\,\text{GeV}$ (and $|\eta| < 2.5$). W-boson backgrounds are reduced by requiring $E_T^{\text{miss}} < 50\,\text{GeV}$.

With the above basic cuts, two non-negligible backgrounds remain: Single W^- production in association with jets (with the W^- decaying leptonically), and QCD multijet production, where one of the jets is misidentified as a lepton. In Ref. [49] the other backgrounds are plotted; they constitute less than $O(5\%)$ of the total background in the major part of the phase space. We thus neglect them here. See also the cutflow table corresponding to the benchmark point of Eq. (3.8) in Table 3.2.

The strategy for this signal region is to look at the invariant mass distribution formed by the leading lepton and jet. The signal is expected to peak in a narrow region around the squark mass, while the background falls monotonically. We present numerical results for our benchmark scenario in Section 3.5.

3.4.3 Signal Region: `SR_e3j`

In this signal region we require one charged electron or muon (or their antiparticles), and at least three jets; we label it as `SR_e3j`. Here, we do not restrict ourselves to only the negatively charged leptons as the cascades in Table 3.1 involve Majorana fermions, *e.g.*, the neutralinos or the gluino, which decay into a final state or its charge conjugate with equal probability.

We implement the following basic cuts for the leading lepton and the three leading jets:

$$p_T(\ell) > 200\,\text{GeV}\,, \tag{3.6}$$

$$p_T^{\text{jet}_1},\ p_T^{\text{jet}_2},\ p_T^{\text{jet}_3} > 50\,\text{GeV}, \tag{3.7}$$

with all objects required to have $|\eta| < 2.5$. As before, to reduce Z-boson backgrounds, we veto events with an extra lepton (satisfying $p_T > 7\,\text{GeV}$ and $|\eta| < 2.5$). Top backgrounds are reduced by a b-jet veto. However, unlike the `SR_ej` case, we do not veto events with extra light jets.

A useful category of cuts is provided by scalar sums of energies of the final state objects. These mostly depend on the energy scales involved and not on the cascade details. We employ two: the sum of $|p_T|$ of all reconstructed jets, H_T; and the total scalar sum of the $|p_T|$ of all reconstructed objects and the missing transverse energy, S_T. We require $H_T > 900\,\text{GeV}$, and $S_T > 1\,500\,\text{GeV}$. We reduce the W-boson background by requiring $E_T^{\text{miss}} < 50\,\text{GeV}$.

With the above cuts, to a good approximation, the main backgrounds are associated single W, associated $t\bar{t}$, and QCD multijet production. One can find the relevant backgrounds plotted as a function of H_T in Ref. [257], where the analysis has some overlap with the cuts we make. There, one can see that the other backgrounds make up less than $O(5\%)$ of the total background. Actually, in our case, the $t\bar{t}$ background is also expected to be much smaller than the associated W one. In general, the former only becomes significant relative to the latter, when one requires a large number of jets in the final state, or if the jets have lower energies.[6] Since our final state of interest only has a few jets and these are energetic, we will focus on the W+ jets and the QCD multijet backgrounds. See also the cutflow table corresponding to the benchmark point of Eq. (3.8) in Table 3.3; we show the $t\bar{t}$ numbers too for comparison, but we do not include them in our numerical studies.

[6] For instance, see the relative contributions of the two backgrounds (in the zero b-jet tag bin) as a function of the number of jets and the energies required in Refs. [145, 240].

We note that in designing the above cuts, we have chosen generality over optimality. The kinematical configuration of the final state objects is decided by the details of the gauge cascade, which in turn depend on the SUSY mass spectrum, to which we choose to remain blind in our approach. Finally, our strategy is to look at invariant mass distributions for the squark and the particle at the end of the cascade (typically the LSP).

3.4.4 Other Signatures

So far we have only focused on resonant squark production at the LHC via the lepton PDFs. Here we briefly mention that a non-zero λ', as we have been considering, can also lead to resonant *slepton* production via quark PDFs.[7] The direct decay gives a resonance bump in the 2-jet cross-section. The cascade decay via a neutralino LSP leads to the promising signature of like-sign dileptons [165, 166, 259]. More relevant to the search presented here is the decay of the neutralino to a neutrino and 2 jets, giving an overall signature of 1 lepton + 2 jets and $E_{\mathrm{T}}^{\mathrm{miss}}$ from a neutrino. However, with 2 jets and possibly a large amount of $E_{\mathrm{T}}^{\mathrm{miss}}$, this is orthogonal to the search at hand, and we do not further consider it. We now present some numerical results.

3.5 Results and discussion

3.5.1 Numerical Setup

For the results presented here, we have generated event samples corresponding to center-of-mass energy $\sqrt{s} = 13\,\mathrm{TeV}$, using the program `MadGraph5_aMC@NLO` [201] linked to `PYTHIA 8.2` [202] for showering and/or decays. Once showered, the event samples are passed through our analysis which has been implemented in `CheckMATE 2` [204–208]; detector effects are accounted for by the linked `DELPHES 3` [210] component. For all electrons in our analysis, we have used the `ATLAS` 'Tight' criterion implemented in `CheckMATE 2` while for jets we use the anti-k_{T} algorithm implemented in `FastJet`, which is the `CheckMATE 2` default. We choose the cone size $\Delta R = 0.4$.

We have generated the signal samples using the `UFO RPV-SUSY` model file available at Ref. [203]. We use the lepton PDFs calculated in Ref. [235], which have been implemented in the `LHAPDF` [260] setup. One subtle point is the handling of initial state leptons during showering; here we have followed the prescription described in Ref. [49]. Note that we have only generated the signal sample at leading order (LO). Both NLO (next-to-leading order) QCD and NLO QED corrections [261, 262] relying on the photon PDF can be significant, but they contribute with opposite signs and comparable magnitudes, leading to a milder-than-expected net correction of $O(10\%)$ to the LO cross-section [263]. This would be important to consider in precision studies; this is not the focus of the present work.

We define the following benchmark scenario that we use to present most of our results in this section:

$$\lambda'_{111} = 0.4\,,\ M_{\tilde{u}_L} = M_{\tilde{d}_R} = 2\,\mathrm{TeV}\,,\ M_{\mathrm{LSP}} = 1\,\mathrm{TeV}\,. \tag{3.8}$$

The above choice is motivated by current LHC squark limits, while the LSP can be drastically lighter [264]. The value of λ'_{111} is chosen to lie near current constraints from low-energy experi-

[7] Note that the bound on λ'_{111} from neutrinoless double beta decay [252, 258] is strongly model dependent and is not relevant for a heavy neutralino and gluino as we discuss here.

Cuts	**Signal**	**W^- + jets**
Generator Level	91	11050
Leading lepton $p_T > 500$ GeV	37	3274
Leading jet $p_T > 500$ GeV	34	2183
$E_T^{miss} < 50$ GeV	21	750
Veto	10	278

Table 3.2: Cutflow corresponding to the basic cuts for SR_ej for 100 fb^{-1} of integrated luminosity. For the signal, the generator level cuts are are the default MadGraph5_aMC@NLO values. For the associated W^- background, an additional cut of $p_T > 400$ GeV on the lepton has been applied. This is why it appears as if the lepton p_T cut affects the signal more than the background, degrading the signal to background ratio; this is a superficial effect. Lastly, the final veto step actually dilutes the signal ratio against the W^-+ jets BG. However, as explained in the main body, it is crucial in reducing the Z-boson, top and QCD backgrounds, which would otherwise dominate over the signal.

ments [252, 265]. We stress that in the above we do not specify the nature of the LSP, or the details of the SUSY parameters. Instead, as mentioned earlier, we treat the branching ratios as the free variables that capture all the relevant information. We do however assume that no RPV coupling other than λ'_{111} contributes to our two signal regions.

For the W^-+ jets background corresponding to SR_ej, we use MadGraph5_aMC@NLO to generate one electron, one anti-neutrino plus one jet at LO in QCD. We have not included the electroweak contribution. We deal with the issue of low statistics in the high-p_T region by implementing a generator level cut on the lepton: $p_T > 400$ GeV, and through phase-space splicing. We split the phase space into several regions based on the p_T of the electron, and then glue them together at the end to get a continuous distribution. We account for NLO QCD corrections by employing a k-factor. In general, k-factors are phase-space dependent; to ensure we get a value that is appropriate for our region of interest, we use MadGraph5_aMC@NLO to calculate the total cross-sections for the above process at LO and NLO in the phase-space region where the electron has $p_T > 400$ GeV. Taking the ratio, this gives us a k-factor of 1.61. We have validated our obtained background against Ref. [49] and find good agreement. We depict the cutflow corresponding to the cuts of SR_ej for the background and the benchmark signal point in Table 3.2.

For the QCD multijet background, ATLAS and CMS usually use data-driven studies over simulation. We use the numbers provided in Ref. [49]; these have been read off from a data-driven study by ATLAS in Ref. [266].

For the W+ jets background in the case of SR_e3j, we use MadGraph5_aMC@NLO linked to PYTHIA 8.2 to generate one electron, one anti-neutrino plus up to 3 jets (and the charge conjugated process) at LO accuracy in QCD using the MLM prescription [267–269], with the xqcut scale set to 70 GeV; we have checked that this gives smooth differential jet rate (DJR) distributions for our process and energy scale [270]. We have not included the electroweak contribution. To obtain sufficient statistics in the tail of the distribution, we again use generator level cuts: lepton $p_T > 150$ GeV, $iH_T > 800$ GeV, and $E_T^{miss} < 50$ GeV, and phase-space splicing and gluing—this time relying on splits based on the iH_T (inclusive scalar sum of jet energies) variable available in MadGraph5_aMC@NLO.

Cuts	Signal	W+ jets	$t\bar{t}$
Generator Level	130	9565	2615
b veto	118	8389	539
Leading lepton $p_T > 200\,\text{GeV}$,			
Extra lepton veto	32	3787	114
$p_T^{\text{jet }1,2,3} > 50\,\text{GeV}$	29	2562	72
$iH_T > 900\,\text{GeV}$	25	1892	26
$S_T > 1\,500\,\text{GeV}$	21	935	10
$E_T^{\text{miss}} < 50\,\text{GeV}$	12	417	3

Table 3.3: Cutflow corresponding to the basic cuts for SR_e3j for $100\,\text{fb}^{-1}$ of integrated luminosity. For the signal, the generator level cuts are the default MadGraph5_aMC@NLO values. For the associated W ($t\bar{t}$) background, extra cuts are used on top of the default ones: Lepton $p_T > 150\,\text{GeV}$, $iH_T > 800\,\text{GeV}$ ($500\,\text{GeV}$), and $E_T^{\text{miss}} < 50\,\text{GeV}$. Consequently, the detector level cuts appear to suppress the signal more strongly that the background.

We account again for NLO effects by employing a k-factor. Here we take the ratio of the total cross-sections for associated W production at NLO and LO with the default MadGraph5_aMC@NLO cuts which gives us a k-factor of 1.286. We expect this to be an overestimate since the k-factor decreases both in the relevant region of phase space [271, 272], as well as when requiring a larger number of associated jets. This avoids the computationally intensive task of calculating the full NLO cross-section with 3 extra partons; similar approaches have been employed by ATLAS and CMS in Refs. [273, 274], and we emphasize that this produces conservative results. We depict the cutflow corresponding to the cuts of SR_e3j for the background and the benchmark signal point in Table 3.3.

We do not calculate the QCD multijet background but rather include it as an extra 30% contribution to the final number of background events after our cuts. This is a very rough estimate using the background distributions plotted in Ref. [257], and accounting for the fact that the extra missing energy cut we make in our analysis targets the W-boson more effectively than it will target multijets. We will study the importance of this assumption in Fig. 3.2.

For SR_ej, after passing the samples through the basic cuts, we look at the invariant mass distribution of the leading lepton and leading jet to reconstruct the squark mass. The width of the bins, for a narrow resonance, is determined by the experimental resolution. Here, we choose it to be approximately 10% of the invariant mass.

For SR_e3j, we first reconstruct the invariant mass distribution for the particle at the end of the cascade, choosing a rather broad binning size of 400 GeV.[8] For events in each bin, we then reconstruct the squark mass by looking at the invariant mass distribution formed by all reconstructed objects, selecting the binning width to be approximately 10% of the invariant mass.

[8] In a spectrum-blind approach, one does not know which final state objects originate from the decay of the cascade-end particle. Experimentally this requires looking at multiple distributions formed by combinations of the reconstructed electron and jets; see, for instance, Ref. [275]. Here we work with simulations where the cascade-end is fixed which means we do not go through this procedure. However, our chosen broad binning size compensates to account for possible inefficient matching between the reconstructed objects and the true parton level decay products.

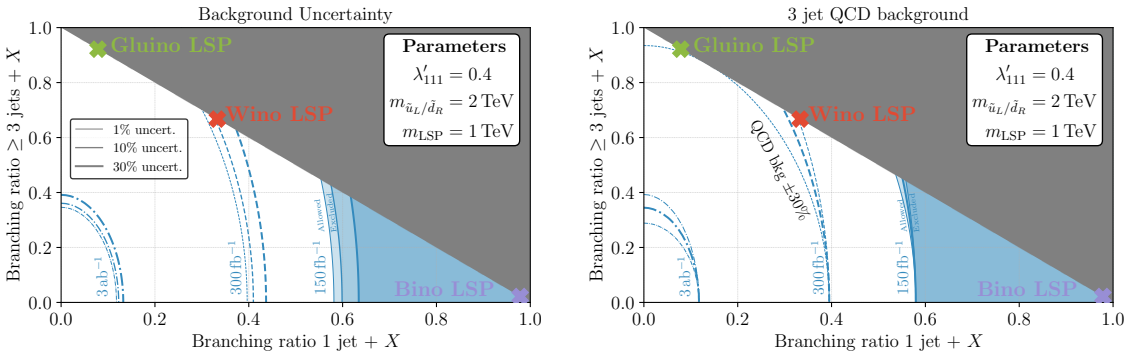

Figure 3.2: Projected constraints based on integrated luminosities of (150, 300, 3000) fb^{-1} shown as blue-(solid, dashed, dot-dashed) contours. These constraints are shown as a function of the branching ratios into the two channels: (*i*) 1 jet + X, (*ii*) ≥ 3 jets + X where X denotes either an electron or a neutrino. As reference points, we show the expected branching ratios for an RPV model featuring a 1 TeV gluino, bino or wino-LSP, see Section 3.4.1 for more details. **Left:** We vary the systematic uncertainty on the background predictions in both channels (1%, 10% and 30%) showing how the exclusion limits change. **Right:** We study how varying the QCD background rate for the three jet channel from the assumed 30% affects our results.

Finally, we calculate the potential exclusion significance [276] for both `SR_ej` and `SR_e3j` by reading off the signal and background numbers in each squark bin and select the highest value as the resulting significance.

3.5.2 Search Sensitivity

We present the projected 95% confidence level (CL) exclusion limits corresponding to the benchmark scenario, Eq. (3.8), for the current data on tape (150 fb^{-1}), as well as projections for the HL-LHC using 300 fb^{-1} and 3 ab^{-1} of integrated luminosity in Fig. 3.2.[9] The projections are shown in a model-independent manner as a function of the branching ratios of Eq. (3.4). We depict on the figure where a supersymmetric model with a 1 TeV gluino-, wino-, or bino-like LSP, respectively, would lie, assuming the resonantly produced squark is the NLSP. Here we have assumed that λ'_{111} is the only non-zero RPV coupling, and no other decays are open. Therefore, they all lie on the line,

$$\text{BR}\,(X + 1j) + \text{BR}\,(X+ \geq 3j) = 1\,. \tag{3.9}$$

We have combined the decay modes corresponding to a charged lepton and a neutrino into a single branching ratio, namely $X \equiv \ell$ or ν. This is convenient for the normalization since in the RPV-MSSM, neglecting lepton masses, the two modes are symmetric to a very good approximation. Our analysis still targets only the charged lepton, *e.g.*, $\text{BR}\,(1\ell + 1j) = 0.5 \times \text{BR}\,(X + 1j)$.

We emphasize that Fig. 3.2 can be used to re-interpret the results for any model. For example, for an additional significant non-zero λ_{121}, we would obtain decays with more than 1 charged lepton in the final state, resulting in a non-zero BR(other),

$$\text{BR}(X + 1j) + \text{BR}(X+ \geq 3j) < 1\,. \tag{3.10}$$

[9] This is assuming no discovery is imminent at the projected reach.

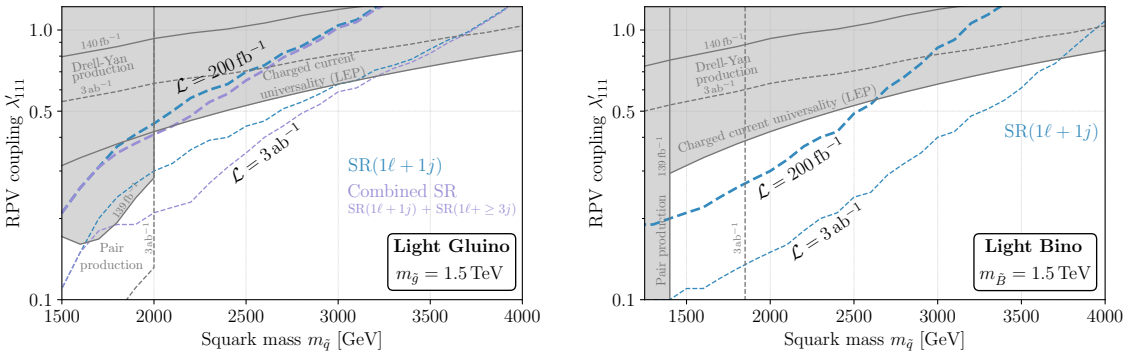

Figure 3.3: The search sensitivities of the single-lepton channel for the light gluino (left) and light bino (right) scenarios corresponding to two different integrated luminosities: $200\,\text{fb}^{-1}$ (thick lines) and $3\,\text{ab}^{-1}$ (thin lines). For the gluino case, the reach of the `SR_ej` search is shown in turquoise and the combined reach of `SR_ej` + `SR_e3j` is shown in purple. For the bino case we just show the reach of `SR_ej`. In both plots we show in gray the area excluded by existing experiments: Drell-Yan [277], charged current universality [278] and squark pair production [213, 279, 280], with each region labeled by its corresponding cause of exclusion. Finally, we show the projected limits assuming $\mathcal{L} = 3\,\text{ab}^{-1}$ for both Drell-Yan, and squark pair production as dashed grey lines.

Such a model would lie in the lower left triangle.

Fig. 3.2 shows that, even with current data, the single-lepton channel can probe large regions of the RPV model space (for instance, the Bino LSP scenario) corresponding to the benchmark point, allowing us to go beyond existing bounds. By the end of HL-LHC runs, nearly the whole space of models corresponding to the benchmark can be probed.

The figure also studies how systematic uncertainties, and our assumption about the QCD background in `SR_e3j` affect our results.

In a next step, we study how the exclusion limits depend on the mass of the squarks and the RPV coupling. We assume $\tilde{u}_L$ and $\tilde{d}_R$ are mass-degenerate, and consider two simplified setups, corresponding to a 1 500 GeV gluino, and a 1 500 GeV bino, respectively, with the rest of the SUSY spectrum decoupled. As before, we also require λ'_{111} to be the only non-zero RPV coupling. The results for the light gluino (left) and light bino (right) scenarios are shown in Fig. 3.3, neglecting systematic uncertainties. We summarize the results of Fig. 3.3 in Table 3.4, depicting the most stringent current bound on λ'_{111} and comparing it with the bound implied by the single-lepton search.

The turquoise line corresponds to the signal region `SR_ej` while the purple line shows the combination of both signal regions `SR_ej` + `SR_e3j`. The thick lines show the search sensitivity for an integrated luminosity of $\mathcal{L} = 200\,\text{fb}^{-1}$ while the thinner lines correspond to $\mathcal{L} = 3\,\text{ab}^{-1}$. The figure also depicts other current relevant bounds as shaded gray regions. Currently the most stringent constraints at large squark masses come from charged current universality measurements at LEP [278]. We have also recast limits from existing pair production [279] and Drell-Yan searches [277], as well as a projection of their reach at HL-LHC determined by assuming $\mathcal{L} = 3\,\text{ab}^{-1}$.

For the light gluino case, the most constraining current exclusion limits are from charged current universality, reaching values of $\lambda'_{111} > 0.3$ for $m_{\tilde{q}} \sim 1\,500$ GeV and $\lambda'_{111} > 0.8$ for $m_{\tilde{q}} \sim 4\,000$ GeV, and from squark pair production that is powerful for low masses, reaching $\lambda'_{111} > 0.16$ for masses of the squarks between $1600 - 1700$ GeV. The pair-production exclusion region below about 2 000 GeV has a slope because the search relies on the direct decay mode of the squark; higher mass squarks

$M_{\tilde{u}_L} = M_{\tilde{d}_R}$	λ'_{111} Current Bound	λ'_{111} Single Lepton Channel	
		$200\,\text{fb}^{-1}$	$3\,\text{ab}^{-1}$
1.5 TeV	0.17 (0.315)	0.21 (0.21)	0.11 (0.11)
2 TeV	0.28 (0.42)	0.41 (0.3)	0.21 (0.15)
2.5 TeV	0.525	0.65 (0.48)	0.35 (0.24)
3 TeV	0.63	1.0 (0.83)	0.58 (0.39)
3.5 TeV	0.735	1.49* (1.37*)	0.8 (0.59)

Table 3.4: Summary of Fig. 3.3. The table compares the best existing bounds (from pair production, Drell-Yan, and LEP) on λ'_{111} and compares it to the bounds implied by the single-lepton search from Fig. 3.3 for various squark masses, for the light gluino (bino) scenarios. For values marked with an asterisk, the perturbativity constraint is stronger.

need a higher RPV coupling to have a sufficient branching ratio for this mode. For squark masses between 1500 – 1600 GeV, the exclusion deteriorates slightly. The experimentally observed data in this regime are above the expected ones while for higher masses, both observed and expected match; see Ref. [279]. The search only excludes squark masses up to 2 000 GeV. Thus, the shaded area extends vertically at this point.

We see that the single-lepton channel probes phase-space regions complementary to those probed by pair production and Drell-Yan, as explained in Section 3.2. Further, it has the potential to compete with/outdo the existing charged current universality constraints, with the added advantage of being a direct search.

For a light gluino, the squarks can have a significant branching ratio into the cascade mode since it proceeds via the strong coupling. To see this, we depict the sensitivity contour corresponding to `SR_ej` alone (turquoise), and to `SR_ej` + `SR_e3j` combined (purple). For low squark masses, `SR_e3j` is relatively unimportant since the squarks have no phase space to decay into the gluino; the direct decay dominates. As the mass increases, the relative importance of `SR_e3j` grows. At very high masses, it becomes less important again because the large λ'_{111} coupling – required to have a sufficiently high signal rate – leads to the direct decay rate increasing as well.

The light bino case is shown in the right plot of Fig. 3.3. Current searches such as Drell-Yan and charged current universality behave as in the gluino LSP case and so they cover almost the same parameter space. However, the squark pair production only reaches values up to 1 400 GeV. As the gluino is now decoupled, the contribution due to t-channel gluino exchange is missing leading to a smaller cross-section. Further, there is no dependence on the coupling since, with the bino kinematically inaccessible in this region, the squark dominantly decays directly with branching ratio nearly 1.

As before, the single-lepton channel is complementary to the existing searches, extending the potential reach. However, the only mode with power of exclusion here is `SR_ej`. The branching ratio of the cascade mode via the bino is small leading to a low sensitivity of `SR_e3j`. Correspondingly, we have not included the `SR_e3j` curves. In comparing with the gluino LSP case on the left, we see that the single-lepton channel excludes more parameter space here. This is because of the higher branching ratio of the direct decay, contributing to `SR_ej`; this mode has a cleaner signature and hence higher exclusion potential than `SR_e3j`.

We note that our proposed search outperforms high-luminosity projections of the searches based on

Drell-Yan and squark pair production (see dashed gray lines in Fig. 3.3). The Drell-Yan constraints begin to be competitive at very high masses; although they are still surpassed by constraints from LEP measurements. On the other hand, for pair production, the reach improves for low squark masses, reaching $m_{\tilde{q}} = 2\,\text{TeV}$ in the light gluino case, and $m_{\tilde{q}} = 1.8\,\text{TeV}$ in the light bino case. These projections are based on current searches, which place a strict cut of 2 TeV on the squark masses. This limits the sensitivity of our projections. Nevertheless, this last search is powerful for low masses exhibiting strong complementarity with the search proposed in this work.

An interesting observation is that `SR_ej` is quite powerful even in cases where the squark has low BR into the direct mode, *e.g*, the light gluino scenario, left plot in Fig. 3.3. This shows that a simple resonance $1\ell + 1j$ search is also a powerful probe of the entire RPV space, even with a more complicated spectrum; not just the leptoquark-like scenario. On the other hand, `SR_e3j` apart from extending the reach of the searches (particularly at high-luminosities), will be crucial to distinguish between leptoquarks and squarks in case of a discovery.

It is also important to emphasize that even though we have considered simplified setups, with most of the SUSY spectrum decoupled, our results are more general. For instance, we would realistically expect the sleptons and electroweakinos to also be light in the light gluino case. In such a scenario, new gauge-cascade chains can open up for the resonant squark, thus diluting the direct and gluino decay modes. However, the signals from these distinct chains will simply add up with those from the gluino mode in the `SR_e3j` bin, as long as the end point of all the cascades is the same. This is exactly what happens, for instance, for small RPV couplings, where all gauge-cascade chains end in the LSP.

Finally, we note that one can perform completely analogous studies for LQD operators involving second generation fermions. For a coupling with a second generation lepton, *e.g.*, λ'_{211} we expect the limits to weaken only slightly as the muon PDFs are only mildly suppressed relative to the electron ones [235]. The case of second generation quarks is slightly more involved. For λ'_{111} the dominant production mode is $eu \to \tilde{d}$ versus $ed \to \tilde{u}$, roughly in the ratio 2:1. Thus, we would expect the case λ'_{112} to be only mildly suppressed compared to our present analysis, whereas the case λ'_{121} to be more suppressed. But both should still be feasible; see Ref. [49] for quantitative estimates.

3.6 Conclusions

In this paper we have shown that the single-lepton channel is a promising signature in the search for new physics beyond the Standard Model. We have considered two specific versions of this channel: (a) A single first or second generation charged lepton, exactly 1 jet and low missing transverse energy, which we denoted `SR_ej`, and (b) A single first or second generation charged lepton, at least 3 jets, and low missing transverse energy, `SR_e3j`. Utilizing the lepton parton distribution functions (PDF) of the proton, we showed that the channel `SR_ej` is promising not only in the search for a single leptoquark or a directly decaying squark, but remains sensitive even when more complicated supersymmetric cascade decays are accessible. Further, the channel `SR_e3j` plays an important role in increasing both the reach and coverage in such scenarios. More importantly, it also acts as a discriminant between a bare scalar leptoquark theory versus one with a more extensive supersymmetric sector featuring kinematically accessible particles beyond just a light squark.

Although `ATLAS` and `CMS` have performed single-lepton searches associated with large jet multiplicity, see Refs. [145, 146, 188, 240], our proposed search covers a variety of scenarios which would not produce a sufficiently large number of jets. Beyond the question of coverage, the resonant s-channel

production mechanism invoked in our analysis benefits tremendously from the forthcoming increase of luminosity at the LHC. We therefore strongly advocate that this type of search be pursued at forthcoming LHC runs, as well as emphasize the necessity of more exhaustive theoretical work surveying the opportunities that will arise in the era of High-Luminosity LHC.

Part III

Ajna

4

A ν Approach to Analyzing Neutrino Data in the R-Parity-Violating MSSM

4.0 Preface

The contents of this chapter and the supplementary material presented in Appendix B have already been published:

- H. K. Dreiner, D. Köhler, and S. Nangia,
  *A ν approach to analyzing neutrino data in the **R**-parity-violating MSSM*,
  Published in Eur. Phys. J. C 83 (2023) 1, 44, arXiv:2210.07253 [hep-ph].

4.0.1 Overview

In this chapter, we turn our attention to the third opportunity identified in Chapter 1 regarding lepton- and baryon-number violating effects; our focus here shall be on neutrino-mass generation in the RPV-MSSM.

As discussed in Chapter 1, the RPV-MSSM can provide an explanation for neutrino masses, with a natural mechanism to account for their small values. This topic has been studied extensively in the literature. The tree-level contribution comes from the bilinear RPV couplings and the sneutrino vacuum expectation values (vevs). As we shall see, these lead to a small amount of mixing (after electroweak symmetry breaking) between the four eigenstates corresponding to the gauginos and higgsinos, and the three eigenstates corresponding to the SM neutrinos. The diagonalization of the resulting mass matrix leads to five mass eigenstates. Since the mixing is small (suppressed by the small RPV parameters, as well as the heavy SUSY masses), we can approximately identify four of these with the regular, heavy neutralinos, while one corresponds almost to an SM neutrino.

Importantly, however, the other two neutrinos remain massless at tree level. This is inconsistent with neutrino oscillation data, which has established that at least two of the SM neutrinos need to be massive. This can be accounted for when one includes the one-loop RPV contributions. There are several contributing diagrams, *e.g.*, diagrams involving squarks or sleptons in the loop corresponding to $LQ\bar{D}$ or $LL\bar{E}$ couplings, etc. The complete list of contributions has already been compiled in the literature; we shall present it in this chapter. Crucially, however, the large number of contributions involving several undetermined RPV couplings, as well as SUSY mass scales severely complicates any phenomenological studies. Indeed, all existing analyses of neutrino oscillation data in the RPV context restrict themselves to specific RPV sub-models, *e.g.*, by considering either models with only specific couplings contributing (for instance, bilinear-only models, etc.), or by considering a simplified framework, *e.g.*, the Constrained MSSM extended by a couple of RPV couplings, etc. While such

frameworks allow for an interpretation of the neutrino oscillation data in the specific RPV context considered, there is no treatment allowing for a more general scope.

In this chapter, we aim to tackle the above issue by taking a different route. Instead of working in a specific RPV scenario that reduces the complexity of the neutrino-mass matrix, we analyze the form of the contributions to this matrix in the most general RPV-MSSM setup. We find that under reasonably mild assumptions, these contributions (up to one-loop order) can be reduced to just two types of structures. Using this, we show that there are just four *minimal* classes of models that can solve the neutrino data, for the case of two massive neutrinos. We refer to models with these features as *Minimal Oscillation Models (MOMs)*. This allows us to study the implications of neutrino oscillation data within the context of all RPV models, as long as the latter satisfy the MOM criteria. As we will demonstrate, this holds for a large number of interesting RPV scenarios.

With the framework defined, we explicitly solve each MOM class and present general analytical expressions, as well as numerical plots showing the solution space corresponding to the current neutrino oscillation data. We, further, describe the qualitative features of the solution spaces. These results can be interpreted in terms of any RPV models that satisfy the MOM criteria. In order to explicitly demonstrate this, we consider several examples of RPV scenarios.

The framework that we have presented here can be extended to include non-minimal classes of models, as well as to the case of three massive neutrinos; the resulting structures of the classes remain simple. However, while this would allow one to study any general RPV-MSSM setup in a unified model-independent manner, the number of classes to consider can become large. More importantly, one would then need more constraints than those coming from neutrino oscillation data alone to make predictions.

4.0.2 Contributions of the Author

The author of this thesis developed the analytical framework of Minimal Oscillation Models (MOMs), after Herbi Dreiner directed him to the topic of neutrino-mass generation in RPV models. The formulation of the theoretical framework in Section 4.4, the explicit solutions to MOMs in Appendix B, as well as the exploration of the solution spaces in Section 4.6 were provided by the author. Further, all plots in Section 4.6 were also made by the author. Finally, the analysis of the example models given in Section 4.8 was performed by the author.

4.1 Introduction

The Standard Model of particle physics (SM) is incomplete. The nature of gravity, dark matter, dark energy, the baryon asymmetry, etc. are important unresolved issues. However, the most conclusive sign of physics beyond the SM comes from the precise neutrino oscillation data. It is now established that at least two of the neutrino species are massive. One way to give neutrinos mass is to add right-handed neutrinos to the SM spectrum. Via the see-saw mechanism, one then 'naturally' obtains very light neutrinos, as required indirectly by cosmology $\left(\sum m_{\nu_i} < 0.12\,\text{eV}\right)$ [13] or, directly, for example, by the KATRIN experiment $\left(m_\nu < 0.8\,\text{eV}\right)$ [14]. However, this requires the right-handed neutrinos to be very heavy.

Supersymmetry (SUSY), a well-motivated extension of the SM [19, 102], is an attractive alternative. The simplest phenomenological realization, the Minimal Supersymmetric Standard Model (MSSM), has been studied extensively. An equally well-motivated [29, 37] setting is provided by adding R-parity-violating (RPV) terms to the MSSM Lagrangian, giving the RPV-MSSM [40]. This framework leads to a starkly different phenomenology compared to the MSSM, allows for lepton- and baryon-number violation, as well as flavor violation. Most importantly for this paper: Neutrino masses arise for free, without the need for any heavy right-handed partners [61, 281].

Neutrino-mass generation in the RPV-MSSM framework has been studied extensively in the literature. Early work on the tree-level calculation can be found in Refs. [61, 282–284], and on the loop-level one in Refs. [61, 281, 285–293]. Ref. [294] gives a (nearly) complete list of one-loop contributions, presented in a basis-independent formalism. Detailed accounts of the one-loop calculation can be found in Refs. [295, 296].

There has also been a lot of work to fit the theory calculations to the neutrino data; see the above references as well as Refs. [297–307]. The main obstacle to a systematic study is the unmanageably large number of contributions to the neutrino mass matrix in the most general RPV-MSSM. Thus, all numerical studies are performed within specific submodels; for instance bilinear-only RPV models [281, 293, 308], trilinear-only RPV models [300], mixed models [297, 301, 304, 309], and constrained MSSM (cMSSM) models extended by one (or two) RPV couplings [296, 299]. For an overview of the various types of models that have been considered, see Ref. [29].

The above studies allow an interpretation of the neutrino data within a predictive framework, but are limited in their scope. In this work, we approach the problem from a different perspective. Working in the general RPV-MSSM setting, allowing for *all* terms, we analyze the possible resulting structures (textures) of the neutrino mass matrix. To this end, we first argue that the most general neutrino mass matrix in the RPV-MSSM, to a good approximation, can be written as a sum of just two types of terms. This expression is general and simple but still has far-too-many free variables to be predictive. However, appealing to minimality, we identify just four structures of the mass matrix that are relevant for the case of two massive neutrinos. We refer to these as Minimal Oscillation Models (MOMs). The advantage of this approach is its simplicity and generality. By analyzing just four cases, it allows us to study qualitative and quantitative features of all RPV models in a unified, model-independent way, as long as they satisfy the MOM criteria; we demonstrate through examples that many interesting scenarios do indeed fulfill this condition. If, in turn, new neutrino measurements arise, then this data can be systematically analyzed in terms of the MOMs we present here, instead of in terms of the many, many different RPV-MSSM neutrino-mass models.

This paper is organized as follows. In Section 4.2, we introduce the RPV-MSSM (and our notation).

In Section 4.3, we discuss neutrino masses in the R-parity-violating context. In Section 4.4, we define the MOM framework and classify the four relevant structures of the neutrino mass matrix that arise in the RPV-MSSM. In Section 4.5, we summarize the current status of the neutrino data. We then analyze the four classes of MOMs, studying their general features in Section 4.6. We solve each class by numerically fitting to the neutrino data in Section 4.7. Finally, in Section 4.8, we consider example applications to show how results from the MOM framework can be directly translated to specific neutrino-mass models in the RPV-MSSM. We conclude in Section 4.9.

4.2 R-Parity Violation: Theoretical Framework

Assuming the $N = 1$ SUSY algebra, and the MSSM particle spectrum, the most general renormalizable superpotential invariant under the SM gauge group is,

$$W = W_{\rm MSSM} + W_{\rm LNV} + W_{\rm BNV}\,, \tag{4.1}$$

with,

$$\begin{aligned} W_{\rm MSSM} &= h_e^{ij} H_d L_i \bar{E}_j + h_d^{ij} H_d Q_i \bar{D}_j + h_u^{ij} Q_i H_u \bar{U}_j \\ &\quad + \mu H_u H_d\,, \\ W_{\rm LNV} &= \frac{1}{2}\lambda^{ijk} L_i L_j \bar{E}_k + \lambda'^{ijk} L_i Q_j \bar{D}_k + \kappa^i H_u L_i\,, \\ W_{\rm BNV} &= \frac{1}{2}\lambda''^{ijk} \bar{U}_i \bar{D}_j \bar{D}_k\,. \end{aligned} \tag{4.2}$$

In the notation we employ, L (Q) and $\bar{E}$ ($\bar{U}, \bar{D}$) label the lepton (quark) $\mathrm{SU}(2)_L$-doublet and -singlet chiral superfields, respectively, while H_u, H_d refer to the $\mathrm{SU}(2)_L$-doublet Higgs chiral superfields. All gauge indices are suppressed while the generational ones have been retained explicitly: $i, j, k = 1, 2, 3$, with a summation implied over repeated indices. The λ's and the h's are dimensionless Yukawa couplings, while μ and the κ's are dimension-one mass parameters.

In Eq. (4.1), the $W_{\rm MSSM}$ terms conserve both lepton- (L) and baryon-number (B), the $W_{\rm LNV}$ terms violate only L, and the $W_{\rm BNV}$ terms violate only B. A disconcerting consequence of allowing unsuppressed L- and B-violating terms simultaneously is proton decay at a rate that is disallowed by experimental constraints on the proton lifetime, $\tau_p > 3.6 \times 10^{29}$ yrs [13]. The usual approach in the MSSM is to invoke R-parity [147], a $\mathbb{Z}_2$ symmetry that allows $W_{\rm MSSM}$, while disallowing the R-parity-violating terms, $W_{\rm RPV} \equiv W_{\rm LNV} + W_{\rm BNV}$. However, to stabilize the proton, R-parity is sufficient, but not necessary. For instance, forbidding either the $W_{\rm BNV}$ or the $W_{\rm LNV}$ terms alone results in a stable proton.[1] Baryon triality, B_3, is such a symmetry that forbids the former and leaves the latter [35]. In fact, unlike R-parity, B_3 even forbids potentially dangerous proton-decay operators of dimension five. We note that R-parity and B_3 are the only $\mathbb{Z}_2$ or $\mathbb{Z}_3$ symmetries possible with the MSSM low-energy particle content free from gauge anomalies [43, 44]; the higher symmetries have been classified in Ref. [249].

R-parity-violating phenomenology differs strongly from the R-parity-conserving case [29, 37, 45,

[1] If the lightest neutralino is lighter than the proton [74], then the proton can also decay with just $W = W_{\rm MSSM} + W_{\rm BNV}$, *e.g.*, $p \to K^+ \tilde{\chi}_1^0$ [60].

47]. Collider signals are no longer dominated by missing transverse momentum, the lightest neutralino is no longer a dark matter candidate, and baryogenesis, lepton-flavor violation and neutrino masses arise naturally. We summarize the last point, central to the further discussion.

4.3 Neutrino Masses and R-parity Violation

For neutrino masses at next-to-leading order, without loss of generality, we specialize to the B_3-MSSM, and abusively call it the RPV-MSSM. Our superpotential is,

$$W_{B_3} = W_{\rm MSSM} + W_{\rm LNV}. \tag{4.3}$$

There is no quantum number distinguishing H_d from L_i and hence, we define the following vectors and matrix:

$$L_\alpha \equiv \left(H_d, L_1, L_2, L_3\right) , \tag{4.4}$$

$$\kappa^\alpha \equiv \left(\mu, \kappa^1, \kappa^2, \kappa^3\right) , \tag{4.5}$$

$$\lambda'^{\alpha jk} \equiv \left(h_d^{jk}, \lambda'^{1jk}, \lambda'^{2jk}, \lambda'^{3jk}\right) , \tag{4.6}$$

$$\lambda^{\alpha\beta k} \equiv \begin{pmatrix} 0 & h_e^{1k} & h_e^{2k} & h_e^{3k} \\ -h_e^{1k} & 0 & \lambda^{12k} & \lambda^{13k} \\ -h_e^{2k} & \lambda^{21k} & 0 & \lambda^{23k} \\ -h_e^{3k} & \lambda^{31k} & \lambda^{32k} & 0 \end{pmatrix} . \tag{4.7}$$

$\alpha, \beta = 0, 1, 2, 3$ label the vector and matrix components, *e.g.*, $L_0 \equiv H_d$, and $\lambda'^{0jk} \equiv h_d^{jk}$. $j, k = 1, 2, 3$ are as before. We can thus write the superpotential as,

$$\begin{aligned} W_{B_3} = &\frac{1}{2}\lambda^{\alpha\beta k} L_\alpha L_\beta \bar{E}_k + \lambda'^{\alpha jk} L_\alpha Q_j \bar{D}_k + h_u^{ij} Q_i H_u \bar{U}_j \\ &+ \kappa^\alpha H_u L_\alpha \, . \end{aligned} \tag{4.8}$$

In addition, there are the soft-breaking terms,

$$\begin{aligned} \mathcal{L}_{soft} = \text{mass terms} + &\frac{1}{2} A^{\alpha\beta k} \tilde{L}_\alpha \tilde{L}_\beta \tilde{\bar{E}}_k + A'^{\alpha jk} \tilde{L}_\alpha \tilde{Q}_j \tilde{\bar{D}}_k \\ &+ A_u^{ij} \tilde{Q}_i H_u \tilde{\bar{U}}_j + B^\alpha H_u \tilde{L}_\alpha + h.c. \, , \end{aligned} \tag{4.9}$$

where the fields appearing in the above equation are the scalar components of the corresponding chiral superfields. The definitions of the parameters with one $\left(B^\alpha, A'^{\alpha jk}\right)$, and two $\left(A^{\alpha\beta k}\right)$ Greek indices are obvious generalizations of the MSSM soft-breaking parameters, *cf.* Eqs. (4.4)-(4.7).

After spontaneous symmetry breaking, the neutrinos, the neutral gauginos, and the higgsinos mix, leading to a 7×7 mass matrix. At tree level in the gauge eigenbasis, $\left(-i\tilde{B}; -i\tilde{W}^0; \tilde{H}_u^0; \nu_\alpha\right)$, with

$\nu_\alpha \equiv \left(\tilde{H}_d^0, \nu_i\right)$, we have the overall mass matrix,

$$\mathbf{M}_N = \begin{pmatrix} \mathbf{M}_{4\times4} & \mathbf{m}_{4\times3} \\ \mathbf{m}_{3\times4}^T & \mathbf{0}_{3\times3} \end{pmatrix}, \tag{4.10}$$

with $\mathbf{M}_{4\times4}$ corresponding to the MSSM neutralino mass matrix,

$$\mathbf{M}_{4\times4} = \begin{pmatrix} M_1 & 0 & \frac{g_1 v_u}{2} & \frac{-g_1 v_d}{2} \\ 0 & M_2 & \frac{-g_2 v_u}{2} & \frac{g_2 v_d}{2} \\ \frac{g_1 v_u}{2} & \frac{-g_2 v_u}{2} & 0 & -\kappa^0 \\ \frac{-g_1 v_d}{2} & \frac{g_2 v_d}{2} & -\kappa^0 & 0 \end{pmatrix}, \tag{4.11}$$

and the sub-block $\mathbf{m}_{4\times3}$ containing the RPV terms,

$$\mathbf{m}_{4\times3} = \begin{pmatrix} \frac{-g_1 v_1}{2} & \frac{-g_1 v_2}{2} & \frac{-g_1 v_3}{2} \\ \frac{g_2 v_1}{2} & \frac{g_2 v_2}{2} & \frac{g_2 v_3}{2} \\ -\kappa^1 & -\kappa^2 & -\kappa^3 \\ 0 & 0 & 0 \end{pmatrix}. \tag{4.12}$$

$\tilde{B}$ and $\tilde{W}^0$ denote the neutral gauginos, $\tilde{H}_u^0$, $\tilde{H}_d^0$ the neutral higgsinos, and ν_i the neutrinos. M_1, M_2, and g_1, g_2 are the electroweakino soft-breaking masses and gauge couplings, respectively. $\frac{v_u}{\sqrt{2}}$, $\frac{v_d}{\sqrt{2}}$, $\frac{v_i}{\sqrt{2}}$, with $i = 1, 2, 3$, are the vacuum expectation values (vevs) of the two neutral Higgs fields and the three sneutrinos, respectively.

The mass matrix of Eq. (4.10) has been discussed abundantly in the literature. The details of the diagonalization procedure can be found, for instance, in Ref. [295]. The scales in the various blocks are expected to have a hierarchy. Given the lower mass bounds on sparticles from the LHC, one expects the lepton-number-conserving SUSY scales of $\mathbf{M}_{4\times4}$ to be at least $\sim O(1\,\text{TeV})$, while the lepton-number-violating scales of $\mathbf{m}_{4\times3}$ are constrained by various stringent low-energy bounds to be much smaller [29]. For example, the cosmological limit on neutrino masses implies v_i, $\kappa^i \lesssim O(1\,\text{MeV})$ [40]. One can then proceed à la see-saw, and end up with an approximately block-diagonal matrix,

$$\mathbf{M}_N^{\text{diag}} \approx \begin{pmatrix} \mathbf{M}_{4\times4} & 0 \\ 0 & \mathbf{M}_\nu \end{pmatrix}, \tag{4.13}$$

where,

$$\mathbf{M}_\nu^{ij} \equiv \frac{\left(M_1 g_2^2 + M_2 g_1^2\right)}{4\det\left(\mathbf{M}_{4\times4}\right)} \left(v_i \kappa^0 - v_d \kappa^i\right)\left(v_j \kappa^0 - v_d \kappa^j\right). \tag{4.14}$$

The neglected contributions to $\mathbf{M}_{4\times4}$ and $\mathbf{M}_\nu$ in the above approximation are of order $\frac{\|\mathbf{m}_{4\times3}^2\|}{\|\mathbf{M}_{4\times4}\|} \lesssim O(1\,\text{eV})$, and $\frac{\|\mathbf{m}_{4\times3}^3\|}{\|\mathbf{M}_{4\times4}^2\|} \lesssim O(10^{-6}\,\text{eV})$, respectively [295]. To this order, $\mathbf{M}_{4\times4}$ is unaffected compared to the MSSM and we identify it as the neutralino mass matrix, and the corresponding mass eigenstates as the neutralinos. The high-scale-suppressed $\mathbf{M}_\nu$ can then be identified as the effective neutrino mass

matrix.

Importantly, $\mathbf{M}_\nu$ is rank one at tree level, *i.e.*, it has only one non-zero eigenvalue. However, at least two neutrinos must be massive to explain the oscillation data. This can be achieved by including one-loop corrections [61], which have been computed several times in the literature. We shall use the results of Ref. [294]. There, an almost complete list of the one-loop contributions to $\mathbf{M}_\nu$ is presented; certain contributions whose effects are expected to be negligible have been dropped.

The advantage of using the formalism of Ref. [294] is that the contributions have been written in terms of basis invariants. It is common practice in the literature to use the U(4) 'flavor' freedom to rotate L_α to a specific basis. Various useful choices have been identified – the most common being the vanishing-κ^i basis [61, 151], and the vanishing-sneutrino-vev basis [291]. The notation of Ref. [294] is invariant under this U(4) and is useful to compare results across works using different bases.

We present an adapted version of all the contributions calculated in Ref. [294] in Table 4.1. Each entry can have multiple diagrams contributing. Further, the expressions are not exact but are meant to indicate the resulting form. For brevity, we have set all the SUSY mass scales to m_{SUSY}, all gauge couplings to g, dropped some factors involving the ratio of vevs – $\tan\beta$, and taken some scalar-sector flavor matrices as diagonal. We discuss the implications of this point in more detail shortly. The δ's appearing in the table are the basis invariants. Throughout, the constraints we derive apply to them but the results can always be translated into a specific basis using the general expressions [294]. For instance, in the vanishing-sneutrino-vev basis, we have,

$$\begin{aligned} \delta^i_\kappa &= \frac{\kappa^i}{|\kappa|}\,, & \delta^i_B &= \frac{B^i}{|B|}\,, \\ \delta^{ijk}_\lambda &= \lambda^{ijk}\,, & \delta^{ijk}_{\lambda'} &= \lambda'^{ijk}\,, \end{aligned} \tag{4.15}$$

with,

$$|\kappa|^2 \equiv \sum_{\alpha=0}^{3} \left|\kappa^\alpha\right|^2, \qquad |B|^2 \equiv \sum_{\alpha=0}^{3} \left|B^\alpha\right|^2. \tag{4.16}$$

Motivated by the above expressions, we often loosely refer to the δ's as 'RPV couplings'.

Even though the contributions in Table 4.1 are in terms of basis invariants, they have been written in a specific basis which corresponds approximately to the charged lepton mass basis. Analogous to the neutral case, the uncolored 5×5 charged fermion mass matrix mixes the charged gaugino, charged Higgsino, and the three charged leptons. However, it also has a hierarchical structure and can be approximately block-diagonalized to obtain separate 3×3 and 2×2 mass matrices, corresponding to the charged leptons and charginos, respectively. The charged lepton matrix, subject to small neglected terms, can then be diagonalized as usual.

With a diagonal charged lepton mass matrix, one can then diagonalize the effective neutrino mass matrix $\mathbf{M}_\nu$:

$$\mathbf{M}_\nu = U^*_{\text{PMNS}} \mathbf{M}_\nu^{\text{diag}} U^\dagger_{\text{PMNS}}\,, \tag{4.17}$$

where $\mathbf{M}_\nu^{\text{diag}}$ is the diagonalized neutrino mass matrix, and U_{PMNS} is the PMNS matrix that appears in the charged-current interactions of the neutrinos. It should be clear that the PMNS matrix, as defined here, is a 3×3 sub-matrix inside the larger 5×7 matrix describing the mixing between all the 5 charged fermions and 7 neutral fermions. Thus U_{PMNS} is not exactly unitary, here. However, these

Contribution	$16\pi^2 m_{\text{SUSY}} \mathbf{M}_\nu^{ij}$
Tree-Level	$16\pi^2 m_0 m_{\text{SUSY}} \delta_\kappa^i \delta_\kappa^j$
1	$\delta_\lambda^{ink} \delta_\lambda^{jkn} m_{e_n} m_{e_k} + (i \leftrightarrow j)$
2	$3\delta_{\lambda'}^{ink} \delta_{\lambda'}^{jkn} m_{d_n} m_{d_k} + (i \leftrightarrow j)$
3	$g^2 \delta_{\text{B}}^i \delta_{\text{B}}^j m_{\text{SUSY}}^2 / 4$
4	$3 \left(\delta_\kappa^i \delta_{\lambda'}^{jkk} + \delta_\kappa^j \delta_{\lambda'}^{ikk} \right) m_{d_k}^2 h_d^k$
5	$\delta_\lambda^{ijk} \delta_{\text{B}}^k m_{e_k} \left(m_{e_j} h_e^j - m_{e_i} h_e^i \right)$
6	$\left(\delta_\kappa^i \delta_\lambda^{jkk} + \delta_\kappa^j \delta_\lambda^{ikk} \right) m_{e_k}^2 h_e^k$
7	$\delta_\kappa^i \delta_\kappa^j m_{e_i} m_{e_j} h_e^i h_e^j + (i \leftrightarrow j)$
8	$\delta_\kappa^i \delta_\kappa^j \left[\left(m_{e_i} h_e^i \right)^2 + \left(m_{e_j} h_e^j \right)^2 \right]$
9	$\delta_{\text{B}}^i \delta_\kappa^j \left(m_{e_i} h_e^i \right)^2 + \delta_{\text{B}}^j \delta_\kappa^i \left(m_{e_j} h_e^j \right)^2$
10	$\delta_\lambda^{ijk} \delta_\kappa^k m_{e_k} \left(m_{e_i} h_e^i - m_{e_j} h_e^j \right)$
11	$\left(\delta_{\text{B}}^i \delta_\kappa^j + \delta_{\text{B}}^j \delta_\kappa^i \right) h_e^i h_e^j m_{e_i} m_{e_j}$
12	$g \left(\delta_\kappa^i \delta_{\text{B}}^j m_{e_i}^2 + \delta_\kappa^j \delta_{\text{B}}^i m_{e_j}^2 \right)$
13	$g \, \delta_\kappa^i \delta_\kappa^j \left(m_{e_i}^2 + m_{e_j}^2 \right)$
14	$g \, m_{\text{SUSY}} \left(\delta_\kappa^i \delta_\lambda^{jkk} + \delta_\kappa^j \delta_\lambda^{ikk} \right) m_{e_k}$
15	$3 \, g \, m_{\text{SUSY}} \left(\delta_\kappa^i \delta_{\lambda'}^{jkk} + \delta_\kappa^j \delta_{\lambda'}^{ikk} \right) m_{d_k}$
16	$g^2 m_{\text{SUSY}}^2 \left(\delta_{\text{B}}^i \delta_\kappa^j + \delta_{\text{B}}^j \delta_\kappa^i \right) / 4$
17	$g \left(\delta_\kappa^i \delta_{\text{B}}^j m_{e_j}^2 + \delta_\kappa^j \delta_{\text{B}}^i m_{e_i}^2 \right)$

Table 4.1: $\mathbf{M}_\nu$ contributions as calculated in Ref. [294]. The numbered entries are due to one-loop diagrams. Summation is implied over all repeated indices other than i, j. The δ's are the RPV basis invariants. m_0 is the tree-level mass scale of Eq. (4.14), the remaining m's are the SM fermion masses, and the h's are the Yukawas.

effects are suppressed by the high-energy scales and we ignore them [295].

4.4 Minimal Oscillation Models

The matrix equation to be solved is,

$$\mathbf{M}_\nu \stackrel{!}{=} \mathbf{M}_\nu^{\text{exp}} = U_{\text{PMNS}}^* \text{diag} \left(m_{\nu_1}, m_{\nu_2}, m_{\nu_3} \right) U_{\text{PMNS}}^\dagger \,, \tag{4.18}$$

where $\mathbf{M}_\nu$ is the one-loop effective neutrino mass matrix computed from the RPV Lagrangian and the right-hand side is to be determined through fits to the neutrino oscillation data. The difficulty of numerically analyzing the *most general* RPV neutrino-mass model should be evident from the large number of contributions in Table 4.1. The goal of this paper is to show that – despite this – due to the structure of the entries, only a small set of truly 'distinct models' is possible. These, in turn, can be systematically analyzed.

Eq. (4.18) is a set of six complex equations, or 12 real constraints. Nine of these are physical, corresponding to the three neutrino masses, the three mixing angles, and the three CP-violating phases

in the PMNS matrix (see the parameterization of the PMNS matrix below). The remaining three are not physical constraints. They correspond to arbitrary phases in the PMNS matrix that can be rotated away [310].

Looking at Table 4.1, it is clear that the most general one-loop mass matrix arising in RPV models, entering Eq. (4.18) on the left-hand side, has too many parameters; the system is very much underdetermined. Just the RPV superpotential has $\left(\kappa^i, \lambda^{ijk}, \lambda'^{ijk}\right)$ $3+9+27=39$ free complex (or 78 real) parameters. As mentioned, the usual approach of numerical studies has been to assume specific models. For instance, bilinear-only models $\left(\lambda^{ijk} = \lambda'^{ijk} = 0\right)$ [281], or unification approaches that begin with a small number of non-zero λ's at M_X, which then generate other non-zero couplings at the low scale through renormalization-group effects [311], etc. Our aim in this work is to remain as general as possible.

In a first step, we observe that all the contributions of Table 4.1 (except entries 5 and 10 – we return to this point) can be reduced to combinations of just two types of structures:

1. $x^i x^j$
2. $x^i y^j + y^i x^j$

Here, the x^i and y^i are place-holding variables with mass-dimension $[M]^{1/2}$ that are directly proportional to the δ's of Table 4.1. For instance, when the first one-loop entry of the table is expanded out, we get,

$$\begin{aligned}\mathbf{M}_\nu^{ij} &= \frac{1}{8\pi^2 m_{\rm SUSY}}\left(\delta_\lambda^{i33}\delta_\lambda^{j33}m_\tau^2 + \delta_\lambda^{i23}\delta_\lambda^{j32}m_\tau m_\mu\right.\\ &\quad\left. + \delta_\lambda^{i32}\delta_\lambda^{j23}m_\tau m_\mu + \delta_\lambda^{i22}\delta_\lambda^{j22}m_\mu^2 + \ldots\right)\\ &= x_1^i x_1^j + \left(x_3^i x_4^j + x_4^i x_3^j\right) + x_2^i x_2^j + \ldots\,,\end{aligned} \tag{4.19}$$

with

$$\begin{aligned} x_1^i &\equiv \frac{\delta_\lambda^{i33} m_\tau}{2\pi\sqrt{2\, m_{\rm SUSY}}}\,, \quad x_2^i \equiv \frac{\delta_\lambda^{i22} m_\mu}{2\pi\sqrt{2\, m_{\rm SUSY}}}\,,\\ x_3^i &\equiv \frac{\delta_\lambda^{i23} m_\mu}{2\pi\sqrt{2m_{\rm SUSY}}}\,, \quad x_4^i \equiv \frac{\delta_\lambda^{i32} m_\tau}{2\pi\sqrt{2m_{\rm SUSY}}}\,. \end{aligned} \tag{4.20}$$

We see that the first and fourth terms correspond to an $x^i x^j$ structure while the second and third terms together form an $x^i y^j + y^i x^j$ structure. The choice of the variables is non-unique. For instance, one can multiply x_3^i by a constant and divide x_4^i by the same constant without changing the total contribution. Similarly, x_1^i, x_2^i are defined only up to a sign. The important point is that the variables are chosen to be directly proportional to the δ's.

One can similarly check the other entries. So, (ignoring the two exceptions) the most general one-loop effective neutrino mass matrix in RPV models can symbolically be written as,

$$\mathbf{M}_\nu^{ij} = \sum_\alpha x^i x^j + \sum_\beta \left(x^i y^j + y^i x^j\right)\,, \tag{4.21}$$

where the sum over α (β) is such that all the contributions of the first (second) type in Table 4.1 are included. Given Eq. (4.21), the simplest neutrino mass matrix that one can construct in the RPV-MSSM is with only one set, x^i:

$$\mathbf{M}_\nu^{ij} = x^i x^j \,. \tag{4.22}$$

The rank of this matrix is one, leading to two massless neutrinos which is inconsistent with oscillation data. The next simplest case involves two sets x^i, x'^i. Consider, for instance,

$$\mathbf{M}_\nu^{ij} = x^i x^j + x'^i x'^j \,. \tag{4.23}$$

This is, in general, a rank two structure and could possibly explain neutrino data if the lightest neutrino is massless. However, it does not work if the two sets are linearly dependent. To see this, let $x'^i = k x^i$; we get,

$$\begin{aligned} \mathbf{M}_\nu^{ij} &= x^i x^j + k^2 x^i x^j = (1+k^2) x^i x^j \\ &= \tilde{x}^i \tilde{x}^j \,, \end{aligned} \tag{4.24}$$

where $\tilde{x}^i \equiv \sqrt{1+k^2}\, x^i$. The structure reduces to the rank one case. Thus, we must have two linearly independent sets.

We emphasize that the number of linearly independent x^i sets is not the same as the number of RPV-coupling sets that give rise to them. For instance, one can check that reducing the tree-level contribution and entry 7 of Table 4.1 to the form of Eq. (4.21) requires two linearly independent sets, x^i and x'^i, even if both contributions arise from just a single RPV-coupling set, δ^i_κ. The inverse is also possible: Several RPV parameters can be written in terms of just one set x^i, *cf.* Appendix B.2.

With the above in mind, all possible structures that can be written with two linearly independent sets, x^i and x'^i, are:

- Class 1: $\mathbf{M}_\nu^{ij} = x^i x'^j + x'^i x^j$
- Class 2: $\mathbf{M}_\nu^{ij} = x^i x^j + (x^i x'^j + x'^i x^j)$
- Class 3: $\mathbf{M}_\nu^{ij} = x^i x^j + x'^i x'^j$
- Class 4: $\mathbf{M}_\nu^{ij} = x^i x^j + x'^i x'^j + A\left(x^i x'^j + x'^i x^j\right)$

These four structures[2] are all rank two – the minimum required, and are the only possible solutions to the neutrino data, as long as one is interested in a minimal setup. This is a crucial observation of this paper. We analyze these structures in the following.

Let us now discuss the exceptions mentioned above – entries 5 and 10 in Table 4.1. Before proceeding, we note that the various contributions to the neutrino mass matrix in Table 4.1 have a natural hierarchy. For instance, consider a scenario with only the $\delta^i_\kappa \neq 0$, leading to four contributions: The tree-level term, and entries 7, 8 and 13. Contributions 7 and 8 are suppressed by at least two extra

[2] The Class 4 structure follows by using Eq. (4.21) to write the most general expression involving only x^i, x'^i, or couplings that are a linear combination of the two; and then suitably redefining the variables such that all the proportionality constants appear only in A. The detailed steps are given in Appendix B.2.

powers of the small lepton-Yukawas compared to the other two. Thus, to a first approximation, we can neglect them.[3] The remaining two contributions can be reduced to a Class 2 MOM structure, *cf.* Section 4.8. This is a general trend, not specific to this example; we explore several examples later.

Indeed, the exceptions 5, 10 are not too worrisome for the same reason. They are Yukawa suppressed compared to the other terms involving the same sets of couplings. Let us see this explicitly for entry 5. The RPV parameters involved are δ_B^i and δ_λ^{ijk}. Assuming other couplings vanish, this entry would be competing with entries 1 and 3. We can estimate the magnitudes of the three contributions as:

$$\begin{aligned}
&\text{Entry 1} \sim |\delta_\lambda|^2 m_\tau^2\,,\\
&\text{Entry 3} \sim \frac{g^2|\delta_B|^2 m_{\text{SUSY}}^2}{4\cos^2\beta}\,,\\
&\text{Entry 5} \sim |\delta_\lambda||\delta_B| m_\tau^2 h_\tau \tan\beta\,,
\end{aligned} \tag{4.25}$$

where we have assumed a common magnitude for all generations of a particular coupling and hence dropped the latin indices. Further, we have only retained the terms proportional to the dominant τ lepton Yukawas for entries 1 and 5. The $\tan\beta$ and $\cos\beta$ factors are read off from the expressions found in Ref. [294]. Substituting the known values, and taking $m_{\text{SUSY}} \sim \mathcal{O}(1\,\text{TeV})$, one can easily prove that there is no configuration of parameters for which Entry 5 becomes important relative to the other two contributions. A similar argument can be made for entry 10.

Going beyond rank two, it is possible that all three neutrinos are massive, requiring a rank three structure and a third linearly independent set, x''^i. Three linearly independent sets is the most general case and hence this approach would capture all RPV-MSSM neutrino-mass models. However, the number of classes to be considered is large making them less conducive for systematic numerical studies. In this paper we focus only on the rank two case.

We should note that the MOM approach does not cover the most general rank two structure possible in an RPV model. In Table 4.1, we assume some scalar-sector mixing matrices are diagonal in the charged lepton mass basis we are working in. This includes matrices that diagonalize the charged doublet and singlet sleptons and down-type squarks, and matrices that describe the left-right sparticle mixings; that is, we assume the sparticle and particle flavors are aligned with no inter-generational mixing. The fact that all contributions can be reduced to one of just two types of structures relies on this assumption. Further, by setting all SUSY scales in Table 4.1 common, we have neglected the possibility that strong hierarchies in the scalar sector may undo some of the hierarchies that we saw above. Finally, it is possible that three linearly independent sets $-x^i, x'^i, x''^i$ – lead to a rank two structure through specific cancellations (see Appendix B.2 for an illustration of this point). The four structures listed above with only two sets would not capture such models. Hence, we shall refer to these as Minimal Oscillation Models (MOMs). MOMs are not minimal in the sense of having the fewest number of RPV parameters. They are, rather, minimal in the sense that the mass matrix has the minimal structure demanded by the data.

In the absence of any experimental information about the scalar sector, we believe the MOM framework provides a minimal setting that is widely applicable for the interpretation of neutrino data. It is simple and predictive. After briefly reviewing the neutrino data, we analyze qualitative and quantitative features of the models in the subsequent sections.

[3] One should make sure that the $\tan\beta$ factors, not shown in Table 4.1, cannot undo the hierarchies. As discussed in Section 4.8, this is indeed not the case here.

4.5 Neutrino Data

The PMNS matrix can be parameterized [13] by the three mixing angles $(\theta_{12}, \theta_{13}, \theta_{23})$, one CP-violating Dirac phase (δ_{CP}), and two CP-violating Majorana phases (η_1, η_2):

$$U_{\text{PMNS}} = \begin{pmatrix} c_{12}c_{13} & s_{12}c_{13} & s_{13}e^{-i\delta_{CP}} \\ -s_{12}c_{23} - c_{12}s_{23}s_{13}e^{i\delta_{CP}} & c_{12}c_{23} - s_{12}s_{23}s_{13}e^{i\delta_{CP}} & s_{23}c_{13} \\ s_{12}s_{23} - c_{12}c_{23}s_{13}e^{i\delta_{CP}} & -c_{12}s_{23} - s_{12}c_{23}s_{13}e^{i\delta_{CP}} & c_{23}c_{13} \end{pmatrix} \begin{pmatrix} e^{i\eta_1} & 0 & 0 \\ 0 & e^{i\eta_2} & 0 \\ 0 & 0 & 1 \end{pmatrix}, \tag{4.26}$$

where $\sin\theta_{ij}$ and $\cos\theta_{ij}$ are written as s_{ij} and c_{ij} respectively. Without loss of generality, the angles θ_{ij} can be taken to lie in the first quadrant, *i.e.*, $\theta_{ij} \in [0, \pi/2]$, and the phases $\delta_{CP}, \eta_i \in [0, 2\pi]$.

We summarize neutrino oscillation data from Ref. [312] in Table 4.2. We follow their assumption of three active oscillating neutrinos. They present the best-fit values of the combined global analysis of atmospheric, solar, reactor, and accelerator neutrinos. Here, we specifically choose their fit including the SK atmospheric data [313, 314]. The data still allows one neutrino to be massless; we work in this limit. For Normal Ordering (NO) $(m_1 < m_2 < m_3)$ this means $m_1 \approx 0$, and for Inverted Ordering (IO) $(m_3 < m_1 < m_2)$ it means $m_3 \approx 0$. In the global neutrino fit, the Normal Ordering is preferred over the inverted ordering, however this has become less pronounced with more recent data [312, 315].

	Normal Ordering	Inverted Ordering
$\theta_{12}/^\circ$	$33.44^{+0.77}_{-0.74}$	$33.45^{+0.78}_{-0.75}$
$\theta_{23}/^\circ$	$49.2^{+0.9}_{-1.2}$	$49.3^{+0.9}_{-1.1}$
$\theta_{13}/^\circ$	$8.57^{+0.12}_{-0.12}$	$8.60^{+0.12}_{-0.12}$
$\delta_{CP}/^\circ$	197^{+27}_{-24}	282^{+26}_{-30}
$\frac{\Delta m^2_{21}}{10^{-5}\,\text{eV}}$	$7.42^{+0.21}_{-0.20}$	$7.42^{+0.21}_{-0.20}$
$\frac{\Delta m^2_{3l}}{10^{-3}\,\text{eV}}$	$+2.517^{+0.026}_{-0.028}$	$-2.498^{+0.028}_{-0.028}$

Table 4.2: Neutrino oscillation parameters from a global fit to data. The first (second) column depicts the best fit assuming NO (IO). Note that $\Delta^2_{3l} \equiv \Delta^2_{31} > 0$ for NO and $\Delta^2_{3l} \equiv \Delta^2_{32} < 0$ for IO.

We use the data as presented in Table 4.2 for our numerical fits, except we set $\delta_{CP} = 0$. Further, we also set the as-yet-undetermined Majorana phases to be zero. That is, we work in the CP-conserving scenario. We do this merely for convenience; the solution space is more symmetric. Nevertheless, to show our analysis can accommodate CP violation, we show a sample plot in Appendix B.3 for $\delta_{CP} \neq 0$.

We will also find it convenient, at times, to use the so-called tri-bi-maximal (TBM) approximation[4] for the angles instead of the values in Table 4.2 [316]:

$$\sin^2(\theta_{12}) = \frac{1}{3}\,, \quad \sin^2(\theta_{23}) = \frac{1}{2}\,, \quad \sin^2(\theta_{13}) = 0\,, \quad \delta_{CP} = 0\,. \tag{4.27}$$

[4] See Ref. [311] for relating the TBM to RPV neutrino-mass models.

Even though this scenario is ruled out by the $\sin\theta_{13}$ measurement, it gives convenient analytical expressions, provides initialization for numerical fits, and allows studying qualitative features that carry through to the experimentally viable scenarios.

4.6 General Features of our Results

In the following, we present solutions to Eq. (4.18) for each of the four classes of MOMs. As we explain below, the solution space is an infinite set. Furthermore, since the neutrino data are quite precise, we shall ignore the experimental errors in the graphical presentation of our results below; technically each line in the plot should be understood to have a finite width.

There are two subtle points applying to all MOM classes worth mentioning before we solve them. The first concerns the basis choice. Even with our basis fixed to the (approximate) charged lepton mass basis, there is remnant freedom in the $U_{\rm PMNS}$ matrix. This corresponds to the freedom to multiply $U_{\rm PMNS}$ by three arbitrary phases [310]:

$$U_{\rm PMNS} \mapsto \mathrm{diag}\left(e^{i\alpha_1}, e^{i\alpha_2}, e^{i\alpha_3}\right) U_{\rm PMNS}\,. \tag{4.28}$$

Using Eq. (4.17), this corresponds to shifting $\mathbf{M}_\nu$:

$$\begin{aligned} \mathbf{M}_\nu \;\mapsto\; & \mathrm{diag}\left(e^{-i\alpha_1}, e^{-i\alpha_2}, e^{-i\alpha_3}\right) \times \mathbf{M}_\nu \times \\ & \times \mathrm{diag}\left(e^{-i\alpha_1}, e^{-i\alpha_2}, e^{-i\alpha_3}\right)\,. \end{aligned} \tag{4.29}$$

This, in turn, can be interpreted as shifts in the phases of the x^i, x'^i variables. For instance, if $\mathbf{M}_\nu$ has a Class 1 MOM structure, the above equation becomes:

$$\begin{aligned} \left(x^i x'^j + x'^i x^j\right) \;\mapsto\; & \sum_{a,b} e^{-i\alpha_i}\delta^{ia}\left(x^a x'^b + x'^a x^b\right)\delta^{bj} e^{-i\alpha_j} \\ = \; & \left(e^{-i\alpha_i}x^i\right)\left(e^{-i\alpha_j}x'^j\right) \\ & + \left(e^{-i\alpha_i}x'^i\right)\left(e^{-i\alpha_j}x^j\right)\,, \end{aligned} \tag{4.30}$$

which is equivalent to the simultaneous transformations:

$$\begin{aligned} x^i &\mapsto \tilde{x}^i \equiv \left(e^{-i\alpha_i}x^i\right)\,, \\ x'^i &\mapsto \tilde{x}'^i \equiv \left(e^{-i\alpha_i}x'^i\right)\,. \end{aligned} \tag{4.31}$$

A change of basis induces simultaneous phase rotations on the RPV couplings. This holds for all MOM classes.

The second subtlety is the issue of degrees of freedom. MOM classes 1-3 have six free (complex) parameters while the fourth has seven. One might expect the six (complex) equations in Eq. (4.18) are enough to determine the system of variables for at least the first three classes. However, for the case at hand, the experimental matrix [right-hand side of Eq. (4.18)] is rank two. Hence, its last row can be written as a linear combination of the first two rows; the sixth constraint is redundant. We, thus, have

an infinite set of solutions characterized by one unconstrained variable. Correspondingly, for Class 4 MOMs, we have two unconstrained variables.

To summarize, our solution space is an infinite set parameterized by one (or two) free variables. Further, the phases of the variables are only meaningful once the basis is completely specified. Our results are presented in the basis $\alpha_1, \alpha_2, \alpha_3 = 0$ with U_{PMNS} given by Eq. (4.26).

We now study the solution spaces for MOMs in detail. The analytical expressions are presented in Appendix B.1; our emphasis here is on a qualitative discussion of the general features. We exclude a study of Class 4 models. They are straightforward to solve numerically (see Section 4.7 for the discussion on numerical fits), but the analytical expressions are rather long and awkward. Furthermore, a visual representation would require non-intuitive three-dimensional plots.

4.6.1 Class 1: $x^i x'^j + x'^i x^j$

The equations we solve are quadratic in x^i, x'^i. Thus, there are multiple distinct solution sets for each MOM class. For instance, from Eq. (B.1) in Appendix B.1, we see that Class 1 MOMs have four solution sets. However, using the symmetries of the equations, we can relate these to each other. Let us assume we know one solution set. Taking x^1 to be our free variable and expressing the other variables as a function of it, this set has the form:

$$S_{\text{I}} : \left[x_{\text{I}}^2\left(x^1\right), x_{\text{I}}^3\left(x^1\right), x_{\text{I}}'^1\left(x^1\right), x_{\text{I}}'^2\left(x^1\right), x_{\text{I}}'^3\left(x^1\right)\right]. \tag{4.32}$$

The subscript I labels the solution set. More explicitly, let us choose the constraints corresponding to the elements $ij = 11, 12, 13, 22, 33$ of $\mathbf{M}_\nu^{ij}$ as our five independent conditions. Then, the Class 1 equations are invariant under the simultaneous transformations,

$$x^2\left(x^1\right) \mapsto -x^2\left(-x^1\right), \qquad x'^2 \mapsto -x'^2\left(-x^1\right). \tag{4.33}$$

To see this, consider the constraint corresponding to $ij = 12$; for the others, the check is trivial. We have,

$$x^1 x'^2\left(x^1\right) + x^2\left(x^1\right) x'^1\left(x^1\right). \tag{4.34}$$

Making the transformations of Eq. (4.33), we get,

$$\begin{aligned} & x^1\left[-x'^2\left(-x^1\right)\right] + \left[-x^2\left(-x^1\right)\right] x'^1\left(x^1\right), \\ = & \left[-x^1\right] x'^2\left(-x^1\right) + x^2\left(-x^1\right)\left[-x'^1\left(x^1\right)\right], \\ = & \left[-x^1\right] x'^2\left(-x^1\right) + x^2\left(-x^1\right) x'^1\left(-x^1\right), \end{aligned} \tag{4.35}$$

where, in the last line, we have used $x'^1\left(x^1\right) = -x'^1\left(-x^1\right)$ which follows straightforwardly from the $ij = 11$ constraint. Finally, replacing the dummy variable $-x^1 \mapsto x^1$, we see that we recover Eq. (4.34).

Thus, given set $S_{\rm I}$, we can obtain a new solution set:

$$S_{\rm II}: \left[x^2_{\rm II}\left(x^1\right), x^3_{\rm II}\left(x^1\right), x'^1_{\rm II}\left(x^1\right), x'^2_{\rm II}\left(x^1\right), x'^3_{\rm II}\left(x^1\right)\right], \tag{4.36}$$

with,

$$\begin{aligned} x^2_{\rm II}\left(x^1\right) &= -x^2_{\rm I}\left(-x^1\right), \\ x'^1_{\rm II}\left(x^1\right) &= x'^1_{\rm I}\left(x^1\right), \\ x'^2_{\rm II}\left(x^1\right) &= -x'^2_{\rm I}\left(-x^1\right), \\ x^{(\prime)3}_{\rm II}\left(x^1\right) &= x^{(\prime)3}_{\rm I}\left(x^1\right). \end{aligned} \tag{4.37}$$

The third set can be obtained by transforming the x^3, x'^3 variables instead of the x^2, x'^2 variables in an analogous manner, and the last one can be obtained by making the transformations on both sets simultaneously.

Consulting the analytical expressions in Appendix B.1, we see that, as long as $\mathbf{M}_\nu^{ii} \neq 0$ for any i, the solution implies that the magnitudes of the x'^i couplings are inversely proportional to the magnitude of x^1 while those of x^2, x^3 are directly proportional to it. Thus, a solution point where any of the $|x'^i|$ are small comes at the price of bigger $|x^i|$, and vice-versa. Knowing which RPV coupling can be made smaller by trading for another is useful from a model-building perspective, since the low-energy bounds on RPV couplings are non-democratic, varying over orders of magnitude [252]. We draw upon this point further when we study applications to specific models.

As an illustration, we plot one solution-set for the IO limit ($m_3 \approx 0$), assuming TBM values for the angles[5] in Fig. 4.1. For visualization, we restrict ourselves to real x^1 values. The solution then constrains x'^1 to be real, while the other couplings are complex, in general. The behavior of the couplings is as described above. We observe a symmetry under $x^1 \leftrightarrow -x^1$; this is an intrinsic feature of the model structure. More generally, for a complex x^1, the magnitude of the couplings is unchanged if $|x^1|$ is unchanged. The relation between the magnitudes of $x^2(x'^2)$ and $x^3(x'^3)$ in Fig. 4.1 is a peculiarity of the numbers involved in the TBM case;[6] it is not present when using experimental data.

Another point of interest is the "total amount of RPV" a particular model requires to explain the neutrino data. As an illustration, consider how the x^i, x'^i variables relate to the RPV parameters, *i.e*, the $\delta' s$ of Table 4.1:

$$x^i = A^i \delta^i, \qquad x'^i = A'^i \delta'^i, \tag{4.38}$$

where no summation is implied. In the above, δ and δ' are general symbols corresponding to any of the invariants in Table 4.1; they can both also correspond to the same invariant. One measure of the "total amount of RPV" we can define in the model is the sum,

$$\sigma \equiv \sum_i \left|\delta^i\right| + \sum_i \left|\delta'^i\right|. \tag{4.39}$$

[5] Even though we use the TBM limit for illustration in this section, all features we discuss are general.

[6] This arises due to the fact that the TBM-IO mass matrix is antisymmetric under an interchange of the second and third columns.

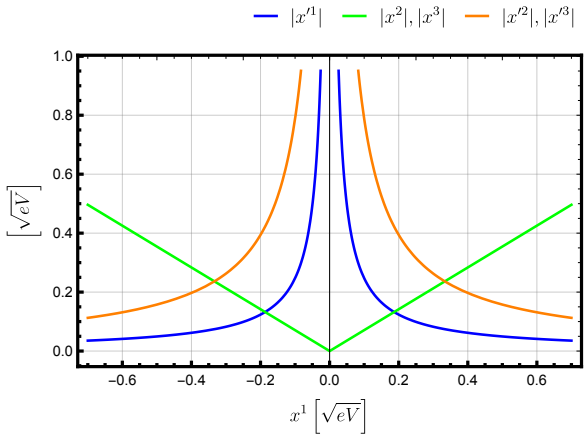

Figure 4.1: Absolute values of the couplings required to fit the IO limit of the TBM scenario in models with Class 1 structure.

The two terms represent the amount of RPV arising due to each individual set. Substituting Eq. (4.38),

$$\sigma = \sum_i \left(\frac{\left|x^i\right|}{\left|A^i\right|} + \frac{\left|x'^i\right|}{\left|A'^i\right|} \right) . \tag{4.40}$$

This will be a function of x^1. One could use the analytical expressions in Appendix B.1 to study how the RPV-amount demanded by each point varies with x^1 and find the point where it is minimal or maximal. In general, this requires that we first fix the constants A^i, A'^i, *i.e.*, we specify the model we wish to study. However, in the special case where $A^i = A\,, A'^i = A'\ \forall i$ (which holds for several contributions in Table 4.1), there is some simplification for Class 1 MOMs. Eq. (4.40), then, gives,

$$\sigma = \sum_i \left(\frac{\left|x^i\right|}{|A|} + \frac{\left|x'^i\right|}{\left|A'\right|} \right) . \tag{4.41}$$

Now, the structure of Class 1 MOMs allows us the freedom to choose x^i, x'^i suitably such that $A' = A$ without losing any generality. Then,

$$\sigma = \frac{1}{|A|} \sum_i \left(\left|x^i\right| + \left|x'^i\right| \right) . \tag{4.42}$$

Thus, with the above choice of the x^i, x'^i variables, the RPV amount is directly proportional to $\sum_i \left(\left|x^i\right| + \left|x'^i\right| \right)$ – a model-independent quantity. This allows us to find the point maximizing or minimizing the RPV amount without specifying the details of the model; determining the absolute scale, though, still requires the constant $|A|$ to be specified.

In Fig. 4.2, we plot the sum of the magnitudes of the x^i and x'^i for the IO limit of the TBM case, as well as the overall sum. We see that the latter varies from a clear minimum to an unbounded

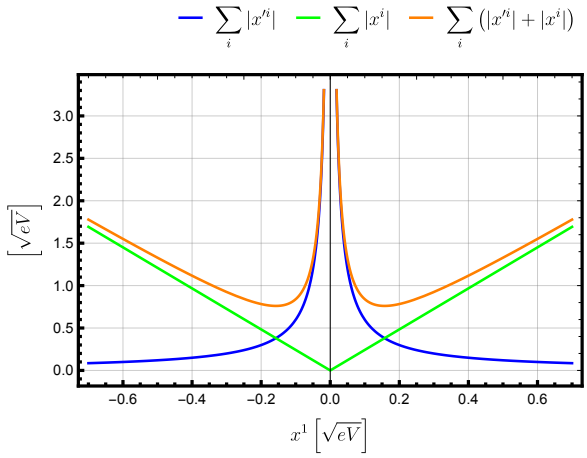

Figure 4.2: A measure of the amount of RPV required by each point in the solution space for Class 1 models. The plot corresponds to the IO limit of the TBM case.

value for $|x^1| \to 0$. Thus, the neutrino data can be described by relatively small or large amounts of RPV, depending on the point one chooses. The minimum is situated precisely at the point where the individual sums of the x^i and x'^i sets are equal. The general expression for this point is lengthy. However, for the CP-conserving case – and if the conditions $\left(\mathbf{M}_\nu^{12}\right)^2 < \mathbf{M}_\nu^{11} \times \mathbf{M}_\nu^{22}$ and an analogous one with the generation index 2 replaced by 3 are satisfied – the point is given by,

$$|x^1| = \sqrt{\frac{\left|\mathbf{M}_\nu^{11}\right|}{2}}\,, \tag{4.43}$$

and the magnitude of the minimum is $\sum_i \sqrt{2\left|\mathbf{M}_\nu^{ii}\right|}$. This holds for a general complex x^1. The condition we mention above is satisfied by the TBM matrix as well as the experimental data we use in our numerical fits.

4.6.2 Class 2: $x^i x^j + \left(x^i x'^j + x'^i x^j\right)$

There are four distinct solution sets related in the same way as in the previous case. Consulting Eq. (B.2) in Appendix B.1, we see that x^2, x^3 satisfy the same relations as for the Class 1 case. The behavior of the x'^i is different, however. For $|x^1| \ll \sqrt{\left|\mathbf{M}_\nu^{11}\right|}$, it is as before. However, for $|x^1| \gg \sqrt{\left|\mathbf{M}_\nu^{11}\right|}$, they grow linearly with $|x^1|$. In particular, x'^1 vanishes precisely at $x^1 = \pm\sqrt{\mathbf{M}_\nu^{11}}$ without any of the other couplings diverging. x^2, x^3 can not vanish without other couplings diverging. $|x'^2|, |x'^3|$ can also vanish but we skip the long general expressions.

We plot one of the solution sets corresponding to the TBM-IO limit for this class in Fig. 4.3, for real x^1. The symmetry under $x^1 \leftrightarrow -x^1$ is evident and again intrinsic. The relation between $x^2(x'^2)$ and $x^3(x'^3)$ is TBM-specific. We see the behavior described above. Indeed $x'^1 = 0$ at $|x^1| = \sqrt{|\mathbf{M}_\nu^{11}|}$;

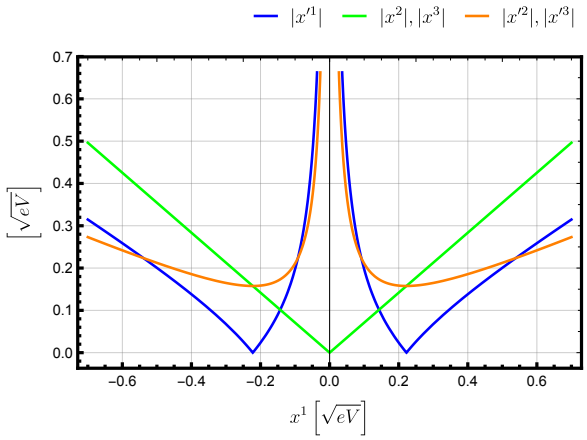

Figure 4.3: Absolute values of the couplings required to fit the IO limit of the TBM scenario in models with Class 2 structure.

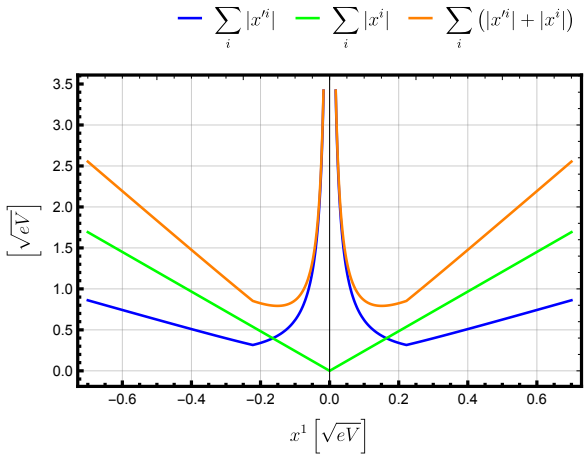

Figure 4.4: A measure of the amount of RPV required by each point in the solution space for Class 2 models. The plot corresponds to the IO limit of the TBM case.

$|x'^2|, |x'^3|$ have their minima at $|x^1| = \sqrt{|\mathbf{M}_\nu^{11}|}$ too. This is not a general feature but holds in the CP-conserving case if, as before, $\left(\mathbf{M}_\nu^{12}\right)^2 < \mathbf{M}_\nu^{11} \times \mathbf{M}_\nu^{22}$ and the analogous condition with the index 2 replaced by 3 are satisfied. $x'^2, x'^3 = 0$ in general requires a non-zero phase for x^1.

We plot the sum of magnitudes for $|x^i|$ and $|x'^i|$ for the IO limit in Fig. 4.4. The individual sums are directly proportional to the RPV amount for each set and can be interpreted as before. However, the overall sum is no longer directly related to the total RPV amount. Unlike the case of Class 1 MOMs, we do not always have the freedom to choose $A = A'$ in Eq. (4.38) for Class 2 MOMs. We still plot the quantity; however, it should only be used for models where $A = A'$ holds.

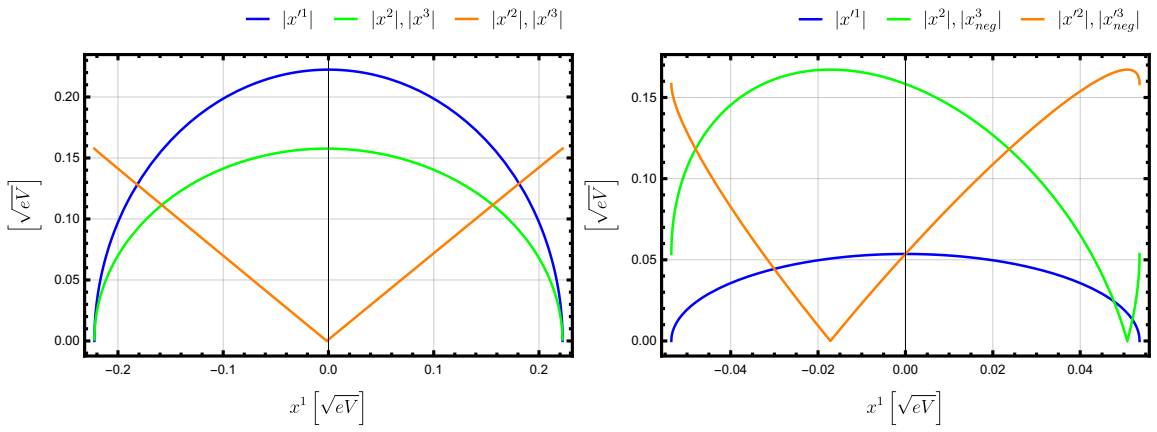

(a) Inverted Ordering

(b) Normal Ordering

Figure 4.5: Absolute values of the couplings required to fit the TBM scenario in models with Class 3 structure. The notation f_{neg} means $f\left(-x^1\right)$ has been plotted instead of $f\left(x^1\right)$.

4.6.3 Class 3: $x^i x^j + x'^i x'^j$

Class 3 MOMs have eight distinct solution sets. Four can be obtained using the same arguments as before; this time the invariance is under the simultaneous transformations,

$$x^2\left(x^1\right) \mapsto -x^2\left(-x^1\right), \qquad x'^2 \mapsto x'^2\left(-x^1\right). \tag{4.44}$$

and the analogous ones for x^3 and x'^3. In addition, the whole system of equations is invariant under the simultaneous transformations,

$$x'^i \mapsto -x'^i. \tag{4.45}$$

Thus, for each of the four solution sets, we can obtain one more by changing the signs of all the x'^i couplings.

In general, the solution space is more complicated than for the other two classes. Consulting Eq. (B.3) in Appendix B.1, in the limit $|x^1| \gg \sqrt{\left|\mathbf{M}_\nu^{11}\right|}$, all the coupling magnitudes increase roughly linearly with $|x^1|$. This class is somewhat special: It allows solutions where all the couplings are simultaneously real; this occurs when $|x^1| \leq \sqrt{|\mathbf{M}_\nu^{11}|}$, with x^1 real. This also requires $\delta_{CP} = 0$, $\left(\mathbf{M}_\nu^{12}\right)^2 < \mathbf{M}_\nu^{11} \times \mathbf{M}_\nu^{22}$ and the analogous condition with the index 2 replaced by 3 to hold.

We plot one solution set for the TBM-IO and TBM-NO limits in Fig. 4.5, restricted to the above region. The symmetry of x'^1 under $x^1 \leftrightarrow -x^1$ is an intrinsic feature of the model structure. Although the TBM-IO limit numbers conspire to make it look otherwise in our plot, the other couplings do not generally possess such a symmetry – this is clear after looking at the NO limit. As before, the $x^2\left(x'^2\right)$ and $x^3\left(x'^3\right)$ relation is TBM-specific.

Within our region of interest, we see that the magnitude of x'^1 always falls as that of x^1 increases and it is zero precisely at the point $x^1 = \pm\sqrt{\mathbf{M}_\nu^{11}}$. There are no such universal trends for the other couplings.

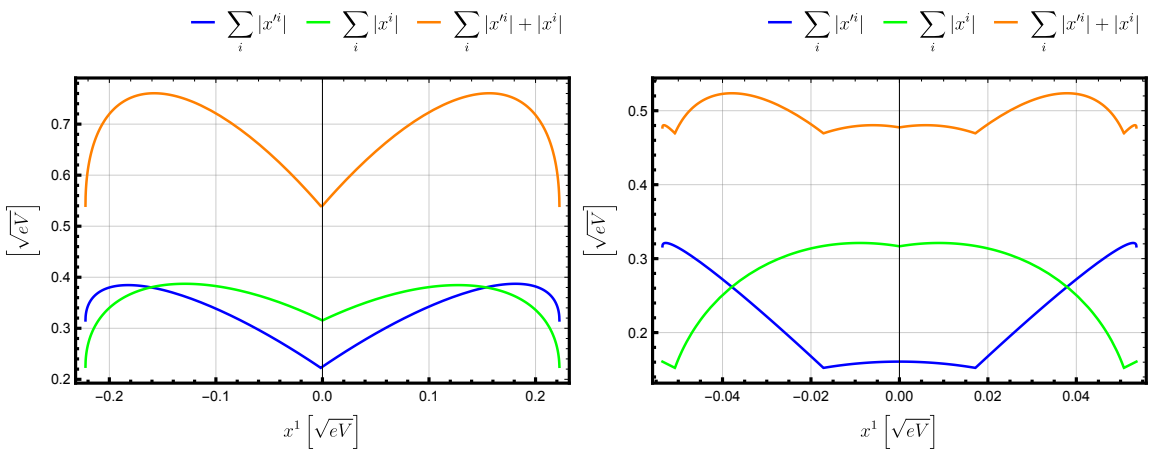

(a) Inverted Ordering

(b) Normal Ordering

Figure 4.6: A measure of the amount of RPV required by each point in the solution space for Class 3 models. The plots correspond to the TBM scenario.

Unlike before, however, they can each be made to vanish in appropriate regions of the solution space. The x^2 $\left(x^3\right)$ vanish at $x^1 = \pm\sqrt{\mathbf{M}_\nu^{11} - \frac{\mathbf{M}_\nu^{12(13)} \times \mathbf{M}_\nu^{12(13)}}{\mathbf{M}_\nu^{22(33)}}}$ while x'^2 $\left(x'^3\right)$ vanish at $\pm\mathbf{M}_\nu^{12(13)} / \sqrt{\mathbf{M}_\nu^{22(33)}}$.

We study the relative RPV amount in Fig. 4.6. As for Class 2 MOMs, the overall sum may only be interpreted as the total RPV amount if $A = A'$ in Eq. (4.38). Here, the amount of RPV is dominated by the x^i for vanishing x^1, with the x'^i share growing as $|x^1|$ grows. The amount of RPV is minimal near the two $|x^1|$ extremes.

4.7 Numerical Fits

We now present the solution space for the experimental data. We numerically solve the first three MOM classes for each of the dependent parameters with x^1 as the free variable. We estimate the couplings by means of an error-weighted least-squares fit. We use the neutrino data of Table 4.2 (with $\delta_{CP} = 0$) at the 1σ level. In order to extract predictions for the couplings, we define a χ^2 function:

$$\chi^2 \equiv \frac{1}{N_{\text{obs}}} \sum_{i=1}^{3} \sum_{j=i}^{3} \left(\frac{x^{ij} - M^{ij}}{\delta^{ij}} \right)^2 , \tag{4.46}$$

where M^{ij} are the central values of the N_{obs} experimentally determined parameters of the mass matrix defined in Eq. (4.18), x^{ij} are the parameters to be determined, and δ^{ij} are the 1σ experimental uncertainties.

We initiate the fit using the TBM approximation for the x^{ij}. We minimize the χ^2 of Eq. (4.46) by using the program package MINUIT2 [317]. We consider both the NO and IO limits. We accept the minimization result as a success if the routine yields $\chi^2 < O(10^{-5})$.

To handle complex couplings, we fit the real and imaginary parts of each parameter separately. This

extends the definition of our χ^2 function:

$$\chi^2 = \frac{1}{N_{\text{obs}}} \sum_{i=1}^{3} \sum_{j=i}^{3} \left[\left(\frac{\text{Re}\left(x^{ij}\right) - \text{Re}\left(M^{ij}\right)}{\delta^{ij}} \right)^2 + \left(\frac{\text{Im}\left(x^{ij}\right) - \text{Im}\left(M^{ij}\right)}{\delta^{ij}} \right)^2 \right], \tag{4.47}$$

where we demand that the imaginary components of the neutrino mass matrix vanish, since we are working in the CP-conserving limit.

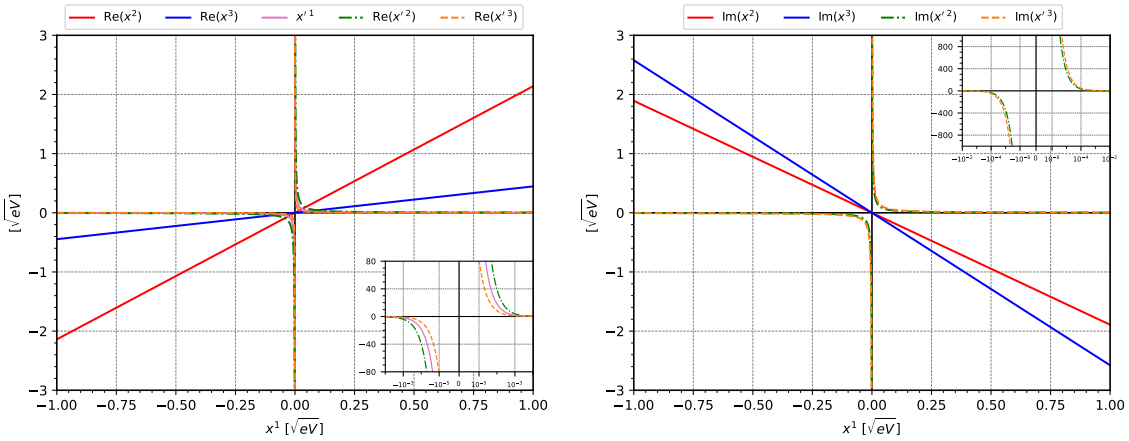

Figure 4.7: Real (top) and imaginary (bottom) values of the couplings required to fit the actual neutrino data for the NO limit in models with Class 1 structure.

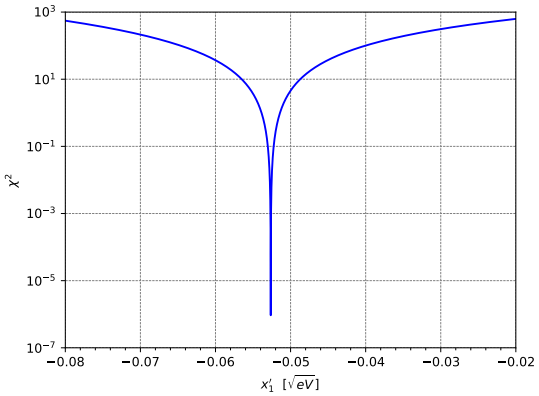

Figure 4.8: Variation of χ^2 as a function of the fitted parameter x_1' for the Class 3 NO scenario around the best-fit point as determined by MINUIT2. The other couplings are held fixed.

Fig. 4.7 shows the numerical result using the neutrino data, assuming the NO limit, for Class 1 MOMs. We restrict ourselves to real x^1. This automatically implies that x'^1 has to be real. As before, we depict only one of the multiple solution sets. We see that the solution space reproduces the general features discussed in Section 4.6.1. The analogous results for the IO limit for Class 1 MOMs (Fig. B.1), as well as the plots corresponding to Class 2 MOMs (Fig. B.2), and Class 3 MOMs (Fig. B.3) can be found in Appendix B.3. A corresponding solution including a non-zero δ_{CP} can be found in Fig. B.4 with more details in Appendix B.3.

To depict the robustness of our procedure, we show, in Fig. 4.8, the variation of χ^2 by varying one of the fitted couplings – x'^1 – about the best-fit point. The other couplings are held fixed. The minimum is extremely well-defined, indicating excellent convergence.

4.8 Example Applications

As long as a model has a MOM structure, our general results can be directly translated into model-specific numbers. We now demonstrate this by considering several examples of RPV models. The statement that only certain RPV couplings are non-vanishing in a given model is U(4)-basis dependent; our statements in this section apply to the vanishing-sneutrino-vev basis.

4.8.1 κ-only Models

In a model where the only RPV sources are the δ_κ invariants, the effective neutrino mass matrix has contributions at tree level, and of types 7, 8 and 13 in Table 4.1 at one-loop level. The expression for the mass matrix is [40, 294],

$$\mathbf{M}_\nu^{ij} = m_0 \delta_\kappa^i \delta_\kappa^j + \frac{g_2 \left[\left(m_{e_i}\right)^2 + \left(m_{e_j}\right)^2 \right]}{16\pi^2 v} \times \\ \times \left(1 + \sin^2\beta + \tan\beta \sin^2\beta\right) \delta_\kappa^i \delta_\kappa^j + \dots , \tag{4.48}$$

where $m_0 = -\frac{M_Z^2 \cos^2\beta m_{\rm SUSY}}{m_{\rm SUSY}^2 - M_Z^2 \sin 2\beta}$ is the tree-level mass scale of Eq. (4.14), v is the electroweak vev, g_2 is the $SU(2)_L$ gauge coupling, and the other notation is as in Table 4.1. There are three separate diagrams of type 13 that lead to the second term [294]. The ellipsis indicates all the terms of higher (fourth) order in the lepton Yukawas, due to contributions of types 7, 8. We have set all SUSY mass scales to $m_{\rm SUSY}$.

Eq. (4.48) does not have a MOM structure. However, we can neglect the terms in the ellipsis to a first approximation, given their suppression by two extra powers of the small Yukawas. Then, making the identifications,

$$x^i = \sqrt{m_0}\,\delta_\kappa^i , \quad \text{and} \\ x'^i = \frac{g_2 \left(m_{e_i}\right)^2}{16\pi^2 v \sqrt{m_0}} \left(1 + \sin^2\beta + \tan\beta \sin^2\beta\right) \delta_\kappa^i , \tag{4.49}$$

we see that the model reduces to a Class 2 MOM structure, and our framework can be applied. One can easily show that such a model cannot solve the neutrino pattern. The above equations imply the following relations involving the lepton masses:

$$\frac{1}{m_e^2}\frac{x'^1}{x^1} = \frac{1}{m_\mu^2}\frac{x'^2}{x^2} = \frac{1}{m_\tau^2}\frac{x'^3}{x^3}\,. \tag{4.50}$$

Consulting Eq. (B.2) in Appendix B.1, there is no point in the solution space of Class 2 models satisfying this.

4.8.2 $\kappa - B$ Models

We next consider a model also including the soft-breaking bilinear terms, *i.e.*, $\delta_\kappa, \delta_B \neq 0$ with all other RPV couplings zero (see also Ref. [281]). We have the contributions, *cf.* Table 4.1: Tree-level, and of types 3, 7, 8, 9, 11, 12, 13, 16 and 17. The complete expression is [294],

$$\begin{aligned}\mathbf{M}_\nu^{ij} &= m_0\delta_\kappa^i\delta_\kappa^j + \frac{g_2^2 m_{\text{SUSY}}}{64\pi^2\cos^2\beta}\delta_B^i\delta_B^j \\ &\quad + \frac{g_2^2 m_{\text{SUSY}}}{64\pi^2\cos\beta}\left(\delta_\kappa^i\delta_B^j + \delta_B^i\delta_\kappa^j\right) + \ldots\,.\end{aligned} \tag{4.51}$$

The ellipsis again proxies contributions of higher (second and above) order in the Yukawas. As before, the full model does not have a MOM structure but neglecting the Yukawa-suppressed terms[7], and making the identifications,

$$\begin{aligned}x^i &= \sqrt{m_0}\delta_\kappa^i\,, \\ x'^i &= \frac{g_2\sqrt{m_{\text{SUSY}}}}{8\pi\cos\beta}\delta_B^i\,, \\ A &= \frac{g_2\sqrt{m_{\text{SUSY}}}}{8\pi\sqrt{m_0}}\,,\end{aligned} \tag{4.52}$$

the model reduces to a Class 4 MOM.

As a numerical illustration, we set $m_{\text{SUSY}} = 1\,\text{TeV}$, $\tan\beta = 10$, and substitute the other known parameters. This gives,

$$\begin{aligned}x^i &\approx \left(9.081\times10^3\,\sqrt{\text{eV}}\right) i\delta_\kappa^i\,, \\ x'^i &= \left(2.607\times10^5\,\sqrt{\text{eV}}\right)\delta_B^i\,, \\ A &\approx -2.857i\,.\end{aligned} \tag{4.53}$$

[7] Some of these Yukawa-suppressed terms have $\tan\beta$ factors which may enhance them for large $\tan\beta$; however, even in this case the second and third terms in Eq. (4.51) dominate due to the $\cos\beta$ factors.

Numerically solving this for the TBM-IO limit – for instance, at the point with $x^1 = 0$ – yields,

$$\begin{aligned} x^2 &= -x^3 \approx 0.052 \ \sqrt{\text{eV}}\,, \\ x'^1 &\approx \ -0.222 \ \sqrt{\text{eV}}\,, \\ x'^2 &= -x'^3 \approx (-0.001 + 0.149i) \ \sqrt{\text{eV}}\,, \end{aligned} \tag{4.54}$$

or, using Eq. (4.53),

$$\begin{aligned} \kappa^1 &= 0\,, \\ \kappa^2 &= -\kappa^3 \approx -|\kappa| \left(5.73 \times 10^{-6} i\right)\,, \\ B^1 &\approx -|B| \left(8.52 \times 10^{-7} i\right)\,, \\ B^2 &= -B^3 \approx -|B| \left(3.84 \times 10^{-9} - 5.72 \times 10^{-7} i\right)\,. \end{aligned} \tag{4.55}$$

In the above, we have made use of the forms of the δ invariants in the vanishing-sneutrino-vev basis, *cf.* Eq. (4.15). Similarly, one could also numerically solve at the point corresponding to the minimal RPV amount, and use that in order to derive a minimal bound on the couplings.

4.8.3 Diagonal Trilinear Models I

We now consider models with the trilinear sector contributing, and assume the other contributions are negligible. The effective neutrino mass matrix is zero at tree level but receives contributions at loop-level of types 1 and 2 in Table 4.1. The expression for the matrix is,

$$\begin{aligned} \mathbf{M}_\nu^{ij} = &\frac{1}{8\pi^2 m_{\text{SUSY}}} \delta_\lambda^{ink} \delta_\lambda^{jkn} m_{e_n} m_{e_k} \\ &+ \frac{3}{8\pi^2 m_{\text{SUSY}}} \delta_{\lambda'}^{ink} \delta_{\lambda'}^{jkn} m_{d_n} m_{d_k}\,, \end{aligned} \tag{4.56}$$

with a summation implied over repeated indices. The equation has too many parameters to have a MOM structure, or any predictivity in general.

In a minimal model where only the diagonal (in the last two indices) trilinear couplings contribute, the above expression simplifies:

$$\begin{aligned} &\mathbf{M}_\nu^{ij} = \\ &\frac{1}{8\pi^2 m_{\text{SUSY}}} \left(\lambda^{i11}\lambda^{j11} m_e^2 + \lambda^{i22}\lambda^{j22} m_\mu^2 + \lambda^{i33}\lambda^{j33} m_\tau^2\right) \\ &+ \frac{3}{8\pi^2 m_{\text{SUSY}}} \left(\lambda'^{i11}\lambda'^{j11} m_d^2 + \lambda'^{i22}\lambda'^{j22} m_s^2 + \lambda'^{i33}\lambda'^{j33} m_b^2\right), \end{aligned} \tag{4.57}$$

where we have used the fact that the δ invariants can be simply replaced by the λ couplings in the vanishing-sneutrino-vev basis.

Eq. (4.57) still has too many terms for a MOM structure. We can further reduce the system, by assuming the couplings have a comparable magnitude. The terms then have a natural hierarchy due to the fermion masses. Considering only the contributions of the two heaviest particles – the b quark and

the τ lepton – the largest neglected term is a factor $\frac{m_\tau^2}{m_\mu^2} \sim 300$ smaller. The model reduces to:

$$\begin{aligned}\mathbf{M}_\nu^{ij} &= \frac{1}{8\pi^2 m_{\text{SUSY}}} \lambda^{i33}\lambda^{j33} m_\tau^2 \\ &\quad + \frac{3}{8\pi^2 m_{\text{SUSY}}} \lambda'^{i33}\lambda'^{j33} m_b^2 \,,\end{aligned} \tag{4.58}$$

which has a Class 3 MOM structure with the identifications,

$$\begin{aligned}x^i &= \sqrt{\frac{1}{8\pi^2 m_{\text{SUSY}}}}\, m_\tau \lambda^{i33} \,, \\ x'^i &= \sqrt{\frac{3}{8\pi^2 m_{\text{SUSY}}}}\, m_b \lambda'^{i33} \,.\end{aligned} \tag{4.59}$$

Due to the antisymmetry of the LLE couplings in the first two indices, $x^3 \sim \lambda^{333} = 0$. This uniquely determines the solution to the point where $x^3 = 0$ vanishes. We had discussed the location of this point earlier. Plugging in the numbers for the TBM-IO limit gives:

$$\begin{aligned}x^1 &\approx -0.2224\,\sqrt{\text{eV}}\,, \quad x^2 = x^3 \approx 0\,\sqrt{\text{eV}}\,, \\ x'^1 &\approx -0.0016\,\sqrt{\text{eV}}\,, \quad x^2 = -x^3 \approx -0.1577\,\sqrt{\text{eV}}\,.\end{aligned} \tag{4.60}$$

One can plug in the values of m_{SUSY} and the lepton masses to see what this implies for the λ couplings.

4.8.4 Diagonal Trilinear Models II

To discuss a slightly more complex application, we consider a cMSSM-like scenario, called the B_3 cMSSM in Ref. [299]. At the GUT scale, the five cMSSM parameters are appended by one (or two) RPV trilinear coupling(s). All other RPV couplings are assumed to be zero. Through the renormalization group equations (RGEs), further couplings are generated at the electroweak scale. Thus, we end up with multiple contributions to the neutrino mass matrix. The most relevant are the bilinear terms since these contribute at tree-level; the RGE-generated trilinear couplings are suppressed and only contribute at one-loop level. The neutrino mass matrix has the structure,

$$\mathbf{M}_\nu^{ij} \sim \delta_\kappa^i \delta_\kappa^j + \delta_B^i \delta_B^j + \delta_{\lambda'}^i \delta_{\lambda'}^j + \delta_\lambda^i \delta_\lambda^j + \dots \,, \tag{4.61}$$

where we assume two non-zero GUT-scale couplings λ, λ' and only symbolically depict the type of terms contributing. The ellipsis indicates potential cross-terms. The above model again has too many terms. To a good approximation, the generated bilinear parameters are of the form,

$$\begin{aligned}\delta_\kappa^i &\approx a_1 \delta_{\lambda'}^i + b_1 \delta_\lambda^i \,, \\ \delta_B^i &\approx a_2 \delta_{\lambda'}^i + b_2 \delta_\lambda^i \,,\end{aligned} \tag{4.62}$$

where the a_i, b_i are numerical constants. Thus, the RGEs ensure that the generated couplings are approximately linearly dependent on the original δ^i_λ, $\delta^i_{\lambda'}$.[8] The model has only two linearly independent structures appearing and the MOM framework applies. Substituting Eq. (4.62) in Eq. (4.61), the matrix reduces to the form,

$$\mathbf{M}_\nu^{ij} \sim \delta^i_{\lambda'}\delta^j_{\lambda'} + \delta^i_\lambda\delta^j_\lambda + \left(\delta^i_{\lambda'}\delta^j_\lambda + \delta^i_{\lambda'}\delta^j_\lambda\right) , \tag{4.63}$$

which is a Class 4 MOM.

4.8.5 Non-diagonal Trilinear Models

Next, we consider the dominant contributions to arise from the non-diagonal (in the last two indices) trilinear couplings. The effective neutrino mass matrix has the form of Eq. (4.56), except now the n, k indices are not equal. Again, we exploit the natural hierarchy of the structures to reduce the model to a MOM. Performing the expansion in the vanishing-sneutrino-vev basis, we have,

$$\mathbf{M}_\nu^{ij} = \frac{3}{8\pi^2 m_{\text{SUSY}}}\left(\lambda'^{i32}\lambda'^{j23} + \lambda'^{j32}\lambda'^{i23}\right) m_b m_s + \dots , \tag{4.64}$$

where the ellipsis hides the other terms. For instance, assuming similar magnitudes of couplings, the next highest contribution is the one proportional to $m_\tau m_\mu$ and is smaller by a factor $\frac{3m_b m_s}{m_\tau m_\mu} \sim 8$ compared to the first term. The factor of 3 here is due to the quark colors. Thus, we only consider the first term. This reduces the model to a MOM of Class 1 structure, with the identifications,

$$\begin{aligned} x^i &= \sqrt{\frac{3m_b m_s}{8\pi^2 m_{\text{SUSY}}}}\lambda'^{i23} , \\ x'^i &= \sqrt{\frac{3m_b m_s}{8\pi^2 m_{\text{SUSY}}}}\lambda'^{i32} . \end{aligned} \tag{4.65}$$

We had mentioned earlier how a broader phenomenological perspective can sometimes make it relevant to know which couplings can be made smaller by trading for others. We can see an example of that here. The λ' couplings above need to satisfy certain single bounds, *cf.* Ref. [252]:

$$\begin{aligned} |\lambda'^{123}| &\le 0.43, \qquad |\lambda'^{132}| \le 1.04 , \\ |\lambda'^{223}| &\le 1.12, \qquad |\lambda'^{232}| \le 1.04 , \\ |\lambda'^{323}| &\le 1.12, \qquad |\lambda'^{332}| \le 1.04 . \end{aligned} \tag{4.66}$$

In addition, there are also product bounds:

$$\begin{aligned} |\lambda'^{123*}\lambda'^{223}| &\le 0.0076 , \\ |\lambda'^{132*}\lambda'^{232}| &\le 0.0076 . \end{aligned} \tag{4.67}$$

In the above, we have assumed all sfermion masses to be 1 TeV, or, if stricter, we have used the

[8] The exact forms of the RGEs can be found in Ref. [299], where this approximation is also discussed.

perturbativity constraint. Thus, for model building, solutions with, for instance, small λ'_{123} are preferable. We recast the solution space for the two limits of Fig. 4.7, and depict it in terms of the RPV couplings using Eq. (4.65) in Fig. 4.9. The plot also depicts the regions ruled out by the above bounds as shaded grey regions.

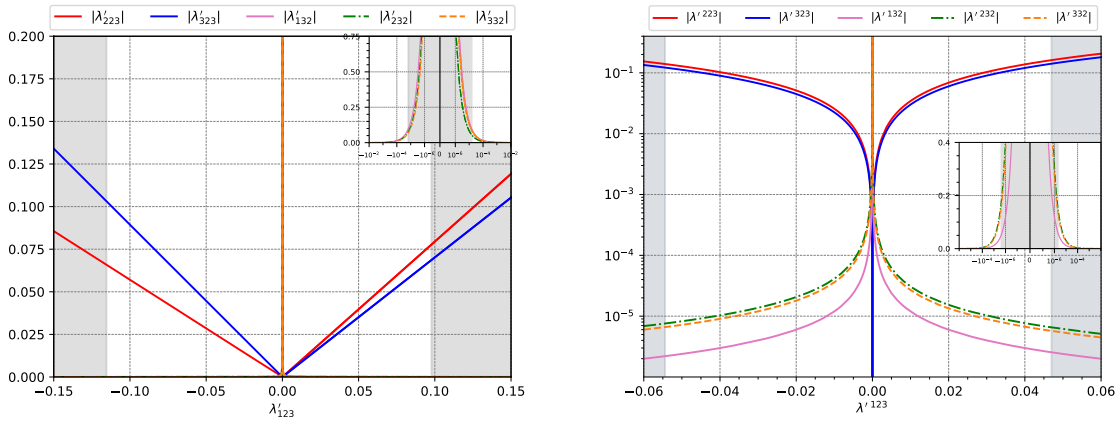

(a) Inverted Ordering

(b) Normal Ordering

Figure 4.9: The IO (left) and NO (right) solution spaces for the non-diagonal trilinear model of Section 4.8.5 including δ_{CP}. The grey regions are the ones ruled out by the bounds of Eq. (4.67). The bounds of Eq. (4.66) are beyond the scale of the plots.

4.8.6 Bilinear-Trilinear Models

The final model we consider has contributions from both the bilinear and trilinear sectors. To have predictivity, we consider a scenario where all the δ_κ bilinears and the *diagonal* trilinears contribute. The effective neutrino mass matrix is,

$$\begin{aligned}\mathbf{M}_\nu^{ij} = m_0 \delta_\kappa^i \delta_\kappa^j + & \frac{g_2 \left[\left(m_e^i\right)^2 + \left(m_e^j\right)^2 \right]}{16\pi^2 v} \\ & \times \left(1 + \sin^2\beta + \tan\beta \sin^2\beta\right) \delta_\kappa^i \delta_\kappa^j \\ & + \frac{3}{8\pi^2 m_{\text{SUSY}}} \delta_{\lambda'}^{i33} \delta_{\lambda'}^{j33} m_b^2 + \dots ,\end{aligned} \tag{4.68}$$

where, the ellipsis indicates terms that are suppressed by extra powers of the Yukawas. The above does not have a MOM structure. However, as long as $\tan\beta$ is not too large, the second term is expected to be suppressed compared to the first and third. The former is due to the extra Yukawas, while the latter follows from the fact that the bilinear invariants typically have to satisfy bounds at least a couple of orders of magnitude more stringent than the trilinear ones in order to fit the neutrino data – for instance, *cf.* the numbers in the previous applications. Ignoring the second term, the model reduces to

a MOM with Class 3 structure, as can be seen by making the identifications,

$$x^i = \sqrt{m_0}\delta^i_\kappa\,,$$
$$x'^i = \sqrt{\frac{3}{8\pi^2 m_{\rm SUSY}}}\, m_b \delta'^{i33}_\lambda\,. \tag{4.69}$$

Once again, we show what the solution space looks like for the above model by recasting the plot corresponding to the NO limit of Fig. B.3 in Fig. 4.10.

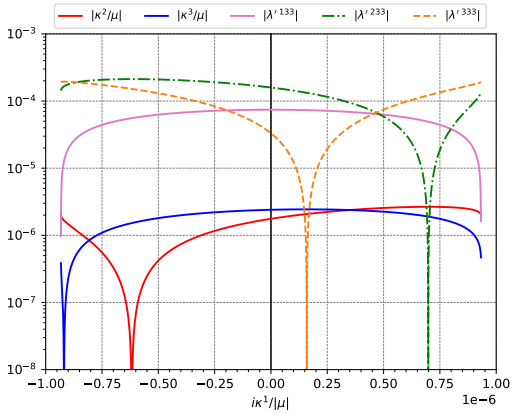

Figure 4.10: The NO limit solution space for the bilinear-trilinear mixed model of Section 4.8.6 including δ_{CP}.

4.9 Conclusions

In this paper, we have explored neutrino-mass generation in the B_3-conserving, but R-parity-violating MSSM. The main obstacle to a systematic phenomonelogical study in general RPV models is the large number of undetermined parameters. Typically, to deal with this, one specializes to specific models; this, however, restricts the applicability of the study. Here, we have taken a different route. By analyzing the structures of the neutrino mass matrix, we have identified four classes of minimal models – the Minimal Oscillation Models (MOMs) – that are consistent with the neutrino oscillation data for the case of two massive neutrinos. This allows for a model-independent study, at least for all models that satisfy the MOM criteria. Our study can be generalized to the case of three massive neutrinos.

We have analyzed each MOM class individually, and shown that it is possible to obtain solution-points consistent with the observed neutrino masses and mixings; for each class there is actually an infinite space of solutions. We have explored the general features of these solution spaces. Finally, we have presented numerical fits that can be adapted to any (MOM-like) specific RPV model without the need for re-performing the least-squares fit. As a demonstration, we have studied several examples that show the wide range of applicability of MOMs. This includes bilinear-only models, trilinear-only models (diagonal and non-diagonal), as well as mixed models.

MOMs do not solve the most general RPV case; we have described the limitations of the framework in the main text. However, given its simplicity, predictivity, and range of applicability, we believe the

MOM framework is a useful way to think about neutrino masses in general RPV settings.

Part IV

Samadarśī

5

Recasting Bounds on Long-lived HNLs in Terms of the RPV-MSSM

5.0 Preface

The contents of this chapter and the supplementary material presented in Appendix C have already been published:

- H. K. Dreiner, D. Köhler, S. Nangia, M. Schürmann, and Z. S. Wang,
  Recasting Bounds on Long-lived Heavy Neutral Leptons in Terms of a Light Supersymmetric R-parity Violating Neutralino,
  `arXiv:2306.14700 [hep-ph]`.

5.0.1 Overview

In the last part of this thesis, spanning this chapter and the next one, we explore the fourth opportunity identified in Chapter 1: the slightly unconventional possibility of finding SUSY at the $O(\text{GeV})$ scale.

As we discussed in Chapter 1, the lightest neutralino ($\tilde{\chi}_1^0$) can be very light if it is bino-like; in the RPV-MSSM, its mass is completely unconstrained. Such neutralinos, if in the mass range $m_{\tilde{\chi}_1^0} \lesssim O(5\,\text{GeV})$, would be produced at our colliders in abundance, through the R-parity violating decays of mesons and leptons.[1] While the RPV couplings can make them decay into SM final states, these neutralinos are expected to be long-lived ($c\tau > O(10 - 100\text{ m})$) due to: (i) their small masses, and (ii) the bounds on the RPV couplings, and (iii) the heavy SUSY mediators involved in the decays. Therefore, their signature at "small-scale" detectors such as those at the LHC would only be an insignificant amount of E_T^{miss},[2] which would have been missed by our current strategies. Thus, such neutralinos represent a gap in SUSY coverage at the LHC.

On the other hand, long-lived particles (LLPs) are not new in the literature. Several candidates have been considered in various theoretical contexts, and have been experimentally searched for. One particularly attractive candidate that has received significant attention is the heavy neutral lepton (HNL). These particles are viable partners to the SM neutrinos that can help explain their masses. Further, they may also address the dark matter, and baryon asymmetry puzzles. Such HNLs can also be produced in rare decays of mesons and the associated missing-energy or displaced-vertex

[1] Light binos can also be produced in R-parity conserving decays, *e.g.*, through Z bosons. However, we will not consider this possibility here as it has been studied elsewhere; see, for instance, Ref. [91].

[2] If the neutralinos come from decays of light SM particles, they are boosted in the far-forward direction. Hence, their missing energy does not contribute to E_T^{miss}.

signatures have already been searched for at many past experiments – including PIENU, NA62, KEK, BEBC, Super-Kamiokande, etc. – leading to stringent exclusion limits on the parameter space of the relevant model. Further, a whole host of currently running and upcoming experiments – including DUNE, MoEDAL-MAPP(2), BaBar, and the dedicated FASER(2) facility at the LHC – will significantly extend the sensitivity reach.

The phenomenology of HNLs is very similar to that of light binos. As we mentioned in Chapter 1, this correspondence can naively be understood through the fact that the bino and the HNL share the same quantum numbers under the SM symmetry group after electroweak symmetry breaking. As a result, one can use a simple recasting procedure to reinterpret the existing exclusion limits on HNL models in terms of the RPV-MSSM, as well as to gauge the SUSY discovery potential of the future experiments. This is what we shall do in this chapter.

We find that, using the above procedure, sensitivity limits can be obtained for a very wide range of RPV-MSSM scenarios (again due to the above fact). For reference, we compile a list of all relevant RPV-MSSM scenarios involving one or two non-vanishing RPV couplings that can be constrained in this way. To show numerical results, we consider a large number of benchmarks out of this list for the recasting. We find that we are able to set stringent limits on the RPV-MSSM space across the benchmarks: these are up to 3-4 orders of magnitude stronger than the currently quoted bounds using data that is already available. Future experiments will further probe the RPV-MSSM space.

5.0.2 Contributions of the Author

The idea to recast the HNL sensitivity limits in terms of the RPV-MSSM was independently thought of by Herbi Dreiner (in the context of BEBC) after stimulating discussions with Subir Sarkar and Giacomo Marocco; Dominik Köhler after he calculated the bounds on the RPV-MSSM coming from the invisible widths of the mesons in a different context; and the author of this thesis after an insightful comment raised by the anonymous referee of the publication presented in Chapter 6 of this thesis. The author guided Martin Schürmann in his calculations for the neturalino decay width via $LL\bar{E}$ operators, and the bino-neutrino mixing parameter. Further, all the experimental data used in this chapter (except for the data corresponding to FASER(2), BaBar, MoEDAL-MAPP(2), and the invisible widths) was provided by the author. Finally, the consolidated lists of RPV scenarios to which HNL searches would be sensitive, as well as all the benchmark scenarios in this chapter were developed by the author.

5.1 Introduction

With the discovery of a Standard-Model (SM)-like Higgs boson at the LHC in 2012 [10, 11], the SM is complete. Yet many questions beyond the Standard Model (BSM) remain. One avenue of exploration which has received considerable attention is new light, feebly interacting particles [156, 318–326]. Such exotic states are predicted in many BSM theories and are often long-lived. Theoretical candidates for such long-lived particles (LLPs) range from heavy neutral leptons (HNLs), axion-like particles, dark scalars, and dark photons, to electroweakinos in variations of supersymmetric models, inelastic dark matter (DM), and many more. See, *e.g.*, Refs. [152, 156, 327, 328] for reviews on LLPs. They are usually motivated as explanations of either the non-vanishing active neutrino masses or of dark matter and could have a spin of 0, $\frac{1}{2}$, 1, . . ., and a mass usually ranging from the sub-MeV scale up to the multi-TeV scale.

As an example, the HNLs (labeled as N in this work) are proposed hypothetical spin-half fermions that are SM-singlets which mix with the light active neutrinos. For certain mass values, they can explain simultaneously the neutrino masses, the observed dark matter, as well as the baryon asymmetry of the Universe [329]. They can give light neutrinos Dirac masses via the Yukawa term LHN in the Lagrangian with L and H being the lepton and Higgs doublets. This implies unnaturally small Yukawa couplings given the tiny neutrino masses [12, 312, 330]. One can also write down a Majorana mass term in the Lagrangian, leading to light Majorana neutrinos via the seesaw mechanisms [331–335]. While the vanilla type-I seesaw mechanism demands the mixing parameters should be small for the tiny active neutrino masses, larger values of mixing are legitimately conceived in other variations such as the linear seesaw model [336–338] and inverse seesaw model [339, 340]. Therefore, in phenomenological studies, the HNL mass and the mixing angles with the SM neutrinos are often assumed to be independent parameters.

Via mixing with the active neutrinos, the HNLs can participate in both charged-current and neutral-current interactions, coupled to both gauge bosons directly and the Higgs boson indirectly. They can thus be produced from decays of these bosons or from mesons, or through direct production at colliders. The HNL can decay leptonically or semi-leptonically, leading to a variety of signatures at the different experimental facilities. In particular, GeV-scale HNLs have received substantial attention in recent years, for they could originate from rare decays of mesons, which are copiously produced, *e.g.*, at beam-dump experiments, B-factories, and high-energy hadron colliders. Given the strict experimental upper bounds on the mixing of the HNLs and the active neutrinos, the more recent focus has been on small mixing angles, for which the GeV-scale HNLs are usually long-lived. Searches for these long-lived HNLs have been performed via many different signatures, including searches for missing energy, peak searches, as well as searches for displaced vertices (DV). See, *e.g.*, Refs. [341, 342] for summaries of these searches. Moreover, one could use the uncertainty on the measurements of the invisible decay width of mesons to put upper bounds on the long-lived HNLs, which contribute to the invisible decay width.

Besides the HNLs, supersymmetric electroweakinos, including charginos and neutralinos, are often considered as LLP candidates. See for instance Refs. [343, 344]. In particular, a specific type of light neutralino in the GeV mass scale is still allowed by all observational and experimental constraints [73, 74, 79, 84, 311, 345–351]; they are necessarily bino-like [73, 74] and have to decay to avoid overclosing the Universe [77, 81, 352]. One possibility is to consider R-parity-violating supersymmetry (RPV-SUSY) (see Refs. [29, 37, 353] for reviews), where the light binos decay via small but non-vanishing RPV couplings (see Ref. [354] for a detailed study of light bino decays).

The minimal version is known as the R-parity-violating Minimal Supersymmetric Standard Model (RPV-MSSM) [40]. The RPV-MSSM solves the SM hierarchy problem as in the MSSM, and also predicts a very rich phenomenology at colliders [45, 47, 150, 355]. *A priori* it is unknown if R-parity is conserved or broken, SUSY models with R-parity conservation or violation are equally legitimate, *e.g.*, see Refs. [44, 249]. Moreover, the RPV-MSSM can explain several experimental anomalies reported in recent years including the B-meson anomalies [230, 231, 356–358], the ANITA anomaly [359, 360], as well as the anomalous magnetic moment of the muon [356–358]. If R-parity is broken, one can write down operators which violate baryon- or lepton-number. Allowing all these operators to be non-vanishing would lead to a too fast proton decay rate, in conflict with the current experimental measurements [60, 361], unless all their couplings are extremely small. Therefore, we assume the discrete anomaly-free baryon triality symmetry B_3 [35, 299, 362], so that baryon-number is conserved. In this work, we restrict ourselves to the lepton-number-violating terms only. Further, the light bino is the lightest supersymmetric particle (LSP) in our study and decays only into SM particles via RPV couplings.

Via the lepton-number-violating RPV operators, the light bino decays lead to very similar final states as the NHL decays. Moreover, the corresponding RPV couplings are all bounded to be small by various low-energy observables and collider searches [29, 252, 363–365]. The GeV-scale binos are hence expected to be long-lived, too, resulting in signatures such as missing energy and displaced vertices at various experiments. These similarities raise the question: is it possible to recast the extensive exclusion bounds on the HNLs in the literature into corresponding bounds on the light binos in the RPV-SUSY? In this work, we answer this question positively, by compiling a list of bounds on long-lived HNLs obtained in searches for all types of signatures mentioned above and recasting them into exclusion limits on the RPV-SUSY couplings as functions of the light bino mass for a selected list of benchmark scenarios.[3] We focus on exclusion bounds acquired in past experiments, as well as predicted search sensitivities for experiments that are ongoing or under construction. For future (and not yet approved) experiments, we consider only `MoEDAL-MAPP2` [366, 367] and `FASER2` [86] with 300 and 3000 fb^{-1} integrated luminosity, respectively, as they would be the successors of some ongoing experiments at the LHC, while the other future concepts such as `MATHUSLA` [327, 368, 369], and `ANUBIS` [370] are independent ones and are hence not studied here. We do not consider the approved experiment `Hyper-Kamiokande` [371, 372] for there is no available HNL-search sensitivity prediction that can be used with our recasting methods.

In the following section, we give the model basics of light binos in the RPV-SUSY and of the HNLs that mix with active neutrinos. The considered experiments are introduced in Sec 5.3, along with an explanation of our recasting procedure. We then present our numerical results for some representative benchmark scenarios in Sec. 5.4. Finally, in Sec. 5.5 we conclude the paper with a summary.

[3] Recently during the completion of this work, Ref. [342] appeared on arXiv; it employed similar strategies to recast the bounds on the HNLs in the minimal scenarios into those on the HNLs in effective field theories.

5.2 Model basics

5.2.1 RPV-MSSM with a light bino

In the R-parity-violating MSSM, the usual MSSM superpotential is extended by the following terms [40, 61]:

$$W_{\text{RPV}} = \kappa_i L_i H_u + \frac{1}{2}\lambda_{ijk} L_i L_j \bar{E}_k + \lambda'_{ijk} L_i Q_j \bar{D}_k + \frac{1}{2}\lambda''_{ijk} \bar{U}_i \bar{D}_j \bar{D}_k \,, \tag{5.1}$$

where L_i, $\bar{E}_i$, Q_i, $\bar{U}_i$, and $\bar{D}_i$ are chiral superfields with generation indices $i, j, k \in \{1, 2, 3\}$ and H_u is one of the MSSM Higgs superfields. The λ_{ijk}, λ'_{ijk} (and λ''_{ijk}) are dimensionless Yukawa couplings, which imply lepton- (baryon-) number violating interactions and κ_i are dimensionful bilinear couplings violating lepton number. The Lagrangian in superfield-component form, as well as a complete list of RPV Feynman rules can be found, *e.g.*, in Appendix L of Ref. [373].

The RPV-MSSM allows for an unstable light long-lived neutralino, which we focus on here. A very light neutralino is necessarily dominantly bino-like [73] and a light bino currently avoids all experimental and astrophysical constraints even if it is massless [79, 311, 346]. In the following, we provide a concise overview of the production and decay of the lightest neutralino via $LL\bar{E}$ or $LQ\bar{D}$ operators. Moreover, for simplicity, we consider the lightest neutralino to be the LSP in this work. Note that we use the two-component fermion notation reviewed in Ref. [373].

Neutralino production and decay via $LL\bar{E}$ operators

For non-zero $LL\bar{E}$ couplings, neutralinos can be produced through charged lepton decays and can decay to lighter leptons. We provide the explicit general forms of the total decay widths for both the charged lepton and neutralino decays, employing the matrix element and necessary phase space integration in Appendix C.1. For all the relevant processes, we assume that all sfermions appear at the energy scale of the decaying particle as mass degenerate, *i.e.*, $m_{\tilde{f}} \approx m_{\text{SUSY}} \gg m_{\tilde{\chi}_1^0}, m_{\ell^\pm}$. Further, the R-parity conserving neutralino gauge coupling is g' ($U(1)_Y$), since the neutralino is bino-like. As a result, we can write out the coefficients appearing in the matrix elements as, (*cf.* Appendix C.1)

$$c_{ijk} \simeq -\frac{\frac{1}{\sqrt{2}}\lambda_{ijk} g'}{m^2_{\text{SUSY}}} \qquad \text{and} \qquad k_{ijk} \simeq \frac{\sqrt{2}\lambda_{ijk} g'}{m^2_{\text{SUSY}}} \,. \tag{5.2}$$

Using Eq. (C.1), the relevant production widths can then be expressed as

$$\Gamma(\ell_k^\pm \to \tilde{\chi}_1^0 + \nu_i + \ell_j^\pm) = \Gamma_{LL\bar{E}}(\ell_k^\pm; \tilde{\chi}_1^0, \nu_i, \ell_j^\pm)[k_{ijk}, c_{ijk}, c_{ijk}] \,, \tag{5.3}$$

$$\Gamma(\ell_k^\pm \to \tilde{\chi}_1^0 + \bar{\nu}_i + \ell_j^\pm) = \Gamma_{LL\bar{E}}(\ell_k^\pm; \tilde{\chi}_1^0, \bar{\nu}_i, \ell_j^\pm)[c_{ikj}, k_{ikj}, c_{ikj}] \,. \tag{5.4}$$

Similarly, the total widths of the subsequent neutralino decays $\tilde{\chi}_1^0 \to \overset{(-)}{\nu}_i + \ell_j^- + \ell_k^+$ can be written as

$$\Gamma(\tilde{\chi}_1^0 \to \nu_i + \ell_j^- + \ell_k^+) = \Gamma_{LL\bar{E}}(\tilde{\chi}_1^0; \nu_i, \ell_j^-, \ell_k^+)[c_{ijk}, c_{ijk}, k_{ijk}] \,, \tag{5.5}$$

$$\Gamma(\tilde{\chi}_1^0 \to \bar{\nu}_i + \ell_j^- + \ell_k^+) = \Gamma_{LL\bar{E}}(\tilde{\chi}_1^0; \bar{\nu}_i, \ell_j^-, \ell_k^+)[c_{ikj}, k_{ikj}, c_{ikj}] \,. \tag{5.6}$$

Neutralino production and decay via $LQ\bar{D}$ operators

Via the $LQ\bar{D}$-operators mesons can decay into a bino accompanied by a lepton l_i. Subsequently, the bino decays via the same or another $LQ\bar{D}$-operator to a lepton and two quarks, where the latter again hadronize into a meson (for a light enough bino). We consider charged mesons M^+_{ab} with quark flavor content $(u_a\,\bar{d}_b)$ as well as neutral mesons M^0_{ab} composed of $(d_a\,\bar{d}_b)$ and their charge conjugated equivalents. Neutral mesons composed of $(u_a\bar{u}_b)$ only contribute to higher multiplicity processes as $M \to \widetilde{\chi}^0 + l_i + M'$, where M' denotes a lighter meson and l_i a charged lepton. We do *not* consider them here, since these are phase space suppressed by two to three orders of magnitude [87]. Both the bino production and decay width are therefore given by Ref. [87]:

$$\Gamma(M_{ab} \to \tilde{\chi}^0_1 + l_i) = \frac{\lambda^{\frac{1}{2}}(m^2_{M_{ab}}, m^2_{\tilde{\chi}^0_1}, m^2_{l_i})}{64\pi m^3_{M_{ab}}} |G^{S,f}_{iab}|^2 (f^S_{M_{ab}})^2 \left(m^2_{M_{ab}} - m^2_{\tilde{\chi}^0_1} - m^2_{l_i}\right), \tag{5.7}$$

$$\Gamma(\tilde{\chi}^0_1 \to M_{ab} + l_i) = \frac{\lambda^{\frac{1}{2}}(m^2_{\tilde{\chi}^0_1}, m^2_{M_{ab}}, m^2_{l_i})}{128\pi m^3_{\tilde{\chi}^0_1}} |G^{S,f}_{iab}|^2 (f^S_{M_{ab}})^2 \left(m^2_{\tilde{\chi}^0_1} + m^2_{l_i} - m^2_{M_{ab}}\right), \tag{5.8}$$

where $\lambda^{\frac{1}{2}}(x,y,z) = \sqrt{x^2+y^2+z^2-2xy-2xz-2yz}$ is the square root of the Källén function and $l_i = \ell_i^{\pm}$ or ν_i depending on the charge of M_{ab}. The coefficients $|G^{S,f}_{iab}|^2$ include the trilinear RPV couplings and are defined in Ref. [87], together with the meson scalar decay constants $f^S_{M_{ab}}$.

Furthermore, the $L_iL_j\bar{E}_j$ and $L_iQ_j\bar{D}_j$ operators additionally open the decay mode $\tilde{\chi}^0_1 \to (\gamma + \nu_i, \gamma + \bar{\nu}_i)$ at the one-loop level, *cf.* Ref. [168], but this signature is not considered in the present paper since to our knowledge the corresponding HNL-decay has to-date not been searched for.

Besides the displaced-vertex signature related to the decay channels computed above, it is possible that the lightest neutralino is so long-lived that it does not decay inside the considered detector and appears as missing energy.

5.2.2 Heavy neutral leptons

Heavy neutral leptons are a common feature of many SM extensions attempting to give an underlying explanation of the observed neutrino sector. The simplest HNL model one can implement is

$$\mathscr{L} \supset i\hat{N}^\dagger_\alpha \bar{\sigma}^\mu \partial_\mu \hat{N}^\alpha - \left[\left(Y_\nu\right)^i_\alpha \left(\Phi^0 \hat{\nu}_i \hat{N}^\alpha - \Phi^+ \ell_i \hat{N}^\alpha\right) + \frac{1}{2} M^\alpha_\beta \hat{N}_\alpha \hat{N}^\beta + \text{h.c.} \right], \tag{5.9}$$

where $i = 1,2,3$, Φ^+ and Φ^0 are the components of the SM $SU(2)_L$ Higgs doublet, and ℓ_i are the charged lepton mass eigenstates. Fields with a hat, $\hat{\nu}$ and $\hat{N}$, are the states before mass-diagonalizing the neutral lepton sector. $\left(Y_\nu\right)^i_\alpha$ are dimensionless Yukawa couplings and $M^\alpha_\beta = \text{diag}(M_{\hat{N}_1}, ...)$ is a diagonal mass matrix. The index $\alpha = 1,2,3,\ldots$ labels the (arbitrary many) HNLs in the theory. During electroweak symmetry breaking, the Higgs obtains a vacuum expectation value (vev) $v/\sqrt{2}$ with $v = 246$ GeV, which gives rise to mixing of the HNLs $\hat{N}_\alpha$ with active neutrinos $\hat{\nu}_i$, described by the mass matrix $M_{\nu N}$:

$$M_{\nu N} = \begin{pmatrix} \mathbb{0}_{3\times 3} & M_D \\ M_D^T & M \end{pmatrix}. \tag{5.10}$$

Here, the off-diagonal entries are given by $(M_D)^i_\alpha = (Y_\nu)^i_\alpha v/\sqrt{2}$. The mass matrix can be perturbatively Takagi-block-diagonalized by introducing a unitary matrix U [373]. For simplicity, we assume there is only one kinematically relevant HNL in our study. In this case, the gauge eigenstate $\hat{\nu}_i$ receives first-order contributions from the mass eigenstate N, proportional to the following mixing matrix entry:

$$U_i \equiv U^i_4 \equiv (Y^*_\nu)^i_1 \frac{v}{\sqrt{2}M} \,. \tag{5.11}$$

The interaction Lagrangian with the neutrino mass eigenstates ν_i and N is then given by:

$$\mathscr{L} \supset -\frac{g}{\sqrt{2}} U^i_4 W^-_\mu \ell^\dagger_i \bar{\sigma}^\mu N - \frac{g}{2c_W} U^i_4 Z_\mu \nu^\dagger_i \bar{\sigma}^\mu N + \text{h.c.}\,, \tag{5.12}$$

where g is the $SU(2)_L$ gauge coupling and $c_W = \cos\theta_W$ is the cosine of the weak mixing angle.

5.2.3 The phenomenology connecting the light bino LSP and the HNL

The phenomenologies of the RPV-MSSM with a light bino $\tilde{\chi}^0_1$ and the SM extensions with one relevant HNL turn out to be very similar. This is not surprising, as the HNL and the bino have the same gauge quantum numbers after electroweak symmetry breaking. Currently existing bounds in the HNL parameter space spanned by (m_N, U^i_4) can thus be translated into bounds in the light-bino-RPV parameter space $(m_{\tilde{\chi}^0_1}, \lambda/m^2_{\text{SUSY}})$, where λ labels here any appropriate $LL\bar{E}$ or $LQ\bar{D}$ coupling.

An additional analogy between the theories can be constructed by considering the bilinear RPV couplings κ_i [374], see Eq. (5.1). After integrating out the heavy higgsinos in the neutral fermion sector of the RPV-MSSM, one obtains a tree-level mixing of neutrinos with the bino, which is of the form

$$\mathscr{L} \supset \frac{g'}{2}\left(v_i - \frac{v_d \kappa_i}{\kappa^0}\right)\hat{\nu}_i \tilde{\chi}^0_1 + \text{h.c.}\,, \tag{5.13}$$

where v_i and v_d are the vevs of the sneutrinos and the MSSM Higgs H_d, respectively. κ^0 is the Higgsino mass parameter and g' the $U(1)_Y$ gauge coupling. This mixing can be interpreted as the off-diagonal entries in the neutral lepton mass matrix given in Eq. (5.10), such that the elements of the matrix U, *cf.* Eqs. (5.11) and (5.12), can be mapped to the neutralino-neutrino mixing considered here:

$$U^i_4 = \frac{g'}{2m_{\tilde{\chi}^0_1}}\left(v_i - \frac{v_d \kappa_i}{\kappa^0}\right) . \tag{5.14}$$

For phenomenological computations, the Lagrangian given in Eq. (5.12) can be used, which would correspond to the trivial replacement

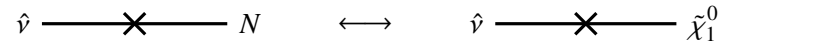

(5.15)

where the inserted crosses denote the mixing. Thus, current HNL exclusion limits can be directly translated into bounds on the mixing strength in Eq. (5.13).

5.3 Experiments and recasting

In this section, we present the details of existing HNL searches and classify them according to their search strategy. We consider experiments employing the signatures:(i) direct decays, (ii) displaced vertices, and (iii) missing energy. For the direct-decay searches, we further partition our analysis into: (i.a) peak searches and (i.b) branching ratio searches. The displaced-vertices searches are also split further into: (ii.a) beam-dump searches and (ii.b) collider searches. Missing-energy searches allow us to derive new and stronger constraints on single RPV couplings. In addition, we present selected benchmark scenarios for which we will obtain single-coupling and coupling-product bounds within the RPV-MSSM framework. We provide an overview of the experiments, discussed in this section, in Table 5.1.

Search Strategy	Ref.	Experiment	Status	HNL Mixing	HNL Mass region
Peak	[375]	PIENU	curr.	$\|U_e\|$	65-153 MeV
	[376]	PIONEER	proj.	$\|U_\mu\|$	15.7-33.8 MeV
	[376]	PIONEER	proj.	$\|U_e\|$	65-135 MeV
	[377]	SIN	curr.	$\|U_\mu\|$	1-16 MeV
	[378]	NA62	curr.	$\|U_\mu\|$	144-462 MeV
	[379]	NA62	curr.	$\|U_e\|$	200-384 MeV
	[380]	KEK	curr.	$\|U_\mu\|$	160-230 MeV
	[381]	KEK	curr.	$\|U_\mu\|$	70-300 MeV
Branching Ratio	[375]	PIENU	curr.	$\|U_e\|$	0-65 MeV
	[376]	PIONEER	proj.	$\|U_e\|$	0-65 MeV
Beam-dump	[382]	DUNE	proj.	$\|U_e\|$, $\|U_\mu\|$, $\|U_\tau\|$	0-1 968.34 MeV
	[383]	T2K	curr.	$\|U_e\|$, $\|U_\mu\|$	10-490 MeV
	[384, 385]	CHARM	curr.	$\|U_e\|$, $\|U_\mu\|$	300-1 869.65 MeV
	[386]	CHARM	curr.	$\|U_\tau\|$	290-1 600 MeV
	[387]	NuTeV	curr.	$\|U_\mu\|$	259-2 000 MeV
	[388]	MicroBooNE	curr.	$\|U_\mu\|$	20-200 GeV
	[389]	BEBC	curr.	$\|U_e\|$, $\|U_\mu\|$	500-1 750 MeV
	[390]	BEBC	curr.	$\|U_\tau\|$	100-1 650 MeV
	[391]	SK	curr.	$\|U_e\|$, $\|U_\mu\|$	150-400 MeV
Collider	[392]	FASER	proj.	$\|U_e\|$, $\|U_\mu\|$, $\|U_\tau\|$	0-6 274.9 MeV
	[393]	MoEDAL-MAPP1	proj.	$\|U_e\|$	0-6 274.9 MeV
	[394]	BaBar	curr.	$\|U_\tau\|$	100-1 360 MeV
Missing Energy	[395]	NA62	curr.	BR($\pi^0 \to$ inv.)	0-134.97 MeV
	[396]	BaBar	curr.	BR($B^0 \to$ inv.)	0-5 279.65 MeV

Table 5.1: Summary of experiments reviewed in Sec. 5.3, sorted by search strategy. We list the relevant references, the status of derived bounds (current or projected), the relevant HNL mixing, and the experimentally accessible HNL mass range.

5.3.1 Direct-decay searches

One of the main ways to produce light HNLs is via the decay of light mesons such as pions and kaons. In direct searches, a beam of charged mesons is brought to a stop inside a scintillator where the mesons decay at rest, or the beam mesons are tagged and their positions, momenta, and timing information are measured by a silicon pixel spectrometer.

The energy spectrum of the visible secondary particle, *i.e.*, a muon or an electron, arising from these meson decays is measured. The signal shape of the energy spectrum can be compared with Monte-Carlo simulations for different HNL mass hypotheses. Finding no extra peaks in the secondary energy spectrum or rejecting each mass hypothesis allows us to exclude the relevant HNL parameters.

Peak searches

In peak searches, the energy spectrum of the secondary particle is scanned for additional peaks hinting at HNLs.

- At the Swiss Institute for Nuclear Research (SIN), a pion beam was used to put bounds on the mixing $|U_\mu|^2$ in the HNL mass range of 1-16 MeV [377].

- A search for massive neutrinos at the PIENU experiment [375] has been made in the decay of pions into positrons. No evidence was found for additional peaks in the positron energy spectrum. Thus, upper limits at 90% confidence level (CL) on $|U_e|^2$ were derived in the HNL mass region 60-135 MeV. In another analysis of the PIENU experiment [397], heavy neutrinos were searched for in pion decays into muons. The energy spectrum did not show any additional peaks other than the expected peak for a light neutrino. Thus, the analysis derived a bound on $|U_\mu|^2$ for the HNL mass range of 15.7-33.8 MeV.

- The PIONEER [376] experiment is a next-generation rare pion decay experiment. The experiment will perform the same search strategy as the PIENU experiment with higher statistics and significantly suppressed background. A peak search in the positron spectrum will allow probing $|U_e|^2$ in the HNL mass region 65-135 MeV. Further, a search for an additional peak within the muon energy spectrum will allow us to test $|U_\mu|^2$ for $15.7\,\text{MeV} < m_N < 33.8\,\text{MeV}$.

- KEK [380] derived an upper bound on $|U_\mu|^2$ for a massive HNL in the mass range of 160-230 MeV. A similar search at KEK [381] led to an upper bound on $|U_\mu|^2$ in the HNL mass range of 70-300 MeV.

- Using a kaon beam, the NA62 collaboration placed bounds on $|U_e|^2$ for an HNL with a mass of 144-462 MeV [378]. The analysis approach is different from PIENU. In this case, a peak-search procedure measures the $K^+ \to e^+ N$ decay rate with respect to the $K^+ \to e^+ \nu$ rate for an assumed HNL mass m_N. The HNL mass is varied over the mentioned mass range. The benefit of this approach is the cancellations of residual detector inefficiencies, as well as trigger inefficiencies, and random veto losses. A similar analysis [379] has been performed to measure $|U_\mu|^2$ within the HNL mass range of 200-384 MeV. Note that both bounds of NA62 are derived with the assumption that the lifetime of the neutral particle exceeds 50 ns.

- The BaBar experiment [394] at SLAC has performed a search for the rare decay $\tau^- \to \pi^-\pi^-\pi^+ + N$ in the mass region of $100 < m_N < 1\,360\,\text{MeV}$. The observed kinematic phase space distribution of the hadronic system allows BaBar to place a stringent bound on $|U_\tau|^2$. However, the search is based on three-prong tau events. Technically, this allows us to derive a single coupling bound on λ'_{311}. However, the four-body production mode of the light neutralino would need proper phase-space consideration. Therefore, we do not include a reinterpretation of this search in our work and shall discuss it elsewhere.

Branching-ratio searches

It is possible to measure branching ratios of different pion decay modes. The ratio

$$R_{e/\mu} = \frac{\Gamma\left(\pi^+ \to e^+ + \nu(\gamma)\right)}{\Gamma\left(\pi^+ \to \mu^+ + \nu(\gamma)\right)}, \tag{5.16}$$

can be used to derive limits on the mixing $|U_e|^2$ in the region $m_N < 65\,\text{MeV}$. This has been performed by PIENU [398] and is planned for PIONEER [376].

5.3.2 Displaced-vertex searches

Beam-dump and collider experiments can produce HNLs via the same processes that produce light neutrinos. A proton beam hitting a fixed target typically produces a large number of pions and kaons, and also heavier mesons. If kinematically allowed, the decay of the primary mesons can produce HNLs, which will propagate freely since they are long-lived and interact only feebly. The HNLs produced at beam-dump experiments are typically boosted in the forward direction, which further increases their decay length in the lab frame. Hence, only a fraction of the produced HNLs decay at the location of the detector. To reduce possible background events, the experiments usually have a system of veto detectors equipped for both charged and neutral particles. The search strategy relies on the visibility of the HNL decay products inside the detector; we will discuss these later.

In the following, we present displaced-vertex searches at beam-dump and collider experiments separately.

Beam-dump search

- At DUNE [66], HNLs can be produced via pion-, kaon-, and D-meson-decays. Ref. [382] predicts constraints on HNLs by searching for their decay products inside the DUNE Near Detector. It is assumed that only the three-neutrino final state is not detectable. The search strategy allows to measure all three mixings $|U_e|^2$, $|U_\mu|^2$ and $|U_\tau|^2$ for an HNL mass range up to the mass of the D_s-meson. Note that in the analysis, a single mixing element is assumed to dominate over the other two at a time.

- The T2K experiment [383] follows the same approach but uses a kaon beam. Thus, they derive bounds on both $|U_e|^2$ and $|U_\mu|^2$ for $10\,\text{MeV} < m_N < 490\,\text{MeV}$.

- Heavy neutral leptons in the CHARM beam-dump experiment are produced from D and D_s-

meson decays.[4] The former allows to set bounds on $|U_e|^2, |U_\mu|^2$ for an HNL mass of 300-1 869.65 MeV [384, 385], and the latter allows to probe $|U_\tau|^2$ for 290 MeV $< m_N <$ 1 600 MeV [386].

- A search for HNLs has been performed at the NuTeV experiment [387] at Fermilab. The data were examined for HNLs decaying into muonic final states to derive bounds on the mixing $|U_\mu|^2$ of HNLs in the 0.25-2.0 GeV mass range. See also Ref. [318] which directly considers the NuTeV data in terms of a light neutralino.

- An analysis of current data from the MicroBooNE experiment [388] can constrain the parameters of HNLs, that mix predominantly with muon-flavored neutrinos, for HNL masses between 20-200 GeV.

- The BEBC experiment derived limits on the HNL-light neutrino mixing parameters from a search for decays of heavy neutrinos in a proton beam-dump experiment [389]. It derived bounds on $|U_e|^2, |U_\mu|^2$ for an HNL mass between 0.5 GeV and 1.75 GeV. A re-analysis [390, 399] has demonstrated that the BEBC detector was also able to place bounds on the $|U_\tau|^2$ mixing for HNL masses higher than the kaon mass. This re-analysis has taken into account several production and decay channels of HNLs.

- For Super-Kamiokande (SK), the largest contribution to HNL production is through the decay of mesons produced in the atmosphere via cosmic rays. A secondary contribution to the flux comes from the HNL production in neutral-current scattering of atmospheric neutrinos passing through the Earth. The total number of HNL decays inside the detector within a given time window results in an upper bound on the HNL mixing. This approach is different from the displaced-decay search limits from beam dumps and allows one to derive bounds on $|U_e|^2$ and $|U_\mu|^2$ in the minimal HNL scenarios for masses between 150-400 MeV [391].

Collider searches

HNLs can be also searched for in (semi-)leptonic decays of mesons produced at the LHC via a similar mechanism as in beam-dump experiments. At colliders, particle collisions produce an abundance of mesons, such as pions, kaons, D-mesons, and B-mesons, which can further decay into HNLs. Far detectors at the LHC are sensitive to decaying, light LLPs with a decay length comparable with their distance to the interaction point, *e.g.*, of $O(1) - O(100)$ m. HNLs decaying inside the detector can be identified by their decay products, except for the invisible three-neutrino final state. To ensure a low background environment, the experiments are proposed to be set far away from the primary proton-proton collision points and require shielding between the interaction points and the detectors.

Some of the new detectors at the LHC are already approved and currently running: FASER [85] and MoEDAL-MAPP1 [366]. We include these running HNL searches in order to reinterpret their projected sensitivity. Their follow-up programs, FASER2 [86] and MoEDAL-MAPP2 [367], have been proposed for operation during the high-luminosity LHC phase, with

[4] In this work, we use "D-mesons" ("B-mesons") to label the $D^\pm$ mesons ($\overset{(-)}{B}{}^0$ and $B^\pm$ mesons), while D_s and B_c mesons are separately discussed. We do not take into account $\overset{(-)}{D}{}^0$ or $\overset{(-)}{B}_s$ mesons.

an expected final integrated luminosity 3 ab^{-1} and 300 fb^{-1} respectively, and are taken into account in our numerical analysis, as well.

FASER(2) [392][5] is intended to detect long-lived particles decaying inside the detector volume. A sensitivity estimate, taking the detector geometry into account, leads to a specific reach in $|U_e|^2$, $|U_\mu|^2$, and $|U_\tau|^2$ for an HNL with a mass up to the mass of the B_c-meson. Similarly, MoEDAL-MAPP1(2) [393, 400] can probe the mixing $|U_e|^2$ for HNL being produced in decays of D- and B-mesons for the same mass range as FASER(2).

In addition, other experimental proposals for LLP far detectors include MATHUSLA [327, 368, 369], ANUBIS [370], CODEX-b [401], and FACET [402]. None of these proposed detectors has been officially approved. We therefore do *not* include them in our reinterpretation strategy. We still want to emphasize the prospect of these experiments in the search for light long-lived particles. Sensitivity estimates, worked out in detail on the minimal HNL scenarios in Ref. [393], would also provide possible discovery potential for the discussed light neutralino scenarios, as worked out for example in Refs. [90–92, 168]. These potential future experiments all intend to look for various BSM signatures which include neutralino decays induced by all of the LH_u, $LL\bar{E}$, and $LQ\bar{D}$ operators.

5.3.3 Missing-energy searches

The NA62 search [395] allows us to derive bounds on the branching ratio of pions decaying into an invisible final state. This is achieved by the reconstruction of the charged particles in the process $K^+ \to \pi^+\pi^0$. The analysis relies on the tracking of the charged K^+ and π^+ and can probe π^0 decay to any invisible final state. NA62 reported a 90% CL upper limit on $\mathrm{BR}(\pi^0 \to \text{inv.}) < 4.4 \times 10^{-9}$. The search can be recast to derive bounds on RPV couplings which also contribute to the invisible decays of the pion. It turns out that the obtained limits are weaker than the currently existing bounds [45, 252] and are, therefore, omitted.

The BaBar experiment has also searched for rare decays $B_0 \to \text{inv.}$ [396]. The search relies on the identification of the other neutral B-meson, as the 'tag side', and thus, can measure a purely invisible decay width of the B-meson. The upper limit at the 90% CL yields $\mathrm{BR}(B_0 \to \text{inv.}) < 2.4 \times 10^{-5}$. We can recast this search into bounds on the production coupling of a light long-lived neutralino.

We could not find existing searches for invisible decays of the other uncharged mesons, *i.e.*, K_S, K_L, and B_s. To derive limits on the decay of these mesons into a neutralino we consider the uncertainty of the total decay width of the mesons. We assume all visible decay modes to be measured within the decay width. The resulting uncertainty can be extended to account for additional invisible decays and potential errors in measurements. Thus, we use the uncertainty to establish an upper limit on the branching ratio into invisible final states, if kinematically allowed. These could contain neutrinos, HNLs, or neutralinos. Assuming the latter saturates the width uncertainty, we derive bounds on the $LQ\bar{D}$ couplings. The measured uncertainties can be found in Ref. [13].

We could not find bounds from direct searches for massive HNLs in the leptonic decays $\mu^- \to e^- + \nu + N$ and $\tau^- \to e^-/\mu^- + \nu + N$. There are only searches for the muons and the τ leptons to decay to a lighter charged lepton plus active neutrinos or a photon [403]. Thus, the existing limits on the branching ratio cannot be generalized for a massive HNL owing to kinematic assumptions. In this

[5] In principle, Ref. [86] employs the most updated geometrical setup of FASER(2), but the results shown therein for the HNLs do not separate the contributions from D- and B-mesons. Therefore, we have chosen to reinterpret the results given in Ref. [392] for the HNLs from the heavy mesons' decays, which are only slightly different from those given in Ref. [86].

case, we again rely on the uncertainty of the decay widths. This allows us to derive bounds on the $LL\bar{E}$ couplings. Again, the uncertainties of the decay width are taken from Ref. [13].

5.3.4 Other searches

For the bilinear coupling scenarios, we use the most relevant and up-to-date constraints on the HNLs existing in the literature, which are summarized in Ref. [342]. Therefore, we supplement the results from the previously discussed experiments with data from `TRIUMF` [404], `PSI` [377], `Borexino` [405, 406], and atmospheric neutrinos scattering in the Earth [407].

5.3.5 The recasting procedure

The procedures for recasting the HNL bounds into limits on RPV scenarios depend on the RPV couplings that are switched on, and the search strategy of the experiments; they fall into one of the following three categories:

- The most straightforward case is for scenarios involving bilinear RPV couplings. As discussed in Sec. 5.2, these couplings lead to mixing between the neutralino and the neutrinos, *cf.* Eq. (5.13). Thus, we directly translate HNL exclusion limits in the mixing vs. mass plane into bounds in the RPV coupling vs. neutralino mass plane, using Eq. (5.14).

- In RPV scenarios involving $LQ\bar{D}$ or $LL\bar{E}$ operators, and a (detector-level) stable neutralino produced in the decay of a meson or lepton, missing-energy searches and peak searches can provide sensitivity. We use the HNL exclusion limits (typically in the mixing vs. mass plane) in order to determine the bounds on the decay width of the relevant meson/lepton into an HNL (see, for instance, Refs. [408, 409]). Since replacing the HNL with a light bino of the same mass does not change the experimental signature and the kinematics, we can simply equate the above with the corresponding decay width of the same meson/lepton into a bino in the RPV model, using the expressions given in Sec. 5.2; this gives us the bound on the relevant RPV coupling in terms of the bino mass.

- For RPV scenarios involving $LQ\bar{D}$ or $LL\bar{E}$ operators where the neutralino is produced in meson/lepton decays, and is *unstable* at the detector scales, displaced-vertex searches (beam dump or collider) can apply. In this case, we use the long-lifetime approximation to calculate the number of decay events reconstructed in the detector, following the arguments outlined in Ref. [400] (see also Ref. [342]); we review the procedure briefly now. Consider a beam-dump or collider experiment that searches for HNLs via displaced vertices. Let the HNL, N, be produced in the decay of a parent particle P (for instance, a pion).[6] Then, the number of detected events for a final state, Y, produced in the decay of N can be estimated as,

$$N_{\text{events}}^{\text{HNL}} = N_P \times \text{BR}(P \to N + X) \times \text{BR}(N \to Y) \times \epsilon\,, \tag{5.17}$$

[6] We are assuming that the direct production of the HNL (or bino) is suppressed compared to indirect production via decays of mesons and leptons, which is typically the case.

where N_P is the number of P produced at the experiment, X are any additional objects produced in P's decay that are not of interest to us, and the BRs are the corresponding branching ratios. ϵ is a factor accounting for the detector acceptance and efficiency. This factor is linearly proportional to the probability for the HNL to decay inside the detector ($P[\text{decay}]$). It also depends on experiment-specific information such as the detector type and its geometry. In the limit of a long-lived HNL, such that the boosted decay length is much larger than the distance ΔL from the interaction point of the experiment to the first edge of the detector along the direction of travel of the HNL, to a good approximation we have [400],

$$P[\text{decay}] \approx \frac{\Delta L \times \Gamma_N}{\beta_N \gamma_N}\,, \tag{5.18}$$

where Γ_N, β_N, and γ_N represent the total decay width, the relativistic velocity, and the Lorentz boost factor of the HNL, respectively. Inserting this in Eq. (5.17), we obtain,

$$N_{\text{events}}^{\text{HNL}} = A \times \frac{\text{BR}(P \to N + X) \times \Gamma(N \to Y)}{\beta_N \gamma_N}\,, \tag{5.19}$$

where all the quantities depending on the HNL model details are written explicitly, and the remaining experiment-specific factors of Eq. (5.19) have been absorbed into the proportionality factor A. Now, assume that there is also an RPV scenario in which the light bino, $\tilde{\chi}_1^0$, is produced in P decays, and has a decay mode into Y. Analogously, we can write,

$$N_{\text{events}}^{\text{RPV}} = A \times \frac{\text{BR}(P \to \tilde{\chi}_1^0 + X') \times \Gamma(\tilde{\chi}_1^0 \to Y)}{\beta_{\tilde{\chi}_1^0} \gamma_{\tilde{\chi}_1^0}}\,, \tag{5.20}$$

where the HNL is now replaced by the bino. Here, since both the light bino and the HNL are produced in the same meson's decay at the identical experiment, the proportionality factor A can be legitimately assumed to be essentially the same. Thus, combining the two equations, we obtain a simple scaling relation between the two models:

$$\frac{N_{\text{events}}^{\text{RPV}}}{N_{\text{events}}^{\text{HNL}}} = \frac{\text{BR}(P \to \tilde{\chi}_1^0 + X') \times \Gamma(\tilde{\chi}_1^0 \to Y) \times \beta_N \gamma_N}{\text{BR}(P \to N + X) \times \Gamma(N \to Y) \times \beta_{\tilde{\chi}_1^0} \gamma_{\tilde{\chi}_1^0}}\,. \tag{5.21}$$

For an HNL and a light bino with the same mass, we can further simplify the above expression in the limit where the HNL and the bino carry the same energy in the lab frame. In this case, the $\beta\gamma$ factors cancel out, and we have,

$$\frac{N_{\text{events}}^{\text{RPV}}}{N_{\text{events}}^{\text{HNL}}} = \frac{\text{BR}(P \to \tilde{\chi}_1^0 + X') \times \Gamma(\tilde{\chi}_1^0 \to Y)}{\text{BR}(P \to N + X) \times \Gamma(N \to Y)}\,, \tag{5.22}$$

which is completely free from any experiment-specific factors. This will be the master expression we use for recasting DV searches. We note that, technically, having different X and X' induces different kinematics for the HNL and the bino. For instance, the two final states could have different masses, or even contain differing number of objects, thus affecting the energy carried by the bino relative to the HNL. However, typically, the experiments we consider produce

the parent particles (or their decay products) with significant boosts, in which case the above formula is only modified mildly. On the other hand, we stress that the HNL and the bino must be produced in the decay of the same (or similar) parents, and must decay into the same final state since these can significantly alter the detector acceptances and efficiencies.[7]

To use Eq. (5.22), assume that a given DV search for HNLs concludes without discovery, and obtains bounds on the HNL model parameters corresponding to a certain signal-event number, $[N_{\text{events}}^{\text{HNL}}]_{\text{bound}}$. Since the signal (and kinematics) in the RPV model is the same, this bound also applies to the light binos: $[N_{\text{events}}^{\text{RPV}}]_{\text{bound}} = [N_{\text{events}}^{\text{HNL}}]_{\text{bound}}$. Plugging this into Eq. (5.22), we arrive at,

$$[\text{BR}(P \to \tilde{\chi}_1^0 + X') \times \Gamma(\tilde{\chi}_1^0 \to Y)]_{\text{bound}} = [\text{BR}(P \to N + X) \times \Gamma(N \to Y)]_{\text{bound}} \,. \quad (5.23)$$

The right-hand side of the above equation can be evaluated by using the bounds on the HNL mass and mixings as input (see, for instance, Refs. [408, 410] for explicit expressions for all relevant decay widths in terms of these parameters), while the expressions for the RPV counterparts appear in Sec. 5.2 and depend on the RPV couplings, sfermion masses, as well as the neutralino mass.

5.4 Numerical results

In order to present our results, we consider benchmark scenarios with one or two non-vanishing RPV couplings. Additional non-zero RPV couplings could allow for further neutralino decay channels to open up; these would modify the relevant branching ratios and neutralino decay length, and hence, the presented sensitivity limits.

5.4.1 One-coupling scenarios

We first consider scenarios where only one non-zero RPV operator contributes to the relevant physical process at a time. For each of the RPV couplings in Eq. (5.1) (except the λ''_{ijk}'s), we list the relevant HNL searches providing constraints in Table 5.2. We now discuss the sensitivity limits for each category of RPV coupling in detail.

Bilinear scenarios

The bilinear couplings (κ^i and the sneutrino vacuum expectation values) induce a mixing between the light bino and the three light neutrinos, *cf.* Eq. (5.13). Thus, all HNL searches constraining the mixing between the HNL and the neutrinos directly imply constraints on these couplings. The exclusion limits are shown in Fig. 5.1. These have been read off from Ref. [342]. The bilinear couplings also generate mass terms for the neutrinos – see, for instance, Refs. [40, 61, 282–284] – leading to the constraint $v_i,\ \kappa^i \lesssim O(1\,\text{MeV})$ [40]; this is depicted as a gray horizontal line in the plot.[8] We find that the reinterpreted bounds from the HNL searches corresponding to the light-flavor neutrinos (e and

[7] Actually, the final states into which the HNL and bino decay need not be identical, *e.g.*, the invisible objects contained in both do not need to match; the crucial part is that the detection efficiencies at the considered experiment must be the same.

[8] We note that the existing limit comes from the cosmological bound on the neutrino masses, and is thus scenario-dependent [13]. Further, there is also dependence on undetermined supersymmetric parameters.

Coupling	Direct Decays	E_T^{miss}	DV	Label
κ^i	ν-mixing [342]	ν-mixing [342]	ν-mixing [342]	$\boldsymbol{\kappa}$
λ'_{a11}	$\pi^\pm \to e_a^\pm + \tilde{\chi}_1^0$ [375, 376, 397, 398]	$\pi^0 \to$ invis. [395]	×	$\boldsymbol{\lambda'_\pi}$
λ'_{311}	(×) $\tau^\pm \to \{\pi^\pm/\rho^\pm\} + \tilde{\chi}_1^0$	$\pi^0 \to$ invis. [395]	$\tau^\pm \to \pi^\pm + \tilde{\chi}_1^0; \tilde{\chi}_1^0 \to \nu_\tau + \{\pi^0/\rho^0/\eta/\eta'/\omega\}$ [382, 392, 393, 400]	
λ'_{a12}	$K^\pm \to e_a^\pm + \tilde{\chi}_1^0$ [378–381]	$K_L^0 \to$ invis. [13]	×	$\boldsymbol{\lambda'_K}$
λ'_{312}	(×) $\tau^\pm \to K^\pm + \tilde{\chi}_1^0$	$K_L^0 \to$ invis. [13]	×	
λ'_{i13}	(×) $B^\pm \to e_i^\pm + \tilde{\chi}_1^0$	$B^0 \to$ invis. [396]	×	$\boldsymbol{\lambda'_{B1}}$
λ'_{i21}	(×) $D^\pm \to e_i^\pm + \tilde{\chi}_1^0$	$K_L^0 \to$ invis. [13]	×	$\boldsymbol{\lambda'_{D/K}}$
λ'_{i22}	(×) $D_s^\pm \to e_i^\pm + \tilde{\chi}_1^0$	×	$D_s^\pm \to e_i^\pm + \tilde{\chi}_1^0; \tilde{\chi}_1^0 \to \nu_e + \{\phi/\eta/\eta'\}$ [382, 392, 393, 400]	$\boldsymbol{\lambda'_{D_s}}$
λ'_{i23}	(×) $B_c^\pm \to e_i^\pm + \tilde{\chi}_1^0$	$B_s^0 \to$ invis. [13]	×	$\boldsymbol{\lambda'_{B_c/B_s}}$
λ'_{i31}	×	$B^0 \to$ invis. [396]	×	$\boldsymbol{\lambda'_{B2}}$
λ'_{i32}	×	$B_s^0 \to$ invis. [13]	×	$\boldsymbol{\lambda'_{B_s}}$
λ'_{i33}	×	×	×	–
λ_{12a}	×	$\mu^\pm \to e^\pm +$ invis. [13]	×	$\boldsymbol{\lambda_\mu}$
$\lambda_{123}; \lambda_{13i}; \lambda_{232}; \lambda_{233}$	×	$\tau^\pm \to \{e^\pm/\mu^\pm\} +$ invis. [13]	×	$\boldsymbol{\lambda_\tau}$
λ_{231}	×	$\{\tau^\pm/\mu^\pm\} \to e^\pm +$ invis. [13]	×	$\boldsymbol{\lambda_{\tau/\mu}}$

Table 5.2: Details of the searches providing constraints when only one non-zero RPV operator contributes at a time. We list all the bilinear, $LQ\bar{D}$, and $LL\bar{E}$ operators in the first column (by coupling). The second to fourth columns contain the physical processes that provide constraints and the references to the relevant existing HNL searches targeting them. The fifth column indicates our labeling scheme for the scenarios. × denotes the absence of a constraining process, while (×) labels that, in principle, the listed process may provide constraints but we could not find a relevant existing HNL search. In the table, $a \in \{1, 2\}$ and $i \in \{1, 2, 3\}$.

μ) have sensitivity to regions beyond the current limits at low neutralino masses below 500 MeV. In this region, the most constraining limits come from PIENU [375, 397, 398], NA62 [378, 379], and T2K [383, 411]. Beyond this mass, and for the tau case – where charged kaon and pion decay into HNLs are kinematically forbidden – existing limits are weaker.

$LQ\bar{D}$ scenarios

For the remaining one-coupling scenarios, all existing limits on the RPV couplings are taken from Ref. [45]. The $L_iQ_1\bar{D}_1$-operators couple to pions. With $i = 1$, the decay $\pi^\pm \to e^\pm + \tilde{\chi}_1^0$ is allowed, for masses $m_{\tilde{\chi}_1^0} \leq m_{\pi^\pm} - m_e$.[9] This process has been searched for in the context of HNLs, and the most stringent existing limits are provided by PIENU [375]. Additionally, the approved PIONEER [376]

[9] In the small region of phase space, $m_{\pi^0} + m_{\nu_e} < m_{\tilde{\chi}_1^0} < m_\pi^\pm - m_e$, $\lambda'_{111} \neq 0$ allows for the neutralino to decay into a neutrino and a pion; displaced-vertex searches can constrain this process. However, we have ignored this in Table 5.2

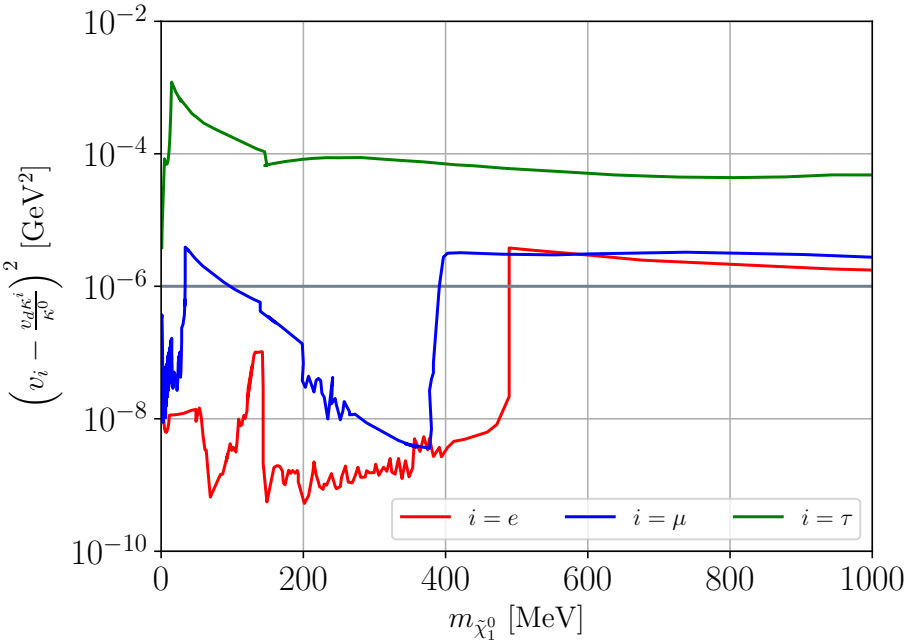

Figure 5.1: Exclusion limits on bilinear RPV couplings as a function of the light bino mass, reinterpreted from existing HNL searches. The current limit on the bilinear couplings is shown as a horizontal gray line.

experiment is projected to have sensitivity beyond these limits. We show the resulting contours in Fig. 5.2(a). The sharp drop in sensitivity at $m_{\tilde{\chi}_1^0} \approx 65\,\text{MeV}$ occurs because branching ratio measurements provide bounds below this mass, and peak searches above this threshold, *cf.* discussion in Sec. 5.3. Similarly, for $i = 2$, the pion can decay into a muon instead of an electron, in the mass range, $m_{\tilde{\chi}_1^0} \leq m_{\pi^\pm} - m_\mu$. This time, the sensitivity range, shown in Fig. 5.2(b), comes from `SIN` [377] in addition to `PIENU` [397] and `PIONEER`. Finally, with $i = 3$, the decays, $\tau^\pm \to \pi^\pm(\rho^\pm) + \tilde{\chi}_1^0$, can occur if kinematically allowed. While we could not find a direct search for such a process involving an HNL, $\lambda'_{311} \neq 0$ additionally allows the neutralino to decay into a tau neutrino and one of $\pi^0/\rho^0/\eta/\eta'/\omega$. Thus, displaced-vertex searches at `DUNE` [382], `FASER(2)` [392] and `MoEDAL-MAPP2` [393, 400] can show sensitivity.[10] We present the corresponding combined projected sensitivity reach in Fig. 5.2(c). In all the plots, we also show the best existing constraints on the RPV couplings for different sfermion masses. For λ'_{111}, this comes from neutrinoless double beta decay searches [363, 414], and is rather stringent compared to the other two couplings. Nevertheless, we see that the reinterpreted bounds easily outperform these existing constraints in the major part of the phase space region. We also note that in all of the above scenarios, the RPV couplings contribute to the invisible decay width of the pion, via the decay into a neutrino and the bino, given the long lifetime of the latter. However, the limits obtained this way are not competitive compared with the above ones.

Next, we consider the kaon scenarios, involving couplings of the type λ'_{i12}. For $i \in \{1, 2\}$, as for the pion case above, the decay mode into an electron or a muon along with the bino opens up for the kaon,

(also analogously for the kaon).

[10] See also Ref. [93] for a proposed search at Belle II [412, 413] for a light bino with non-vanishing RPV couplings λ'_{311} or λ'_{312}.

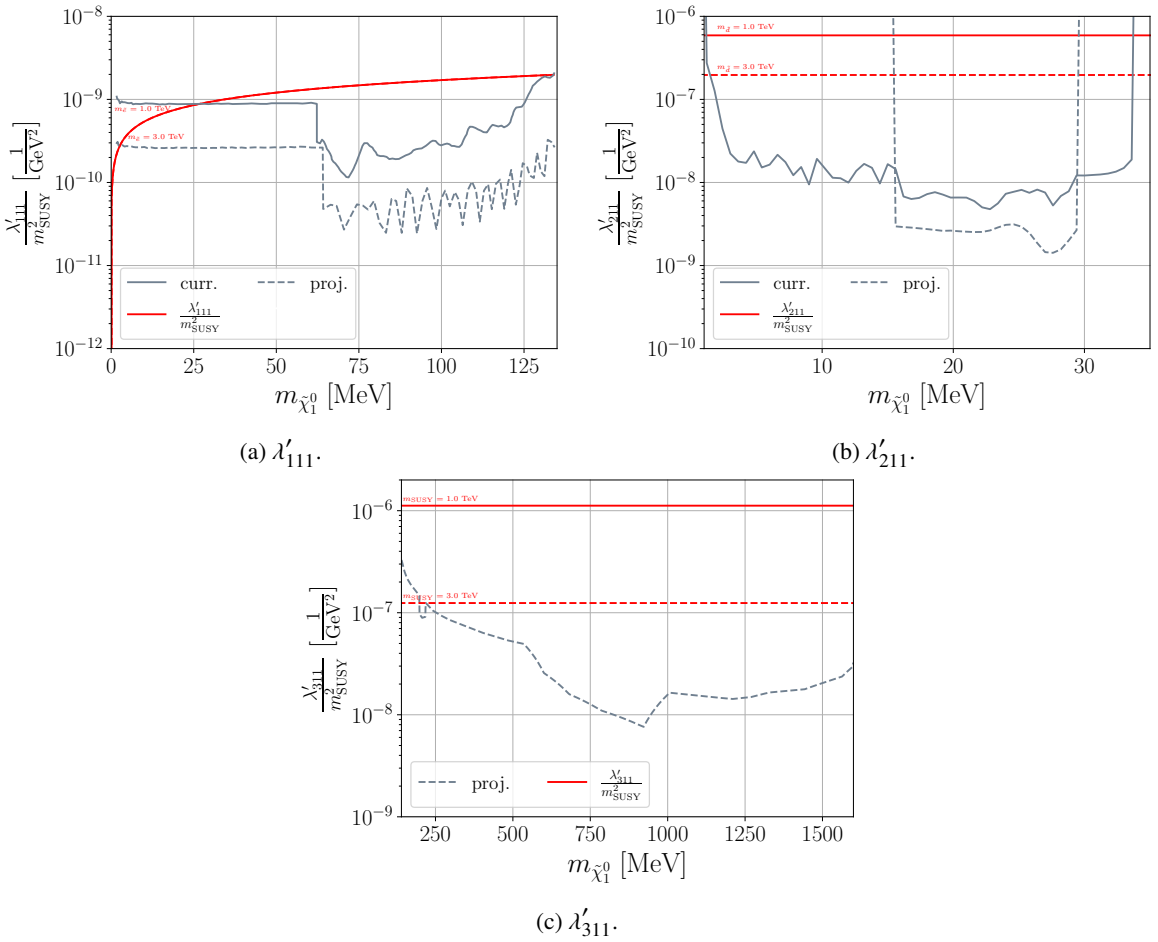

(a) λ'_{111}. (b) λ'_{211}.

(c) λ'_{311}.

Figure 5.2: Sensitivity limits on the λ'_{π} one-coupling scenarios of Table 5.2 as a function of the light bino mass, reinterpreted from existing HNL searches. Current (projected) limits obtained from the reinterpretation are shown as solid (dashed) gray lines. The existing limits on the RPV couplings are also shown in red, with the solid and dashed lines corresponding to varying assumptions of unknown SUSY mass scales.

below the relevant kinematic thresholds. The most constraining current limits come from KEK [380, 381] and NA62 [378, 379], and are depicted in Fig. 5.3(a) (electron case), and Fig. 5.3(b) (muon case). The degradation at $m_{\tilde{\chi}_1^0} \sim 200\,\text{MeV}$ in Fig. 5.3(b) occurs because the KEK-limit only applies up to this mass; beyond it the NA62 limit applies. Once again, both $L_i Q_1 \bar{D}_2$ also contribute to the invisible decays of the kaon but the resulting limits are weaker than those shown. However, for λ'_{312} – where we could not find an existing HNL direct search for the charged decay, $\tau^{\pm} \to K^{\pm} + \tilde{\chi}_1^0$ (see Footnote 10), the invisible width of K_L^0 can indeed be used to derive limits. Since there is no direct bound on this width, we use the uncertainty on the total measured width of K_L^0 [13] to estimate the upper bound, $\text{BR}(K_L^0 \to \text{invis.}) < 4.1 \times 10^{-3}$. This, then, can be used to constrain λ'_{312} since it induces the decay of K_L^0 into a neutrino and a bino. Analogously, the invisible width also provides limits on couplings of the type λ'_{i21}. Here also, we could not find existing direct searches for the relevant charged decay of D into a lepton and an HNL. All these constraints are displayed in Fig. 5.3(c). Once again, we can see that the reinterpreted bounds exclude regions of phase space orders of magnitude beyond those ruled

out by the existing constraints on the RPV operators (also shown in the plots).

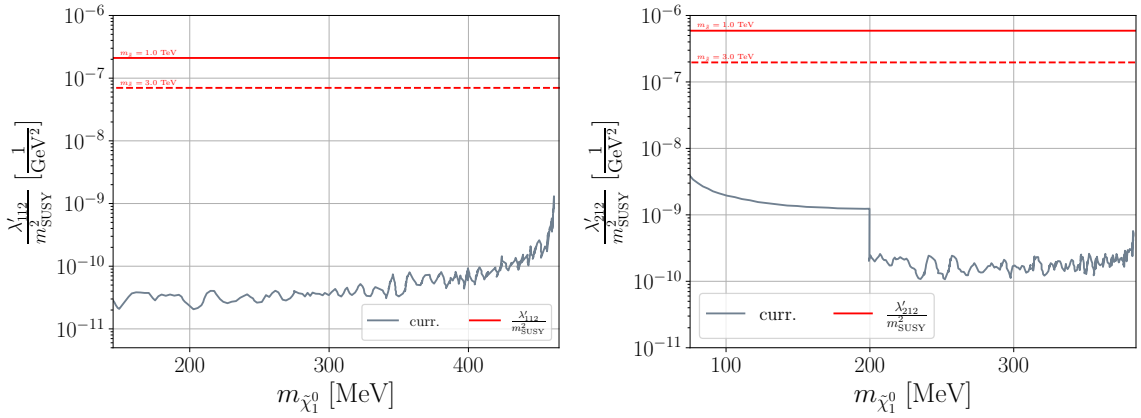

(a) λ'_{112}. (b) λ'_{212}.

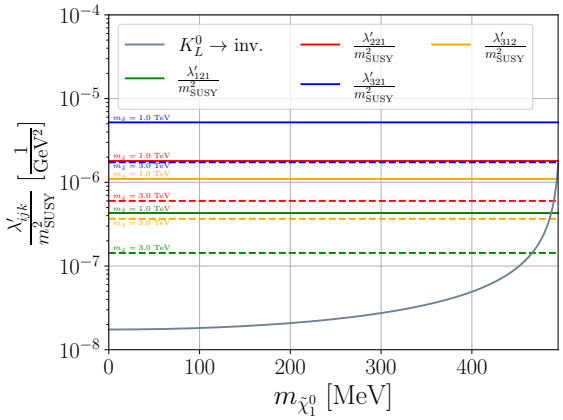

(c) λ'_{312} and λ'_{i21}.

Figure 5.3: As in Fig. 5.2 but for the $\boldsymbol{\lambda'_K}$ and $\boldsymbol{\lambda'_{D/K}}$ benchmarks of Table 5.2. The existing limits on the RPV couplings are shown in red, yellow, green, and blue.

Similarly, for couplings of the type λ'_{i13} and λ'_{i31}, we can use the invisible width of B^0. Here, direct measurements at BaBar [396] provide the stringent constraint, $\mathrm{BR}(B^0 \to \text{invis.}) < 2.4 \times 10^{-5}$. The resulting bounds are shown in Fig. 5.4.

For the couplings λ'_{a22}, with $a \in \{1, 2\}$, we use potential future displaced-vertex searches from DUNE [382], FASER2 [392], and MoEDAL-MAPP2 [393, 400] since we could not find a direct search for the decay of $D_s^\pm$ into an HNL. In these scenarios, the neutralino decays via the RPV operator into a neutrino and one of $\phi/\eta/\eta'$. This implies the mass range, $548\,\mathrm{MeV} \lesssim m_{\tilde{\chi}_1^0} < m_{D_s} - m_{e_a}$. Thus, the corresponding scenario with $\lambda'_{322} \neq 0$ involving a tau lepton is not possible. We show the resulting sensitivity limits in Fig. 5.5.

For the remaining $LQ\bar{D}$ operators, there are either no relevant processes providing constraints through meson or lepton decays ($\lambda'_{322}, \lambda'_{i33}$), or the obtained limits are not competitive with the existing bounds ($\lambda'_{i23}, \lambda'_{i32}$).

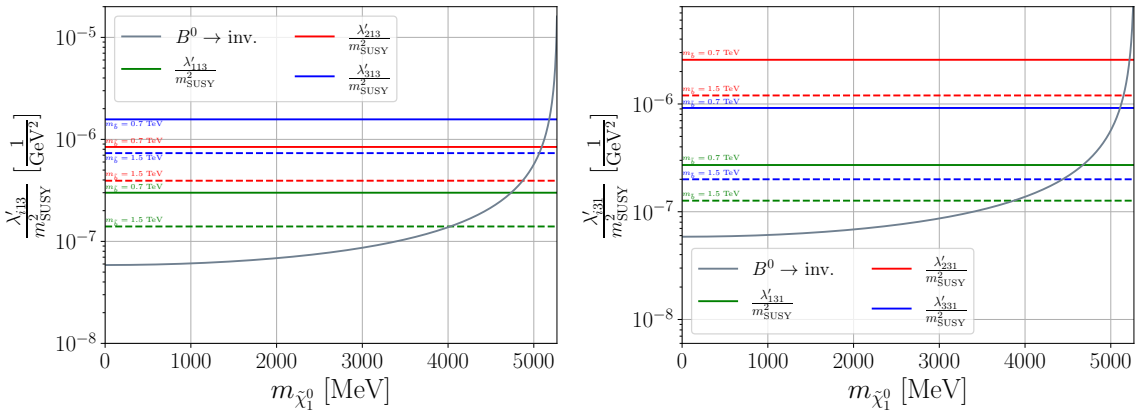

(a) λ'_{i13}. (b) λ'_{i31}.

Figure 5.4: As in Fig. 5.2 but for the $\boldsymbol{\lambda'_{B1}}$ and $\boldsymbol{\lambda'_{B2}}$ benchmarks of Table 5.2. The existing limits on the RPV couplings are shown in red, green, and blue.

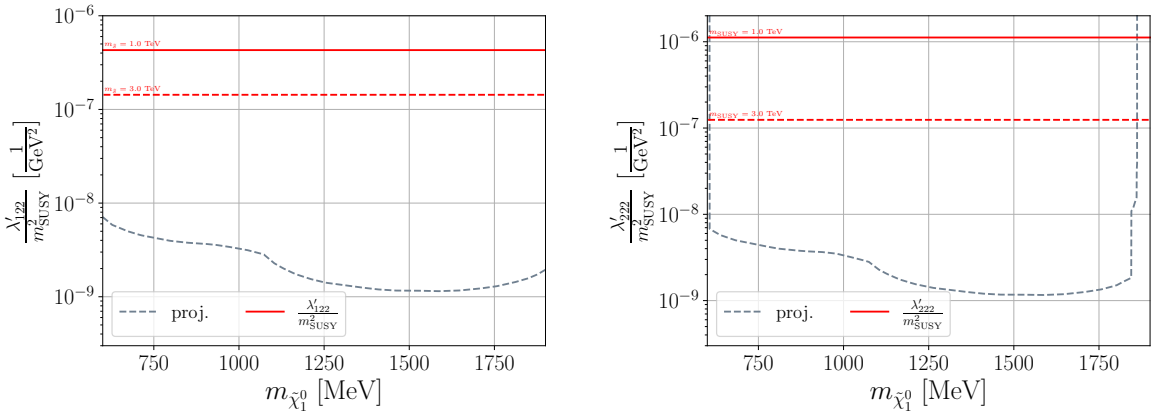

(a) λ'_{122}. (b) λ'_{222}.

Figure 5.5: As in Fig. 5.2 but for the $\boldsymbol{\lambda'_{D_s}}$ benchmarks of Table 5.2.

$LL\bar{E}$ scenarios

For the $\boldsymbol{\lambda_\mu}, \boldsymbol{\lambda_\tau}$ and $\boldsymbol{\lambda_{\tau/\mu}}$ scenarios of Table 5.2, the corresponding operators contribute to the leptonic decays of the muon and the tau. Since we could not find direct measurements for the process $\mu^\pm \to e^\pm +$ invis. (and analogously for $\tau \to e$ and $\tau \to \mu$), where the invisible final state may be massive, we use the uncertainty on the muon decay width [13] to obtain an estimated bound, $\text{BR}(\mu^\pm \to e^\pm + \text{invis.}) < 1.0 \times 10^{-6}$. This leads to constraints on the $\boldsymbol{\lambda_\mu}$ and $\boldsymbol{\lambda_{\tau/\mu}}$ scenarios, as shown in Fig. 5.6. The analogous procedure with τ leads to limits weaker than the existing constraints and are hence not presented here.

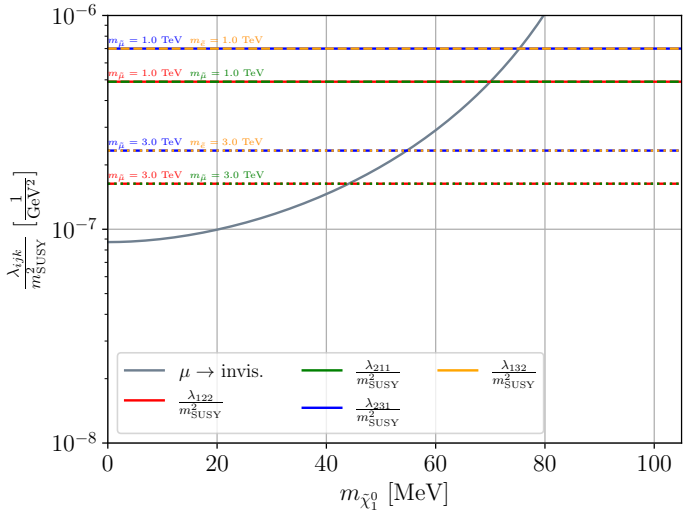

Figure 5.6: As in Fig. 5.2 but for the λ'_μ and $\lambda'_{\tau/\mu}$ benchmarks of Table 5.2. The existing limits on the RPV couplings are shown in red, yellow, green, and blue.

5.4.2 Two-coupling scenarios

Next, we consider scenarios where two RPV operators are simultaneously switched on; one corresponds to the production of the bino LSP, while the other leads to the decay. We can classify these scenarios based on the parent particle producing the neutralino; this then fixes the production RPV coupling. The relevant possibilities for the parent particles at beam-dump searches and colliders are: pions, kaons, D mesons, D_s mesons, B mesons, B_c mesons, and τ leptons.[11] The corresponding production RPV couplings (and processes) can be read off from Table 5.2, *e.g.*, λ'_{a11} for the pion, etc.

The produced neutralino, owing to its long lifetime, then travels a certain macroscopic distance and decays via the other RPV coupling. Thus, displaced-vertex searches for HNLs are sensitive to such scenarios, if the final states match the decay products of the bino. We list, in Table 5.3, all relevant final states of such searches, along with the relevant kinematic thresholds at which the HNL can decay into them. Consulting the discussion in Sec. 5.2, we see that each of these final states can also arise from bino decays.

In Table 5.4, we list, for each production category, the relevant RPV operator(s) leading to the final states of Table 5.3. ✕ indicates that the given final state can not arise for the considered production mode, owing to kinematics. This table can be used to identify all relevant two-coupling RPV scenarios that can be constrained by existing HNL DV searches. Note that we have not included bino production modes corresponding to the $LL\bar{E}$ decays of the τ leptons in the table since these lead to weak limits, as in the one-coupling scenarios. We now discuss numerical results for a representative subset of the possibilities in the table.

[11] τ leptons are dominantly produced in the decay of the D_s mesons at these experiments.

Channel	Threshold	Channel	Threshold
$\nu e^+ e^-$	1.02 MeV	$\mu^\mp K^\pm$	599 MeV
$\nu e^\pm \mu^\mp$	105 MeV	$\nu \rho^0$	776 MeV
$\nu \pi^0$	135 MeV	$e^\mp \rho^\pm$	776 MeV
$e^\mp \pi^\pm$	140 MeV	$\nu \omega$	783 MeV
$\nu \mu^+ \mu^-$	210 MeV	$\mu^\mp \rho^\pm$	882 MeV
$\mu^\mp \pi^\pm$	245 MeV	$\nu \eta'$	958 MeV
$e^\mp K^\pm$	494 MeV	$\nu \phi$	1 019 MeV
$\nu \eta$	548 MeV		

Table 5.3: Relevant final states from HNL (and bino) decay sorted by threshold mass. The active neutrino is considered massless.

Pion scenarios

For the $\pi^\pm$ category, we consider the two benchmark scenarios listed in Table 5.5. The relevant mass range is identified by requiring that the production of the neutralino, and its subsequent decay (*cf.* Table 5.4), should be both kinematically accessible.

We use this opportunity to explain one more subtlety of our recasting procedure for DV searches. In the HNL model, the relevant pion decay process occurs via the neutrino-mixings, *e.g.*, $\pi^\pm \to e^\pm + N$ via U_e. However, a non-zero U_e also induces the production of the HNL via decays of other particles, *e.g.*, $K^\pm \to e^\pm + N$ and the three-body decay, $K^\pm \to e^\pm + \pi^0 + N$. On the other hand, in our RPV benchmarks, this is not the case since λ'_{i11} only couples to the pion. This affects the kinematics of the HNL relative to the bino, and can be an issue for our simple scaling procedure, *cf.* the discussion in Sec. 5.3. For the pion benchmarks of Table 5.5, this is not a problem since the kaon modes are sub-dominant ($O(1\%)$) for the mass range identified above: $1\,\text{MeV} \lesssim m_N \lesssim 139\,\text{MeV}$; see, for instance, Ref. [415] for a plot with the relevant branching ratios in the HNL scenario. However, in later benchmarks, we deal with this issue – if it arises – by restricting the mass range of the benchmark to ensure that the types of contributing parents are the same in both models (neglecting sub-dominant contributions up to $O(10\%)$), so that the assumption of the same kinematics taken in the DV quick recasting method still holds.

We show the reinterpreted limits for the benchmarks $\boldsymbol{\pi_1}$ and $\boldsymbol{\pi_2}$ in the RPV coupling vs. mass plane in Fig. 5.7(a) and Fig. 5.7(b), respectively. For two-dimensional visualization, we have set the production and decay couplings to be equal. The exclusion limits come from a corresponding HNL search at `Super-Kamiokande` [391], as well as projections of sensitivity at `DUNE` [382]. The former only constrains the mass range $m_N \gtrsim 50\,\text{MeV}$ and, hence, does not have sensitivity to $\boldsymbol{\pi_2}$. We also show the existing bounds on the RPV couplings, taken from Ref. [45]. There are no existing product bounds on the pairs considered [29, 252]. From Fig. 5.7(a), it appears that the existing bound on λ'_{111} outperforms the reinterpreted bound. However, this is an artefact of the choice to set the production and decay couplings equal. We show the same exclusion limits again in Fig. 5.7(c) – this time in the coupling vs. coupling plane for a fixed neutralino mass, $m_{\tilde{\chi}_1^0} = 120\,\text{MeV}$; one can see that the reinterpreted sensitivity projection can probe a small region of the phase space still allowed by the current limits.

Category	$\tilde{\chi}_1^0$ Production \ $\tilde{\chi}_1^0$ Decay	νee	$\nu e\mu$	$\nu\mu\mu$	$e\{\pi/\rho\}$	$\mu\{\pi/\rho\}$	eK	μK	$\nu\{\pi/\rho/\omega\}$	$\nu\{\eta/\eta'/\phi\}$
π	$\lambda'_{111} : \pi^\pm \to e^\pm + \tilde{\chi}_1^0$ ($m_{\tilde{\chi}_1^0} \lesssim 139\,\text{MeV}$)	$\lambda_{121};\lambda_{131}$	$\lambda_{121};\lambda_{122};\lambda_{321};\lambda_{312}$	×	×	×	×	×	×	×
	$\lambda'_{211} : \pi^\pm \to \mu^\pm + \tilde{\chi}_1^0$ ($m_{\tilde{\chi}_1^0} \lesssim 34\,\text{MeV}$)	$\lambda_{121};\lambda_{131}$	×	×	×	×	×	×	×	×
K	$\lambda'_{112} : K^\pm \to e^\pm + \tilde{\chi}_1^0$ ($m_{\tilde{\chi}_1^0} \lesssim 493\,\text{MeV}$)	$\lambda_{121};\lambda_{131}$	$\lambda_{121};\lambda_{122};\lambda_{321};\lambda_{312}$	$\lambda_{122};\lambda_{322}$	λ'_{111}	λ'_{211}	×	×	λ'_{i11}	×
	$\lambda'_{212} : K^\pm \to \mu^\pm + \tilde{\chi}_1^0$ ($m_{\tilde{\chi}_1^0} \lesssim 388\,\text{MeV}$)	$\lambda_{121};\lambda_{131}$	$\lambda_{121};\lambda_{122};\lambda_{321};\lambda_{312}$	$\lambda_{122};\lambda_{322}$	λ'_{111}	λ'_{211}	×	×	λ'_{i11}	×
D	$\lambda'_{a21} : D^\pm \to e_a^\pm + \tilde{\chi}_1^0$ ($m_{\tilde{\chi}_1^0} \leq m_D - m_{e_a}$)	$\lambda_{121};\lambda_{131}$	$\lambda_{121};\lambda_{122};\lambda_{321};\lambda_{312}$	$\lambda_{122};\lambda_{322}$	λ'_{111}	λ'_{211}	λ'_{112}	λ'_{212}	λ'_{i11}	$\lambda'_{i11};\lambda'_{i22}$
D_s	$\lambda'_{a22} : D_s^\pm \to e_a^\pm + \tilde{\chi}_1^0$ ($m_{\tilde{\chi}_1^0} \leq m_{D_s} - m_{e_a}$)	$\lambda_{121};\lambda_{131}$	$\lambda_{121};\lambda_{122};\lambda_{321};\lambda_{312}$	$\lambda_{122};\lambda_{322}$	λ'_{111}	λ'_{211}	λ'_{112}	λ'_{212}	λ'_{i11}	$\lambda'_{i11};\lambda'_{322}$
B	$\lambda'_{i13} : B^\pm(B^0) \to e_i^\pm(\nu_i) + \tilde{\chi}_1^0$ ($m_{\tilde{\chi}_1^0} \leq m_B - m_{e_i}$)	$\lambda_{121};\lambda_{131}$	$\lambda_{121};\lambda_{122};\lambda_{321};\lambda_{312}$	$\lambda_{122};\lambda_{322}$	λ'_{111}	λ'_{211}	λ'_{112}	λ'_{212}	λ'_{i11}	$\lambda'_{i11};\lambda'_{i22}$
B_c	$\lambda'_{i23} : B_c^\pm \to e_i^\pm + \tilde{\chi}_1^0$ ($m_{\tilde{\chi}_1^0} \leq m_{B_c} - m_{e_i}$)	$\lambda_{121};\lambda_{131}$	$\lambda_{121};\lambda_{122};\lambda_{321};\lambda_{312}$	$\lambda_{122};\lambda_{322}$	λ'_{111}	λ'_{211}	λ'_{112}	λ'_{212}	λ'_{i11}	$\lambda'_{i11};\lambda'_{i22}$
τ	$\lambda'_{311} : \tau^\pm \to \{\pi^\pm/\rho^\pm\} + \tilde{\chi}_1^0$ ($m_{\tilde{\chi}_1^0} \lesssim 1\,637\,\text{MeV}$)	$\lambda_{121};\lambda_{131}$	$\lambda_{121};\lambda_{122};\lambda_{321};\lambda_{312}$	$\lambda_{122};\lambda_{322}$	λ'_{111}	λ'_{211}	λ'_{112}	λ'_{212}	λ'_{a11}	$\lambda'_{a11};\lambda'_{i22}$
	$\lambda'_{312} : \tau^\pm \to K^\pm + \tilde{\chi}_1^0$ ($m_{\tilde{\chi}_1^0} \lesssim 1\,283\,\text{MeV}$)	$\lambda_{121};\lambda_{131}$	$\lambda_{121};\lambda_{122};\lambda_{321};\lambda_{312}$	$\lambda_{122};\lambda_{322}$	λ'_{111}	λ'_{211}	λ'_{112}	λ'_{212}	λ'_{i11}	$\lambda'_{i11};\lambda'_{i22}$

Table 5.4: Relevant two-coupling RPV scenarios probed by HNL DV searches. Column one categorizes the parent meson/lepton; column two shows the corresponding RPV coupling, production process, and bino mass range; the remaining columns list the relevant final states of Table 5.3 arising from bino decays and the corresponding decay RPV coupling(s) for each production category. × indicates that the decay is kinematically disallowed.

Label	Production	Decay	$m_{\tilde{\chi}_1^0}$
$\boldsymbol{\pi_1}$	λ'_{111}	λ_{321}	106 MeV – 139 MeV
$\boldsymbol{\pi_2}$	λ'_{211}	λ_{121}	1 MeV – 34 MeV

Table 5.5: Details of the two-coupling RPV benchmark scenarios we study, corresponding to bino production from pions. The decay coupling in the third column leads to the final state that can be read off from Table 5.4. See the main text for details on how the mass range is determined.

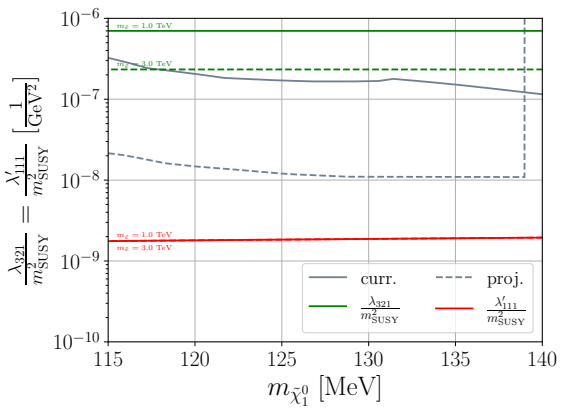

(a) Limits in the RPV coupling vs. bino mass plane for the benchmark $\boldsymbol{\pi_1}$ of Table 5.5.

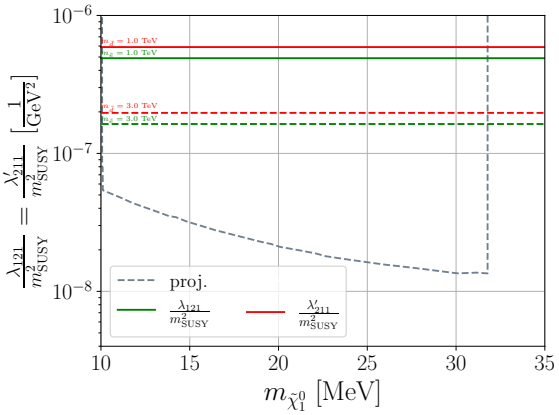

(b) Limits in the RPV coupling vs. bino mass plane for the benchmark $\boldsymbol{\pi_2}$ of Table 5.5.

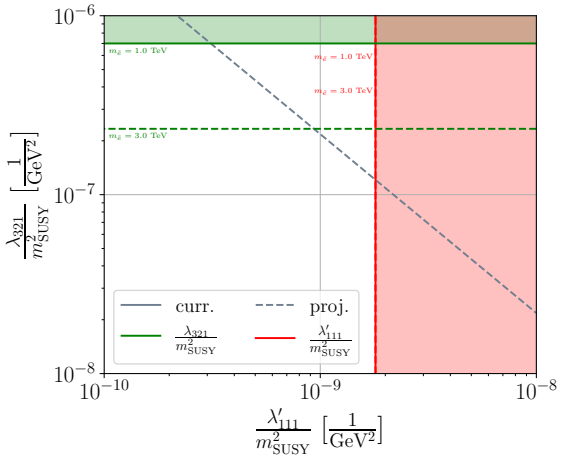

(c) Limits in the production coupling vs. decay coupling plane for the benchmark $\boldsymbol{\pi_1}$ of Table 5.5, with neutralino mass fixed at 120 MeV.

Figure 5.7: Current exclusion (solid lines) and projected sensitivity (dashed lines) limits corresponding to the two-coupling RPV scenarios with binos produced from pions; reinterpreted from HNL searches. The existing limits on the RPV couplings are shown in red, and green.

Kaon scenarios

Next, we study benchmarks corresponding to bino production via $K^{\pm}$ decays; the details are summarized in Table 5.6. Note, that for some benchmarks, (*e.g.*, $\boldsymbol{K_3}$), the lower end of the mass range lies significantly above the kinematic threshold requirement of bino decay. This is, as discussed above, to ensure that kaons are the only parents in the HNL model, as they are in the RPV model.

Label	Production	Decay	$m_{\tilde{\chi}_1^0}$
$\boldsymbol{K_1}$	λ'_{112}	λ'_{111}	140 MeV – 493 MeV
$\boldsymbol{K_2}$	λ'_{112}	λ'_{311}	140 MeV – 493 MeV
$\boldsymbol{K_3}$	λ'_{112}	λ_{321}	140 MeV – 493 MeV
$\boldsymbol{K_4}$	λ'_{212}	λ'_{211}	140 MeV – 388 MeV
$\boldsymbol{K_5}$	λ'_{212}	λ_{131}	35 MeV – 388 MeV

Table 5.6: As in Table 5.5 but for bino production from kaons.

The sensitivity limits for the kaon benchmarks are shown in Fig. 5.8. The single and – wherever relevant – product bounds (taken from Ref. [29, 252]) on RPV couplings are also shown. Current exclusion limits are obtained by combining the results from existing HNL searches at `T2K` [383], `Super-Kamiokande` [391], `NuTeV` [387], and `MicroBooNE` [388, 416], while the projections are all from `DUNE` [382]. Once again, we see that the reinterpreted limits exclude (or are projected to probe) large swathes of parameter space allowed by the current bounds. The sharp reduction in sensitivity in Fig. 5.8(e) below $m_{\tilde{\chi}_1^0} \approx 150\,\text{MeV}$ arises because the most constraining current limit comes from `T2K` and only probes regions corresponding to $m_N \gtrsim 150\,\text{MeV}$; below this the low-mass searches from `Super-K` and `MicroBooNE` provide exclusion.

D, D_s, and τ scenarios

We summarize the details for the τ benchmarks we consider, as well as the $D^{\pm}$ and $D_s^{\pm}$ meson ones in Table 5.7. We group them together in this section since, at the considered experiments, τ leptons are most copiously produced in the decays of the D_s mesons. The corresponding sensitivity limits are shown in Fig. 5.9 for the τ, and in Fig. 5.10 for the mesons.

Label	Production	Decay	$m_{\tilde{\chi}_1^0}$
$\boldsymbol{\tau_1}$	λ'_{311}	λ_{212}	211 MeV – 1 637 MeV
$\boldsymbol{\tau_2}$	λ'_{312}	λ'_{311}	140 MeV – 1 283 MeV
$\boldsymbol{D_1}$	λ'_{122}	λ'_{111}	600 MeV – 1 968 MeV
$\boldsymbol{D_2}$	λ'_{122}	λ'_{211}	600 MeV – 1 968 MeV
$\boldsymbol{D_3}$	λ'_{122}	λ'_{112}	600 MeV – 1 968 MeV
$\boldsymbol{D_4}$	λ'_{122}	λ_{121}	600 MeV – 1 968 MeV
$\boldsymbol{D_5}$	λ'_{222}	λ'_{211}	600 MeV – 1 863 MeV
$\boldsymbol{D_6}$	λ'_{222}	λ_{131}	600 MeV – 1 863 MeV
$\boldsymbol{D_7}$	λ'_{221}	λ_{232}	260 MeV – 1 764 MeV

Table 5.7: As in Table 5.5 but for bino production from τ leptons, and D and D_s mesons.

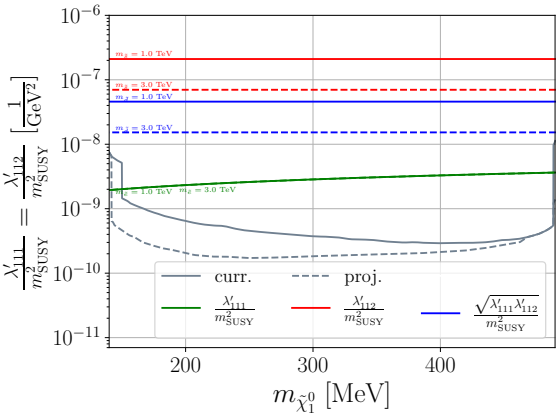

(a) Benchmark $\boldsymbol{K_1}$ from Table 5.6.

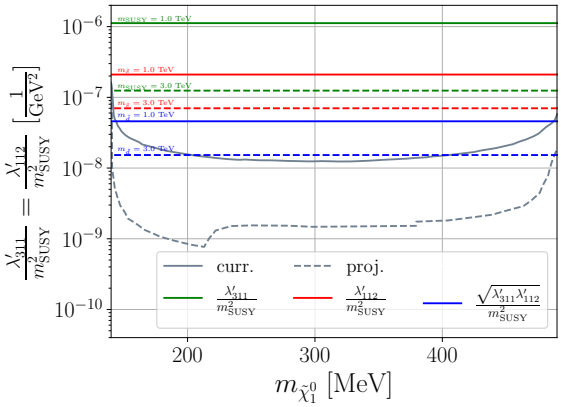

(b) Benchmark $\boldsymbol{K_2}$ from Table 5.6.

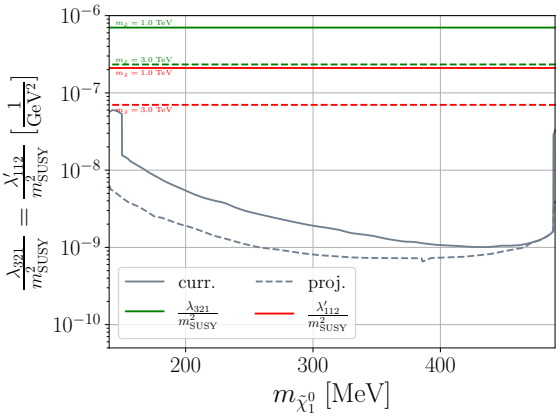

(c) Benchmark $\boldsymbol{K_3}$ from Table 5.6.

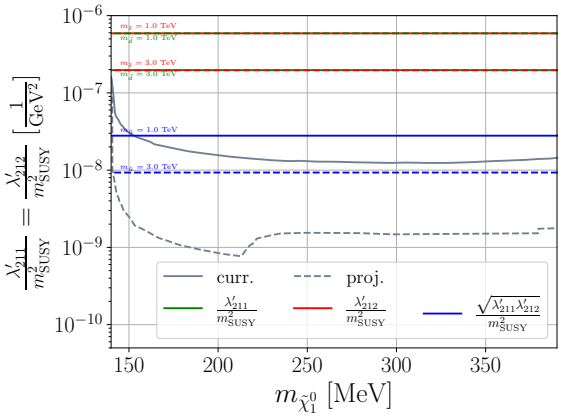

(d) Benchmark $\boldsymbol{K_4}$ from Table 5.6.

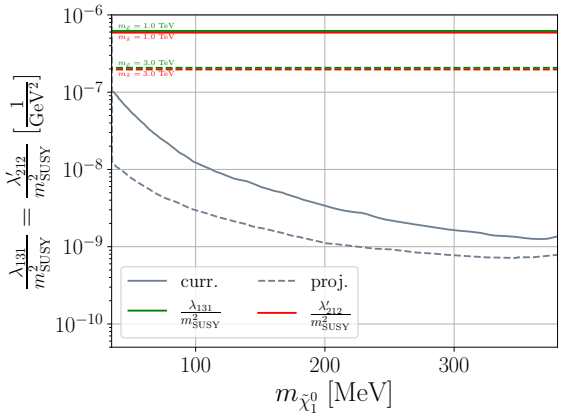

(e) Benchmark $\boldsymbol{K_5}$ from Table 5.6.

Figure 5.8: Current exclusion (solid lines) and projected sensitivity (dashed lines) limits corresponding to the two-coupling RPV scenarios with binos produced from kaons in the RPV coupling vs. bino mass plane; reinterpreted from HNL searches. The existing limits on the RPV couplings are shown in red and green (single bounds), and blue (product bound).

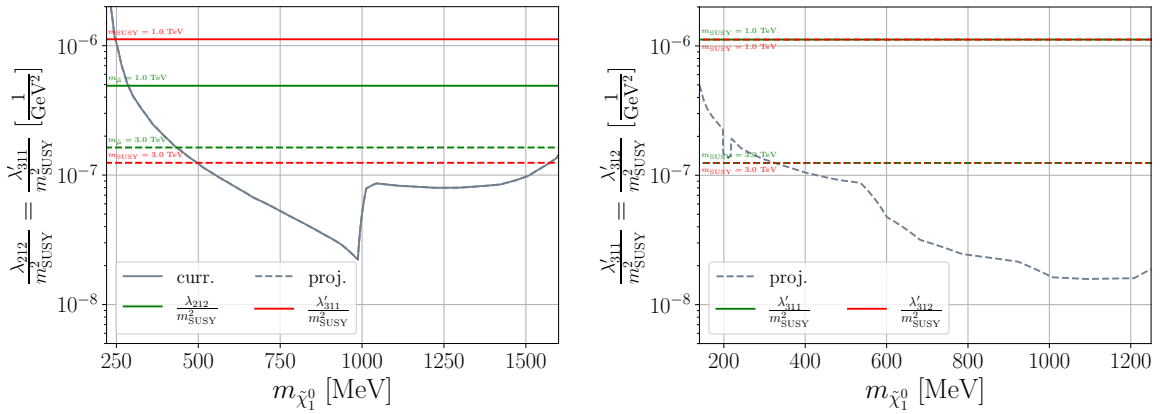

(a) Benchmark $\boldsymbol{\tau_1}$ from Table 5.7.

(b) Benchmark $\boldsymbol{\tau_2}$ from Table 5.7.

Figure 5.9: As in Fig. 5.8 but for binos produced from τ leptons.

For the τ lepton scenarios, the exclusion and projected search sensitivity, shown in Fig. 5.9, come from BEBC [389, 390], CHARM [384, 417], and ArgoNeuT [418]; and DUNE [382], FASER2 [392, 400], and MoEDAL-MAPP2 [393, 400], respectively. There is no current search targeting the final state of $\boldsymbol{\tau_2}$, while the current limit on $\boldsymbol{\tau_1}$ beats even the projected search sensitivity at DUNE and FASER. The sharp drop in sensitivity in Fig. 5.9(a) at $m_{\tilde{\chi}_1^0} \approx 1\,000\,\text{MeV}$ occurs because the ρ and bino decay mode of the τ lepton in the RPV model (*cf.* Table 5.2) becomes kinematically inaccessible, leading to the reduction in production.

For the D and D_s mesons, current exclusions are provided by searches at BEBC [389, 390], CHARM [384], and NuTeV [387]. Further, DUNE [382], FASER2 [392], and MoEDAL-MAPP2 [393, 400] are projected to improve this reach. For all D_s benchmarks except $\boldsymbol{D_7}$, we only consider neutralinos with mass, $m_{\tilde{\chi}_1^0} > 600\,\text{MeV}$. This is because either the above experiments only constrain the corresponding parameter region in the HNL model, or because kaons and pions dominate the HNL production for lower masses. One exception is BEBC, where nearly all produced pions and kaons are absorbed by a high-density target before they can decay, and HNL production is dominated by D meson decays. Since benchmark $\boldsymbol{D_7}$ involves production from D-mesons, we can probe lower bino masses in our scenario. The kink in the corresponding sensitivity limit in Fig. 5.10(g) at $m_{\tilde{\chi}_1^0} \approx 500\,\text{MeV}$ occurs because CHARM takes over from BEBC. We note that the final states of benchmarks $\boldsymbol{D_1}$ and $\boldsymbol{D_3}$ are not covered by the existing searches but will be covered by the upcoming experiments.

Once again, we see – for all the plots in this section – that reinterpreting existing and projected limits on HNL models in terms of our RPV scenarios gives bounds on the parameter space that improve upon existing limits by orders of magnitude.

B and B_c scenarios

Here, the bino is produced in $B(B^{\pm}/\overset{(-)}{B}{}^0)$ or $B_c^{\pm}$ decays, *cf.* Table 5.8. While HNL production in these modes only becomes dominant above the D-meson thresholds, the projected search sensitivity for FASER(2) provided in Ref. [392] shows the results separately for the HNLs from B-meson decays and from D-meson and kaon decays, enabling us to choose benchmarks with masses lower than

the D thresholds. Up to about $m_N \approx 2\,700\,\text{MeV}$, the production is dominated by B decays and we choose the first three benchmarks accordingly. Beyond this, B_c decays also become significant, and for $m_N \gtrsim 3\,500\,\text{MeV}$, they become the dominant modes; the last two benchmarks focus on this.

Label	**Production**	**Decay**	$\boldsymbol{m_{\tilde{\chi}_1^0}}$
$\boldsymbol{B_1}$	λ'_{113}	λ'_{122}	548 MeV − 2 700 MeV
$\boldsymbol{B_2}$	λ'_{113}	λ_{131}	160 MeV − 2 700 MeV
$\boldsymbol{B_3}$	λ'_{213}	λ'_{211}	160 MeV − 2 700 MeV
$\boldsymbol{B_4}$	λ'_{123}	λ'_{311}	3 500 MeV − 6 275 MeV
$\boldsymbol{B_5}$	λ'_{123}	λ_{131}	3 500 MeV − 6 275 MeV

Table 5.8: As in Table 5.5 but for bino production from B and B_c mesons.

The corresponding sensitivity limits are presented in Fig. 5.11. There are no existing constraints; however, projections from `FASER2` [392, 400] and `MoEDAL-MAPP2` [393, 400] show that we should be able to probe the RPV parameter space up to 2-3 orders of magnitude beyond what is ruled out by current limits.

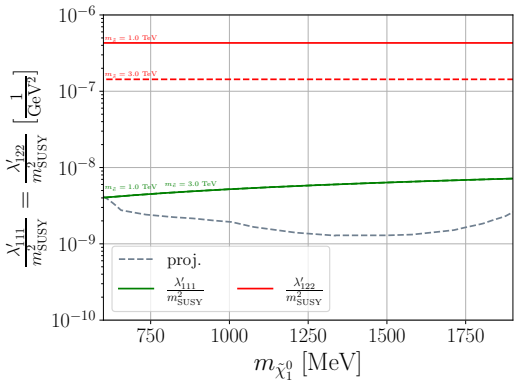

(a) Benchmark $\boldsymbol{D_1}$ from Table 5.7.

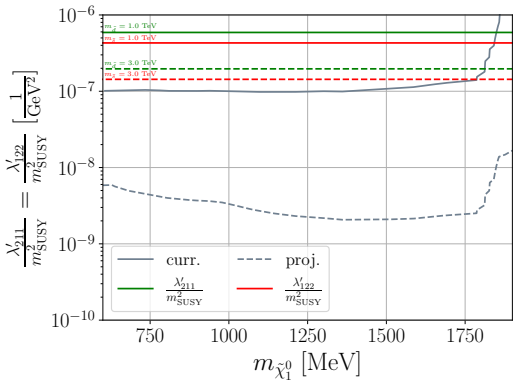

(b) Benchmark $\boldsymbol{D_2}$ from Table 5.7.

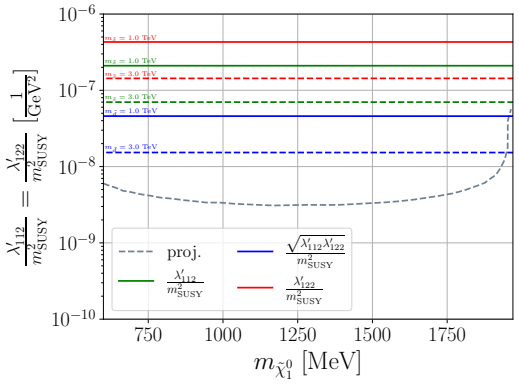

(c) Benchmark $\boldsymbol{D_3}$ from Table 5.7.

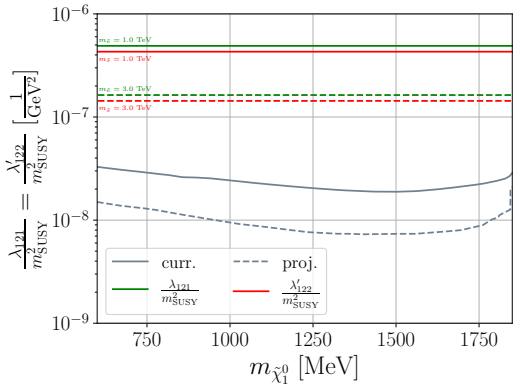

(d) Benchmark $\boldsymbol{D_4}$ from Table 5.7.

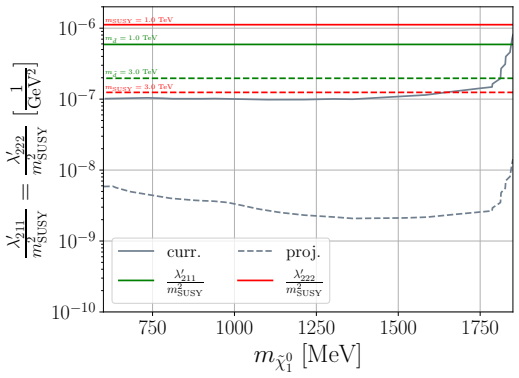

(e) Benchmark $\boldsymbol{D_5}$ from Table 5.7.

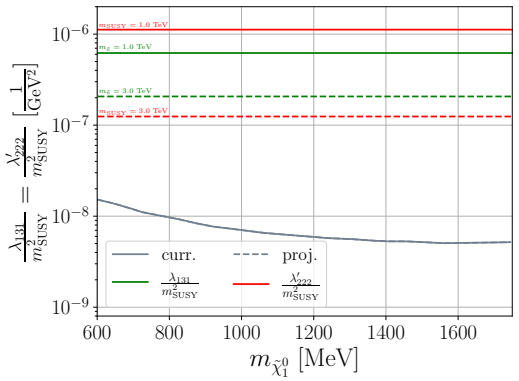

(f) Benchmark $\boldsymbol{D_6}$ from Table 5.7.

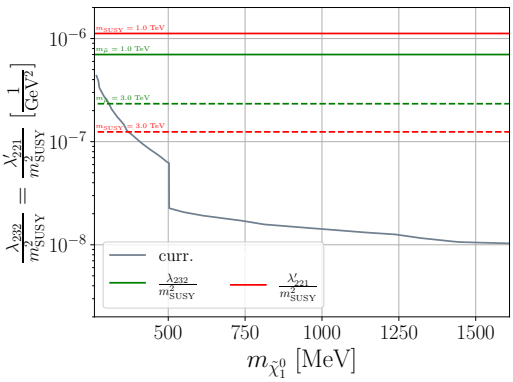

(g) Benchmark $\boldsymbol{D_7}$ from Table 5.7.

Figure 5.10: As in Fig. 5.8 but for binos produced from D and D_s mesons.

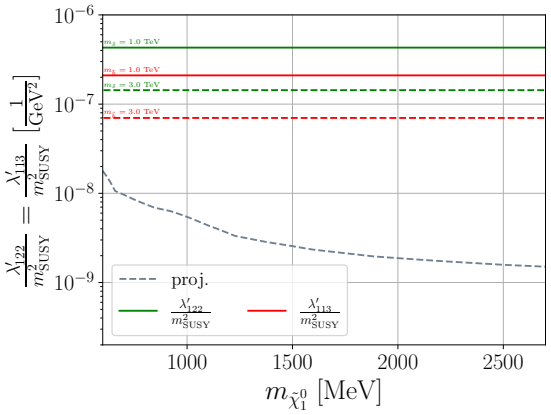

(a) Benchmark $\boldsymbol{B_1}$ from Table 5.8.

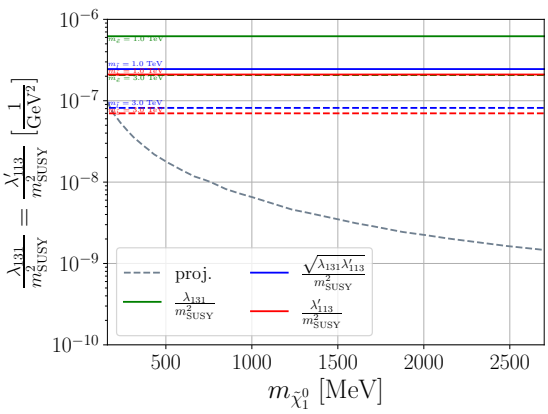

(b) Benchmark $\boldsymbol{B_2}$ from Table 5.8.

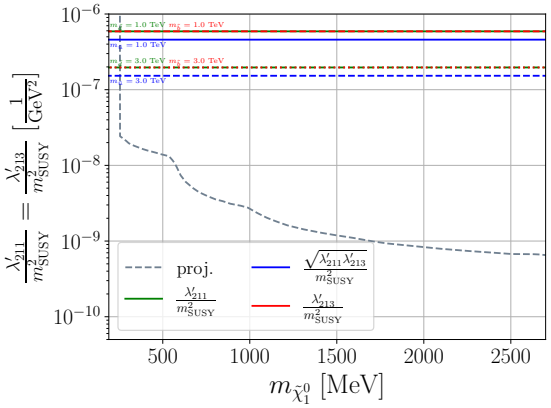

(c) Benchmark $\boldsymbol{B_3}$ from Table 5.8.

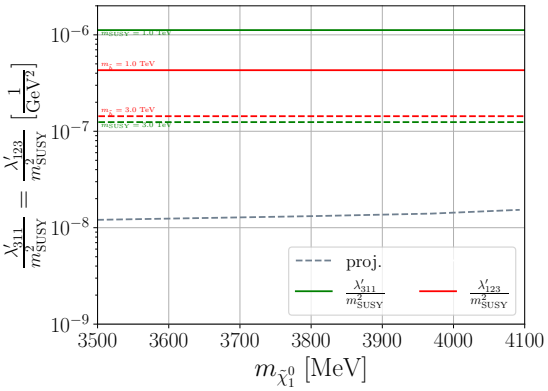

(d) Benchmark $\boldsymbol{B_4}$ from Table 5.8.

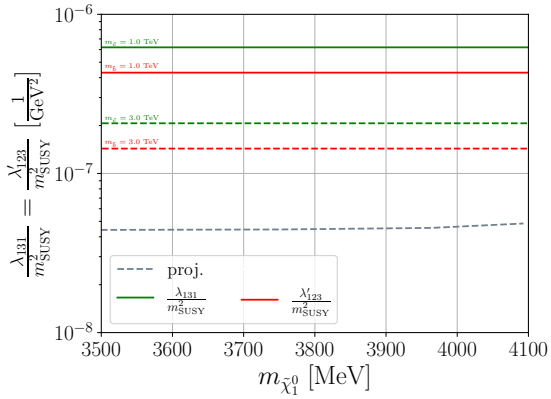

(e) Benchmark $\boldsymbol{B_5}$ from Table 5.8.

Figure 5.11: As in Fig. 5.8 but for binos produced from B and B_c mesons.

5.5 Conclusions

In this work, we have considered a GeV-scale or lighter long-lived lightest neutralino, which is necessarily bino-like, in the minimal R-parity-violating (RPV) supersymmetric model. We have focused on lepton-number-violating operators in the RPV superpotential: LH_u, $LL\bar{E}$, and $LQ\bar{D}$. Such light neutralinos are still allowed by all experimental and observational constraints, as long as they decay, for instance via RPV couplings, so as to avoid overclosing the Universe. Since these RPV couplings are bounded to be small, such light binos, which we assume to be the lightest supersymmetric particle in our theory, are expected to have a relatively long lifetime. Via the considered couplings, the binos can decay leptonically or semi-leptonically. For their production, we have focused on rare decays of mesons and charged leptons which are copiously produced at various facilities such as beam-dump and collider experiments. Once produced, these light binos can lead to exotic signatures such as displaced vertices (DVs) or missing energy. We have used searches for these signatures to constrain the RPV couplings associated with a light bino.

These various strategies are experimentally widely utilized to constrain heavy neutral leptons (HNLs) which may decay to almost the same final-state particles as the lightest neutralino in the RPV models. We have thus used the existing HNL searches to set new strict bounds on the relevant RPV couplings. Furthermore we have translated the prjected sensitivity to the HNL parameters at certain future experiments into the corresponding search sensitivity for the light neutralinos.

We have studied comprehensively the past experiments `PIENU`, `NA62`, `T2K`, and `BaBar`, as well as the approved experiments `FASER`, `MoEDAL-MAPP1`, `PIONEER`, and `DUNE`. We did not consider future experiments that are not yet approved such as `MATHUSLA` and `ANUBIS`, with two exceptions, namely `FASER2` and `MoEDAL-MAPP2` since they would be the follow-up programs of the two currently running experiments `FASER` and `MoEDAL-MAPP1`.

Given the various types and flavor-indices of the RPV operators that can be switched on, we have investigated separately different theoretical benchmark scenarios, which can be bounded by distinct experiments and strategies. For the selected representative benchmark scenarios, we have performed numerical computation and presented the final exclusion bounds. Further, we have compared these recast bounds with the existing limits on the RPV couplings which mainly stem from low-energy processes of meson and lepton decays. In general, we find that in most cases the exclusion limits obtained from recasting past HNL searches surpass the existing bounds on the RPV couplings by orders of magnitude, and the expected limits at the considered ongoing and future experiments can be even stronger.

Simple and analytic reinterpretation methods are becoming an important research tool. This is because most published experimental reports present results only for a limited number of simple models, and a recast with full simulation is often complicated and time-consuming. Some existing works such as Refs. [342, 390, 400] have shown the power of simple and quick reinterpretation of searches for long-lived particles by considering heavy neutral leptons in various models and axion-like particles as examples. Our work exemplifies again the strengths and convenience of such reinterpretation methods, by recasting the bounds on the HNLs in the minimal scenario, into those on the lightest neutralinos in the RPV supersymmetric models, and hence motivates the development of further studies with these reinterpretation methods.

6

Single Photon Searches for R-parity-violating Supersymmetry at FASER

6.0 Preface

The contents of this chapter have already been published:

- H. K. Dreiner, D. Köhler, S. Nangia, and Z. S. Wang,
  Searching for a single photon from lightest neutralino decays in R-parity-violating supersymmetry at FASER,
  Published in JHEP 02 (2023) 120, arXiv:2207.05100 [hep-ph].

6.0.1 Overview

In this chapter, we continue with our study of a very light neutralino in the context of the RPV-MSSM. In the previous chapter, we demonstrated that the phenomenology of a light bino is very similar to that of (light) heavy neutral leptons (HNLs). Thus, we were able to use a simple recasting procedure to convert the sensitivity limits on the model space of the latter – which have been analyzed extensively – into sensitivity limits for the RPV-MSSM. Due to the overlap in production mechanisms and final state signatures, such an approach allowed us to analyze a wide range of light-bino scenarios involving several (combinations of) RPV couplings. On the flip side, however, this meant we were restricted to scenarios where either the bino had a significant mixing with the active neutrinos, or where its decay products matched some final state that has been analyzed in the context of HNL searches. Typically, such searches focus on decays into a meson and a lepton, or two charged leptons and a neutrino; in the case of the light bino, these states can be obtained through tree-level decays involving $LQ\bar{D}$ and $LL\bar{E}$ operators, respectively. Similarly, other studies analyzing the sensitivity of various experiments to light binos, mentioned in Chapter 1, have also considered only the tree-level decay modes of the bino.

However, one more interesting possibility exists. As we will demonstrate in this chapter, the RPV-MSSM also allows the neutralino to decay radiatively at one loop into a final state of a single photon and a(n) (anti-)neutrino:

$$\tilde{\chi}_1^0 \to \left(\gamma + \nu_i \,, \gamma + \bar{\nu}_i\right) \,. \tag{6.1}$$

The above involves a virtual sfermion in the loop and proceeds via any operators of the type, $L_i Q_j \bar{D}_j$ or $L_i L_j \bar{E}_j$, with diagrams corresponding to the heavier generations having a larger width, as we will show. Despite the loop-suppression, this mode can become dominant for very light neutralinos as it has no kinematic threshold (neglecting the masses of the (anti-)neutrinos). Even for neutralinos that

are not too light (still, of course lighter than the $\mathcal{O}(5\,\text{GeV})$ threshold we are interested in focusing on), the available RPV decay operator may only couple to final states involving heavy mesons or charged leptons that are kinematically inaccessible. In such cases, the loop-decay mode can become the only relevant probe.

Such a decay mode can have an interesting signature at FASER, which has already begun taking data at the LHC. The neutralino is produced primarily, as before, through the decays of mesons and is highly boosted in the far-forward direction. After traveling a macroscopic distance, if it then decays inside the FASER detector material (situated 480 m downstream from the ATLAS detector), one would detect an isolated, highly-energetic photon ($\mathcal{O}(0.1) - \mathcal{O}(1)$ TeV), with the associated neutrino expected to escape undetected. As we shall discuss, such a signal is expected to suffer from low SM backgrounds, and hence, offers a clean probe of new physics.

Thus, in this chapter, we analyze the sensitivity of FASER(2) to the above possibility. We consider five benchmarks involving two RPV couplings as well as one benchmark involving just a single coupling, covering all relevant (for FASER) RPV-MSSM scenarios where the radiative decay mode can be dominant. We use the package FORESEE to simulate the neutralino spectrum in the far-forward direction, as well as to estimate the number of decays that would occur inside the detector material. We find that FASER(2) has sensitivity reach to regions lying up to 2 orders of magnitude beyond the current bounds in our benchmarks.

The results of this chapter extend those of the previous one by allowing for additional RPV-coupling combinations to be probed.

6.0.2 Contributions of the Author

The author of this thesis proposed using the radiative decay mode of the bino to constrain the RPV-MSSM. The corresponding one-loop decay width was calculated by the author, based on the framework of Ref. [419]. Further, all benchmarks presented in this chapter were developed by the author. Finally, the interpretation of the results was performed by the author together with Dominik Köhler, with insights from Zeren Simon Wang.

6.1 Introduction

The discovery of a Higgs boson [10, 11] at the Large Hadron Collider (LHC) at CERN, Switzerland, has completed the spectrum of the Standard Model (SM) of particle physics. Despite the huge successes, the SM provides an incomplete description of the Universe. For instance, the observed neutrino oscillations [12, 312, 420] require massive neutrinos, in disagreement with the SM. The fine-tuning problem of the Higgs boson – or hierarchy problem [100, 101] – is only resolved beyond the SM (BSM), *e.g.*, by supersymmetry (SUSY) [19, 102]. Furthermore, dark matter and dark energy, as well as baryogenesis in the early Universe are all unexplained within the SM.

Searches for BSM physics have been performed since even prior to the Higgs-boson discovery, on various experimental and observational fronts. These probes include colliders, beam-dump experiments, nuclear- and electron-recoil experiments, and astrophysical observations.

Here, we focus on collider probes for BSM-physics searches. In particular, we study high-energy proton-proton collisions at the LHC, currently aiming to reach a center-of-mass energy of 14 TeV in the near future. The two largest experiments at the LHC – ATLAS [421] and CMS [422] – have hitherto mainly searched for events with large missing energy and/or high p_T objects (jets, leptons, etc.), emphasizing signatures expected to stem from heavy new fields.

Among various signatures, high-energy photons plus missing energy is one interesting example as it is clean with modest SM background, and is predicted in well-motivated theoretical models. One classic example is Gauge-mediated Supersymmetry Breaking (GMSB) models [423]. Given a light and stable gravitino as the lightest supersymmetric particle (LSP), the lightest Minimal Supersymmetric Standard Model (MSSM) superpartner is actually the next-to-lightest supersymmetric particle (NLSP). If the NLSP is neutral, it can be either a neutralino, or a sneutrino. The lightest neutralino can be bino, wino, Higgsino, or a mixture, and can decay to a photon and a non-observable gravitino, either promptly or with a long lifetime; see, *e.g.*, Refs. [424–427] for some LHC phenomenology studies. This signature has been searched for at the Tevatron – at CDF and D0 [428, 429] – and at the LHC – at ATLAS [430] and CMS [431].

One additional theory benchmark is a class of models with universal extra dimensions [432]. If the new dimensions are only accessible to gravity, the lightest Kaluza-Klein particle (LKP) can decay to a photon and a gravity excitation. Both the lightest neutralino (assuming R-parity conservation) and the LKP should be pair-produced, and thus lead to the signature of two highly energetic photons plus missing energy at the LHC.

Here, we consider R-parity-violating (RPV) supersymmetry in its minimal form – the RPV Minimal Supersymmetric Standard Model (RPV-MSSM) [40] – with a bino-like lightest neutralino as the LSP (see Refs. [29, 37, 353] for reviews). The RPV-MSSM is as well-motivated as the R-parity-conserving (RPC) MSSM. It not only solves the hierarchy problem, but also provides a natural solution to the neutrino masses [35, 61, 281, 291, 299], as well as a much richer collider phenomenology than the RPC-MSSM. In addition, it can explain various experimental anomalies observed in recent years, such as the B-anomalies [230, 231, 356–359], muon $g-2$ [357–359], and the ANITA anomaly [359, 360].

As we discuss in more detail in Section 6.2 below, in the RPV-MSSM, it is possible to have a light neutralino of mass below 10 GeV, or even massless. Once produced, the neutralino decays via non-vanishing RPV couplings into SM particles. Since these couplings are required by various (low-energy) experiments to be small [29, 252, 363], light LSP neutralinos with mass below the GeV scale are expected to be long-lived; after production at a collider, they travel a macroscopic distance before decaying to SM particles.

Long-lived particles (LLPs) have in recent years received increased attention [152, 156, 327, 433–435]. LLPs are predicted in a wide range of BSM models such as split SUSY, RPV-SUSY, a class of portal-physics models [axion-like particles (ALPs), heavy neutral leptons, a dark Higgs scalar, dark photons], and models of neutral naturalness – which are often related to the non-vanishing neutrino masses or dark matter. In particular, a series of dedicated far-detector programs have been proposed to be operated in the vicinity of LHC interaction points (IPs), mainly aiming to look for LLPs with a proper decay length $c\tau \sim (1 - 100)$ m, or even larger. Some examples currently under discussion include FASER [85, 86], FACET [402], MATHUSLA [327, 368, 369], CODEX-b [401], ANUBIS [370], and MoEDAL-MAPP [436].

FASER has been approved and installed at the LHC TI12 tunnel. It consists of a small cylindrical decay volume of $\sim 0.05\,\mathrm{m}^3$. It is expected to achieve excellent constraining power for a number of theoretical benchmark models such as ALPs [437], dark photons [85], and inelastic dark matter [438]. It is now under operation with the ongoing LHC Run 3. For the high-luminosity LHC (HL-LHC) period, a larger version of FASER, known as FASER2 [86], is also planned to be installed and running, potentially at the same location or at a collective facility – the Forward Physics Facility (FPF) [439] – hosting various experiments, all in the very forward region of the LHC, including FORMOSA [440] and FLArE [441]. These potential future experiments are all intended to look for various BSM signatures.

Here, we focus on long-lived light neutralinos. They have been studied extensively for various present and future experiments including SHiP [87, 88], ATLAS [87], far detectors at the LHC [89–92], Belle II [93], Super-Kamiokande [94], and future lepton colliders [442, 443]. These works mostly consider the signature of a neutralino decay into a charged lepton plus a meson, induced by $LQ\bar{D}$ operators [354], while the production can result from decays of either mesons, τ leptons, or Z-boson.

In this work, we propose a novel signature associated with very light lightest-neutralino $\left(\tilde{\chi}_1^0\right)$ decays: A single photon plus missing energy. Such a signature can appear as a result of the radiative decay associated with neutrinos,

$$\tilde{\chi}_1^0 \to \nu_i + \gamma \text{ or } \bar{\nu}_i + \gamma\,, \tag{6.2}$$

arising at the loop level via the RPV couplings λ'_{ijj} of the $LQ\bar{D}$ operators or λ_{ijj} of the $LL\bar{E}$ operators. This decay can dominate in certain mass ranges and for certain choices of RPV couplings.[1] We consider the lightest neutralino to be produced from rare decays of mesons such as pions and B-mesons copiously created at the LHC, and study the probing potential of FASER and FASER2 to these scenarios, for the signature of a single, displaced photon. As discussed in Section 6.5, the background is expected to be negligible.

The paper is organized as follows. We briefly introduce the RPV-MSSM, as well as the light neutralino scenario in the next section. In Section 6.3 we present a list of representative benchmark scenarios, which we investigate in this paper. In Section 6.4 we discuss the experimental setup at FASER and FASER2, and in Section 6.5 we detail our simulation procedure for estimating the sensitivity reach. The results are then presented with a discussion in Section 6.6. We conclude the paper with a summary and an outlook in Section 6.7.

[1] We note that light long-lived particles (LLPs) decaying to a light neutrino and a photon may explain the MiniBooNE anomaly [444, 445], but given the recent negative results by MicroBooNE [446], and possible SM explanations for the anomaly [447, 448], we do not consider it any further here.

6.2 Theoretical Framework

Here, we discuss the underlying supersymmetric model, as well as details of the light neutralino scenario.

6.2.1 The R-parity-violating MSSM

Given the $(N = 1)$ supersymmetry algebra, and the MSSM particle content, the most general $\mathrm{SU}(3)_C \times \mathrm{SU}(2)_L \times \mathrm{U}(1)_Y$-invariant, renormalizable superpotential can be written as,

$$W = W_{\mathrm{MSSM}} + W_{\mathrm{LNV}} + W_{\mathrm{BNV}}\,, \tag{6.3}$$

where W_{MSSM} is the usual MSSM superpotential – see, for instance, Ref. [40] – while the terms,

$$W_{\mathrm{LNV}} = \frac{1}{2}\lambda^{ijk} L_i L_j \bar{E}_k + \lambda'^{ijk} L_i Q_j \bar{D}_k + \kappa^i H_u L_i\,, \qquad W_{\mathrm{BNV}} = \frac{1}{2}\lambda''^{ijk} \bar{U}_i \bar{D}_j \bar{D}_k\,, \tag{6.4}$$

violate lepton- and baryon-number, respectively. In the above, L (Q), and $\bar{E}$ $(\bar{U}, \bar{D})$ are the MSSM lepton (quark) $\mathrm{SU}(2)_L$-doublet and $\mathrm{SU}(2)_L$-singlet chiral superfields, respectively, while H_u, H_d label the $\mathrm{SU}(2)_L$-doublet Higgs chiral superfields. We do not show gauge indices explicitly but write the generational ones: $i, j, k = 1, 2, 3$ with a summation implied over repeated indices. The λ's are dimensionless coupling parameters, the κ's are dimension-one mass parameters.

The combined lepton- and baryon-violation contained in the above terms may cause the proton to decay too quickly [60, 449]. Thus, in the MSSM, all operators in $W_{\mathrm{LNV}} + W_{\mathrm{BNV}}$ are set to zero by invoking a $\mathbb{Z}_2$ symmetry called R-parity [147]. This allows W_{MSSM} while disallowing $W_{\mathrm{RPV}} \equiv W_{\mathrm{LNV}} + W_{\mathrm{BNV}}$. However, the proton can be protected without completely forbidding W_{RPV}. For instance, forbidding W_{BNV}, while keeping W_{LNV}, results in a stable proton. Baryon triality – B_3 – is a $\mathbb{Z}_3$-symmetry that achieves exactly this [35, 44, 148, 249].

Importantly, RPV phenomenology can be starkly different compared to the RPC case [29, 37, 45, 47, 150]. The LSP is no longer guaranteed to be stable leading to vastly different final state signatures. The collider phenomenology of RPV models is rich and complex [45, 47], and it is crucial that our SUSY search strategies cover all possibilities. We now discuss in some detail one interesting realization of RPV-SUSY: A very light neutralino.

6.2.2 A Very light Lightest-Neutralino

In principle, any supersymmetric particle can be the LSP in RPV models [45, 169, 450]. Here, we restrict ourselves to the case of a neutralino. Potentially important mass bounds come from colliders, dark matter (cosmology), and astrophysics. For collider searches of a stable neutralino, the strongest bound comes from LEP, $m_{\tilde{\chi}_1^0} \gtrsim 46\,\mathrm{GeV}$ [449]. This is based on chargino searches, and assumes the grand-unified mass relation is satisfied between the electroweak supersymmetry breaking gaugino masses, $M_1 = \frac{5}{3}\tan^2\theta_W M_2 \approx 0.5 M_2$, with θ_W the electroweak mixing angle. However, once the relation is dropped, the mass of the lightest neutralino is experimentally unconstrained [74]. Such a scenario typically requires the lightest neutralino to be dominantly bino-like [73, 74].

A stable lightest neutralino is further constrained by dark matter limits. The Lee-Weinberg bound gives $m_{\tilde{\chi}_1^0} \gtrsim O(10\,\mathrm{GeV})$ [74–82]. However, in RPV models where the LSP is unstable, this bound

does not apply [74].

Then, from our discussion above, if the RPV couplings are small – which is what one expects – the neutralino can be stable on collider scales while unstable on cosmological scales, thus evading all existing constraints. Such a neutralino is allowed to be very light and, in principle, even massless [74, 449]. It is also consistent with astrophysical constraints, such as the cooling of supernoavae and white dwarfs, if the sfermions are heavy enough [79, 83, 84].

We next consider the phenomenology of RPV-SUSY scenarios with such light neutralinos as the LSP. If the neutralino is massive enough, and/or the RPV couplings are sizeable, such that the proper decay length of the neutralino is $c\tau \lesssim O(1\,\text{m})$, various RPV searches performed at ATLAS and CMS – including those for displaced vertices – apply; see, *e.g.*, Refs. [155, 451]. These searches rely on detecting the decay products of the neutralino, which can contain jets and leptons, depending on the dominant RPV couplings. On the other hand, for very light neutralinos, and/or if the RPV couplings are very small, the neutralino LSP is stable on macroscopic scales. Then, the signature is invisible to colliders, just as in the RPC case. Thus, as long as heavier SUSY particles are produced at the LHC, that then cascade-decay down to the neutralino LSP, the RPC searches for large missing transverse momentum apply even to the RPV case.

However, in light of to-date unsuccessful supersymmetry searches, one possibility is that the heavier SUSY spectrum may be inaccessible at the LHC. Very light neutralinos, $m_{\tilde{\chi}_1^0} \lesssim O(4.5\,\text{GeV})$, can still be produced in abundance in such a scenario in RPV models through the rare decays of mesons via an $LQ\bar{D}$ operator [73, 87, 318]. These neutralinos would be highly boosted in the forward direction of the momentum of the decaying meson. None of the above search strategies applies in such a case, and the scenario represents a realistic possibility of low-scale SUSY manifesting in a way that would have escaped our searches so far. With the long-lived particle programs at the LHC picking up pace, there is the possibility of filling this gap. If the highly boosted, light neutralino decays with a proper decay length, $c\tau \sim O(1 - 100\,\text{m})$, it may be visible in dedicated far-detector experiments such as FASER. Before we discuss the decay modes of such light neutralinos, we provide, for completeness, the unpolarized decay width of pseudoscalar mesons into a light neutralino and a lepton via an $LQ\bar{D}$ operator, reproduced from Ref. [87],

$$\Gamma\left(M_{ab} \to \tilde{\chi}_1^0 + l_i\right) = \frac{\lambda^{\frac{1}{2}}\left(m_{M_{ab}}^2, m_{\tilde{\chi}_1^0}^2, m_{l_i}^2\right)}{64\pi m_{M_{ab}}^3} \left|G_{iab}^{S,f}\right|^2 \left(f_{M_{ab}}^S\right)^2 \left(m_{M_{ab}}^2 - m_{\tilde{\chi}_1^0}^2 - m_{l_i}^2\right), \tag{6.5}$$

where l_i denotes a charged lepton $\ell_i^\pm$ or a neutrino ν_i, depending on whether M_{ab} is charged or neutral, and $\lambda^{\frac{1}{2}}$ is the Källén function $\lambda^{\frac{1}{2}}(x, y, z) \equiv \sqrt{x^2 + y^2 + z^2 - 2xy - 2xz - 2yz}$. The coupling constants $G_{iab}^{S,f}$ and the meson decay constant $f_{M_{ab}}^S$ are defined as in Ref. [87]. In particular, the $LQ\bar{D}$ coupling λ' is proportional to $G_{iab}^{S,f}$. In the above, the charge-conjugated mode is implied.

6.2.3 Neutralino Decay

The dominant decay mode of the neutralino is dictated by the relative sizes of the RPV couplings, as well as the neutralino mass [354]. For $m_{\tilde{\chi}_1^0} \lesssim O(4.5\,\text{GeV})$, the neutralino can decay into a meson and a lepton via an $LQ\bar{D}$ operator, if kinematically allowed. Similarly, it can decay as $\tilde{\chi}_1^0 \to \ell^+\ell'^-\nu + \text{c.c.}$ via

the $LL\bar{E}$ operators. For operators $L_iQ_j\bar{D}_j$ or $L_iL_j\bar{E}_j$, there is also the possibility for the loop-induced decays,

$$\tilde{\chi}_1^0 \to \left(\gamma + \nu_i\,, \gamma + \bar{\nu}_i\right)\,, \tag{6.6}$$

which has essentially no kinematic threshold. We show example Feynman diagrams in Fig. 6.1. The fermions/sfermions in the loop have generation index j. The decay rate is given by [61, 354, 419, 452]:

$$\begin{aligned}\Gamma(\tilde{\chi}_1^0 \to \gamma + \nu_i) &= \frac{\lambda^2\alpha^2 m^3_{\tilde{\chi}_1^0}}{512\pi^3\cos^2\theta_W}\left[\sum_f \frac{e_f N_c m_f\left(4e_f+1\right)}{m^2_{\tilde{f}}}\left(1+\log\frac{m_f^2}{m^2_{\tilde{f}}}\right)\right]^2 \\ &= \Gamma\left(\tilde{\chi}_1^0 \to \gamma + \bar{\nu}_i\right)\,.\end{aligned} \tag{6.7}$$

In the above expression, λ is the relevant $L_iQ_j\bar{D}_j$ or $L_iL_j\bar{E}_j$ coupling, α is the (QED) fine-structure constant, while θ_W is the electroweak mixing angle. e_f, N_c and $m_f(m_{\tilde{f}})$ are the electric charge in units of e, color factor (3 for $LQ\bar{D}$, 1 for $LL\bar{E}$), and the mass, respectively, of the fermion (sfermion) inside the loop. We note that the above simple formula for the width neglects any mixings in the scalar sector. While this effect – depending on the supersymmetric parameters – may become significant, it introduces several undetermined SUSY-parameters in the expression. At the level of precision of our study, we find it convenient to work with this simplified approximation. The two decay widths in Eq. (6.7) are equal as a result of the Majorana nature of the neutralino. The logarithmic function in Eq. (6.7), $\log\frac{m_f^2}{m^2_{\tilde{f}}}$, changes only by about a factor of two if we vary $m_{\tilde{f}}$ between 1 TeV and 100 TeV. Therefore, in our numerical simulations, we will fix $m_{\tilde{f}}$ at 1 TeV for the log term, so that we can use $\lambda/m^2_{\tilde{f}}$ as a single combined parameter, without separating λ and $m_{\tilde{f}}$.

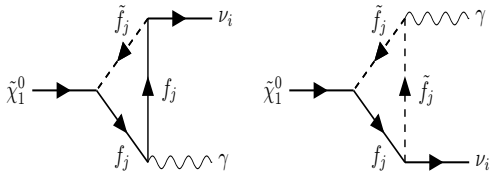

Figure 6.1: Feynman diagrams for the radiative neutralino decay.

Despite the loop-suppression, the radiative mode, Eq. (6.6), can be relevant for very light neutralinos. The partial width is proportional to $\left(m^3_{\tilde{\chi}_1^0} m_f^2\right)/m^4_{\tilde{f}}$, compared to $m^5_{\tilde{\chi}_1^0}/m^4_{\tilde{f}}$ for the tree-level three-body decay into fermions [47, 61, 452], and can thus be important for small masses. Depending on the generation indices of the dominant RPV coupling(s) and the neutralino mass, it might even be the only kinematically allowed mode. In this paper we focus on the scenario where the neutralino dominantly decays as in Eq. (6.6), as this channel has not been considered before in the context of long-lived light neutralino searches. We now present some benchmark scenarios for phenomenological studies.

6.3 Benchmark Scenarios

In order to study the phenomenology of a very light neutralino decaying only via the radiative mode, Eq. (6.6), we present some representative benchmark scenarios which we believe cover all relevant possibilities, and which we investigate in detail in the next section. We list the corresponding parameters in Table 6.1. In each case, we assume the listed couplings are the only non-negligible RPV couplings. The neutralino is produced through the rare decay of the meson M via the coupling $\lambda^{\rm P}_{ijk}$: $M \to \tilde{\chi}^0_1 + \ell\,(\nu)$ [73, 87, 318, 347], and then decays in one of the ways discussed in the previous section via the coupling $\lambda^{\rm D}_{ijj}$.[2] In the table, we also list the current best bounds on the couplings $\lambda^{\rm P}_{ijk}$ and $\lambda^{\rm D}_{ijj}$.

For benchmark **B1**, the neutralino is produced via the most abundant mesons at the LHC – pions – in association with muons (neutrinos). This occurs via the coupling $\lambda^{\rm P}_{ijk} = \lambda'_{211}$. The charged production mode ($\pi^\pm \to \tilde{\chi}^0_1 + \mu^\pm$) is only possible if the mass of the neutralino satisfies the bound,

$$m_{\tilde{\chi}^0_1} < m_{\pi^\pm} - m_{\mu^\pm} \approx 35\,\text{MeV}\,. \tag{6.8}$$

For neutralinos heavier than the above threshold, only the neutral production mode ($\pi^0 \to \tilde{\chi}^0_1 + \nu_\mu$) contributes; however, this mode is suppressed owing to the short lifetime of the neutral pion which translates into a low decay branching fraction into neutralinos. For the benchmark, we choose $m_{\tilde{\chi}^0_1} = 30\,\text{MeV}$; the lightness of the neutralino means that the radiative mode is the only kinematically allowed decay. In principle, with the coupling $\lambda^{\rm P}_{ijk} = \lambda'_{111}$ instead, a heavier neutralino can be produced in charged pion decays: $\pi^\pm \to \tilde{\chi}^0_1 + e^\pm$, but the severe bound, [252]

$$\lambda'_{111} \lesssim 0.001 \left(\frac{m_{\tilde{d}_R}}{1\,\text{TeV}}\right)^2\,, \tag{6.9}$$

implies this mode can not be probed at the experiments we consider here.

For the decay coupling, we choose $\lambda^{\rm D}_{ijj} = \lambda'_{333}$. The decay width, Eq. (6.7), is roughly proportional to m_f^2. Thus, the heavier the fermion in the loop, the shorter the lifetime of the neutralino. For the very light neutralino in **B1**, we require a heavy fermion in the loop to get testable scenarios at FASER; we expect maximum sensitivity to couplings λ'_{i33} or λ_{i33}.

For the benchmarks **B2** and **B3**, we choose the parameters such that the neutralinos are produced in kaon decays. This time, unlike the pion case, both the charged and neutral modes have comparable contributions. For **B2**, the neutralino decays only radiatively, as in Eq. (6.6). For **B3**, the decay coupling $\lambda^{\rm D} = \lambda_{322}$ also allows for tree-level leptonic decays:

$$\tilde{\chi}^0_1 \to \left(\nu_\tau \mu^\pm \mu^\mp,\, \tau^\pm \mu^\mp \nu_\mu\right) + \text{c.c.}\,. \tag{6.10}$$

However, these are kinematically blocked for $m_{\tilde{\chi}^0_1} \lesssim 2m_\mu$. Thus, we have chosen $m_{\tilde{\chi}^0_1} = 200\,\text{MeV}$. Later, when we present numerical results, we go beyond the strict parameters in the benchmark scenarios and consider plots in the RPV coupling vs. neutralino mass plane. One then has to account

[2] We note that, in this work, we are neglecting the effects of the suppressed three-body decay that can proceed at one-loop level via an off-shell Z, e.g., $\tilde{\chi}^0_1 \to 3\nu$. We thank Florian Domingo for a discussion on this topic.

Scenario	$\mathbf{m}_{\tilde{\chi}_1^0}$	Production $\left(\lambda^{\mathrm{P}}_{ijk}\right)$	Decay $\left(\lambda^{\mathrm{D}}_{ijj}\right)$	Current Constraints
B1	30 MeV	$\lambda'_{211}\left(M=\pi^{\pm},\pi^0\right)$	λ'_{333}	$\lambda'_{211}<0.59\left(\frac{m_{\tilde{d}_R}}{1\,\mathrm{TeV}}\right),\ \lambda'_{333}<1.04$
B2	75 MeV	$\lambda'_{212}\left(M=K^{\pm},K^0_{L/S}\right)$	λ'_{333}	$\lambda'_{212}<0.59\left(\frac{m_{\tilde{s}_R}}{1\,\mathrm{TeV}}\right),\ \lambda'_{333}<1.04$
B3	200 MeV	$\lambda'_{112}\left(M=K^{\pm},K^0_{L/S}\right)$	λ_{322}	$\lambda'_{112}<0.21\left(\frac{m_{\tilde{s}_R}}{1\,\mathrm{TeV}}\right),\ \lambda_{322}<0.7\left(\frac{m_{\tilde{\mu}_R}}{1\,\mathrm{TeV}}\right)$
B4	300 MeV	$\lambda'_{221}\left(M=D^{\pm},K^0_{L/S}\right)$	λ_{233}	$\lambda'_{221}<1.12,\ \lambda_{233}<0.7\left(\frac{m_{\tilde{\tau}_R}}{1\,\mathrm{TeV}}\right)$
B5	500 MeV	$\lambda'_{222}\left(M=D_S^{\pm}\right)$	λ'_{222}	$\lambda'_{222}<1.12$
B6	1 GeV	$\lambda'_{313}\left(M=B^{\pm},B^0\right)$	λ'_{333}	$\lambda'_{313}<1.12,\ \lambda'_{333}<1.04$

Table 6.1: Benchmark scenarios considered in this paper. The neutralino is produced through the rare decay of the meson M via the coupling $\lambda^{\mathrm{P}}_{ijk}$: $M\to\tilde{\chi}_1^0+\ell\,(\nu)$. The neutralino decay is as in Eq. (6.6) via the coupling $\lambda^{\mathrm{D}}_{ijj}$. The photon energy in the neutralino rest frame is $E_\gamma=m_{\tilde{\chi}_1^0}/2$, but can range from $O(0.1)$ to $O(1)$ TeV at FASER. In the furthest-to-the-right column, we list the current best bounds on the couplings, see for example, Ref. [252].

for the fact that additional decay modes can open. Note that in **B3**, we now select a decay coupling that is not third generation in the last two indices, since the neutralino is now heavy enough to avoid a too-small decay width, even for lighter fermions in the loop.

We have chosen benchmark **B4** such that a single coupling leads to production of the neutralinos from both kaons and $D^{\pm}$. Since kaons are more abundant at the LHC than D-mesons, the former production mode contributes more to the neutralino flux. For the selected mass of 300 MeV, there are no other relevant decay modes of the neutralino than the radiative one. But for the coupling vs. mass plot, the neutralino can decay into kaons above the relevant thresholds. The neutralino *production* through kaons is, of course, blocked for these heavier masses. In addition, for this scenario and the ones below, there can also be three-body decays into two mesons and a lepton, mediated via the $LQ\bar{D}$ operators; these can become relevant in the very high mass regime, $m_{\tilde{\chi}_1^0}\gtrsim O(1.5\,\mathrm{GeV})$. These are neglected for simplicity in the present work as their impact for sub-GeV neutralinos – which are the focus of our study – is minor. We will also neglect any Cabibbo-Kobayashi-Maskawa-mixing effects for similar reasons. More details on these effects can be found in Ref. [354].

Benchmark **B5** is a special case: It requires only a single non-zero RPV coupling (λ'_{222}) for both production (via $D_S^{\pm}$ mesons) and decay. This is absent in the tree-level neutralino decay case [87], except for an extremely small mass-window of around 4 MeV. For the given mass, $m_{\tilde{\chi}_1^0}=500\,\mathrm{MeV}$, the neutralino decays only radiatively. But at higher masses, it may decay into η,η', or ϕ.

Finally, we have chosen benchmark **B6** such that the neutralinos are produced via B-meson decays, thereby allowing the neutralino to be relatively heavy, leading to more energetic photons. The neutralino is produced in association with a $\tau^{\pm}\left(\nu_\tau\right)$ via the charged (neutral) mode; the two modes have comparable contributions. For $m_{\tilde{\chi}_1^0}>m_{B^{\pm}}-m_{\tau^{\pm}}$, only the neutral mode is kinematically allowed. The radiative mode is the only relevant decay channel.

We note in passing the interesting observation that the radiative decay of a neutralino gives us a method of producing significant ν_τ fluxes. These are suppressed in the SM. With FASERν [453, 454] under operation, this may give us an interesting opportunity to detect the neutralino by looking for ν_τ events. However, we leave an investigation in this direction for the future.

Before closing the section, we provide a plot in Fig. 6.2, showing the decay branching ratios of the

lightest neutralino into our signature, $\gamma + \overset{(-)}{\nu}$, as a function of the neutralino mass, for all the considered benchmark scenarios.

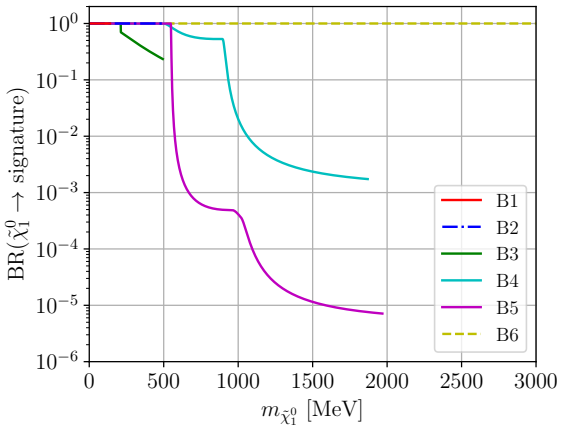

Figure 6.2: Branching ratios of the lightest neutralino into the single-photon signature, with varying neutralino mass.

6.4 FASER Experiment

The FASER experiment [85, 86] is a cylindrical detector that has recently been installed inside the TI12 tunnel, 480 m from the ATLAS IP along the beam collision axis line of sight. The detector is composed of tracking stations, scintillators, and a calorimeter. The cylinder axis is along the extended beam collision axis. Its decay volume has a radius of 10 cm and a length of 1.5 m. It is currently running during Run 3 of the LHC and is expected to collect data from proton-proton collisions of around 150 fb^{-1} integrated luminosity. At the front end of FASER, an additional emulsion detector known as FASERν [453, 454] has been installed, which is aimed at detecting high-energy neutrinos produced at the ATLAS IP. In this work, we do not study the potential of FASERν.

A follow-up experiment – FASER2 [86] – is currently slated to be operated during the HL-LHC period. If it is to be installed at the same position as FASER, it will be at a distance of 480 m from the ATLAS IP. Otherwise, it could be one of the experiments to be hosted at the FPF [439], 620 m from the ATLAS IP, also along the beam axis. We expect the difference between 480 m and 620 m distance to the IP to lead to only relatively minor changes in the sensitivity reach, as discussed in Ref. [439]. For this study, we work with the geometrical setup of a radius of 1 m and a length of 5 m for the FASER2 decay fiducial volume, and consider it 480 m away from the IP. By the end of Run 5 at the LHC, FASER2 should have collected about 3 ab^{-1} integrated luminosity of collision data. Similarly, an emulsion detector has been proposed to be installed at the front face of FASER2, known as FASERν2. We will assume the detector components of FASER2 and hence detection principles and efficiencies are similar to those of FASER, except for the different geometrical acceptances.

In Ref. [437], the authors studied axion-like particles (ALPs) at FASER, where the ALPs decay to *a pair* of photons. They estimated that the calorimeter spatial resolution should be sufficiently good for resolving the two photons with an efficiency of about 50%, and the background should be negligible for diphoton events. Here, our signature includes only *one* photon. To provide a discussion on the

expected background level, we follow the arguments given in Ref. [455]. At FASER, the single photons are detected as high-energy deposits in the electromagnetic calorimeter. Other objects may also cause such deposits, *e.g.*, neutrinos interacting deep inside the calorimeter via charged-current interactions. In order to differentiate the photon signal, a pre-shower station has been installed right before the calorimeter [456] which first converts the photon, thereby identifying it. Moreover, during Run 3 of the LHC program, the FASER detector is planned to be upgraded with a high-precision preshower detector. This would allow to distinguish two very closely spaced highly energetic photons [457]. Furthermore, neutrinos and muons coming from the IP can penetrate the 100 m of rock in front of FASER and reach the detector with energies in the TeV scale. These neutrinos could interact with the detector resulting in energetic particles including individual photons. However, these energetic photons are accompanied by tens of charged particles, allowing to veto such events easily with the tracker stations. The muons could radiate high-energy photons as well, mainly via Bremsstrahlung, but the veto stations positioned right in front of the FASER decay volume [456] should enable the rejection of muon-associated events.[3] Finally, neutral pions produced in hadronic showers initiated by muons in the absorber-rock material could also constitute a background for our signal if the two photons produced in their decays cannot be spatially resolved or only one of them is observed.[4] In such a case, requiring an energy threshold for the signal may help since the photons from our signal are expected to be more energetic; see Ref. [455] for more details on the point of using energy thresholds. A detailed estimate, however, requires a full simulation of hadronic interactions inside the rock. In this work, we will assume zero background for our signal.

Since the search proposed here with the single-photon signature does not require the usage of the tracker, in principle the tracker volume could be considered as effectively part of the fiducial volume. Taking this into account would allow to enlarge the length of the fiducial volume of FASER and FASER2 by roughly 1 m [456] and 5 m [439], respectively, enhancing the sensitivity reach to some extent. In this work, we only comment on this possibility and choose to stay with the standard benchmark geometries, as given explicitly above.

There are several other past and ongoing experiments that should have sensitivity to a radiatively decaying light neutralino. These include beam-dump experiments such as LSND [458], E613 [459], MiniBooNE [460], E137 [461], and NA64 [462–464], as well as B-factory experiments such as BaBar [465] and Belle II [412, 413]. Typically, each of these experiments is optimized to primarily produce only a certain type of meson, at rates which could be higher than the LHC. Correspondingly, they can probe a subset of the RPV models we have presented here in a somewhat cleaner environment. The LHC has the advantage of producing all types of mesons at significant rates, thus providing a scenario-independent probe. However, given a signal, it could be difficult to disentangle the underlying model(s). Further, given the different center-of-mass energies (and hence the spectra of the produced neutralinos), and the detector layouts, the phase-space region probed by these other experiments may complement that probed by FASER. However, detailed simulations are required to make more precise statements; this is beyond the scope of the present work.

Further, limits coming from searches for heavy neutral leptons can also be relevant for us. We will include these in our plots in Section 6.6.

[3] One possible background that we neglect here could come from off-axis muons that can penetrate FASER without passing through the veto stations; estimating such a background would require a detailed simulation. We thank Max Fieg for bringing up this point.

[4] We thank Michael Albrow for bringing this to our attention.

Detector	$\mathcal{L}$	$\sqrt{s}$	L	Δ	R
FASER	$150\,\text{fb}^{-1}$	14 TeV	480 m	1.5 m	10 cm
FASER2	$3\,000\,\text{fb}^{-1}$	14 TeV	480 m	5 m	1 m

Table 6.2: Integrated luminosities and geometries of the detectors used in the simulations. Here, $\mathcal{L}$, $\sqrt{s}$, **L**, Δ, and **R** label, respectively, the integrated luminosity, the collider center-of-mass energy, the distance from the IP, the detector length, and the detector radius.

Finally, we note that our signature could also be probed by FACET – a proposed new subsystem of the CMS experiment. In this study, however, we only focus on FASER and FASER2.

6.5 Simulation

We now proceed to describe the simulation procedure for estimating the number of signal events in the two experiments. We use the package FORESEE [466] to obtain the neutralino spectrum in the far-forward region, relevant for FASER and FASER2. As mentioned, the dominant sources of the neutralinos are the rare decays of mesons produced at the ATLAS IP:

$$M \to \tilde{\chi}_1^0 + \ell\,(\nu)\ . \tag{6.11}$$

Direct pair-production of neutralinos, in comparison, is expected to be several orders of magnitude lower [87, 89, 318], and is hence neglected here. We include all possible production modes for the different benchmark scenarios, summing over all meson contributions, to estimate the total number of produced neutralinos over the runtime of the experiment. However, it is necessary but not sufficient for the mother meson to decay into a neutralino: The meson itself may be long-lived, *e.g.*, charged pions and kaons. Thus, we require the meson to decay before hitting any absorber material or leaving the beam pipe; otherwise, the meson could be stopped and the neutralino is no longer boosted in the direction of FASER. Keeping this in mind, we use FORESEE to determine the neutralino production rate and spectrum from the meson spectrum by specifying the decay branching ratios corresponding to Eq. (6.11). The generated spectrum is two-dimensional, in terms of angle and momentum.

We also use FORESEE to compute the probability for the neutralino to decay inside the detector volume. See Table 6.2 for the values corresponding to the detector position and geometry we employ in our simulation for FASER and FASER2. We take into account the full neutralino lifetime, $\tau_{\tilde{\chi}_1^0}$, as well as its kinematics. The former is computed using all possible decay channels of the neutralino (including the decay into pseudoscalar and vector mesons) as a function of its mass and the non-vanishing RPV couplings, *cf.* the discussion in Section 6.3. However, in the numerical results presented in the next section, we have chosen an explicit signal for detecting the neutralino decay. Although all neutralino decays inside the detector are technically visible, we estimate the signal strength based on the specific radiative mode alone. This is done to avoid the consideration of background events; the decay into a neutrino and a photon gives a clean and unique signature.

Given the neutralino spectra, we estimate the number of decays that occur inside the detector defined by its position and geometry. For the analysis, the simulation takes into account the distance L between the ATLAS IP and the FASER detector, and the acceptance rate $P[\tilde{\chi}_1^0]$ in terms of the

neutralino's three-momentum, its position of production (accounting for the mesons' lifetimes), as well as the lifetime of the neutralino itself. In our simulation, we do not make any momentum cuts. By further specifying the branching ratio into the radiative mode, the simulation counts the number of signal events passing the selection criteria. Thus, we can finally estimate the number of single-photon neutralino decay observations,

$$N^{\text{obs}}_{\tilde{\chi}^0_1} = P[\tilde{\chi}^0_1] \cdot \text{BR}\left[\tilde{\chi}^0_1 \to \left(\gamma + \nu_i\,, \gamma + \bar{\nu}_i\right)\right] \cdot \sum_{\text{mesons}} N^{\text{prod}}_{\tilde{\chi}^0_1}\,. \tag{6.12}$$

We stress again that we assume zero background, *cf.* the discussion in Section 6.4. Further, we assume a detector efficiency of 100%.

6.6 Numerical Results

We now present our numerical results. For the sensitivity limits, we require the observation of 3 radiative decays of the lightest neutralino in the detector for an integrated luminosity at the LHC of $150\,\text{fb}^{-1}$ for FASER, and $3\,000\,\text{fb}^{-1}$ for FASER2. This corresponds to a potential 95 % confidence-level exclusion limit under the assumption of vanishing background.

We first show, in Fig. 6.3, results for the benchmark scenario **B1** of Table 6.1. On the left, we plot the sensitivity in the $\lambda^{\text{P}}/m^2_{\text{SUSY}} = \lambda'_{211}/m^2_{\text{SUSY}}$ versus $\lambda^{\text{D}}/m^2_{\text{SUSY}} = \lambda'_{333}/m^2_{\text{SUSY}}$ plane for a fixed neutralino mass of 30 MeV. In gray we include the low-energy bounds given in Table 6.1, for fixed sfermion masses of 1 TeV (the same choice is taken for the other model-dependent plots in this section). We see that FASER has no new sensitivity for this scenario beyond the low-energy bounds, whereas FASER2 can extend the reach by more than an order of magnitude in $\lambda^{\text{P}}/m^2_{\text{SUSY}}$ or $\lambda^{\text{D}}/m^2_{\text{SUSY}}$ in units of GeV^{-2}. The right plot in Fig. 6.3 is model-independent, in that it is valid for any new, neutral long-lived particle (LLP) produced in charged pion decays, which decays with a signature at FASER or FASER2, here specifically with a mass of 10 or 30 MeV. The maximum sensitivity (the minima of the curves) depends on the location of the detector, and also on the momentum distribution of the produced pions and, correspondingly, of the pions' decay product neutralinos [90]. That is why the minimum of the curve shifts to slightly smaller LLP lifetimes for lighter LLP masses, which are more boosted. We see that FASER (FASER2) can probe the product of the decay branching fractions of the charged pion into an LLP and a muon and the LLP into the signature, down to a few times 10^{-9} $\left(10^{-12}\right)$. We note that existing searches for heavy neutral leptons (HNLs), N, which mix with active neutrinos and are produced from pion decays, may be recast into bounds on the right plot. The leading bounds for HNLs of mass 10 MeV and 30 MeV in $\pi^\pm \to \mu^\pm + N$ decays stem from two peak searches: Ref. [377], and Ref. [397], respectively. The former shows a bound of 10^{-5} on $\text{BR}(\pi^\pm \to \mu^\pm + N)$ for mass 10 MeV. Ref. [397] presents 90% confidence-level exclusion limits in the mixing-squared vs. mass plane; we convert these into limits on $\text{BR}(\pi^\pm \to \mu^\pm + N)$ [409], obtaining a bound of 6.9×10^{-6} for mass 30 MeV. These two bounds are model-independent and are plotted as shaded areas in the right plot of Fig. 6.3, using $\text{BR}(\tilde{\chi}^0_1 \to \text{signature}) = 1$. One easily observes that FASER and FASER2 are sensitive to large parts of the parameter space beyond these existing bounds.

Fig. 6.4 shows the sensitivity reach of FASER2 for the benchmark scenario **B1** of Table 6.1, but allowing the neutralino mass to vary and fixing $\lambda^P = \lambda^D$. The gray band, as before, indicates the low-energy constraints on the couplings. Since FASER does not provide any new sensitivity reach

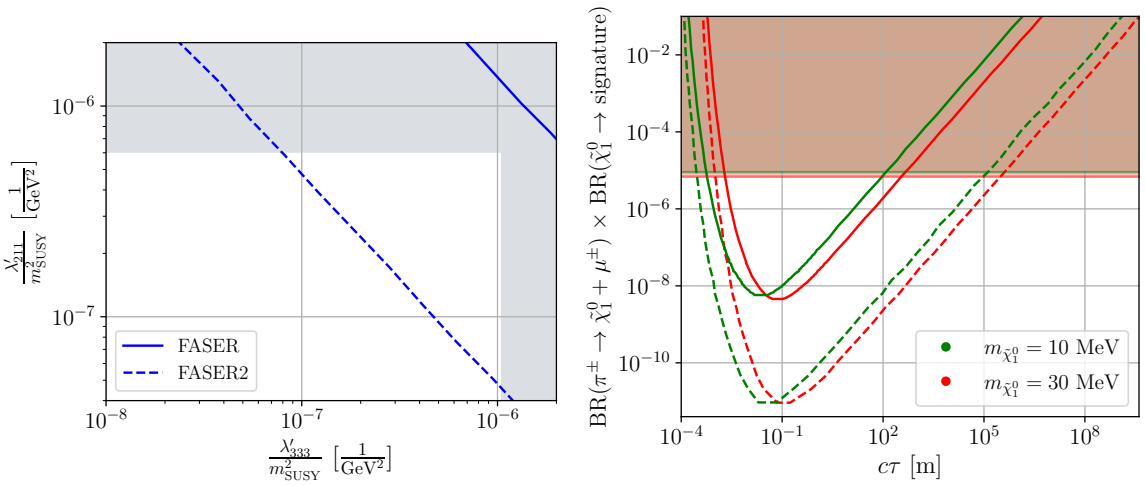

Figure 6.3: Sensitivity reach for FASER (solid lines) and FASER2 (dashed lines) for the benchmark scenario **B1**, *cf.* Table 6.1. The left plot shows the sensitivity reach in the production coupling ($\frac{\lambda'^2_{211}}{m^2_{\text{SUSY}}}$) vs. decay coupling ($\frac{\lambda'^2_{333}}{m^2_{\text{SUSY}}}$) plane, for a neutralino mass of 30 MeV. The gray areas are excluded by the low-energy bounds, also given in Table 6.1. The right plot shows the sensitivity reach in $\text{BR}(\pi^\pm \to \tilde{\chi}_1^0 + \mu^\pm) \times \text{BR}(\tilde{\chi}_1^0 \to \text{signature})$ as a function of the neutralino decay length, $c\tau$, for $m_{\tilde{\chi}_1^0} = 10$ and 30 MeV. The shaded regions correspond to existing constraints from HNL searches.

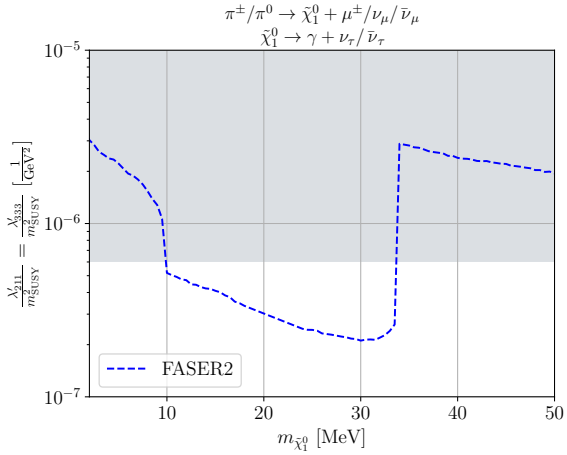

Figure 6.4: Sensitivity reach in the neutralino mass-coupling plane for FASER2 for the same physics scenario as in **B1** but with variable neutralino mass. The production ($\frac{\lambda'^2_{211}}{m^2_{\text{SUSY}}}$) and decay ($\frac{\lambda'^2_{333}}{m^2_{\text{SUSY}}}$) couplings have been set equal. The gray areas are excluded by the low-energy bounds.

beyond these low-energy bounds, we do not depict it in the plot. We see a maximum sensitivity is reached for neutralino masses between 10 and 35 MeV. In general, the sensitivity reach in the couplings improves; for instance, as we increase the neutralino mass up to 30 MeV, and again in the region beyond 35 MeV. Heavier neutralinos translate into shorter lifetimes, and hence more decays of the neutralino within the volume of FASER2, *cf.* Eq. (6.7). There is, however, a sharp drop in sensitivity

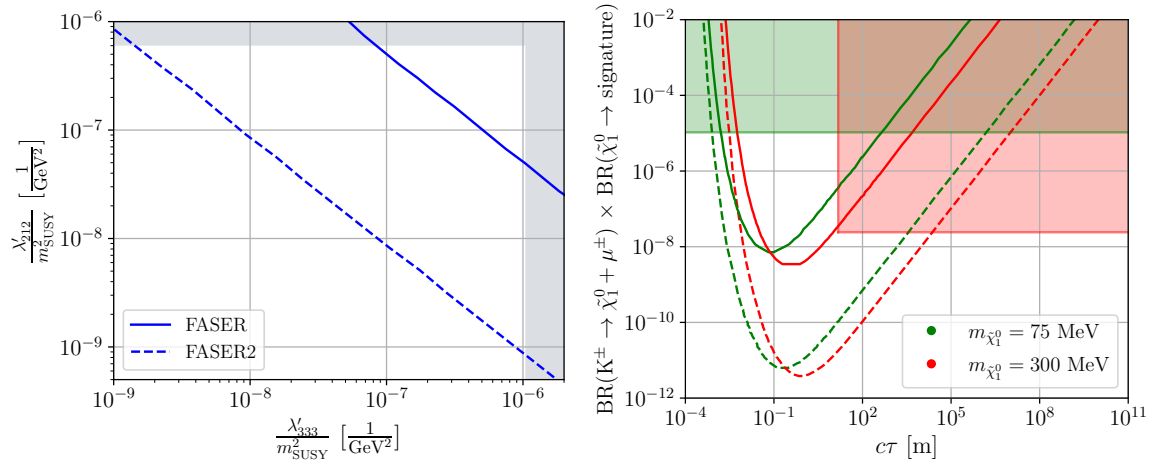

Figure 6.5: As in Fig. 6.3 but for the benchmark scenario **B2** with $m_{\tilde{\chi}_1^0} = 75\,\text{MeV}$, *cf.* Table 6.1. The right plot shows the sensitivity reach in BR($K^\pm \to \tilde{\chi}_1^0 + \mu^\pm$)×BR($\tilde{\chi}_1^0 \to$ signature) as a function of the neutralino decay length, $c\tau$, for $m_{\tilde{\chi}_1^0} = 75$ and 300 MeV.

near the neutralino mass, $m_{\tilde{\chi}_1^0} \sim 34\,\text{MeV}$. This is the threshold for the decay of charged pions to neutralinos accompanied by a muon. The branching fraction of the neutral pion mode, $\pi^0 \to \tilde{\chi}_1^0 + \nu_\mu$, is suppressed by the short lifetime.

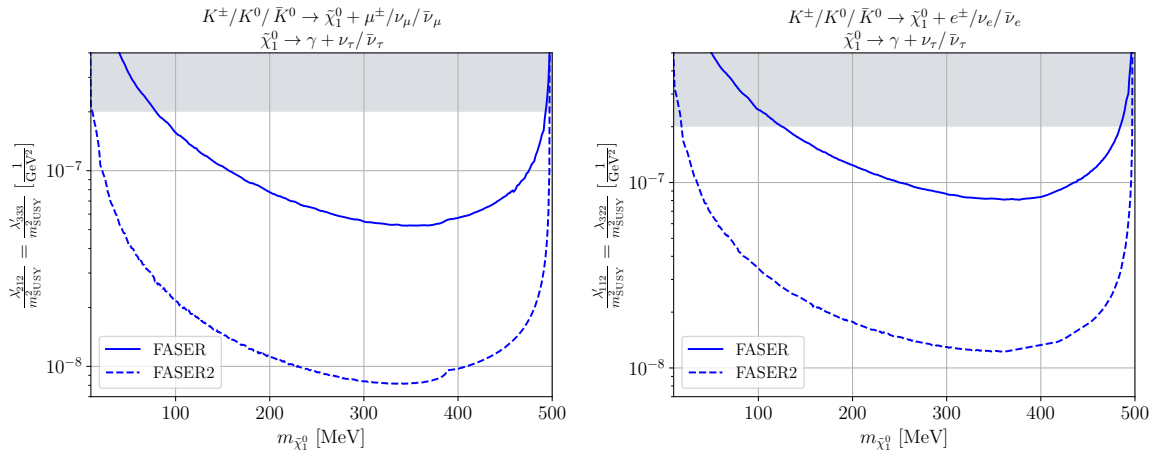

Figure 6.6: As in Fig. 6.4 but for the benchmark scenarios **B2** (left) and **B3** (right). The sensitivity reach corresponds to `FASER` (solid line) and `FASER2` (dashed line).

In Figs. 6.5 and 6.6 (left), we display the sensitivity plots for benchmark scenario **B2**. The left plot of Fig. 6.5 shows that now both `FASER` and `FASER2` have significant new reach in the couplings, λ^{P} and λ^{D}, for $m_{\tilde{\chi}_1^0} = 75\,\text{MeV}$. The right plot in Fig. 6.5 looks similar to the right plot of Fig. 6.3, but it is now a plot of the branching ratio product BR($K^\pm \to \tilde{\chi}_1^0 + \mu^\pm$)×BR($\tilde{\chi}_1^0 \to$ signature) versus the neutralino decay length, $c\tau$, and we have considered heavier LLP masses: 75 and 300 MeV. Similar to **B1**, we overlap these results with existing bounds from searches for HNLs from kaon two-body decays,

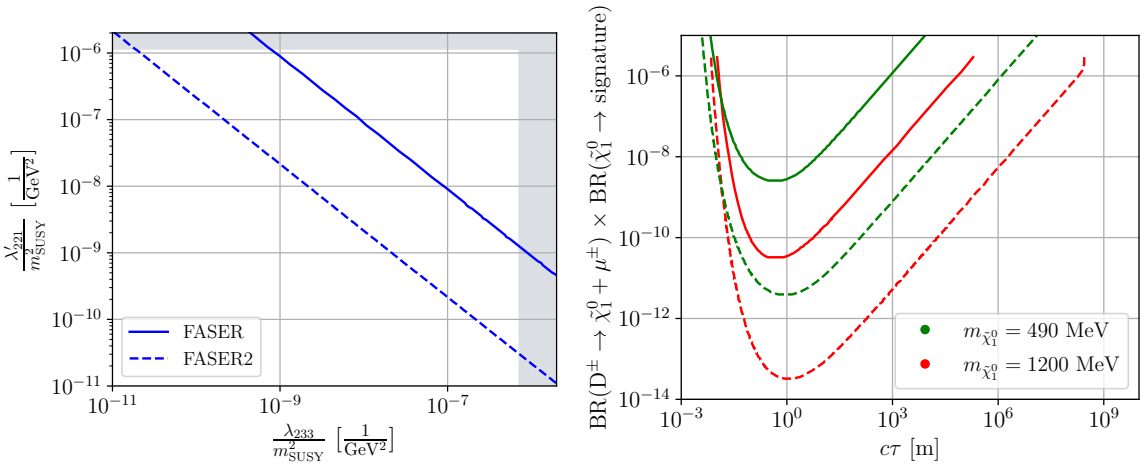

Figure 6.7: As in Fig. 6.3 but for the benchmark scenario **B4** with $m_{\tilde{\chi}^0_1} = 300\,\text{MeV}$, *cf.* Table 6.1. The right plot shows the sensitivity reach in $\text{BR}(D^\pm \to \tilde{\chi}^0_1 + \mu^\pm) \times \text{BR}(\tilde{\chi}^0_1 \to \text{signature})$ as a function of the neutralino decay length, $c\tau$, for $m_{\tilde{\chi}^0_1} = 490$ and $1\,200\,\text{MeV}$.

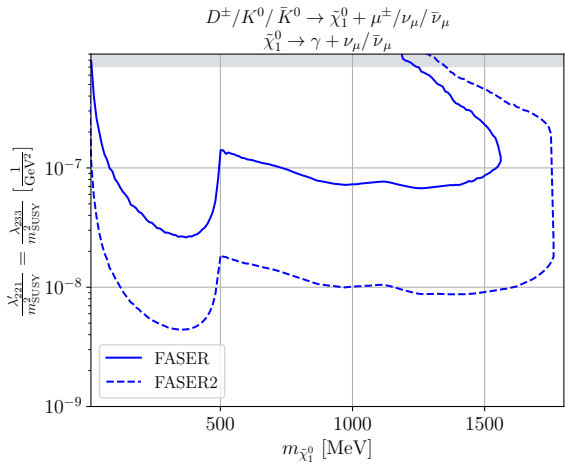

Figure 6.8: As in Fig. 6.4 but for the benchmark scenario in **B4** while varying the neutralino mass. The sensitivity reach corresponds to FASER (solid line) and FASER2 (dashed line).

$K^\pm \to \mu^\pm + N$. Refs. [379, 467] give the strongest current limits for HNL masses of 75 MeV and 300 MeV. Ref. [467] is a peak search and bounds the HNL mixing-squared with the muon neutrino at 1.3×10^{-5} for HNL mass of 75 MeV. Ref. [379] searches for invisible particles and places a limit of 10^{-8} on the mixing-squared. We convert these limits into bounds on $\text{BR}(K^\pm \to \mu^\pm + N)$ and obtain 10^{-5} and 2.4×10^{-8}, respectively. We depict these bounds in the right plot of Fig. 6.5, using $\text{BR}(\tilde{\chi}^0_1 \to \text{signature}) = 1$. In particular, since Ref. [379] is a missing-energy search, the limits are valid only for proper decay length larger than 15 m, as explicitly mentioned in the abstract of the paper. We find that FASER and FASER2 can probe the BR-product down to values significantly lower than these current limits.

In the neutralino mass-couping plane plot of Fig. 6.6 (left), we observe that the sensitivity at FASER2 is reduced for lower masses compared to that in benchmark scenario **B1**, but, unlike the pion case, is robust over the entire higher-mass regime, right up to the kaon mass. This is because even though the charged decay production mode is kinematically forbidden beyond $m_{\tilde{\chi}_1^0} = m_{K^\pm} - m_{\mu^\pm} \approx 390\,\text{MeV}$ – leading to the small bump in the plot at that point – the neutral decay mode has a comparable branching fraction.

The two plots of $\lambda^{\text{P}}/m^2_{\text{SUSY}}$ vs. $\lambda^{\text{D}} m^2_{\text{SUSY}}$ and branching ratio product vs. $c\tau$ for **B3** with neutralino mass of 200 MeV, are very similar to Fig. 6.5 for **B2** and are hence not shown explicitly here. In Fig. 6.6 (right), we present the sensitivity plot for scenario **B3** for $\lambda'_{112} = \lambda^{\text{P}} = \lambda^{\text{D}} = \lambda_{322}$, as a function of the neutralino mass. We note that for $m_{\tilde{\chi}_1^0} \gtrsim 2m_\mu$, the decay mode $\tilde{\chi}_1^0 \to \mu^\pm \mu^\mp \nu_\tau + \text{c.c.}$ opens up, leading to additional visible events. These are not included in Fig. 6.6 (right).

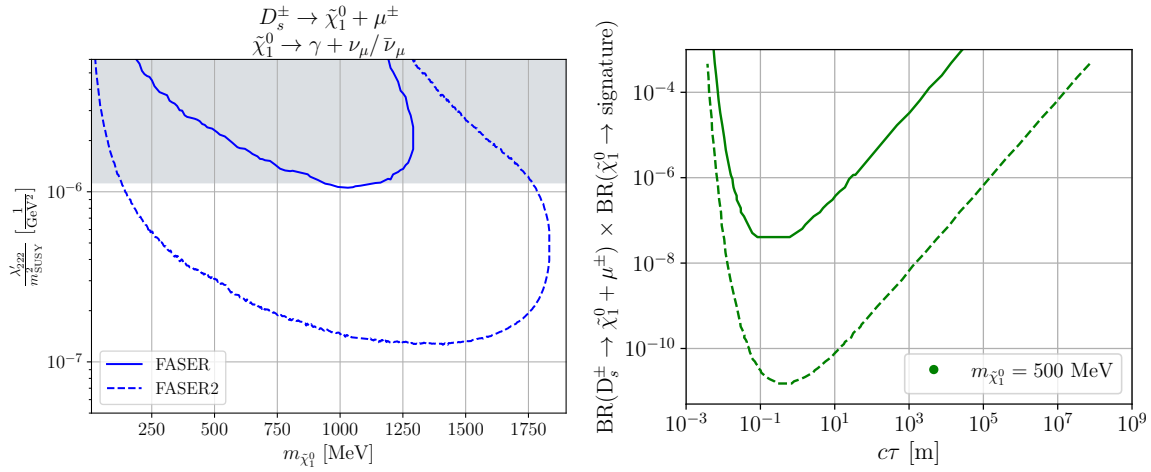

Figure 6.9: The left plot is as in Fig. 6.4 but for the single coupling benchmark scenario in **B5** while varying the neutralino mass. The right plot shows the sensitivity reach in $\text{BR}(D_S^\pm \to \tilde{\chi}_1^0 + \mu^\pm) \times \text{BR}(\tilde{\chi}_1^0 \to \text{signature})$ as a function of the neutralino decay length, $c\tau$, for $m_{\tilde{\chi}_1^0} = 500\,\text{MeV}$. The sensitivity reaches correspond to FASER (solid line) and FASER2 (dashed line).

In Figs. 6.7 and 6.8, we show the corresponding plots for the benchmark involving both D and K mesons – scenario **B4**. One interesting feature in the mass-coupling plane is the kink in the sensitivity curve near the kaon mass, $m_{K^0} \sim 497\,\text{MeV}$. This is because for $m_{\tilde{\chi}_1^0} \gtrsim m_{K^0}$, the kaon production mode, $K^0/\bar{K}^0 \to \tilde{\chi}_1^0 + \nu_\mu/\bar{\nu}_\mu$ switches off. Since kaons are more abundant than D mesons at the LHC, this leads to reduced senstivity beyond this threshold. For larger masses, the neutralino has decay modes into K^0 and K^{*0} plus neutrino opening up at the respective mass thresholds; as before, we only count the photon events as signal. There is an additional interesting feature for this scenario: The sensitivity curve starts to 'turn back' in the large coupling, large mass region indicating a drop in sensitivity. This happens as the lifetime of the neutralino becomes too short, decaying well before reaching FASER or FASER2; this effect is made more acute by the additional decay modes that open up. To our knowledge, there are no existing searches for HNLs in $D^\pm \to \mu^\pm + N$ decays; therefore, we do not place any existing bounds in the right plot of Fig. 6.7.

Fig. 6.9 shows the sensitivity reach for scenario **B5**, where only one RPV coupling is switched on (thus, there is no coupling-coupling plane plot). The left plot shows the sensitivity reach of FASER and

FASER2 in the mass-coupling plane. Once again, for the plots, we do not consider the additional decay modes into η, η' or ϕ plus neutrino that open up at the respective mass thresholds, for our signature. The large mass, large coupling regime has reduced sensitivity for the same reason stated above. The right plot then contains the sensitivities of FASER and FASER2 to the decay branching fraction product as a function of $c\tau$ for $m_{\tilde{\chi}_1^0} = 500\,\text{MeV}$. For this plot, as in **B4**, there is no existing limit that can be obtained from an HNL search in $D_s^\pm \to \mu^\pm + N$ decays.

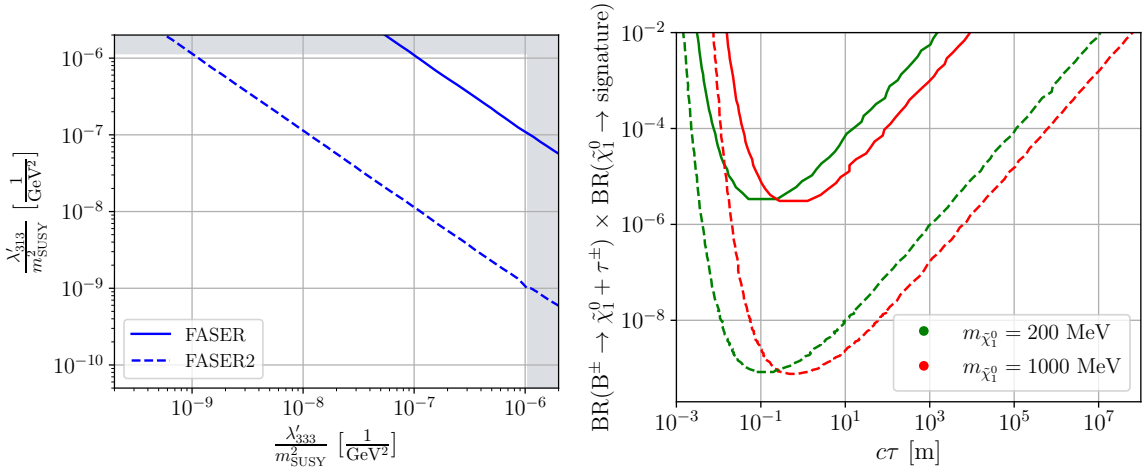

Figure 6.10: As in Fig. 6.3 but for the benchmark scenario **B6** with $m_{\tilde{\chi}_1^0} = 1\,\text{GeV}$, *cf.* Table 6.1. The right plot shows the sensitivity reach in $\text{BR}(B^\pm \to \tilde{\chi}_1^0 + \tau^\pm) \times \text{BR}(\tilde{\chi}_1^0 \to \text{signature})$ as a function of the neutralino decay length, $c\tau$, for $m_{\tilde{\chi}_1^0} = 200$ and $1\,000\,\text{MeV}$.

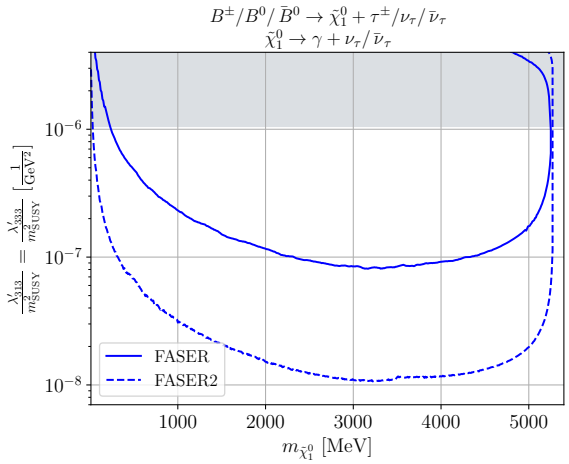

Figure 6.11: As in Fig. 6.4 but for the benchmark scenario in **B6** while varying the neutralino mass. The sensitivity reach corresponds to FASER (solid line) and FASER2 (dashed line).

Finally, Figs. 6.10 and 6.11 contain the sensitivity plots for benchmark scenario **B6**, involving B mesons. We observe in the right plot of Fig. 6.10, that the reaches in the branching ratio product

are weaker than those in the previous scenarios, because the production rates of the B mesons are orders-of-magnitude smaller than those of the lighter mesons at the LHC. As in the previous two benchmark scenarios, we do not find an existing search for HNLs in $B^{\pm} \to \tau^{\pm} + N$ decays that could be recast into bounds relevant to us, in the BR-product vs. $c\tau$ plane. In Fig. 6.11, as before, we see that the sensitivity in the mass-coupling plane is robust across the kinematically allowed mass range since the neutral mode is available even when the charged mode is switched off for $m_{\tilde{\chi}_1^0} \geq m_{K^{\pm}} - m_{\tau^{\pm}}$. This time the drop in sensitivity in the large mass, large coupling region is milder compared to the previous two cases as there are no additional decay modes contributing.

6.7 Conclusions

We have estimated the sensitivity reach of FASER and FASER2 at the LHC, for a sub-GeV bino-like lightest neutralino decaying to a photon in the context of R-parity-violating supersymmetry. With R-parity broken, the lightest neutralino can be lighter than the GeV scale, or even massless, without violating observational and experimental bounds, as long as it decays. Assuming the lightest neutralino is the lightest supersymmetric particle (LSP), it can be produced from rare meson decays, and can decay to a photon and a neutrino, via certain RPV couplings.

In the sub-GeV mass range, since the RPV couplings are required to be small by existing constraints, the bino-like neutralino is expected to have a long lifetime. Once produced from mesons' decays at the LHC, it is highly boosted in the very forward direction. Therefore, we have chosen to focus on the experimental setups of FASER and FASER2 for observing the single-photon signature resulting inside the detector decay volumes.

We have considered several theoretical benchmark scenarios and performed Monte Carlo simulations in order to determine the projected sensitivity reaches at FASER and FASER2. Our study has found that these experiments are sensitive to parameter space beyond the current bounds by orders of magnitude.

7
Summary and Outlook

Despite its tremendous success at describing Nature through an elegant theoretical framework based on symmetries, the Standard Model (SM) has serious shortcomings. Some of the most important ones are its inability to explain the origin of neutrino masses, gravity, the nature of dark matter and dark energy, the matter-antimatter asymmetry, etc. Various theoretical and experimental hints, mentioned in Chapter 1, also point towards the need for physics beyond the SM.

One of the most promising candidates for such new physics is provided by Supersymmetry (SUSY). Based on the same symmetry principle that has worked so well for the SM, the SUSY framework identifies a unique extension of the SM symmetries enabling it to address several of the above concerns. However, extensive experimental searches over the last few years, particularly at the Large Hadron Collider (LHC), have not found any hints for SUSY yet.

This brings us to the central question that has motivated this thesis: *is the stacking experimental evidence already compelling enough to rule SUSY out at energies accessible to us, or can it still have a lifeline?*

We have argued for the latter view here. In particular, we have stressed that the minimal SUSY setup automatically includes lepton- and baryon-number violating terms in the Lagrangian. Given the strict observational bounds on such interactions, an additional symmetry called R-parity is imposed in the Minimal Supersymmetric Standard Model (MSSM) – the SUSY framework that traditionally received the most amount of attention in the early literature. However, as we have argued, this strict restriction is not necessary: all experimental bounds can still be satisfied without dismissing R-parity violating (RPV) terms altogether, *e.g.*, through alternative choice of discrete symmetry. Further, theoretical considerations also do not strongly favor either the MSSM, or its RPV counterpart, the RPV-MSSM. The MSSM does provide us with a more favorable dark matter candidate, but, on the other hand, the RPV-MSSM has ingredients to describe neutrino masses and the baryon asymmetry.

Most pertinent to us, RPV-SUSY models can have signatures that are significantly different from the MSSM. While, recently, RPV frameworks have received increasing attention, as we have discussed in Chapter 1, the space of predictions is vast and very diverse, depending on many parameters that are unknown. Thus, more work is needed to systematically explore the entire phenomenological landscape, as there may still be unexplored opportunities. In this thesis, we have identified and focused on four such opportunities to probe SUSY. We now summarize our findings and provide some outlook in the context of each.

7.1 Traversing the Landscape

Allowing for RPV couplings in our model can drastically change the phenomenology that is expected at our colliders, such as the Large Hadron Collider (LHC). As we discussed in Chapter 1, one of

the main implications is that the lightest supersymmetric particle (LSP) is no longer guaranteed to be stable. Hence, unlike in the MSSM, it is no longer restricted to be electrically uncharged and uncolored, and can, in general, be any of the supersymmetric particles (sparticles). Thus, instead of the missing transverse energy, E_T^{miss}, signature that is typical of RPC scenarios, one needs to consider a whole host of possibilities, depending on the type of RPV coupling, its magnitude, as well as the model spectrum. While some studies in the literature have classified the expected signatures in specific RPV scenarios, there has been no model-independent treatment analyzing the coverage of the most general RPV-MSSM setup so far. Such a study is crucial (i) to understand the extent to which our searches exclude the RPV-MSSM model space, and, more importantly, (ii) to check for any gaps in our coverage.

In Part I, we addressed the above in the context of small RPV couplings. By developing a new system of classification, we analyzed all final state topologies that can arise in the most general RPV-MSSM framework, relying on minimal assumptions about the model details. We found that these can be organized into a minimal set of just 17 signatures: 6 corresponding to $LL\bar{E}$ operators, 6 to $LQ\bar{D}$ ones, and 5 to $\bar{U}\bar{D}\bar{D}$ ones. Together, this minimal set provides complete coverage to the RPV-MSSM, independent of mass spectrum details.

Using our framework, we then gauged the coverage of the above signatures through our existing searches at ATLAS and CMS. We found that all signatures have been covered, at least at the level of topologies. However, we do stress that strong experimental improvements are needed for some final states (corresponding to $LQ\bar{D}$ and $\bar{U}\bar{D}\bar{D}$ operators) in order to probe the electroweak production cross-sections.

Lastly, we ran numerical simulations to derive exclusion limits on the RPV-MSSM for scenarios involving $LL\bar{E}$ operators, by reinterpreting the existing searches. We found bounds on the sparticle spectrum are stronger than or comparable to the bounds in the MSSM. Apart from demonstrating application of our framework, these results provide explicit exclusion limits on RPV-MSSM scenarios in a (largely) model-independent way, for the first time in the literature.

Our results from Part I represent one step towards a model-independent treatment of the RPV-MSSM collider phenomenology. In particular, an analogous systematic classification of signatures for the case of large RPV couplings is also desired. Further, a reinterpretation of the existing searches for scenarios with $LQ\bar{D}$ and $\bar{U}\bar{D}\bar{D}$ operators would be especially interesting, given the point we made above regarding the need for experimental improvements in these contexts.

7.2 The Future is Bright

With the upcoming High-Luminosity LHC (HL-LHC) upgrade, there is merit to exploring possibilities that, although suppressed, can offer us new interesting mechanisms to probe physics. As described in Chapter 1, one such opportunity, in the context of the RPV-MSSM, is provided by the leptonic content of the proton. The lepton parton distribution functions (PDFs), although tiny, can initiate resonant squark production via $LQ\bar{D}$ operators at the LHC. Such a channel benefits greatly from the kinematic advantage of having to produce just a single heavy squark, as well as the dynamic boost from resonance. Further, as we have discussed, it can have a very clean signature, largely free from SM background, consisting of a single charged lepton, no E_T^{miss}, and either one or a few jets in the final state. We call this the "single-lepton channel". Such a signature has not been searched for at the LHC, yet.

In Part II of this thesis, we explored the ability of the single-lepton channel to probe kinematically accessible squarks in the RPV-MSSM. We demonstrated that by combining two new signal regions – consisting of (i) 1 first or second generation charged lepton, exactly 1 jet and no/low E_T^{miss}, and (ii) 1 first or second generation charged lepton, at least 3 jets, and no/low E_T^{miss} – the single-lepton channel gives us sensitivity to large parts of the RPV-MSSM parameter space. We further demonstrated that such a strategy is largely independent from the mass-spectrum details, giving us sensitivity to both cascade as well as direct decays of the resonantly produced squarks.

In order to make the above more explicit, we ran numerical simulations and computed sensitivity limits on the RPV coupling vs squark mass plane. The obtained limits cover vast regions of parameter space allowed by existing constraints coming from pair production and Drell-Yan, and even outperform the stringent low-energy bounds coming from charged universality constraints.

Our results show that the single-lepton channel can be a promising signature that should be implemented at the LHC. Dedicated studies are also needed to extend the strategy for the case involving third generation leptons and/or jets (and squarks).

7.3 ν Physics

The lepton- and baryon-number violating couplings of the RPV-MSSM can also have interesting implications for low-energy physics. This provides us with another probe for SUSY, complementary to the high-energy analyses at colliders such as the LHC. For instance, as noted in Chapter 1, these interactions can generate neutrino masses, and allow for the possibility of proton decay. In this thesis, we have focused on the former. A study of the latter is currently being completed.

Neutrino-mass generation in the RPV-MSSM context has been studied extensively in the literature. However, it is difficult to analyze the implications of the neutrino oscillation data in the most general setup. This is because the theory prediction for the neutrino-mass matrix gets contributions from a large number of diagrams, and depends on several unknown RPV couplings and SUSY mass scales. Thus, all phenomenological studies in the literature, so far, have only analyzed simplified setups where only a few RPV couplings can contribute.

In Part III of this thesis, we developed a new approach to tackle the above problem. We analyzed the contributions to the neutrino-mass matrix in the most general RPV-MSSM setup, and found that, under reasonable assumptions, all of them (to one-loop order) can be reduced to just two types of structures. For the case of two massive neutrinos, by appealing to minimality, we were able to identify just four classes of models that can satisfy the neutrino data. We refer to such models as "Minimal Oscillation Models (MOMs)". We then explored the general features of each MOM class in detail, qualitatively and quantitatively. We presented analytical expressions for the corresponding solution spaces. Further, we presented numerical solutions corresponding to the current neutrino oscillation data for each class.

Our results can be used directly for all RPV models that satisfy the MOM criteria. Through several explicit examples, we demonstrated that this holds for a large class of RPV scenarios. Thus, MOMs provide a simple but powerful way to interpret neutrino data in the RPV context: by analyzing just four classes, one can gain insight into a large class of RPV-MSSM models.

However, we note that the MOM framework still does not represent the most general RPV-MSSM setup. To cover the latter, the framework needs to be extended by dropping the minimality criterion. Further, one can also extend the framework to analyze the case of three massive neutrinos. In both

the above extensions, there are two complications: (i) the number of classes to be analyzed is much larger, and (ii) there are far more undetermined parameters than constraints coming from the neutrino data; thus, further considerations are required to have predictivity. Even so, the approach retains the advantage of having simple structures that can be solved once to gain insight into the whole space of models, in a unified way.

7.4 Let There $\tilde{B}$ Light

The RPV-MSSM also allows for the exciting possibility that SUSY already lies at very low energies. Indeed, as we mentioned in Chapter 1, the mass of the lightest neutralino in the RPV-MSSM is unconstrained by all experimental data, if it is bino-like. This opens up several new opportunities to look for SUSY. In particular, as discussed in Chapter 1, if the neutralino is lighter than $O(5\,\text{GeV})$, it may be produced in R-parity violating decays of mesons and leptons – which are produced in abundance at our colliders – via the $LQ\bar{D}$ and $LL\bar{E}$ operators, respectively. However, such neutralinos are expected to be long-lived and can, thus, escape all our current search strategies at the LHC.

On the other hand, similar long-lived particles have been considered in other theoretical contexts for quite some time now; one prominent example is the heavy neutral lepton (HNL). Such long-lived particles have also been searched for extensively in many past experiments, and will further be probed at many dedicated currently running and upcoming experiments, including FASER at the LHC. These offer an opportunity to bridge the above gap for the neutralino. However, once again, the vast number of possibilities for the signatures – depending on the (combinations of) RPV coupling considered – means that work is needed to ensure complete coverage of the model space.

In Part IV, we made progress towards this by considering two separate studies. First, in Chapter 5, we demonstrated that the phenomenology of the light bino is very similar to that of a light HNL; there is a correspondence in production mechanisms and decay signatures for both. The exclusion and sensitivity limits for HNLs have been analyzed extensively in the literature. Thus, we argued that one can use a simple recasting procedure to derive the corresponding limits on the RPV-MSSM. We first compiled a list of all relevant RPV-MSSM scenarios (involving one or two non-zero RPV couplings) that can be probed by such a scenario. We found that such a procedure allows us to analyze a wide range of RPV scenarios (due to the overlapping phenomenologies). Next, we explicitly carried out the recasting by considering several benchmarks. We found that the obtained exclusion limits on the RPV-MSSM space lie up to 3-4 orders of magnitude beyond currently quoted values; future experiments will extend this further.

Next, in Chapter 6, we considered the ability of the radiative loop-decay mode of the light bino into a single photon and a neutrino to probe the RPV-MSSM. Such a study has not been considered in the literature so far. We demonstrated that, though loop-suppressed, this mode can become relevant when other tree-level modes are not kinematically accessible. Further, we argued that the final state would lead to a clean signature at FASER, free from any SM background. Finally, we compiled all benchmarks where such a mode can be relevant at FASER and ran numerical simulations to analyze the resulting sensitivity. We found that the radiative mode can probe regions up to 2 orders of magnitude beyond current bounds. Importantly, the study allowed us to get sensitivity to scenarios that we would not have been able to probe at tree level.

While our combined results from the two studies have provided strong exclusion and sensitivity limits for a wide range of RPV-MSSM scenarios, in order to make sure the whole landscape of

possibilities is covered, more work needs to be done.

7.5 Concluding Remarks

On the note of "more work needs to be done", we conclude this thesis. Through the opportunities we have identified and addressed here, we hope to have demonstrated:

- To the "believers": Although SUSY (at energies accessible to us) may be under pressure from all the experimental null results, the RPV-MSSM still provides opportunities that need to be explored more thoroughly before we should be ready to give up on the idea completely.
- To the "non-believers": The opportunities we have identified in the context of the RPV-MSSM have connections to several distinct areas: collider coverage of new physics signatures, leptoquarks, neutrino masses, proton decay, baryogenesis, long-lived particles – to name just the ones we explicitly mentioned in this thesis. These are topics that deserve attention, irrespective of whether in the context of SUSY or some other framework; studying the RPV-MSSM can then just be seen as an excuse of analyzing them all in one place.

These opportunities are particularly relevant given the recent and upcoming developments we have stressed. Finally, we wish to emphasize the importance of being model-independent as well, in order to not leave out any gaps.

A

Supplement to Chapter 2

A.1 Decay Modes for Numerical Simulations

We discuss the details of the decay modes used in the numerical simulations here. As mentioned in Section 2.4, all two-body decays are computed using `MadGraph5_aMC@NLO`; we only discuss the higher-body decays that we set by hand here.

Gluino LSP Benchmarks: For a given coupling, λ_{iki} with $i, k \in \{1, 2, 3\}$, we assume the chain: $\tilde{g} \to (\tilde{q}/\tilde{q}_3)^* + j \to \tilde{B}^* + 2j \to 2L + E_T^{\rm miss} + 2j$, where $2L = \{L_i^+ + L_i^-\}, \{L_i^+ + L_k^-\}, \{L_k^+ + L_i^-\}$, and we set the corresponding branching ratios (BRs) to be 0.5, 0.25, and 0.25, respectively. In the above, the asterisk denotes off-shell particles, and the nature of the (s)quark is fixed by the scenario considered. We stress that the chosen decay chain and BRs represent a non-trivial choice to facilitate numerical computation; alternate choices are possible – *e.g.*, the bino can be replaced by a wino or one flavor of slepton can be decoupled, thus, affecting the BRs. That is, we take the perspective where the branching ratios are taken to be the free variables, rather than the sparticle masses. Apart from being a simpler approach, this also saves computational time since we no longer need to calculate complicated high-multiplicity decays. Even with alternate BR choices, we expect the general implications of our results to hold.

Squark LSP Benchmarks: This is very similar to the above. For a coupling λ_{iki}, we assume the decay chain for the squarks to be: $(\tilde{q}/\tilde{q}_3)^* \to \tilde{B}^* + j \to 2L + E_T^{\rm miss} + j$, where $2L = \{L_i^+ + L_i^-\}, \{L_i^+ + L_k^-\}, \{L_k^+ + L_i^-\}$, and the BRs are set to 0.5, 0.25, and 0.25, respectively.

Electroweakino LSP Benchmarks:

- $\mathrm{D}_{\tilde{W}}$: The neutral wino decays as: $\tilde{W}^0 \to 2L + E_T^{\rm miss}$, for a coupling λ_{iki}, where $2L = \{L_i^+ + L_i^-\}, \{L_i^+ + L_k^-\}, \{L_k^+ + L_i^-\}$. We set the corresponding BRs to 0.5, 0.25, and 0.25, respectively. For the charged wino, we have the decay modes: $\tilde{W}^+ \to \{L_i^+ + L_i^- + L_k^+\}, \{L_i^+ + L_i^+ + L_k^-\}, \{L_i^+ + E_T^{\rm miss}\}, \{L_k^+ + E_T^{\rm miss}\}$ (analogous for $\tilde{W}^-$). We set the BR to 0.25 for each mode.
- $\mathrm{I}_{\tilde{g}\to\tilde{W}}$: The gluino decays as: $\tilde{g} \to \tilde{q}^* + j_l \to \tilde{W} + 2j_l$.
- $\mathrm{I}_{\tilde{q}\to\tilde{W}}$: The (singlet) squarks decay as: $\tilde{u}/\tilde{d} \to \tilde{g}^* + j_l \to \tilde{q}^* + 2j_l \to \tilde{W} + 3j_l$.
- $\mathrm{D}_{\tilde{H}}$: The neutral Higgsinos decay as: $\tilde{H}^0_{1(2)} \to \tilde{B}^* + Z(h) \to 2L + E_T^{\rm miss} + Z(h)$, for a coupling λ_{iki}, where $2L = \{L_i^+ + L_i^-\}, \{L_i^+ + L_k^-\}, \{L_k^+ + L_i^-\}$, with the BRs fixed to 0.5, 0.25, and 0.25, respectively. The case for $\tilde{H}^\pm$ is analogous, with $Z(h)$ replaced by $W^\pm$.

- $\mathrm{I}_{\tilde{g}\to\tilde{H}}$: Here, the gluino is assumed to decay as: $\tilde{g} \to \tilde{q_3}^* + j_3 \to \tilde{H} + 2j_3$.
- In all $\tilde{B}$ LSP scenarios, the bino decays as: $\tilde{B} \to 2L + E_T^{\mathrm{miss}}$, for a coupling λ_{iki}, where $2L = \{L_i^+ + L_i^-\}, \{L_i^+ + L_k^-\}, \{L_k^+ + L_i^-\}$, with the BRs set to 0.5, 0.25, and 0.25, respectively.
- $\mathrm{I}_{\tilde{g}\to\tilde{B}}$: The gluino is assumed to decay as: $\tilde{g} \to \tilde{q_3}^* + j_3 \to \tilde{B} + 2j_3$.

Slepton LSP Benchmarks:

- For all $\mathrm{D}_{\tilde{L}}$ scenarios, if a particular lepton does not couple directly to the considered operator, the decay is assumed to proceed via an off-shell bino, *e.g.*, $\tilde{\mu}_R \to \tilde{B}^* + \mu \to 2L + \mu + E_T^{\mathrm{miss}}$, where $2L = \{L_i^+ + L_i^-\}, \{L_i^+ + L_k^-\}, \{L_k^+ + L_i^-\}$ (for a coupling λ_{iki}). The corresponding BRs are set to 0.5, 0.25, and 0.25, respectively; and so on.
- $\mathrm{I}_{\tilde{g}\to\tilde{L}}$: The gluino is assumed to decay as: $\tilde{g} \to \tilde{q}^* + j_l \to \tilde{B}^* + 2j_l \to \tilde{L} + 2j_l + L$. Here, $\tilde{L}$ refers to all the sleptons.
- $\mathrm{I}_{\tilde{W}\to\tilde{L}}$: We assume that the only contributing decays are the two-body decay modes of the wino into the left-handed sleptons; we set the decay widths of the modes into the right-handed sleptons to be zero. This can occur if, for instance, any virtual mediators that can lead to such a decay are completely decoupled.

A.2 Auxiliary Tables

A.2.1 Production Table

While compiling the 'RPV Dictionary' in Section 2.3, we have taken a model-independent approach. In order to completely cover the RPV-MSSM landscape (within our framework assumptions), it is necessary to perform the searches compiled in Tables 2.2-2.11. Often, however, one is not interested in being completely general but may have a bias for certain classes of models. For instance, it is usual in the literature to focus on scenarios where a given LSP is produced at the LHC in cascade decays of the colored sparticles; scenarios where all sparticles other than the LSP are completely decoupled are less common. Given such a bias, one can optimize the 'RPV Dictionary' by adding the objects that would arise from such cascades.

In order to facilitate the inclusion of the above, Table A.1 provides a list of the objects that arise in cascade-decays for each relevant production mode for each LSP. For instance, with a gluino LSP, the only relevant mode is gluino-pair production since every other channel will have a lower cross-section. For squark LSP(s), however, squark-pair, gluino-pair, and associated production are all relevant since the latter two contribute with high cross-sections when a gluino is not decoupled. Table A.1 shows that the cascade to the LSP from gluino-pair (associated-pair) production leads to 2 extra jets (1 extra jet). These can then be used to optimize searches for models with squark LSPs and non-decoupled gluinos by adding the extra jet(s) to the relevant squark LSP signatures in Tables 2.2-2.11. We note that each value in the table represents the maximal set of objects that is *guaranteed to arise* in the cascade without knowing the details of the spectrum; however, more objects can always be present in specific scenarios. Further, to be economical, we have grouped left-handed and right-handed sparticles into one category but it is straightforward to expand them out.

Table A.1: Objects arising in the cascade decays of various pairs of parent sparticles (columns) down to the LSP(s) (rows). These can be added to the corresponding LSP signatures given in Tables 2.2-2.11 to optimize searches. $+-$ indicates an empty set while $\times$ indicates that the corresponding production channel is not relevant for the given LSP because the cross-section is either lower than or comparable to the cross-section for direct pair production of the LSP.

LSP	$\tilde{g}\tilde{g}$	$\tilde{g}\tilde{q}/\tilde{g}\bar{u}/\tilde{g}\bar{d}$	Squark Pair (1st,2nd gen.)	Squark Pair (3rd gen.)	$\tilde{W}\tilde{W}$	$\tilde{H}\tilde{H}$	Slepton Pair (1st, 2nd gen.)	Slepton Pair (3rd gen.)	$\tilde{B}\tilde{B}$
$\tilde{g}$	$+-$	$\times$	$\times$	$\times$	$\times$	$\times$	$\times$	$\times$	$\times$
$\tilde{q}/\bar{u}/\bar{d}$	$+2j_1$	$+j_1$	$+-$	$\times$	$\times$	$\times$	$\times$	$\times$	$\times$
$\tilde{q}_3/\bar{t}/\bar{b}$	$+2j_3$	$+j_1+2j_3$	$+2j_1+2j_3$	$+-$	$\times$	$\times$	$\times$	$\times$	$\times$
$\tilde{W}$	$+4j$	$+j_1+2j$	$+2j_1$	$+2j_3$	$+-$	$\times$	$\times$	$\times$	$\times$
$\tilde{H}$	$+4j$	$+j_1+2j$	$+2j_1$	$+2j_3$	$\times$	$+-$	$\times$	$\times$	$\times$
$\tilde{\ell}(\tilde{\nu})/\tilde{e}$	$\tilde{\ell}\bar{\ell}/\tilde{e}\bar{e}:\ +2\ell+4j$	$+2\ell+j_1+2j$	$+2\ell+2j_1$	$+2\ell+2j_3$	$+\ell+E_T^{\rm miss}$	$+2\ell$	$+-$	$\times$	$\times$
	$\tilde{\ell}\tilde{\nu}:\ +\ell+4j+E_T^{\rm miss}$	$+\ell+j_1+2j+E_T^{\rm miss}$	$+\ell+2j_1+E_T^{\rm miss}$	$+\ell+2j_3+E_T^{\rm miss}$	$+2\ell$	$+\ell+E_T^{\rm miss}$	$+-$	$\times$	$\times$
$\tilde{\tau}_L(\tilde{\nu}_\tau)/\tilde{\tau}_R$	$\tilde{\tau}_L\bar{\tilde{\tau}}_L/\tilde{\tau}_R\bar{\tilde{\tau}}_R:\ +2\tau+4j$	$+2\tau+j_1+2j$	$+2\tau+2j_1$	$+2\tau+2j_3$	$+\tau+E_T^{\rm miss}$	$+2\tau$	$+-$	$\times$	$\times$
	$\tilde{\tau}_L\tilde{\nu}_\tau:\ +\tau+4j+E_T^{\rm miss}$	$+\tau+j_1+2j+E_T^{\rm miss}$	$+\tau+2j_1+E_T^{\rm miss}$	$+\tau+2j_3+E_T^{\rm miss}$	$+2\tau$	$+\tau+E_T^{\rm miss}$	$+-$	$\times$	$\times$
$\tilde{B}$	$+4j$	$+j_1+2j$	$+2j_1$	$+2j_3$	$+3\ell+E_T^{\rm miss}/2\ell+E_T^{\rm miss}/4j/2v$	$+4j_3/2v$	$+2\ell/\ell+E_T^{\rm miss}$	$+2\tau/\tau+E_T^{\rm miss}$	$+-$

A.2.2 Flavor, Sign Configurations of Leptons

Here, we compile tables that show the possible flavor and sign combinations of the leptons in the signatures of Tables 2.2-2.11. In all the tables below, the indices $i, j, k \in \{1, 2, 3\}$, while the indices $a, b \in \{1, 2\}$; $\tilde{\ell}_3$ denotes a τ. For each listed configuration, the charge conjugated state (if different) is also possible but we omit listing it explicitly.

LLE Signatures

The flavor and sign combinations of the leptons corresponding to the various $LL\bar{E}$ topologies are shown in Table A.2 ($2L + E_T^{\text{miss}}$); Table A.3 ($3L + E_T^{\text{miss}}$); Table A.4 ($4L$); Table A.5 ($4L + (0-4)j + E_T^{\text{miss}}$); Table A.6 ($5L + E_T^{\text{miss}}$); and Table A.7 ($6L + E_T^{\text{miss}}$). The combinations corresponding to $\tilde{B}$ also apply to the Higgsino and all colored-sector LSPs.

Table A.2: $2L + E_T^{\text{miss}}$.

LSP	Coupling	Signature
$\tilde{e}_a$	$\lambda_{aba}\ a \neq b$	$\ell_a^+\ell_a^-/\ell_b^+\ell_b^-/\ell_a^+\ell_b^-$
$\tilde{e}_b$	λ_{a3b}	$\ell_a^+\ell_a^-/\ell_a^+\tau^-$
$\tilde{\tau}_R$	$\lambda_{ab3}\ a \neq b$	$\ell_a^+\ell_a^-/\ell_b^+\ell_b^-/\ell_a^+\ell_b^-$
$\tilde{\tau}_R$	λ_{a33}	$\ell_a^+\ell_a^-/\ell_a^+\tau^-$

Table A.3: $3L + E_T^{\text{miss}}$.

LSP	Coupling	Signature
$\tilde{\ell}_a\ (\tilde{\nu}_a)$	$\lambda_{abc}\ a \neq b$	$\ell_b^+\ell_c^+\ell_c^-/\ell_b^-\ell_c^+\ell_c^+$
$\tilde{\ell}_a\ (\tilde{\nu}_a)$	λ_{a3b}	$\ell_b^+\ell_b^+\tau^-/\ell_b^+\ell_b^-\tau^+$
$\tilde{\ell}_a\ (\tilde{\nu}_a)$	$\lambda_{ab3}\ a \neq b$	$\ell_b^+\tau^+\tau^-/\ell_b^-\tau^+\tau^+$
$\tilde{\ell}_a\ (\tilde{\nu}_a)$	λ_{a33}	$\tau^+\tau^+\tau^-$
$\tilde{\tau}_L\ (\tilde{\nu}_\tau)$	λ_{a3b}	$\ell_a^-\ell_b^+\ell_b^+/\ell_a^+\ell_b^+\ell_b^-$
$\tilde{\tau}_L\ (\tilde{\nu}_\tau)$	λ_{a33}	$\ell_a^+\tau^+\tau^-/\ell_a^-\tau^+\tau^+$

Table A.4: $4L$.

LSP	Coupling	Signature
$\tilde{\ell}_a\ (\tilde{\nu}_a)$	$\lambda_{abc}\ a \neq b$	$\ell_b^+\ell_b^+\ell_c^-\ell_c^-/\ell_b^+\ell_b^-\ell_c^+\ell_c^-$
$\tilde{\ell}_a\ (\tilde{\nu}_a)$	λ_{a3b}	$\ell_b^-\ell_b^-\tau^+\tau^+/\ell_b^+\ell_b^-\tau^+\tau^-$
$\tilde{\ell}_a\ (\tilde{\nu}_a)$	$\lambda_{ab3}\ a \neq b$	$\ell_b^-\ell_b^-\tau^+\tau^+/\ell_b^+\ell_b^-\tau^+\tau^-$
$\tilde{\ell}_a\ (\tilde{\nu}_a)$	λ_{a33}	$\tau^+\tau^+\tau^-\tau^-$
$\tilde{\tau}_L\ (\tilde{\nu}_\tau)$	λ_{a3b}	$\ell_a^+\ell_a^+\ell_b^-\ell_b^-/\ell_a^+\ell_a^-\ell_b^+\ell_b^-$
$\tilde{\tau}_L\ (\tilde{\nu}_\tau)$	λ_{a33}	$\ell_a^-\ell_a^-\tau^+\tau^+/\ell_a^+\ell_a^-\tau^+\tau^-$

UDD Tables

For the $\bar{U}\bar{D}\bar{D}$ topologies, the possible combinations are shown in Table A.8 ($1L + 2j_l + 4j + E_T^{\text{miss}}$); and Table A.9 ($2L + 2j_l + 4j$).

Table A.5: $4L + (0-4)j + E_T^{\text{miss}}$.

LSP	Coupling	Signature
$\tilde{B}$	$\lambda_{ijk}\ i \neq j$	$\ell_i^+\ell_i^+\ell_k^-\ell_k^- / \ell_i^+\ell_i^-\ell_k^+\ell_k^- / \ell_j^+\ell_j^+\ell_k^-\ell_k^- / \ell_j^+\ell_j^-\ell_k^+\ell_k^- / \ell_i^+\ell_j^+\ell_k^-\ell_k^- / \ell_i^+\ell_j^-\ell_k^+\ell_k^-$
$\tilde{W}$	$\lambda_{ijk}\ i \neq j$	$\ell_i^+\ell_j^+\ell_k^-\ell_k^- / \ell_i^+\ell_j^-\ell_k^+\ell_k^-$

Table A.6: $5L + E_T^{\text{miss}}$.

LSP	Coupling	Signature
$\tilde{\tau}_L\ (\tilde{\nu})$	$\lambda_{aba}\ a \neq b$	$\ell_a^+\ell_a^+\ell_a^-\ell_a^-\tau^+ / \ell_a^+\ell_a^-\ell_b^+\ell_b^-\tau^+ / \ell_a^+\ell_a^+\ell_b^-\ell_b^-\tau^+ / \ell_a^+\ell_a^+\ell_a^-\ell_b^+\tau^+$
$\tilde{\tau}_L\ (\tilde{\nu})$	$\lambda_{ab3}\ a \neq b$	$\ell_a^-\ell_a^-\tau^+\tau^+\tau^+ / \ell_b^-\ell_b^-\tau^+\tau^+\tau^+ / \ell_a^+\ell_a^-\tau^+\tau^+\tau^- / \ell_b^+\ell_b^-\tau^+\tau^+\tau^- / \ell_a^-\ell_b^-\tau^+\tau^+\tau^+ / \ell_a^+\ell_b^-\tau^+\tau^+\tau^-$

Table A.7: $6L + E_T^{\text{miss}}$.

LSP	Coupling	Signature
$\tilde{e}_a$	$\lambda_{ab3}\ a \neq b$	$\ell_a^+\ell_a^-\ell_a^-\ell_a^-\tau^+\tau^+ / \ell_a^+\ell_a^-\ell_b^-\ell_b^-\tau^+\tau^+ / \ell_a^+\ell_a^+\ell_a^-\ell_a^-\tau^+\tau^- / \ell_a^+\ell_a^-\ell_b^+\ell_b^-\tau^+\tau^- / \ell_a^+\ell_a^-\ell_a^-\ell_b^-\tau^+\tau^+ / \ell_a^+\ell_a^+\ell_a^-\ell_b^-\tau^+\tau^-$
$\tilde{e}_b$	λ_{a33}	$\ell_a^+\ell_a^-\ell_a^-\tau^+\tau^+\tau^- / \ell_a^+\ell_a^-\ell_a^-\ell_a^-\tau^+\tau^+ / \ell_a^+\ell_a^+\ell_a^-\ell_a^-\tau^+\tau^-$
$\tilde{\tau}_L\ (\tilde{\nu})$	$\lambda_{aba}\ a \neq b$	$\ell_a^+\ell_a^+\ell_a^-\ell_a^-\tau^+\tau^- / \ell_a^+\ell_a^-\ell_b^+\ell_b^-\tau^+\tau^- / \ell_a^+\ell_a^+\ell_b^-\ell_b^-\tau^+\tau^- / \ell_a^+\ell_a^+\ell_a^-\ell_b^+\tau^+\tau^-$
$\tilde{\tau}_L\ (\tilde{\nu})$	$\lambda_{ab3}\ a \neq b$	$\ell_a^-\ell_a^-\tau^+\tau^+\tau^+\tau^- / \ell_b^-\ell_b^-\tau^+\tau^+\tau^+\tau^- / \ell_a^+\ell_a^-\tau^+\tau^+\tau^-\tau^- / \ell_b^+\ell_b^-\tau^+\tau^+\tau^-\tau^- / \ell_a^-\ell_b^-\tau^+\tau^+\tau^+\tau^- / \ell_a^+\ell_b^-\tau^+\tau^+\tau^-\tau^-$
$\tilde{\tau}_R$	$\lambda_{aba}\ a \neq b$	$\ell_a^+\ell_a^+\ell_a^-\ell_a^-\tau^+\tau^- / \ell_a^+\ell_a^-\ell_b^+\ell_b^-\tau^+\tau^- / \ell_a^+\ell_a^+\ell_b^-\ell_b^-\tau^+\tau^- / \ell_a^+\ell_a^-\ell_a^-\ell_b^+\tau^+\tau^-$
$\tilde{\tau}_R$	λ_{a3b}	$\ell_a^+\ell_a^+\ell_b^-\ell_b^-\tau^+\tau^- / \ell_a^+\ell_a^-\ell_b^+\ell_b^-\tau^+\tau^- / \ell_a^+\ell_b^-\ell_b^-\tau^+\tau^+\tau^- / \ell_a^-\ell_b^+\ell_b^-\tau^+\tau^+\tau^-$

LQD Tables

Finally, for the $LQ\bar{D}$ topologies, the possible configurations are shown in Table A.10 ($1L + (2-6)j + E_T^{\text{miss}}$); Table A.11 ($2L + (2-6)j + (E_T^{\text{miss}})$); Table A.12 ($3L + 4j + E_T^{\text{miss}}$); and Table A.13 ($4L + 4j$). The $\tilde{B}$ configurations apply to the other electroweakinos, and the colored LSPs.

Table A.8: $1L + 2j_l + 4j + E_T^{\text{miss}}$.

LSP	Coupling	Signature
$\tilde{\ell}_a\,(\tilde{\nu}_a)$	λ''_{ijk}	ℓ_a^+
$\tilde{\tau}_L\,(\tilde{\nu})$	λ''_{ijk}	τ^+

Table A.9: $2L + 2j_l + 4j$.

LSP	Coupling	Signature
$\tilde{\ell}_a\,(\tilde{\nu}_a)$	λ''_{ijk}	$\ell_a^+\ell_a^-$
$\tilde{e}_a$	λ''_{ijk}	$\ell_a^+\ell_a^-$
$\tilde{\tau}_L\,(\tilde{\nu})$	λ''_{ijk}	$\tau^+\tau^-$
$\tilde{\tau}_R$	λ''_{ijk}	$\tau^+\tau^-$

Table A.10: $1L + (2-6)j + E_T^{\text{miss}}$.

LSP	Coupling	Signature
$\tilde{B}$	λ'_{ijk}	ℓ_i^+
$\tilde{\ell}_a(\tilde{\nu}_a)$	λ'_{33k}	ℓ_a^+
$\tilde{\tau}_L\,(\tilde{\nu}_\tau)$	λ'_{a3k}	τ^+

Table A.11: $2L + (2-6)j + (E_T^{\text{miss}})$.

LSP	Coupling	Signature
$\tilde{B}$	λ'_{ijk}	$\ell_i^+\ell_i^-/\ell_i^+\ell_i^+$
$\tilde{\ell}_a(\tilde{\nu}_a)$	λ'_{3ak}	$\ell_a^+\tau^+/\ell_a^+\tau^-$
$\tilde{\ell}_a(\tilde{\nu}_a)$	λ'_{33k}	$\ell_a^+\ell_a^-/\ell_a^+\tau^+/\ell_a^+\tau^-$
$\tilde{\tau}_L\,(\tilde{\nu}_\tau)$	λ'_{abk}	$\ell_a^+\tau^+/\ell_a^+\tau^-$
$\tilde{\tau}_L\,(\tilde{\nu}_\tau)$	λ'_{a3k}	$\ell_a^+\tau^+/\ell_a^+\tau^-/\tau^+\tau^-$
$\tilde{e}_a$	λ'_{i3k}	$\ell_a^+\ell_a^-$
$\tilde{\tau}$	λ'_{i3k}	$\tau^+\tau^-$

Table A.12: $3L + 4j + E_T^{\text{miss}}$.

LSP	Coupling	Signature
$\tilde{\ell}_a(\tilde{\nu}_a)$	λ'_{3jk}	$\ell_a^+\ell_a^-\tau^+/\ell_a^+\tau^+\tau^-/\ell_a^+\tau^+\tau^+/\ell_a^+\tau^-\tau^-$
$\tilde{\tau}_L\,(\tilde{\nu}_\tau)$	λ'_{ajk}	$\ell_a^+\ell_a^-\tau^+/\ell_a^+\ell_a^+\tau^+/\ell_a^-\ell_a^-\tau^+/\ell_a^+\tau^+\tau^-$
$\tilde{e}_a$	λ'_{ijk}	$\ell_a^+\ell_a^-\ell_i^+$
$\tilde{\tau}$	λ'_{i3k}	$\ell_i^+\tau^+\tau^-$

Table A.13: $4L + 4j$.

LSP	Coupling	Signature
$\tilde{\ell}_a(\tilde{\nu}_a)$	λ'_{3jk}	$\ell_a^+\ell_a^-\tau^+\tau^-/\ell_a^+\ell_a^-\tau^+\tau^+$
$\tilde{\tau}_L\,(\tilde{\nu}_\tau)$	λ'_{ajk}	$\ell_a^+\ell_a^-\tau^+\tau^-/\ell_a^+\ell_a^+\tau^+\tau^-$
$\tilde{e}_a$	λ'_{ijk}	$\ell_a^+\ell_a^-\ell_i^+\ell_i^-/\ell_a^+\ell_a^-\ell_i^+\ell_i^+$
$\tilde{\tau}$	λ'_{i3k}	$\ell_i^+\ell_i^-\tau^+\tau^-/\ell_i^+\ell_i^+\tau^+\tau^-$

A.3 abc-rpv, the RPV Python Library

abc-rpv[1] is a Python library that provides a framework for analyzing the collider signatures of the RPV-MSSM. Users are provided with various functionalities to explore the landscape of RPV-MSSM physics within the context of small RPV couplings. In this section, we provide a short introduction to the library. A complete manual will be provided as a separate document/paper in the future.

A.3.1 Introduction

The code starts by generating all possible transitions from one sparticle to another, based on the vertices provided in the input table (table_notsup.csv) stored in the input directory. Using this, it can obtain the resulting signature for a decay chain from any LSP to a sparticle directly coupled to an RPV operator; the latter, then, simply decays into purely Standard Model objects. Going through all combinations of LSP type, and RPV couplings (in terms of categories defined in Tables 2.2-2.11), all possible decay chains and signatures are compiled into tables. These tables are the output available to the user that can then be analyzed using the functions described below. By default, all output tables are already generated using the default input table, and are readily available in the data directory. The user does not need to generate the tables unless the input table is modified.

A.3.2 Assumptions and Caveats

In the implementation of our code, there are a few assumptions and caveats worth noting:

- All possible transitions are constructed from vertices provided in table_notsup.csv in the input directory. The vertices provided in this table need not be a 3-point vertex.
- The input table (table_notsup.csv) contains vertices that allow transitions from one sparticle to another while producing standard model particles. By default, only non-suppressed transitions based on the MSSM interactions are included; we use modified versions of the tables compiled in Ref. [48] for classifying vertices as suppressed or non-suppressed. Note that the input table can be modified by the user, as needed. This allows one to regenerate the output tables with custom vertices.
- While generating the decay chains for the LSPs, only the shortest chain is constructed by default. Users also have the option to generate all possible chains up to 3 transitions.
- The decay chains do not contain repeating sparticles.

A.3.3 Usage

Please refer to Tutorial.ipynb available at https://github.com/kys-sheng/abc-rpv.git for a complete tutorial of the Python library. We only discuss basic functionality here.

Syntax

Tables A.14 and A.15 show the syntax used in the code. One can also refer to rpv_definitions.py for more information.

[1] abc-rpv Python library is available at: https://github.com/kys-sheng/abc-rpv.git

Table A.14: Syntax for sparticles used in the code.

Code Syntax	Sparticles
B	Bino, B
W^+	Charged Wino
W^0	Neutral Wino
G	Gluino
H^+	Charged Higgsino
H^0	Neutral Higgsino
q	$\tilde{u}_L$, $\tilde{d}_L$, $\tilde{c}_L$, $\tilde{s}_L$
d	$\tilde{d}_R$, $\tilde{s}_R$
u	$\tilde{u}_R$, $\tilde{c}_R$
l	$\tilde{e}_L$, $\tilde{\mu}_L$
nu	$\tilde{\nu}_e$, $\tilde{\nu}_\mu$
e	$\tilde{e}_R$, $\tilde{\mu}_R$
t_L	$\tilde{t}_L$
b_L	$\tilde{b}_L$
t	$\tilde{t}_R$
b	$\tilde{b}_R$
tau_L	$\tilde{\tau}_L$
tau	$\tilde{\tau}_R$
nu_tau	$\tilde{\nu}_\tau$

Table A.15: One-character syntax for final state objects used in the code.

Symbol	Particles (Final State Objects)
l	e/μ
T	τ
L	$e/\mu/\tau$
j	$u/d/c/s$ jets
b	b jets
t	t jets
3	t/b jets
J	$u/d/c/s/t/b$ jets
v	$W/Z/h$
X	MET

Dictionaries

In the library, there are a few built-in dictionaries that contain the output tables generated from the code.

- ONE_LSP_RPV_DECAY_DICT : Contains details for all possible RPV decays of one LSP. Information regarding RPV coupling category, signature, decay chains, number of vertices is included.
- TWO_LSP_RPV_DECAY_DICT : Contains details for all possible RPV decays of a pair[2] of LSPs (decay via same category of RPV coupling). Information regarding RPV coupling category, signature, decay chains, number of vertices is included.
- TWO_LSP_MIXED_RPV_DECAY_DICT : Contains details for all possible RPV decays of a pair of LSPs (decay via different categories of RPV couplings). Information regarding RPV coupling categories, signature, decay chains, number of vertices is included.
- ONE_LSP_SIG_CAT_DICT : Contains final state signatures arising from decay of one LSP, categorized by RPV coupling; similar to Tables 2.2-2.11.
- TWO_LSP_SIG_CAT_DICT : Contains final state signatures arising from decay of pair of LSPs, categorized by RPV coupling; similar to Tables 2.2-2.11.

Note that the above dictionaries are regenerated upon using different input transition tables, as well as different table generation choices (*e.g.*, decay chain length).

Main Functions

Although the dictionaries by themselves contain all relevant information, it is more efficient and powerful to use the functions provided in the library to analyze the data. We describe the basic usage here; refer to Tutorial.ipynb for more details.

One LSP Decay:

- find_one_lsp_from_signature
  Using the signature as input, this function finds all LSPs with decay chains leading to the given final state. Alongside with the LSP, the relevant RPV couplings and decay chains are also returned.
- find_one_lsp_from_signature_inclusive
  Similar to find_one_lsp_from_signature, but in the inclusive mode (*e.g.*, one can choose n_{jets} ¿ 3 instead of $n_{jets} = 3$).
- find_signatures_from_one_lsp
  Using the LSP as input, this function finds all possible signatures that can arise in the LSP decay. Alongside with the signatures, the relevant RPV couplings and decay chains are also returned.

[2] We restrict to the case where both LSPs are the same, or belong to the same $SU(2)_L$ doublet.

LSP Pair Decay; Same Coupling Category:

- `find_two_lsp_from_signature`:
  Similar to `find_one_lsp_from_signature` but returns all pairs of LSPs leading to the input signature.
- `find_two_lsp_from_signature_inclusive`:
  Inclusive mode of `find_two_lsp_from_signature`.
- `find_signatures_from_two_lsp`:
  Similar to `find_signatures_from_one_lsp` but for a pair of input LSPs.

In all of the above, the pair is assumed to decay via the same (category of) RPV coupling.

LSP Pair Decay; Different Coupling Categories:

- `find_two_lsp_from_signature_mixed_couplings`
- `find_two_lsp_from_signature_mixed_couplings_inclusive`
- `find_signatures_from_two_lsp_mixed_couplings`

Analogous to the above but for LSP pair decaying via different (categories of) RPV couplings.

Advanced Usage

By default, all dictionaries and tables are regenerated automatically from the input table if all the csv files in the data directory are deleted. Thus, users can generate all the tables based on their custom input table (`table_notsup.csv`) by deleting the csv files in the data directory and reimporting the library. A step-by-step example demonstrating this will be provided in the complete manual.

B

Supplement to Chapter 4

B.1 Analytical Expressions for the MOM Solution Spaces

We write the explicit analytical solutions for the first three MOM classes here. As mentioned in the main text, the expressions for Class 4 MOMs are lengthy; we skip presenting them. Throughout, we treat x^1 as our free variable and solve Eq. (4.18) for the other variables. For short, we use the notation $M^{ij} \equiv \mathbf{M}_\nu^{ij}$.

Class 1: $x^i x'^j + x'^i x^j$

$$
\begin{aligned}
x'^1 &= \frac{M^{11}}{2x^1}\,, \quad x'^2 = \frac{M^{22}}{2x^2}\,, \quad x'^3 = \frac{M^{33}}{2x^3}\,, \quad \text{with} \\
x^2 &= \frac{M^{12}}{M^{11}}x^1 \pm \frac{\sqrt{\left(M^{12}\right)^2\left(x^1\right)^2 - M^{11}M^{22}\left(x^1\right)^2}}{M^{11}}\,, \\
x^3 &= \frac{M^{13}}{M^{11}}x^1 \pm \frac{\sqrt{\left(M^{13}\right)^2\left(x^1\right)^2 - M^{11}M^{33}\left(x^1\right)^2}}{M^{11}}\,.
\end{aligned}
\tag{B.1}
$$

This represents four distinct solutions corresponding to the various sign choices. The above expressions are general as long as $M^{ii} \neq 0$ for any i, which is true for the experimental neutrino mass matrix.

Class 2: $x^i x^j + \left(x^i x'^j + x'^i x^j\right)$

$$
\begin{aligned}
x'^1 &= \frac{M^{11} - \left(x^1\right)^2}{2x^1}\,, \quad x'^2 = \frac{M^{22} - \left(x^2\right)^2}{2x^2}\,, \\
x'^3 &= \frac{M^{33} - \left(x^3\right)^2}{2x^3}\,, \quad \text{with}
\end{aligned}
$$

$$x^2 = \frac{M^{12}}{M^{11}}x^1 \pm \frac{\sqrt{\left(M^{12}\right)^2\left(x^1\right)^2 - M^{11}M^{22}\left(x^1\right)^2}}{M^{11}},$$
$$x^3 = \frac{M^{13}}{M^{11}}x^1 \pm \frac{\sqrt{\left(M^{13}\right)^2\left(x^1\right)^2 - M^{11}M^{33}\left(x^1\right)^2}}{M^{11}}. \tag{B.2}$$

This represents four distinct solutions. Once again, the expressions are valid as long as $M^{ii} \neq 0$ for any i.

Class 3: $x^i x^j + x'^i x'^j$

$$x'^2 = \frac{M^{12} - x^1x^2}{x'^1}, \quad x'^3 = \frac{M^{13} - x^1x^3}{x'^1}, \quad \text{with}$$
$$x'^1 = \pm\sqrt{M^{11} - \left(x^1\right)^2},$$
$$x^2 = \frac{M^{12}}{M^{11}}x^1 \pm \sqrt{\frac{\left(M^{12}\right)^2}{\left(M^{11}\right)^2}\left(x^1\right)^2 - \frac{M^{22}}{M^{11}}\left(x^1\right)^2 - \frac{\left(M^{12}\right)^2}{M^{11}} + M^{22}},$$

$$x^3 = \frac{M^{13}}{M^{11}}x^1 \pm \sqrt{\frac{\left(M^{13}\right)^2}{\left(M^{11}\right)^2}\left(x^1\right)^2 - \frac{M^{33}}{M^{11}}\left(x^1\right)^2 - \frac{\left(M^{13}\right)^2}{M^{11}} + M^{33}}. \tag{B.3}$$

This represents eight distinct solutions. The above expressions are valid for $\left(x^1\right)^2 \neq M^{11}$, and $M^{11} \neq 0$. For the case $\left(x^1\right)^2 = M^{11}$, the solution sets are:

$$x'^1 = 0, \quad x'^2 = \pm\frac{\sqrt{M^{11}M^{22} - \left(M^{12}\right)^2}}{\sqrt{M^{11}}},$$
$$x'^2 = \pm\frac{\sqrt{M^{11}M^{33} - \left(M^{13}\right)^2}}{\sqrt{M^{11}}},$$
$$x^2 = \frac{M^{12}}{x^1}, \quad x^3 = \frac{M^{13}}{x^1}. \tag{B.4}$$

B.2 A Mini-guide to MOMs

In this appendix, we expand upon certain points related to MOMs that were only briefly mentioned in the main text.

RPV parameters and Linearly Independent x^i

Recall from the main text that the variables x^i are directly proportional to the RPV couplings. Nevertheless, there is no simple relation between the number of contributing RPV parameters in a model and the number of linearly independent x^i needed to describe their contributions. We demonstrate this through an explicit example.

Consider a κ-only model with all other RPV parameters zero in some basis. Consulting Table 4.1, our neutrino mass matrix receives contributions at tree level, as well as of types 7, 8 and 13 at one-loop level:

$$\begin{aligned}
\mathbf{M}_\nu^{ij} &\sim m_0 \delta_\kappa^i \delta_\kappa^j + \frac{\delta_\kappa^i \delta_\kappa^j m_{e_i} m_{e_j} h_e^i h_e^j}{16\pi^2 m_{\text{SUSY}}} \\
&+ \frac{\delta_\kappa^i \delta_\kappa^j \left[\left(m_{e_i} h_e^i \right)^2 + \left(m_{e_j} h_e^j \right)^2 \right]}{16\pi^2 m_{\text{SUSY}}} \\
&+ \frac{g\, \delta_\kappa^i \delta_\kappa^j \left(m_{e_i}^2 + m_{e_j}^2 \right)}{16\pi^2 m_{\text{SUSY}}} \\
&\sim x^i x^j + x'^i x'^j \\
&+ \left(x^i x''^j + x''^i x^j \right) \\
&+ \left(x^i x'''^j + x'''^i x^j \right) ,
\end{aligned} \tag{B.5}$$

where, we have defined,

$$\begin{aligned}
x^i &\equiv \sqrt{m_0}\, \delta_\kappa^i , & x'^i &\equiv \frac{m_{e_i} h_e^i \delta_\kappa^i}{4\pi \sqrt{m_{\text{SUSY}}}} , \\
x''^i &\equiv \frac{\left(m_{e_i} h_e^i \right)^2 \delta_\kappa^i}{16\pi^2 m_{\text{SUSY}} \sqrt{m_0}} , & x'''^i &\equiv \frac{2g\, \delta_\kappa^i m_{e_i}^2}{16\pi^2 m_{\text{SUSY}} \sqrt{m_0}} .
\end{aligned} \tag{B.6}$$

It can easily be checked that any three of these four sets are linearly independent. Even though all the contributions come from only one RPV parameter set – κ^i – we need three linearly independent sets to describe the structure.

We can also have situations where the opposite is true, *i.e.*, where several RPV parameter sets lead to fewer linearly independent sets x^i. We already saw an example of this in Section 4.8.4.

Deriving the Class 4 MOM Structure

Recall our observation that the neutrino mass matrix only has contributions of two forms: $x^i x^j$, and $x^i x'^j + x'^i x^j$. Given this fact, and restricting ourselves to the case of two linearly independent sets, it is immediately clear how the first three classes of MOMs arise. Here, we describe how we get the fourth one.

With only the linearly independent sets, x^i and x'^i, contributing, the most general form of the neutrino mass matrix is,

$$\mathbf{M}_\nu^{ij} = x^i x^j + x'^i x'^j + \left(x^i x'^j + x'^i x^j\right) . \tag{B.7}$$

Now, consider an additional contributing set, x''^i. The most general form the matrix can then take is,

$$\begin{aligned}\mathbf{M}_\nu^{ij} &= x^i x^j + x'^i x'^j + \left(x^i x'^j + x'^i x^j\right) \\ &\quad + x''^i x''^j + \left(x^i x''^j + x''^i x^j\right) + \left(x'^i x''^j + x''^i x'^j\right) .\end{aligned} \tag{B.8}$$

Since we assume there are only two linearly independent sets, there have to be some a, b (not both zero) such that $x''^i = a x^i + b x'^i$. Substituting this in the above expression, we get, after some algebra,

$$\begin{aligned}\mathbf{M}_\nu^{ij} &= \left(1 + a^2 + 2a\right) x^i x^j + \left(1 + b^2 + 2b\right) x'^i x'^j \\ &\quad + (1 + ab + 2a + 2b) \left(x^i x'^j + x'^i x^j\right) .\end{aligned} \tag{B.9}$$

Finally, defining,

$$\begin{aligned}\tilde{x}^i &\equiv \sqrt{\left(1 + a^2 + 2a\right)} x^i , \quad \tilde{x}'^i \equiv \sqrt{\left(1 + b^2 + 2b\right)} x'^i , \\ A &\equiv \frac{(1 + ab + 2a + 2b)}{\sqrt{\left(1 + a^2 + 2a\right)}\sqrt{\left(1 + b^2 + 2b\right)}} ,\end{aligned} \tag{B.10}$$

we get,

$$\mathbf{M}_\nu^{ij} = \tilde{x}^i \tilde{x}^j + \tilde{x}'^i \tilde{x}'^j + A \left(\tilde{x}^i \tilde{x}'^j + \tilde{x}'^i \tilde{x}^j\right) , \tag{B.11}$$

which is the Class 4 MOM structure. Note that this is not the most general form of A since further couplings could contribute; the arguments remain the same.

Most General Solution and MOMs

We stressed in the main text that the MOM approach does not solve the most general case since there can always be conspiring cancellations. We demonstrate this here with an example.

Consider a scenario where we have three linearly independent sets – x^i, x'^i, x''^i – with the explicit

form,

$$\begin{aligned} x^i &= (1,0,0)\ , \\ x'^i &= (0,1,0)\ , \\ x''^i &= (0,0,1)\ . \end{aligned} \tag{B.12}$$

Now, consider a fourth contribution x'''^i. This can always be written in the form,

$$x'''^i = ax^i + bx'^i + cx''^i\ , \tag{B.13}$$

for some a, b, c. Finally, consider the matrix with the structure,

$$\mathbf{M}_\nu^{ij} = x^i x^j + x'^i x'^j + \left(x''^i x'''^j + x'''^i x''^j\right)\ . \tag{B.14}$$

The above matrix clearly does not have a MOM form since it has three linearly independent sets. However, the matrix is rank two as long as the condition $a^2 + b^2 = 2c$ is satisfied. Thus, a matrix being rank two does not imply that the matrix has a MOM-form. There can always be additional hidden structure – for instance through specific cancellations/relations as in the above case.

B.3 Numerical Plots

CP-Conserving Solutions of MOMs

This appendix contains the numerical fits to the experimental data. Fig. B.1 shows the solution for Class 1 structures, assuming Inverted Ordering. In Fig. B.2 and Fig. B.3, we display the solution for Class 2 and Class 3 structures correspondingly. The fits have been performed using the neutrino data of Table 4.2 (with $\delta_{CP} = 0$) as described in Section 4.7.

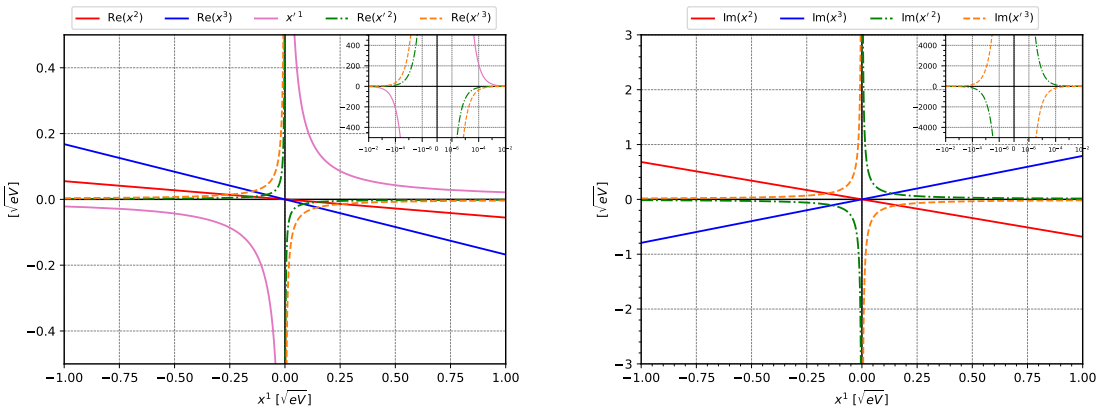

Figure B.1: Real (top) and imaginary (bottom) values of the couplings required to fit the actual neutrino data for the Inverted Ordering limit in models with Class 1 structure.

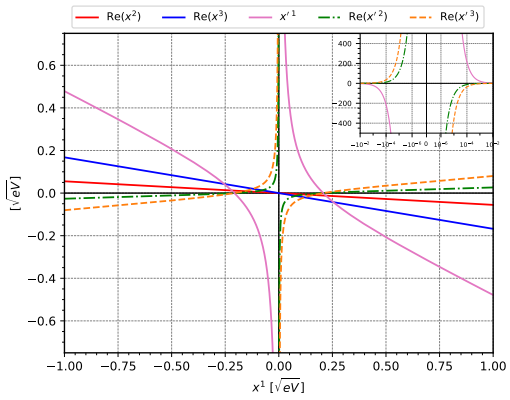

(a) Inverted Ordering

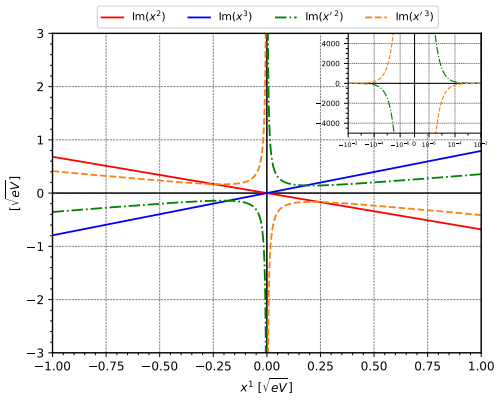

(b) Inverted Ordering

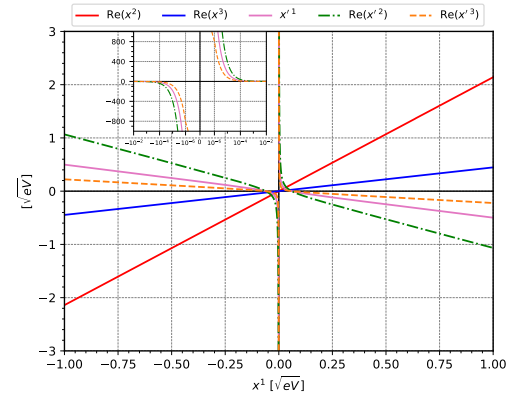

(c) Normal Ordering

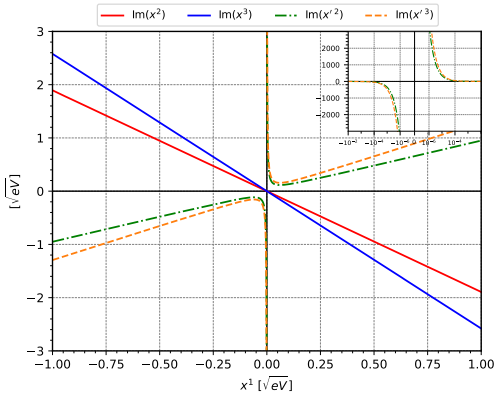

(d) Normal Ordering

Figure B.2: Real (left) and imaginary (right) values of the couplings required in models with Class 2 structure to fit the actual neutrino data for the two mass orderings: IO (top) and NO (bottom).

MOMs and a Non-zero δ_{CP}

We include, here, a fit with non-zero δ_{CP} to show that it is possible to accommodate CP violation in our framework. We show, in Fig. B.4, the fit corresponding to the Normal Ordering data of Table 4.2 for Class 2 MOMs, including the best-fit value for δ_{CP}. The qualitative features are as before. The overall goodness of the fit is also stable, indicating that the minimum of the χ^2 is determined as robustly as before.

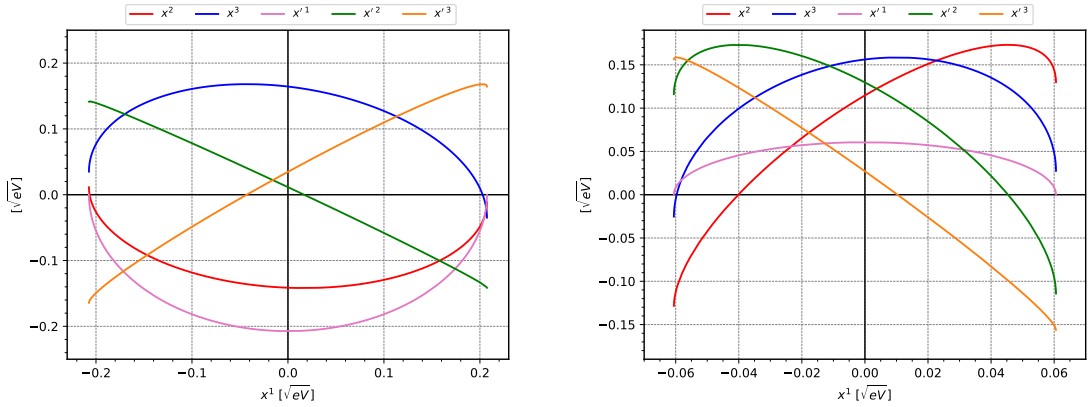

Figure B.3: Values of the couplings required in models with Class 3 structure to fit the actual neutrino data for the two mass orderings: IO (left) and NO (right). For this class, all couplings are real.

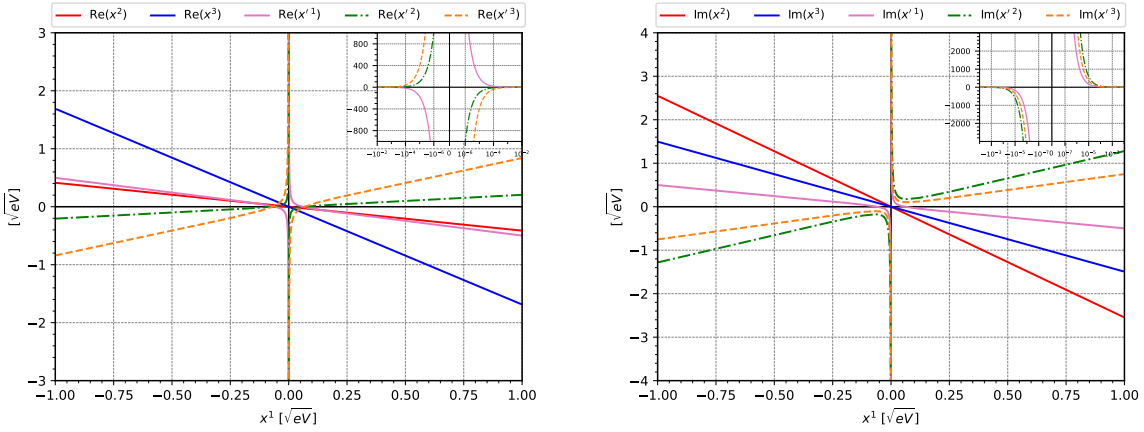

(a) Inverted Ordering

(b) Normal Ordering

Figure B.4: Values of the couplings required to fit the actual neutrino data including δ_{CP} in models with Class 2 structures for normal ordering.

C

Supplement to Chapter 5

C.1 Explicit neutralino production/decay widths with $LL\bar{E}$ operators

In this appendix, we will give the explicit general formulae needed for both the neutralino production and decay via $LL\bar{E}$ couplings at tree level. In the framework of the RPV-MSSM, the relevant processes will always involve four external two-component fermions and one intermediate scalar. The external fermions may carry momenta p_i and have masses m_i, where i is a generic label with $i = 0$ (incoming) and $i = 1, 2, 3$ (outgoing). Following Ref. [373], we express the total decay width as

$$\Gamma_{LL\bar{E}}(0;1,2,3)[\alpha,\beta,\gamma] = \frac{m_0}{2^8\pi^3}\int_{z_3^{\min}}^{z_3^{\max}} \mathrm{d}z_3 \int_{z_1^{\min}}^{z_1^{\max}} \mathrm{d}z_1\, \overline{|\mathcal{M}|^2}\,, \tag{C.1}$$

where the spin-averaged matrix element takes the form

$$\begin{aligned}\overline{|\mathcal{M}|^2} = \frac{m_0^4}{2}\Big[&|\alpha|^2\mathcal{Z}_1 + |\beta|^2\mathcal{Z}_2 + |\gamma|^2\mathcal{Z}_3 \\ &- \Re\{\alpha\beta^*\}\Big(+\mathcal{Z}_1 + \mathcal{Z}_2 - \mathcal{Z}_3\Big) \\ &- \Re\{\beta\gamma^*\}\Big(-\mathcal{Z}_1 + \mathcal{Z}_2 + \mathcal{Z}_3\Big) \\ &- \Re\{\alpha\gamma^*\}\Big(+\mathcal{Z}_1 - \mathcal{Z}_2 + \mathcal{Z}_3\Big)\Big]\,,\end{aligned} \tag{C.2}$$

with

$$\mathcal{Z}_i \equiv z_i\left(1 - z_i + 2\xi_i^2 - \sum_{j=1}^{3}\xi_j^2\right). \tag{C.3}$$

The kinematic variables z_i are defined as

$$z_i \equiv 2p_0\cdot p_i/m_0^2 = 2E_i/m_0\,, \tag{C.4}$$

and fulfill the relation $\sum_{i=1}^{3} z_i = 2$. Furthermore we introduce the mass ratios

$$\xi_i \equiv \frac{m_i}{m_0} \quad (i \neq 0)\,. \tag{C.5}$$

The (in general) complex valued coefficients α, β, γ follow from the Feynman rules relevant for the respective process, and can be simplified with the assumption of degenerate sfermion masses,

cf. Sec. 5.2. Their explicit expressions are given in Eq. (5.2). The integration limits in Eq. (C.1) can be obtained from the minimal and maximal values of the invariant masses of the "1 – 2" and "2 – 3" systems, *cf.* Ref. [361]:

$$(m_{12}^2)_{\max} = (m_0 - m_3)^2 \,, \tag{C.6}$$

$$(m_{12}^2)_{\min} = (m_1 + m_2)^2 \,, \tag{C.7}$$

$$(m_{23}^2)_{\max} = (E_2^* + E_3^*)^2 - \left(\sqrt{E_2^{*2} - m_2^2} - \sqrt{E_3^{*2} - m_3^2}\right)^2 \,, \tag{C.8}$$

$$(m_{23}^2)_{\min} = (E_2^* + E_3^*)^2 - \left(\sqrt{E_2^{*2} - m_2^2} + \sqrt{E_3^{*2} - m_3^2}\right)^2 \,, \tag{C.9}$$

where the energies $E_{2,3}^*$ in the "1 – 2" rest frame are given in terms of m_{12} by,

$$E_2^* = (m_{12}^2 - m_1^2 + m_2^2)/2m_{12} \,, \tag{C.10}$$

$$E_3^* = (m_0^2 - m_{12}^2 - m_3^2)/2m_{12} \,. \tag{C.11}$$

From energy-momentum conservation one can deduce that

$$z_3 = \frac{m_0^2 + m_3^2 - m_{12}^2}{m_0^2} \qquad \text{and} \qquad z_1 = \frac{m_0^2 + m_1^2 - m_{23}^2}{m_0^2} \,, \tag{C.12}$$

which then finally yield the integration limits:

$$z_3^{\max} = 1 + \xi_3^2 - \frac{(m_{12}^2)_{\min}}{m_0^2} \,, \tag{C.13}$$

$$z_3^{\min} = 1 + \xi_3^2 - \frac{(m_{12}^2)_{\max}}{m_0^2} = 2\xi_3 \,, \tag{C.14}$$

$$z_1^{\max} = 1 + \xi_1^2 - \frac{(m_{23}^2)_{\min}}{m_{\tilde{\chi}_1^0}^2} \,, \tag{C.15}$$

$$z_1^{\min} = 1 + \xi_1^2 - \frac{(m_{23}^2)_{\max}}{m_{\tilde{\chi}_1^0}^2} \,. \tag{C.16}$$

Bibliography

[1] S. Weinberg, *The Quantum theory of fields. Vol. 1: Foundations*, Cambridge University Press, 2005, ISBN: 978-0-521-67053-1, 978-0-511-25204-4.

[2] S. Weinberg, *The quantum theory of fields. Vol. 2: Modern applications*, Cambridge University Press, 2013, ISBN: 978-1-139-63247-8, 978-0-521-67054-8, 978-0-521-55002-4.

[3] J. Erler and M. Schott, *Electroweak Precision Tests of the Standard Model after the Discovery of the Higgs Boson*, Prog. Part. Nucl. Phys. **106** (2019) 68, arXiv: 1902.05142 [hep-ph].

[4] G. Arnison et al., *Experimental Observation of Isolated Large Transverse Energy Electrons with Associated Missing Energy at* $\sqrt{s}$ = 540 *GeV*, Phys. Lett. B **122** (1983) 103.

[5] M. Banner et al., *Observation of Single Isolated Electrons of High Transverse Momentum in Events with Missing Transverse Energy at the CERN anti-p p Collider*, Phys. Lett. B **122** (1983) 476.

[6] G. Arnison et al., *Experimental Observation of Lepton Pairs of Invariant Mass Around 95-GeV/c**2 at the CERN SPS Collider*, Phys. Lett. B **126** (1983) 398.

[7] P. Bagnaia et al., *Evidence for* $Z^0 \to e^+e^-$ *at the CERN* $\bar{p}p$ *Collider*, Phys. Lett. B **129** (1983) 130.

[8] F. Abe et al., *Observation of top quark production in* $\bar{p}p$ *collisions*, Phys. Rev. Lett. **74** (1995) 2626, arXiv: hep-ex/9503002.

[9] S. Abachi et al., *Observation of the top quark*, Phys. Rev. Lett. **74** (1995) 2632, arXiv: hep-ex/9503003.

[10] G. Aad et al., *Observation of a new particle in the search for the Standard Model Higgs boson with the ATLAS detector at the LHC*, Phys. Lett. B **716** (2012) 1, arXiv: 1207.7214 [hep-ex].

[11] S. Chatrchyan et al., *Observation of a New Boson at a Mass of 125 GeV with the CMS Experiment at the LHC*, Phys. Lett. B **716** (2012) 30, arXiv: 1207.7235 [hep-ex].

[12] P. F. de Salas et al., *2020 global reassessment of the neutrino oscillation picture*, JHEP **02** (2021) 071, arXiv: 2006.11237 [hep-ph].

[13] R. L. Workman et al., *Review of Particle Physics*, PTEP **2022** (2022) 083C01.

[14] M. Aker et al., *Direct neutrino-mass measurement with sub-electronvolt sensitivity*, Nature Phys. **18** (2022) 160, arXiv: 2105.08533 [hep-ex].

[15] G. Steigman, *Observational tests of antimatter cosmologies*, Ann. Rev. Astron. Astrophys. **14** (1976) 339.

[16] L. Canetti, M. Drewes and M. Shaposhnikov, *Matter and Antimatter in the Universe*, New J. Phys. **14** (2012) 095012, arXiv: 1204.4186 [hep-ph].

[17] D. London and J. Matias, *B Flavour Anomalies: 2021 Theoretical Status Report*, Ann. Rev. Nucl. Part. Sci. **72** (2022) 37, arXiv: 2110.13270 [hep-ph].

[18] A. Keshavarzi, K. S. Khaw and T. Yoshioka, *Muon g-2: A review*, Nucl. Phys. B **975** (2022) 115675, arXiv: 2106.06723 [hep-ex].

[19] S. P. Martin, *A Supersymmetry primer*, Adv. Ser. Direct. High Energy Phys. **18** (1998) 1, ed. by G. L. Kane, arXiv: hep-ph/9709356.

[20] O. Witzel, *Review on Composite Higgs Models*, PoS **LATTICE2018** (2019) 006, arXiv: 1901.08216 [hep-lat].

[21] S. R. Coleman and J. Mandula, *All Possible Symmetries of the S Matrix*, Phys. Rev. **159** (1967) 1251, ed. by A. Zichichi.

[22] R. Haag, J. T. Lopuszanski and M. Sohnius, *All Possible Generators of Supersymmetries of the s Matrix*, Nucl. Phys. B **88** (1975) 257.

[23] G. 't Hooft, *Computation of the Quantum Effects Due to a Four-Dimensional Pseudoparticle*, Phys. Rev. D **14** (1976) 3432, ed. by M. A. Shifman, [Erratum: Phys.Rev.D 18, 2199 (1978)].

[24] N. S. Manton, *Topology in the Weinberg-Salam Theory*, Phys. Rev. D **28** (1983) 2019.

[25] J. A. Harvey and M. S. Turner, *Cosmological baryon and lepton number in the presence of electroweak fermion number violation*, Phys. Rev. D **42** (1990) 3344.

[26] H. K. Dreiner and G. G. Ross, *Sphaleron erasure of primordial baryogenesis*, Nucl. Phys. B **410** (1993) 188, arXiv: hep-ph/9207221.

[27] A. Takenaka et al., *Search for proton decay via $p \to e^+\pi^0$ and $p \to \mu^+\pi^0$ with an enlarged fiducial volume in Super-Kamiokande I-IV*, Phys. Rev. D **102** (2020) 112011, arXiv: 2010.16098 [hep-ex].

[28] J. R. Ellis, G. B. Gelmini, J. L. Lopez, D. V. Nanopoulos and S. Sarkar, *Astrophysical constraints on massive unstable neutral relic particles*, Nucl. Phys. B **373** (1992) 399.

[29] R. Barbier et al., *R-parity violating supersymmetry*, Phys. Rept. **420** (2005) 1, arXiv: hep-ph/0406039.

[30] H. Goldberg, *Constraint on the Photino Mass from Cosmology*, Phys. Rev. Lett. **50** (1983) 1419, ed. by M. A. Srednicki, [Erratum: Phys.Rev.Lett. 103, 099905 (2009)].

[31] J. R. Ellis, J. S. Hagelin, D. V. Nanopoulos, K. A. Olive and M. Srednicki, *Supersymmetric Relics from the Big Bang*, Nucl. Phys. B **238** (1984) 453, ed. by M. A. Srednicki.

[32] *SUSY Summary Plots March 2023*, (2023).

[33] N. Arkani-Hamed and S. Dimopoulos, *Supersymmetric unification without low energy supersymmetry and signatures for fine-tuning at the LHC*, JHEP **06** (2005) 073, arXiv: hep-th/0405159.

[34] G. F. Giudice and A. Romanino, *Split supersymmetry*, Nucl. Phys. B **699** (2004) 65, [Erratum: Nucl.Phys.B 706, 487–487 (2005)], arXiv: hep-ph/0406088.

[35] H. K. Dreiner, C. Luhn, H. Murayama and M. Thormeier,
Baryon triality and neutrino masses from an anomalous flavor U(1),
Nucl. Phys. B **774** (2007) 127, arXiv: hep-ph/0610026.

[36] A. D. Sakharov,
Violation of CP Invariance, C asymmetry, and baryon asymmetry of the universe,
Pisma Zh. Eksp. Teor. Fiz. **5** (1967) 32.

[37] H. K. Dreiner, *An Introduction to explicit R-parity violation*,
Adv. Ser. Direct. High Energy Phys. **21** (2010) 565, ed. by G. L. Kane,
arXiv: hep-ph/9707435.

[38] M. Bento, L. Hall and G. Ross, *Generalised matter parities from the superstring*,
Nuclear Physics B **292** (1987) 400, ISSN: 0550-3213,
URL: http://www.sciencedirect.com/science/article/pii/0550321387906523.

[39] M. Kurimaya, H. Nakajima and T. Watari, *Theoretical framework for R-parity violation*,
Phys. Rev. D **79** (7 2009) 075002,
URL: https://link.aps.org/doi/10.1103/PhysRevD.79.075002.

[40] B. C. Allanach, A. Dedes and H. K. Dreiner, *R parity violating minimal supergravity model*,
Phys. Rev. D **69** (2004) 115002, [Erratum: Phys.Rev.D 72, 079902 (2005)],
arXiv: hep-ph/0309196.

[41] L. M. Krauss and F. Wilczek, *Discrete gauge symmetry in continuum theories*,
Phys. Rev. Lett. **62** (11 1989) 1221,
URL: https://link.aps.org/doi/10.1103/PhysRevLett.62.1221.

[42] T. Banks, *Effective lagrangian description on discrete gauge symmetries*,
Nuclear Physics B **323** (1989) 90, ISSN: 0550-3213,
URL: http://www.sciencedirect.com/science/article/pii/0550321389905890.

[43] L. E. Ibanez and G. G. Ross, *Discrete gauge symmetry anomalies*,
Phys. Lett. B **260** (1991) 291.

[44] L. E. Ibanez and G. G. Ross, *Discrete gauge symmetries and the origin of baryon and lepton number conservation in supersymmetric versions of the standard model*,
Nucl. Phys. B **368** (1992) 3.

[45] D. Dercks, H. Dreiner, M. E. Krauss, T. Opferkuch and A. Reinert,
R-Parity Violation at the LHC, Eur. Phys. J. C **77** (2017) 856, arXiv: 1706.09418 [hep-ph].

[46] J. A. Evans, Y. Kats, D. Shih and M. J. Strassler,
Toward Full LHC Coverage of Natural Supersymmetry, JHEP **07** (2014) 101,
arXiv: 1310.5758 [hep-ph].

[47] H. K. Dreiner and G. G. Ross, *R-parity violation at hadron colliders*,
Nucl. Phys. B **365** (1991) 597.

[48] H. K. Dreiner, F. Staub, A. Vicente and W. Porod,
General MSSM signatures at the LHC with and without R-parity,
Phys. Rev. D **86** (2012) 035021, arXiv: 1205.0557 [hep-ph].

[49] L. Buonocore, U. Haisch, P. Nason, F. Tramontano and G. Zanderighi, *Lepton-Quark Collisions at the Large Hadron Collider*, Phys. Rev. Lett. **125** (2020) 231804, arXiv: 2005.06475 [hep-ph].

[50] V. A. Kuzmin, V. A. Rubakov and M. E. Shaposhnikov, *On the Anomalous Electroweak Baryon Number Nonconservation in the Early Universe*, Phys. Lett. B **155** (1985) 36.

[51] M. E. Shaposhnikov, *Baryon Asymmetry of the Universe in Standard Electroweak Theory*, Nucl. Phys. B **287** (1987) 757.

[52] M. B. Gavela, P. Hernandez, J. Orloff and O. Pene, *Standard model CP violation and baryon asymmetry*, Mod. Phys. Lett. A **9** (1994) 795, arXiv: hep-ph/9312215.

[53] M. B. Gavela, P. Hernandez, J. Orloff, O. Pene and C. Quimbay, *Standard model CP violation and baryon asymmetry. Part 2: Finite temperature*, Nucl. Phys. B **430** (1994) 382, arXiv: hep-ph/9406289.

[54] S. Weinberg, *Supersymmetry at Ordinary Energies. 1. Masses and Conservation Laws*, Phys. Rev. D **26** (1982) 287.

[55] N. Sakai and T. Yanagida, *Proton Decay in a Class of Supersymmetric Grand Unified Models*, Nucl. Phys. B **197** (1982) 533.

[56] S. W. Hawking, D. N. Page and C. N. Pope, *THE PROPAGATION OF PARTICLES IN SPACE-TIME FOAM*, Phys. Lett. B **86** (1979) 175.

[57] I. Antoniadis, J. R. Ellis, J. S. Hagelin and D. V. Nanopoulos, *The Flipped SU(5) x U(1) String Model Revamped*, Phys. Lett. B **231** (1989) 65.

[58] A. Y. Smirnov and F. Vissani, *Upper bound on all products of R-parity violating couplings lambda-prime and lambda-prime-prime from proton decay*, Phys. Lett. B **380** (1996) 317, arXiv: hep-ph/9601387.

[59] E. Dudas, T. Gherghetta, K. Kaneta, Y. Mambrini and K. A. Olive, *Limits on R-parity Violation in High Scale Supersymmetry*, Phys. Rev. D **100** (2019) 035004, arXiv: 1905.09243 [hep-ph].

[60] N. Chamoun, F. Domingo and H. K. Dreiner, *Nucleon decay in the R-parity violating MSSM*, Phys. Rev. D **104** (2021) 015020, arXiv: 2012.11623 [hep-ph].

[61] L. J. Hall and M. Suzuki, *Explicit R-Parity Breaking in Supersymmetric Models*, Nucl. Phys. B **231** (1984) 419.

[62] D. Chang and W.-Y. Keung, *New limits on R-parity breakings in supersymmetric standard models*, Phys. Lett. B **389** (1996) 294, arXiv: hep-ph/9608313.

[63] K. Choi, E. J. Chun and J. S. Lee, *Proton decay with a light gravitino or axino*, Phys. Rev. D **55** (1997) 3924, arXiv: hep-ph/9611285.

[64] K. Choi, K. Hwang and J. S. Lee, *Constraints on R-parity and B violating couplings in gauge mediated supersymmetry breaking models*, Phys. Lett. B **428** (1998) 129, arXiv: hep-ph/9802323.

[65] K. Abe et al.,
Search for proton decay via $p \to \nu K^+$ using 260 kiloton·year data of Super-Kamiokande,
Phys. Rev. D **90** (2014) 072005, arXiv: 1408.1195 [hep-ex].

[66] B. Abi et al., *Deep Underground Neutrino Experiment (DUNE), Far Detector Technical Design Report, Volume I Introduction to DUNE*, JINST **15** (2020) T08008,
arXiv: 2002.02967 [physics.ins-det].

[67] B. Abi et al., *Deep Underground Neutrino Experiment (DUNE), Far Detector Technical Design Report, Volume III: DUNE Far Detector Technical Coordination*,
JINST **15** (2020) T08009, arXiv: 2002.03008 [physics.ins-det].

[68] B. Abi et al., *Deep Underground Neutrino Experiment (DUNE), Far Detector Technical Design Report, Volume IV: Far Detector Single-phase Technology*, JINST **15** (2020) T08010,
arXiv: 2002.03010 [physics.ins-det].

[69] B. Abi et al., *Deep Underground Neutrino Experiment (DUNE), Far Detector Technical Design Report, Volume II: DUNE Physics*, (2020), arXiv: 2002.03005 [hep-ex].

[70] Z. Djurcic et al., *JUNO Conceptual Design Report*, (2015),
arXiv: 1508.07166 [physics.ins-det].

[71] F. An et al., *Neutrino Physics with JUNO*, J. Phys. G **43** (2016) 030401,
arXiv: 1507.05613 [physics.ins-det].

[72] K. Abe et al., *Hyper-Kamiokande Design Report*, (2018),
arXiv: 1805.04163 [physics.ins-det].

[73] D. Choudhury, H. K. Dreiner, P. Richardson and S. Sarkar,
A Supersymmetric solution to the KARMEN time anomaly, Phys. Rev. D **61** (2000) 095009,
arXiv: hep-ph/9911365.

[74] H. K. Dreiner et al., *Mass Bounds on a Very Light Neutralino*, Eur. Phys. J. C **62** (2009) 547,
arXiv: 0901.3485 [hep-ph].

[75] B. W. Lee and S. Weinberg, *Cosmological Lower Bound on Heavy Neutrino Masses*,
Phys. Rev. Lett. **39** (1977) 165, ed. by M. A. Srednicki.

[76] G. Belanger, F. Boudjema, A. Cottrant, R. M. Godbole and A. Semenov,
The MSSM invisible Higgs in the light of dark matter and g-2, Phys. Lett. B **519** (2001) 93,
arXiv: hep-ph/0106275.

[77] D. Hooper and T. Plehn, *Supersymmetric dark matter: How light can the LSP be?*,
Phys. Lett. B **562** (2003) 18, arXiv: hep-ph/0212226.

[78] A. Bottino, N. Fornengo and S. Scopel, *Light relic neutralinos*,
Phys. Rev. D **67** (2003) 063519, arXiv: hep-ph/0212379.

[79] H. K. Dreiner, C. Hanhart, U. Langenfeld and D. R. Phillips,
Supernovae and light neutralinos: SN1987A bounds on supersymmetry revisited,
Phys. Rev. D **68** (2003) 055004, arXiv: hep-ph/0304289.

[80] D. Albornoz Vasquez, G. Belanger, C. Boehm, A. Pukhov and J. Silk,
Can neutralinos in the MSSM and NMSSM scenarios still be light?,
Phys. Rev. D **82** (2010) 115027, arXiv: 1009.4380 [hep-ph].

[81] L. Calibbi, J. M. Lindert, T. Ota and Y. Takanishi,
Cornering light Neutralino Dark Matter at the LHC, JHEP **10** (2013) 132,
arXiv: 1307.4119 [hep-ph].

[82] R. Kumar Barman, G. Belanger and R. M. Godbole, *Status of low mass LSP in SUSY*,
Eur. Phys. J. ST **229** (2020) 3159, arXiv: 2010.11674 [hep-ph].

[83] M. Kachelriess, *The KARMEN anomaly, light neutralinos and supernova SN1987A*,
JHEP **02** (2000) 010, arXiv: hep-ph/0001160.

[84] H. K. Dreiner, J.-F. Fortin, J. Isern and L. Ubaldi, *White Dwarfs constrain Dark Forces*,
Phys. Rev. D **88** (2013) 043517, arXiv: 1303.7232 [hep-ph].

[85] J. L. Feng, I. Galon, F. Kling and S. Trojanowski, *ForwArd Search ExpeRiment at the LHC*,
Phys. Rev. D **97** (2018) 035001, arXiv: 1708.09389 [hep-ph].

[86] A. Ariga et al., *FASER's physics reach for long-lived particles*,
Phys. Rev. D **99** (2019) 095011, arXiv: 1811.12522 [hep-ph].

[87] J. de Vries, H. K. Dreiner and D. Schmeier,
R-Parity Violation and Light Neutralinos at SHiP and the LHC,
Phys. Rev. D **94** (2016) 035006, arXiv: 1511.07436 [hep-ph].

[88] D. Gorbunov and I. Timiryasov,
Decaying light particles in the SHiP experiment. II. Signal rate estimates for light neutralinos,
Phys. Rev. D **92** (2015) 075015, arXiv: 1508.01780 [hep-ph].

[89] J. C. Helo, M. Hirsch and Z. S. Wang, *Heavy neutral fermions at the high-luminosity LHC*,
JHEP **07** (2018) 056, arXiv: 1803.02212 [hep-ph].

[90] D. Dercks, J. De Vries, H. K. Dreiner and Z. S. Wang,
R-parity Violation and Light Neutralinos at CODEX-b, FASER, and MATHUSLA,
Phys. Rev. D **99** (2019) 055039, arXiv: 1810.03617 [hep-ph].

[91] D. Dercks, H. K. Dreiner, M. Hirsch and Z. S. Wang, *Long-Lived Fermions at AL3X*,
Phys. Rev. D **99** (2019) 055020, arXiv: 1811.01995 [hep-ph].

[92] H. K. Dreiner, J. Y. Günther and Z. S. Wang,
R-parity violation and light neutralinos at ANUBIS and MAPP,
Phys. Rev. D **103** (2021) 075013, arXiv: 2008.07539 [hep-ph].

[93] S. Dey et al., *Long-lived light neutralinos at Belle II*, JHEP **02** (2021) 211,
arXiv: 2012.00438 [hep-ph].

[94] P. Candia, G. Cottin, A. Méndez and V. Muñoz,
Searching for light long-lived neutralinos at Super-Kamiokande,
Phys. Rev. D **104** (2021) 055024, arXiv: 2107.02804 [hep-ph].

[95] P. Konar, K. T. Matchev, M. Park and G. K. Sarangi,
How to look for supersymmetry under the lamppost at the LHC,
Phys. Rev. Lett. **105** (2010) 221801, arXiv: 1008.2483 [hep-ph].

[96] Y. A. Golfand and E. P. Likhtman,
Extension of the Algebra of Poincare Group Generators and Violation of p Invariance,
JETP Lett. **13** (1971) 323.

[97] D. V. Volkov and V. P. Akulov, *Is the Neutrino a Goldstone Particle?*, Phys. Lett. B **46** (1973) 109.

[98] J. Wess and B. Zumino, *A Lagrangian Model Invariant Under Supergauge Transformations*, Phys. Lett. B **49** (1974) 52.

[99] J. Wess and B. Zumino, *Supergauge Transformations in Four-Dimensions*, Nucl. Phys. B **70** (1974) 39, ed. by A. Salam and E. Sezgin.

[100] E. Gildener, *Gauge Symmetry Hierarchies*, Phys. Rev. D **14** (1976) 1667.

[101] M. J. G. Veltman, *The Infrared - Ultraviolet Connection*, Acta Phys. Polon. B **12** (1981) 437.

[102] H. P. Nilles, *Supersymmetry, Supergravity and Particle Physics*, Phys. Rept. **110** (1984) 1.

[103] M. Drees, R. Godbole and P. Roy, *Theory and phenomenology of sparticles: An account of four-dimensional N=1 supersymmetry in high energy physics*, 2004.

[104] G. Aad et al., *Search for new phenomena in final states with large jet multiplicities and missing transverse momentum using $\sqrt{s}$ = 13 TeV proton-proton collisions recorded by ATLAS in Run 2 of the LHC*, JHEP **10** (2020) 062, arXiv: 2008.06032 [hep-ex].

[105] G. Aad et al., *Search for a scalar partner of the top quark in the all-hadronic $t\bar{t}$ plus missing transverse momentum final state at $\sqrt{s}$ = 13 TeV with the ATLAS detector*, Eur. Phys. J. C **80** (2020) 737, arXiv: 2004.14060 [hep-ex].

[106] G. Aad et al., *Search for squarks and gluinos in final states with same-sign leptons and jets using 139 fb^{-1} of data collected with the ATLAS detector*, JHEP **06** (2020) 046, arXiv: 1909.08457 [hep-ex].

[107] G. Aad et al., *Search for bottom-squark pair production with the ATLAS detector in final states containing Higgs bosons, b-jets and missing transverse momentum*, JHEP **12** (2019) 060, arXiv: 1908.03122 [hep-ex].

[108] A. Tumasyan et al., *Search for higgsinos decaying to two Higgs bosons and missing transverse momentum in proton-proton collisions at $\sqrt{s}$ = 13 TeV*, JHEP **05** (2022) 014, arXiv: 2201.04206 [hep-ex].

[109] A. Tumasyan et al., *Combined searches for the production of supersymmetric top quark partners in proton–proton collisions at $\sqrt{s}$ = 13 TeV*, Eur. Phys. J. C **81** (2021) 970, arXiv: 2107.10892 [hep-ex].

[110] A. Tumasyan et al., *Search for supersymmetry in final states with two or three soft leptons and missing transverse momentum in proton-proton collisions at $\sqrt{s}$ = 13 TeV*, JHEP **04** (2022) 091, arXiv: 2111.06296 [hep-ex].

[111] A. M. Sirunyan et al., *Search for supersymmetry in final states with two oppositely charged same-flavor leptons and missing transverse momentum in proton-proton collisions at $\sqrt{s}$ = 13 TeV*, JHEP **04** (2021) 123, arXiv: 2012.08600 [hep-ex].

[112] A. M. Sirunyan et al., *Search for physics beyond the standard model in events with jets and two same-sign or at least three charged leptons in proton-proton collisions at $\sqrt{s}$ = 13 TeV*, Eur. Phys. J. C **80** (2020) 752, arXiv: 2001.10086 [hep-ex].

[113] A. M. Sirunyan et al., *Search for supersymmetry in proton-proton collisions at $\sqrt{s}$ = 13 TeV in events with high-momentum Z bosons and missing transverse momentum*, JHEP **09** (2020) 149, arXiv: 2008.04422 [hep-ex].

[114] *Search for supersymmetry in final states with missing transverse momentum and three or more b-jets in 139 fb^{-1} of proton–proton collisions at $\sqrt{s}$ = 13 TeV with the ATLAS detector*, (2022), arXiv: 2211.08028 [hep-ex].

[115] A. M. Sirunyan et al., *Search for supersymmetry in pp collisions at $\sqrt{s}$ = 13 TeV with 137 fb^{-1} in final states with a single lepton using the sum of masses of large-radius jets*, Phys. Rev. D **101** (2020) 052010, arXiv: 1911.07558 [hep-ex].

[116] A. M. Sirunyan et al., *Search for top squark pair production in a final state with two tau leptons in proton-proton collisions at $\sqrt{s}$ = 13 TeV*, JHEP **02** (2020) 015, arXiv: 1910.12932 [hep-ex].

[117] A. M. Sirunyan et al., *Searches for physics beyond the standard model with the M_{T2} variable in hadronic final states with and without disappearing tracks in proton-proton collisions at $\sqrt{s}$ = 13 TeV*, Eur. Phys. J. C **80** (2020) 3, arXiv: 1909.03460 [hep-ex].

[118] A. M. Sirunyan and other, *Search for supersymmetry in proton-proton collisions at 13 TeV in final states with jets and missing transverse momentum*, JHEP **10** (2019) 244, arXiv: 1908.04722 [hep-ex].

[119] *Search for supersymmetry in final states with a single electron or muon using angular correlations and heavy-object identification in proton-proton collisions at $\sqrt{s}$ = 13 TeV*, (2022), Submitted to JHEP, arXiv: 2211.08476 [hep-ex].

[120] *Search for new phenomena in final states with photons, jets and missing transverse momentum in pp collisions at $\sqrt{s}$ = 13 TeV with the ATLAS detector*, (2022), arXiv: 2206.06012 [hep-ex].

[121] G. Aad et al., *Search for new phenomena in pp collisions in final states with tau leptons, b-jets, and missing transverse momentum with the ATLAS detector*, Phys. Rev. D **104** (2021) 112005, arXiv: 2108.07665 [hep-ex].

[122] G. Aad et al., *Search for new phenomena in events with two opposite-charge leptons, jets and missing transverse momentum in pp collisions at $\sqrt{s}$ = 13 TeV with the ATLAS detector*, JHEP **04** (2021) 165, arXiv: 2102.01444 [hep-ex].

[123] G. Aad et al., *Search for new phenomena in final states with b-jets and missing transverse momentum in $\sqrt{s}$ = 13 TeV pp collisions with the ATLAS detector*, JHEP **05** (2021) 093, arXiv: 2101.12527 [hep-ex].

[124] G. Aad et al., *Search for squarks and gluinos in final states with one isolated lepton, jets, and missing transverse momentum at $\sqrt{s}$ = 13 with the ATLAS detector*, Eur. Phys. J. C **81** (2021) 600, [Erratum: Eur.Phys.J.C 81, 956 (2021)], arXiv: 2101.01629 [hep-ex].

[125] G. Aad et al.,
Search for new phenomena with top quark pairs in final states with one lepton, jets, and missing transverse momentum in pp collisions at $\sqrt{s} = 13$ TeV with the ATLAS detector,
JHEP **04** (2021) 174, arXiv: 2012.03799 [hep-ex].

[126] G. Aad et al., *Search for squarks and gluinos in final states with jets and missing transverse momentum using 139 fb^{-1} of $\sqrt{s}$ =13 TeV pp collision data with the ATLAS detector*,
JHEP **02** (2021) 143, arXiv: 2010.14293 [hep-ex].

[127] A. Tumasyan et al., *Search for electroweak production of charginos and neutralinos in proton-proton collisions at $\sqrt{s} = 13$ TeV*, JHEP **04** (2022) 147,
arXiv: 2106.14246 [hep-ex].

[128] A. M. Sirunyan et al., *Search for electroweak production of charginos and neutralinos in multilepton final states in proton-proton collisions at $\sqrt{s} = 13$ TeV*, JHEP **03** (2018) 166,
arXiv: 1709.05406 [hep-ex].

[129] A. Tumasyan et al., *Search for chargino-neutralino production in events with Higgs and W bosons using 137 fb^{-1} of proton-proton collisions at $\sqrt{s} = 13$ TeV*, JHEP **10** (2021) 045,
arXiv: 2107.12553 [hep-ex].

[130] A. M. Sirunyan et al., *Search for supersymmetric partners of electrons and muons in proton-proton collisions at $\sqrt{s} = 13$ TeV*, Phys. Lett. B **790** (2019) 140,
arXiv: 1806.05264 [hep-ex].

[131] *Search for direct pair production of supersymmetric partners of τ leptons in the final state with two hadronically decaying τ leptons and missing transverse momentum in proton-proton collisions at $\sqrt{s} = 13$ TeV*, (2022), Accepted for publication in Phys. Rev. D,
arXiv: 2207.02254 [hep-ex].

[132] A. M. Sirunyan et al., *Search for Supersymmetry with a Compressed Mass Spectrum in Events with a Soft τ Lepton, a Highly Energetic Jet, and Large Missing Transverse Momentum in Proton-Proton Collisions at $\sqrt{s}$ = TeV*, Phys. Rev. Lett. **124** (2020) 041803,
arXiv: 1910.01185 [hep-ex].

[133] A. M. Sirunyan et al.,
Search for supersymmetry using Higgs boson to diphoton decays at $\sqrt{s} = 13$ TeV,
JHEP **11** (2019) 109, arXiv: 1908.08500 [hep-ex].

[134] A. Tumasyan et al.,
Search for electroweak production of charginos and neutralinos at s=13TeV in final states containing hadronic decays of WW, WZ, or WH and missing transverse momentum,
Phys. Lett. B **842** (2023) 137460, arXiv: 2205.09597 [hep-ex].

[135] *Search for direct pair production of sleptons and charginos decaying to two leptons and neutralinos with mass splittings near the W-boson mass in $\sqrt{s} = 13$ TeV pp collisions with the ATLAS detector*, (2022), arXiv: 2209.13935 [hep-ex].

[136] A. M. Sirunyan et al., *Search for direct pair production of supersymmetric partners to the τ lepton in proton-proton collisions at $\sqrt{s} = 13$ TeV*, Eur. Phys. J. C **80** (2020) 189,
arXiv: 1907.13179 [hep-ex].

[137] G. Aad et al., *Search for charginos and neutralinos in final states with two boosted hadronically decaying bosons and missing transverse momentum in pp collisions at $\sqrt{s}$ = 13 TeV with the ATLAS detector*, Phys. Rev. D **104** (2021) 112010, arXiv: 2108.07586 [hep-ex].

[138] G. Aad et al., *Search for chargino–neutralino pair production in final states with three leptons and missing transverse momentum in $\sqrt{s}$ = 13 TeV pp collisions with the ATLAS detector*, Eur. Phys. J. C **81** (2021) 1118, arXiv: 2106.01676 [hep-ex].

[139] G. Aad et al., *Search for chargino-neutralino production with mass splittings near the electroweak scale in three-lepton final states in $\sqrt{s}$=13 TeV pp collisions with the ATLAS detector*, Phys. Rev. D **101** (2020) 072001, arXiv: 1912.08479 [hep-ex].

[140] G. Aad et al., *Searches for electroweak production of supersymmetric particles with compressed mass spectra in $\sqrt{s}$ = 13 TeV pp collisions with the ATLAS detector*, Phys. Rev. D **101** (2020) 052005, arXiv: 1911.12606 [hep-ex].

[141] G. Aad et al., *Search for direct stau production in events with two hadronic τ-leptons in $\sqrt{s}$ = 13 TeV pp collisions with the ATLAS detector*, Phys. Rev. D **101** (2020) 032009, arXiv: 1911.06660 [hep-ex].

[142] G. Aad et al., *Search for direct production of electroweakinos in final states with one lepton, missing transverse momentum and a Higgs boson decaying into two b-jets in pp collisions at $\sqrt{s}$ = 13 TeV with the ATLAS detector*, Eur. Phys. J. C **80** (2020) 691, arXiv: 1909.09226 [hep-ex].

[143] P. Bechtle et al., *What if the LHC does not find supersymmetry in the $\sqrt{s}$ = 7 TeV run?*, Phys. Rev. D **84** (2011) 011701, arXiv: 1102.4693 [hep-ph].

[144] M. Lisanti, P. Schuster, M. Strassler and N. Toro, *Study of LHC Searches for a Lepton and Many Jets*, JHEP **11** (2012) 081, arXiv: 1107.5055 [hep-ph].

[145] G. Aad et al., *Search for R-parity-violating supersymmetry in a final state containing leptons and many jets with the ATLAS experiment using $\sqrt{s}$ = 13TeV proton–proton collision data*, Eur. Phys. J. C **81** (2021) 1023, arXiv: 2106.09609 [hep-ex].

[146] A. M. Sirunyan et al., *Search for top squarks in final states with two top quarks and several light-flavor jets in proton-proton collisions at $\sqrt{s}$ = 13 TeV*, Phys. Rev. D **104** (2021) 032006, arXiv: 2102.06976 [hep-ex].

[147] G. R. Farrar and P. Fayet, *Phenomenology of the Production, Decay, and Detection of New Hadronic States Associated with Supersymmetry*, Phys. Lett. B **76** (1978) 575.

[148] H. K. Dreiner, M. Hanussek and C. Luhn, *What is the discrete gauge symmetry of the R-parity violating MSSM?*, Phys. Rev. D **86** (2012) 055012, arXiv: 1206.6305 [hep-ph].

[149] H. K. Dreiner, M. Kramer and J. Tattersall, *How low can SUSY go? Matching, monojets and compressed spectra*, EPL **99** (2012) 61001, arXiv: 1207.1613 [hep-ph].

[150] F. de Campos et al., *Probing bilinear R-parity violating supergravity at the LHC*, JHEP **05** (2008) 048, arXiv: 0712.2156 [hep-ph].

[151] H. K. Dreiner and M. Thormeier, *Supersymmetric Froggatt-Nielsen models with baryon and lepton number violation*, Phys. Rev. D **69** (2004) 053002, arXiv: hep-ph/0305270.

[152] L. Lee, C. Ohm, A. Soffer and T.-T. Yu, *Collider Searches for Long-Lived Particles Beyond the Standard Model*, Prog. Part. Nucl. Phys. **106** (2019) 210, [Erratum: Prog.Part.Nucl.Phys. 122, 103912 (2022)], arXiv: 1810.12602 [hep-ph].

[153] A. Tumasyan et al., *Search for long-lived particles decaying to a pair of muons in proton-proton collisions at $\sqrt{s} = 13$ TeV*, JHEP **05** (2023) 228, arXiv: 2205.08582 [hep-ex].

[154] *Search for long-lived particles using out-of-time trackless jets in proton-proton collisions at $\sqrt{s} = 13$ TeV*, (2022), Accepted for publication in JHEP, arXiv: 2212.06695 [hep-ex].

[155] A. M. Sirunyan et al., *Search for long-lived particles decaying to jets with displaced vertices in proton-proton collisions at $\sqrt{s} = 13$ TeV*, Phys. Rev. D **104** (2021) 052011, arXiv: 2104.13474 [hep-ex].

[156] J. Alimena et al., *Searching for long-lived particles beyond the Standard Model at the Large Hadron Collider*, J. Phys. G **47** (2020) 090501, arXiv: 1903.04497 [hep-ex].

[157] D. Acosta et al., *Review of opportunities for new long-lived particle triggers in Run 3 of the Large Hadron Collider*, (2021), ed. by J. Alimena et al., arXiv: 2110.14675 [hep-ex].

[158] *Search for long-lived, massive particles in events with displaced vertices and multiple jets in pp collisions at $\sqrt{s} = 13$ TeV with the ATLAS detector*, (2023), arXiv: 2301.13866 [hep-ex].

[159] G. Aad et al., *Search for Displaced Leptons in $\sqrt{s} = 13$ TeV pp Collisions with the ATLAS Detector*, Phys. Rev. Lett. **127** (2021) 051802, arXiv: 2011.07812 [hep-ex].

[160] G. Aad et al., *Search for long-lived, massive particles in events with a displaced vertex and a muon with large impact parameter in pp collisions at $\sqrt{s} = 13$ TeV with the ATLAS detector*, Phys. Rev. D **102** (2020) 032006, arXiv: 2003.11956 [hep-ex].

[161] A. M. Sirunyan et al., *Search for long-lived particles using displaced jets in proton-proton collisions at $\sqrt{s} = 13$ TeV*, Phys. Rev. D **104** (2021) 012015, arXiv: 2012.01581 [hep-ex].

[162] A. Tumasyan et al., *Search for long-lived particles decaying to leptons with large impact parameter in proton–proton collisions at $\sqrt{s} = 13$ TeV*, Eur. Phys. J. C **82** (2022) 153, arXiv: 2110.04809 [hep-ex].

[163] A. Tumasyan et al., *Search for long-lived particles decaying into muon pairs in proton-proton collisions at $\sqrt{s} = 13$ TeV collected with a dedicated high-rate data stream*, JHEP **04** (2022) 062, arXiv: 2112.13769 [hep-ex].

[164] S. Dimopoulos, R. Esmailzadeh, L. J. Hall and G. D. Starkman, *Cross-Sections for Lepton and Baryon Number Violating Processes from Supersymmetry at p anti-p Colliders*, Phys. Rev. D **41** (1990) 2099.

[165] H. K. Dreiner, P. Richardson and M. H. Seymour, *Resonant slepton production in hadron hadron collisions*, Phys. Rev. D **63** (2001) 055008, arXiv: hep-ph/0007228.

[166] H. K. Dreiner and T. Stefaniak, *Bounds on R-parity Violation from Resonant Slepton Production at the LHC*, Phys. Rev. D **86** (2012) 055010, arXiv: 1201.5014 [hep-ph].

[167] A. Monteux, *New signatures and limits on R-parity violation from resonant squark production*, JHEP **03** (2016) 216, arXiv: 1601.03737 [hep-ph].

[168] H. K. Dreiner, D. Köhler, S. Nangia and Z. S. Wang, *Searching for a single photon from lightest neutralino decays in R-parity-violating supersymmetry at FASER*, JHEP **02** (2023) 120, arXiv: 2207.05100 [hep-ph].

[169] H. K. Dreiner and S. Grab, *All Possible Lightest Supersymmetric Particles in R-Parity Violating mSUGRA*, Phys. Lett. B **679** (2009) 45, arXiv: 0811.0200 [hep-ph].

[170] A. M. Sirunyan et al., *Search for new physics in events with two soft oppositely charged leptons and missing transverse momentum in proton-proton collisions at $\sqrt{s}$ = 13 TeV*, Phys. Lett. B **782** (2018) 440, arXiv: 1801.01846 [hep-ex].

[171] G. Aad et al., *Search for electroweak production of charginos and sleptons decaying into final states with two leptons and missing transverse momentum in $\sqrt{s}$ = 13 TeV pp collisions using the ATLAS detector*, Eur. Phys. J. C **80** (2020) 123, arXiv: 1908.08215 [hep-ex].

[172] S. Chatrchyan et al., *Search for Top Squarks in R-Parity-Violating Supersymmetry using Three or More Leptons and B-Tagged Jets*, Phys. Rev. Lett. **111** (2013) 221801, arXiv: 1306.6643 [hep-ex].

[173] A. M. Sirunyan et al., *Search for physics beyond the standard model in multilepton final states in proton-proton collisions at $\sqrt{s}$ = 13 TeV*, JHEP **03** (2020) 051, arXiv: 1911.04968 [hep-ex].

[174] G. Aad et al., *Search for new phenomena in three- or four-lepton events in pp collisions at $\sqrt{s}$ =13 TeV with the ATLAS detector*, Phys. Lett. B **824** (2022) 136832, arXiv: 2107.00404 [hep-ex].

[175] M. Aaboud et al., *Search for lepton-flavor violation in different-flavor, high-mass final states in pp collisions at $\sqrt{s}$ = 13 TeV with the ATLAS detector*, Phys. Rev. D **98** (2018) 092008, arXiv: 1807.06573 [hep-ex].

[176] G. Aad et al., *Search for type-III seesaw heavy leptons in leptonic final states in pp collisions at $\sqrt{s}$ = 13 TeV with the ATLAS detector*, (2022), arXiv: 2202.02039 [hep-ex].

[177] G. Aad et al., *Search for heavy Higgs bosons decaying into two tau leptons with the ATLAS detector using pp collisions at $\sqrt{s}$ = 13 TeV*, Phys. Rev. Lett. **125** (2020) 051801, arXiv: 2002.12223 [hep-ex].

[178] V. Khachatryan et al., *Searches for R-parity-violating supersymmetry in ppcollisions at $\sqrt{s}$ = 8 TeV in final states with 0-4 leptons*, Phys. Rev. D **94** (2016) 112009, arXiv: 1606.08076 [hep-ex].

[179] G. Aad et al., *Search for supersymmetry in events with four or more charged leptons in 139 fb^{-1} of $\sqrt{s}$ = 13 TeV pp collisions with the ATLAS detector*, JHEP **07** (2021) 167, arXiv: 2103.11684 [hep-ex].

[180] A. M. Sirunyan et al., *Search for pair-produced resonances decaying to quark pairs in proton-proton collisions at $\sqrt{s}$ = 13 TeV*, Phys. Rev. D **98** (2018) 112014, arXiv: 1808.03124 [hep-ex].

[181] *Search for resonant and nonresonant production of pairs of dijet resonances in proton-proton collisions at $\sqrt{s}$ = 13 TeV*, (2022), Accepted for publication in JHEP, arXiv: 2206.09997 [hep-ex].

[182] M. Aaboud et al., *A search for pair-produced resonances in four-jet final states at $\sqrt{s}$ = 13 TeV with the ATLAS detector*, Eur. Phys. J. C **78** (2018) 250, arXiv: 1710.07171 [hep-ex].

[183] M. Aaboud et al., *Search for R-parity-violating supersymmetric particles in multi-jet final states produced in p-p collisions at $\sqrt{s}$ = 13 TeV using the ATLAS detector at the LHC*, Phys. Lett. B **785** (2018) 136, arXiv: 1804.03568 [hep-ex].

[184] A. M. Sirunyan et al., *Search for pair-produced three-jet resonances in proton-proton collisions at $\sqrt{s}$ =13 TeV*, Phys. Rev. D **99** (2019) 012010, arXiv: 1810.10092 [hep-ex].

[185] G. Aad et al., *Search for phenomena beyond the Standard Model in events with large b-jet multiplicity using the ATLAS detector at the LHC*, Eur. Phys. J. C **81** (2021) 11, [Erratum: Eur.Phys.J.C 81, 249 (2021)], arXiv: 2010.01015 [hep-ex].

[186] A. M. Sirunyan et al., *Search for pair-produced resonances each decaying into at least four quarks in proton-proton collisions at $\sqrt{s}$ = 13 TeV*, Phys. Rev. Lett. **121** (2018) 141802, arXiv: 1806.01058 [hep-ex].

[187] V. Khachatryan et al., *Search for new phenomena in events with high jet multiplicity and low missing transverse momentum in proton–proton collisions at $\sqrt{s}$ = 8 TeV*, Phys. Lett. B **770** (2017) 257, arXiv: 1608.01224 [hep-ex].

[188] A. M. Sirunyan et al., *Search for R-parity violating supersymmetry in pp collisions at $\sqrt{s}$ = 13 TeV using b jets in a final state with a single lepton, many jets, and high sum of large-radius jet masses*, Phys. Lett. B **783** (2018) 114, arXiv: 1712.08920 [hep-ex].

[189] *Search for pair-produced vector-like leptons in final states with third-generation leptons and at least three b quark jets in proton-proton collisions at $\sqrt{s}$ = 13 TeV*, (2022), Accepted for publication in Phys. Lett. B, arXiv: 2208.09700 [hep-ex].

[190] V. Khachatryan et al., *Search for R-parity violating decays of a top squark in proton-proton collisions at $\sqrt{s}$ = 8 TeV*, Phys. Lett. B **760** (2016) 178, arXiv: 1602.04334 [hep-ex].

[191] *Search for direct production of electroweakinos in final states with one lepton, jets and missing transverse momentum and in p p collisions at $\sqrt{s}$ = 13 TeV with the ATLAS detector*, tech. rep., All figures including auxiliary figures are available at https://atlas.web.cern.ch/Atlas/GROUPS/PHYSICS/CONFNOTES/ATLAS-CONF-2022-059: CERN, 2022, URL: https://cds.cern.ch/record/2826702.

[192] A. M. Sirunyan et al., *Search for singly and pair-produced leptoquarks coupling to third-generation fermions in proton-proton collisions at s=13 TeV*, Phys. Lett. B **819** (2021) 136446, arXiv: 2012.04178 [hep-ex].

[193] *Search for direct production of winos and higgsinos in events with two same-sign or three leptons in pp collision data at $\sqrt{s}$ = 13 TeV with the ATLAS detector*, tech. rep., All figures including auxiliary figures are available at https://atlas.web.cern.ch/Atlas/GROUPS/PHYSICS/CONFNOTES/ATLAS-CONF-2022-057: CERN, 2022, URL: https://cds.cern.ch/record/2826603.

[194] M. Aaboud et al., *Search for B-L R -parity-violating top squarks in $\sqrt{s}$ =13 TeV pp collisions with the ATLAS experiment*, Phys. Rev. D **97** (2018) 032003, arXiv: 1710.05544 [hep-ex].

[195] *Search for pair-produced scalar and vector leptoquarks decaying into third-generation quarks and first- or second-generation leptons in pp collisions with the ATLAS detector*, (2022), arXiv: 2210.04517 [hep-ex].

[196] G. Aad et al., *Search for pair production of scalar leptoquarks decaying into first- or second-generation leptons and top quarks in proton–proton collisions at $\sqrt{s}$ = 13 TeV with the ATLAS detector*, Eur. Phys. J. C **81** (2021) 313, arXiv: 2010.02098 [hep-ex].

[197] A. M. Sirunyan et al., *Search for an excited lepton that decays via a contact interaction to a lepton and two jets in proton-proton collisions at $\sqrt{s}$ = 13 TeV*, JHEP **05** (2020) 052, arXiv: 2001.04521 [hep-ex].

[198] *Search for pair production of squarks or gluinos decaying via sleptons or weak bosons in final states with two same-sign or three leptons with the ATLAS detector*, tech. rep., All figures including auxiliary figures are available at https://atlas.web.cern.ch/Atlas/GROUPS/PHYSICS/CONFNOTES/ATLAS-CONF-2023-017: CERN, 2023, URL: https://cds.cern.ch/record/2855335.

[199] M. Aaboud et al., *Search for pair production of higgsinos in final states with at least three b-tagged jets in $\sqrt{s}$ = 13 TeV pp collisions using the ATLAS detector*, Phys. Rev. D **98** (2018) 092002, arXiv: 1806.04030 [hep-ex].

[200] A. M. Sirunyan et al., *Search for Higgsino pair production in pp collisions at $\sqrt{s}$ = 13 TeV in final states with large missing transverse momentum and two Higgs bosons decaying via $H \to b\bar{b}$*, Phys. Rev. D **97** (2018) 032007, arXiv: 1709.04896 [hep-ex].

[201] J. Alwall et al., *The automated computation of tree-level and next-to-leading order differential cross sections, and their matching to parton shower simulations*, JHEP **07** (2014) 079, arXiv: 1405.0301 [hep-ph].

[202] T. Sjöstrand et al., *An introduction to PYTHIA 8.2*, Comput. Phys. Commun. **191** (2015) 159, arXiv: 1410.3012 [hep-ph].

[203] https://feynrules.irmp.ucl.ac.be/wiki/RPVMSSM, accessed 2021-12-01.

[204] D. Dercks et al., *CheckMATE 2: From the model to the limit*, Comput. Phys. Commun. **221** (2017) 383, arXiv: 1611.09856 [hep-ph].

[205] M. Cacciari, G. P. Salam and G. Soyez, *FastJet User Manual*, Eur. Phys. J. C **72** (2012) 1896, arXiv: 1111.6097 [hep-ph].

[206] M. Cacciari and G. P. Salam, *Dispelling the N^3 myth for the k_t jet-finder*, Phys. Lett. B **641** (2006) 57, arXiv: hep-ph/0512210.

[207] M. Cacciari, G. P. Salam and G. Soyez, *The anti-k_t jet clustering algorithm*, JHEP **04** (2008) 063, arXiv: 0802.1189 [hep-ph].

[208] A. L. Read, *Presentation of search results: The CL(s) technique*, J. Phys. G **28** (2002) 2693, ed. by M. R. Whalley and L. Lyons.

[209] https://checkmate.hepforge.org/, accessed 2022-12-01.

[210] J. de Favereau et al., *DELPHES 3, A modular framework for fast simulation of a generic collider experiment*, JHEP **02** (2014) 057, arXiv: 1307.6346 [hep-ex].

[211] M. Aaboud et al., *Search for supersymmetry in final states with two same-sign or three leptons and jets using 36 fb^{-1} of $\sqrt{s}$ = 13 TeV pp collision data with the ATLAS detector*, JHEP **09** (2017) 084, [Erratum: JHEP 08, 121 (2019)], arXiv: 1706.03731 [hep-ex].

[212] C. Borschensky et al., *Squark and gluino production cross sections in pp collisions at $\sqrt{s}$ = 13, 14, 33 and 100 TeV*, Eur. Phys. J. C **74** (2014) 3174, arXiv: 1407.5066 [hep-ph].

[213] S. Bornhauser, M. Drees, H. K. Dreiner and J. S. Kim, *Electroweak contributions to squark pair production at the LHC*, Phys. Rev. D **76** (2007) 095020, arXiv: 0709.2544 [hep-ph].

[214] *Beam Performance Tracking in the CERN accelerator complex*, https://bpt.web.cern.ch/lhc/, [Online; accessed 06-February-2023], 2023.

[215] *High-Luminosity Large Hadron Collider (HL-LHC): Technical Design Report V. 0.1*, **4/2017** (2017), ed. by G. Apollinari et al., Report number CERN -2017-007-M (2017); doi=10.23731/CYRM-2017-004.

[216] *First Level Track Jet Trigger for Displaced Jets at High Luminosity LHC*, tech. rep., CERN, 2018, URL: https://cds.cern.ch/record/2647987.

[217] B. Bhattacherjee, S. Mukherjee, R. Sengupta and P. Solanki, *Triggering long-lived particles in HL-LHC and the challenges in the rst stage of the trigger system*, JHEP **08** (2020) 141, arXiv: 2003.03943 [hep-ph].

[218] Y. Gershtein, *CMS Hardware Track Trigger: New Opportunities for Long-Lived Particle Searches at the HL-LHC*, Phys. Rev. D **96** (2017) 035027, arXiv: 1705.04321 [hep-ph].

[219] Y. Gershtein and S. Knapen, *Trigger strategy for displaced muon pairs following the CMS phase II upgrades*, Phys. Rev. D **101** (2020) 032003, arXiv: 1907.00007 [hep-ex].

[220] J. A. Evans, A. Gandrakota, S. Knapen and H. Routray,
Searching for exotic B -meson decays enabled by the CMS L1 track trigger,
Phys. Rev. D **103** (2021) 015026, arXiv: 2008.06918 [hep-ph].

[221] Y. Gershtein, S. Knapen and D. Redigolo,
Probing naturally light singlets with a displaced vertex trigger,
Phys. Lett. B **823** (2021) 136758, arXiv: 2012.07864 [hep-ph].

[222] R. Aaij et al., *Test of Lepton Flavor Universality by the measurement of the $B^0 \to D^{*-}\tau^+\nu_\tau$ branching fraction using three-prong τ decays*, Phys. Rev. D **97** (2018) 072013,
arXiv: 1711.02505 [hep-ex].

[223] R. Aaij et al., *Test of lepton universality in beauty-quark decays*, Nature Phys. **18** (2022) 277,
arXiv: 2103.11769 [hep-ex].

[224] G. W. Bennett et al.,
Measurement of the positive muon anomalous magnetic moment to 0.7 ppm,
Phys. Rev. Lett. **89** (2002) 101804, [Erratum: Phys.Rev.Lett. 89, 129903 (2002)],
arXiv: hep-ex/0208001.

[225] G. W. Bennett et al.,
Measurement of the negative muon anomalous magnetic moment to 0.7 ppm,
Phys. Rev. Lett. **92** (2004) 161802, arXiv: hep-ex/0401008.

[226] G. W. Bennett et al.,
Final Report of the Muon E821 Anomalous Magnetic Moment Measurement at BNL,
Phys. Rev. D **73** (2006) 072003, arXiv: hep-ex/0602035.

[227] B. Abi et al., *Measurement of the Positive Muon Anomalous Magnetic Moment to 0.46 ppm*,
Phys. Rev. Lett. **126** (2021) 141801, arXiv: 2104.03281 [hep-ex].

[228] M. Bauer and M. Neubert,
Minimal Leptoquark Explanation for the $R_{D^{(*)}}$, R_K , and $(g-2)_\mu$ Anomalies,
Phys. Rev. Lett. **116** (2016) 141802, arXiv: 1511.01900 [hep-ph].

[229] P. Fileviez Perez, C. Murgui and A. D. Plascencia,
Leptoquarks and matter unification: Flavor anomalies and the muon g-2,
Phys. Rev. D **104** (2021) 035041, arXiv: 2104.11229 [hep-ph].

[230] S. Trifinopoulos, *B -physics anomalies: The bridge between R -parity violating supersymmetry and flavored dark matter*, Phys. Rev. D **100** (2019) 115022,
arXiv: 1904.12940 [hep-ph].

[231] Q.-Y. Hu, Y.-D. Yang and M.-D. Zheng,
Revisiting the B-physics anomalies in R-parity violating MSSM,
Eur. Phys. J. C **80** (2020) 365, arXiv: 2002.09875 [hep-ph].

[232] M. Chakraborti, S. Iwamoto, J. S. Kim, R. Mase lek and K. Sakurai,
Supersymmetric explanation of the muon g – 2 anomaly with and without stable neutralino,
JHEP **08** (2022) 124, arXiv: 2202.12928 [hep-ph].

[233] J. Ohnemus, S. Rudaz, T. F. Walsh and P. M. Zerwas,
Single leptoquark production at hadron colliders, Phys. Lett. B **334** (1994) 203,
arXiv: hep-ph/9406235.

[234] V. Bertone, S. Carrazza, D. Pagani and M. Zaro, *On the Impact of Lepton PDFs*, JHEP **11** (2015) 194, arXiv: 1508.07002 [hep-ph].

[235] L. Buonocore, P. Nason, F. Tramontano and G. Zanderighi, *Leptons in the proton*, JHEP **08** (2020) 019, arXiv: 2005.06477 [hep-ph].

[236] S. Chatrchyan et al., *Search for Microscopic Black Holes in pp Collisions at $\sqrt{s} = 8$ TeV*, JHEP **07** (2013) 178, arXiv: 1303.5338 [hep-ex].

[237] G. Aad et al., *Search for microscopic black holes and string balls in final states with leptons and jets with the ATLAS detector at sqrt(s) = 8 TeV*, JHEP **08** (2014) 103, arXiv: 1405.4254 [hep-ex].

[238] *A model independent general search for new phenomena with the ATLAS detector at $\sqrt{s} = 13$ TeV*, (2017), ATLAS-CONF-2017-001.

[239] *MUSiC, a Model Unspecific Search for New Physics, in pp Collisions at $\sqrt{s} = 8$ TeV*, (), report number: CMS-PAS-EXO-14-016 (2017).

[240] M. Aaboud et al., *Search for new phenomena in a lepton plus high jet multiplicity final state with the ATLAS experiment using $\sqrt{s} = 13$ TeV proton-proton collision data*, JHEP **09** (2017) 088, arXiv: 1704.08493 [hep-ex].

[241] U. Haisch and G. Polesello, *Resonant third-generation leptoquark signatures at the Large Hadron Collider*, JHEP **05** (2021) 057, arXiv: 2012.11474 [hep-ph].

[242] W. Buchmuller, R. Ruckl and D. Wyler, *Leptoquarks in Lepton - Quark Collisions*, Phys. Lett. B **191** (1987) 442, [Erratum: Phys.Lett.B 448, 320–320 (1999)].

[243] J. Butterworth and H. K. Dreiner, *R-parity violation at HERA*, Nucl. Phys. B **397** (1993) 3, arXiv: hep-ph/9211204.

[244] H. K. Dreiner and P. Morawitz, *Signals for supersymmetry at HERA*, Nucl. Phys. B **428** (1994) 31, [Erratum: Nucl.Phys.B 574, 874–875 (2000)], arXiv: hep-ph/9405253.

[245] A. Crivellin, D. Müller and L. Schnell, *Combined constraints on first generation leptoquarks*, Phys. Rev. D **103** (2021) 115023, arXiv: 2104.06417 [hep-ph].

[246] A. J. Buras, A. Crivellin, F. Kirk, C. A. Manzari and M. Montull, *Global analysis of leptophilic Z' bosons*, JHEP **06** (2021) 068, arXiv: 2104.07680 [hep-ph].

[247] H. K. Dreiner, H. Murayama and M. Thormeier, *Anomalous flavor U(1)(X) for everything*, Nucl. Phys. B **729** (2005) 278, arXiv: hep-ph/0312012.

[248] C. Csaki, E. Kuflik and T. Volansky, *Dynamical R-Parity Violation*, Phys. Rev. Lett. **112** (2014) 131801, arXiv: 1309.5957 [hep-ph].

[249] H. K. Dreiner, C. Luhn and M. Thormeier, *What is the discrete gauge symmetry of the MSSM?*, Phys. Rev. D **73** (2006) 075007, arXiv: hep-ph/0512163.

[250] B. C. Allanach, A. Dedes and H. K. Dreiner, *Two loop supersymmetric renormalization group equations including R-parity violation and aspects of unification*, Phys. Rev. D **60** (1999) 056002, [Erratum: Phys.Rev.D 86, 039906 (2012)], arXiv: hep-ph/9902251.

[251] B. C. Allanach, *SOFTSUSY: a program for calculating supersymmetric spectra*, Comput. Phys. Commun. **143** (2002) 305, arXiv: hep-ph/0104145.

[252] B. C. Allanach, A. Dedes and H. K. Dreiner, *Bounds on R-parity violating couplings at the weak scale and at the GUT scale*, Phys. Rev. D **60** (1999) 075014, arXiv: hep-ph/9906209.

[253] P. Richardson, *Simulations of R-parity violating SUSY models*, Ph.D. thesis, Oxford U., arXiv:hep-ph/0101105, PhD thesis, 2000, arXiv: hep-ph/0101105.

[254] H. K. Dreiner, P. Richardson and M. H. Seymour, *Parton shower simulations of R-parity violating supersymmetric models*, JHEP **04** (2000) 008, arXiv: hep-ph/9912407.

[255] G. Corcella et al., *HERWIG 6: An Event generator for hadron emission reactions with interfering gluons (including supersymmetric processes)*, JHEP **01** (2001) 010, arXiv: hep-ph/0011363.

[256] W. Porod, *SPheno, a program for calculating supersymmetric spectra, SUSY particle decays and SUSY particle production at e+ e- colliders*, Comput. Phys. Commun. **153** (2003) 275, arXiv: hep-ph/0301101.

[257] V. Khachatryan et al., *Search for supersymmetry in events with one lepton and multiple jets in proton-proton collisions at $\sqrt{s}$ = 13 TeV*, Phys. Rev. D **95** (2017) 012011, arXiv: 1609.09386 [hep-ex].

[258] M. Hirsch, H. V. Klapdor-Kleingrothaus and S. G. Kovalenko, *Supersymmetry and neutrinoless double beta decay*, Phys. Rev. D **53** (1996) 1329, arXiv: hep-ph/9502385.

[259] H. K. Dreiner, S. Grab, M. Kramer and M. K. Trenkel, *Supersymmetric NLO QCD corrections to resonant slepton production and signals at the Tevatron and the CERN LHC*, Phys. Rev. D **75** (2007) 035003, arXiv: hep-ph/0611195.

[260] A. Buckley et al., *LHAPDF6: parton density access in the LHC precision era*, Eur. Phys. J. C **75** (2015) 132, arXiv: 1412.7420 [hep-ph].

[261] R. Gauld, *Precise predictions for multi-TeV and PeV energy neutrino scattering rates*, Phys. Rev. D **100** (2019) 091301, arXiv: 1905.03792 [hep-ph].

[262] A. Garcia, R. Gauld, A. Heijboer and J. Rojo, *Complete predictions for high-energy neutrino propagation in matter*, JCAP **09** (2020) 025, arXiv: 2004.04756 [hep-ph].

[263] A. Greljo and N. Selimovic, *Lepton-Quark Fusion at Hadron Colliders, precisely*, JHEP **03** (2021) 279, arXiv: 2012.02092 [hep-ph].

[264] V. A. Mitsou, *SUSY searches in ATLAS and CMS*, tech. rep., CERN, 2020, URL: https://cds.cern.ch/record/2714089.

[265] M. Hirsch, H. V. Klapdor-Kleingrothaus and S. G. Kovalenko,
New constraints on R-parity broken supersymmetry from neutrinoless double beta decay,
Phys. Rev. Lett. **75** (1995) 17.

[266] G. Aad et al., *Search for Quantum Black Hole Production in High-Invariant-Mass Lepton+Jet Final States Using pp Collisions at $\sqrt{s}$ = 8 TeV and the ATLAS Detector*,
Phys. Rev. Lett. **112** (2014) 091804, arXiv: 1311.2006 [hep-ex].

[267] M. L. Mangano, M. Moretti and R. Pittau, *Multijet matrix elements and shower evolution in hadronic collisions: $Wb\bar{b}$ + n jets as a case study*, Nucl. Phys. B **632** (2002) 343,
arXiv: hep-ph/0108069.

[268] J. Alwall et al., *Comparative study of various algorithms for the merging of parton showers and matrix elements in hadronic collisions*, Eur. Phys. J. C **53** (2008) 473,
arXiv: 0706.2569 [hep-ph].

[269] J. Alwall, S. de Visscher and F. Maltoni,
QCD radiation in the production of heavy colored particles at the LHC, JHEP **02** (2009) 017,
arXiv: 0810.5350 [hep-ph].

[270] https://www.physics.sjtu.edu.cn/madgraphschool/sites/www.physics.sjtu.edu.cn.madgraphschool/files/tuto_matching.pdf, accessed 2021-12-01.

[271] J. Huston, *LO, NLO, LO* and Jet Algorithms*, PoS **RADCOR2009** (2010) 079,
arXiv: 1001.2581 [hep-ph].

[272] C. F. Berger et al.,
Next-to-Leading Order QCD Predictions for W+3-Jet Distributions at Hadron Colliders,
Phys. Rev. D **80** (2009) 074036, arXiv: 0907.1984 [hep-ph].

[273] *ATLAS simulation of boson plus jets processes in Run 2*,
(2017), report number: ATL-PHYS-PUB-2017-006 (2017).

[274] A. M. Sirunyan et al., *Measurement of the differential cross sections for the associated production of a W boson and jets in proton-proton collisions at $\sqrt{s}$ = 13 TeV*,
Phys. Rev. D **96** (2017) 072005, arXiv: 1707.05979 [hep-ex].

[275] A. M. Sirunyan et al., *Search for a heavy resonance decaying to a top quark and a vector-like top quark in the lepton+jets final state in pp collisions at $\sqrt{s}$ = 13 TeV*,
Eur. Phys. J. C **79** (2019) 208, arXiv: 1812.06489 [hep-ex].

[276] G. Cowan, K. Cranmer, E. Gross and O. Vitells,
Asymptotic formulae for likelihood-based tests of new physics,
Eur. Phys. J. C **71** (2011) 1554, [Erratum: Eur.Phys.J.C 73, 2501 (2013)],
arXiv: 1007.1727 [physics.data-an].

[277] A. M. Sirunyan et al., *Search for resonant and nonresonant new phenomena in high-mass dilepton final states at $\sqrt{s}$ = 13 TeV*, JHEP **07** (2021) 208, arXiv: 2103.02708 [hep-ex].

[278] V. D. Barger, G. F. Giudice and T. Han,
Some New Aspects of Supersymmetry R-Parity Violating Interactions,
Phys. Rev. D **40** (1989) 2987.

[279] G. Aad et al., *Search for pairs of scalar leptoquarks decaying into quarks and electrons or muons in $\sqrt{s}$ = 13 TeV pp collisions with the ATLAS detector*, JHEP **10** (2020) 112, arXiv: 2006.05872 [hep-ex].

[280] W. Beenakker et al., *Squark and Gluino Hadroproduction*, Int. J. Mod. Phys. A **26** (2011) 2637, arXiv: 1105.1110 [hep-ph].

[281] M. Hirsch, M. A. Diaz, W. Porod, J. C. Romao and J. W. F. Valle, *Neutrino masses and mixings from supersymmetry with bilinear R parity violation: A Theory for solar and atmospheric neutrino oscillations*, Phys. Rev. D **62** (2000) 113008, [Erratum: Phys.Rev.D 65, 119901 (2002)], arXiv: hep-ph/0004115.

[282] A. S. Joshipura and M. Nowakowski, *'Just so' oscillations in supersymmetric standard model*, Phys. Rev. D **51** (1995) 2421, arXiv: hep-ph/9408224.

[283] M. Nowakowski and A. Pilaftsis, *W and Z boson interactions in supersymmetric models with explicit R-parity violation*, Nucl. Phys. B **461** (1996) 19, arXiv: hep-ph/9508271.

[284] T. Banks, Y. Grossman, E. Nardi and Y. Nir, *Supersymmetry without R-parity and without lepton number*, Phys. Rev. D **52** (1995) 5319, arXiv: hep-ph/9505248.

[285] S. Davidson and M. Losada, *Neutrino masses in the R(p) violating MSSM*, JHEP **05** (2000) 021, arXiv: hep-ph/0005080.

[286] A. Abada, S. Davidson and M. Losada, *Neutrino masses and mixings in the MSSM with soft bilinear R(p) violation*, Phys. Rev. D **65** (2002) 075010, arXiv: hep-ph/0111332.

[287] R. Hempfling, *Neutrino masses and mixing angles in SUSY GUT theories with explicit R-parity breaking*, Nucl. Phys. B **478** (1996) 3, arXiv: hep-ph/9511288.

[288] E. J. Chun and S. K. Kang, *One loop corrected neutrino masses and mixing in supersymmetric standard model without R-parity*, Phys. Rev. D **61** (2000) 075012, arXiv: hep-ph/9909429.

[289] D. Kaplan and A. E. Nelson, *Solar and atmospheric neutrino oscillations from bilinear R parity violation*, JHEP **01** (2000) 033, arXiv: hep-ph/9901254.

[290] Y. Grossman and H. E. Haber, *Sneutrino mixing phenomena*, Phys. Rev. Lett. **78** (1997) 3438, arXiv: hep-ph/9702421.

[291] Y. Grossman and H. E. Haber, *(S)neutrino properties in R-parity violating supersymmetry. 1. CP conserving phenomena*, Phys. Rev. D **59** (1999) 093008, arXiv: hep-ph/9810536.

[292] Y. Grossman and S. Rakshit, *Neutrino masses in R-parity violating supersymmetric models*, Phys. Rev. D **69** (2004) 093002, arXiv: hep-ph/0311310.

[293] M. Diaz, M. Hirsch, W. Porod, J. Romao and J. Valle, *Solar neutrino masses and mixing from bilinear R parity broken supersymmetry: Analytical versus numerical results*, Phys. Rev. D **68** (2003) 013009, [Erratum: Phys.Rev.D 71, 059904 (2005)], arXiv: hep-ph/0302021.

[294] S. Davidson and M. Losada, *Basis independent neutrino masses in the R(p) violating MSSM*, Phys. Rev. D **65** (2002) 075025, arXiv: hep-ph/0010325.

[295] A. Dedes, S. Rimmer and J. Rosiek, *Neutrino masses in the lepton number violating MSSM*, JHEP **08** (2006) 005, arXiv: hep-ph/0603225.

[296] B. Allanach and C. Kom, *Lepton number violating mSUGRA and neutrino masses*, JHEP **04** (2008) 081, arXiv: 0712.0852 [hep-ph].

[297] F. Borzumati, Y. Grossman, E. Nardi and Y. Nir, *Neutrino masses and mixing in supersymmetric models without R parity*, Phys. Lett. B **384** (1996) 123, arXiv: hep-ph/9606251.

[298] S. Rakshit, *Neutrino masses and R-parity violation*, Mod. Phys. Lett. A **19** (2004) 2239, arXiv: hep-ph/0406168.

[299] H. K. Dreiner, M. Hanussek, J.-S. Kim and C. Kom, *Neutrino masses and mixings in the baryon triality constrained minimal supersymmetric standard model*, Phys. Rev. D **84** (2011) 113005, arXiv: 1106.4338 [hep-ph].

[300] M. Drees, S. Pakvasa, X. Tata and T. ter Veldhuis, *A Supersymmetric resolution of solar and atmospheric neutrino puzzles*, Phys. Rev. D **57** (1998) 5335, arXiv: hep-ph/9712392.

[301] E. Chun, S. Kang, C. Kim and U. Lee, *Supersymmetric neutrino masses and mixing with R-parity violation*, Nucl. Phys. B **544** (1999) 89, arXiv: hep-ph/9807327.

[302] A. S. Joshipura and S. K. Vempati, *Sneutrino vacuum expectation values and neutrino anomalies through trilinear R-parity violation*, Phys. Rev. D **60** (1999) 111303, arXiv: hep-ph/9903435.

[303] K. Choi, K. Hwang and E. J. Chun, *Atmospheric and solar neutrino masses from horizontal U(1) symmetry*, Phys. Rev. D **60** (1999) 031301, arXiv: hep-ph/9811363.

[304] O. C. Kong, *Neutrino oscillations and flavor structure of supersymmetry without R-parity*, Mod. Phys. Lett. A **14** (1999) 903, arXiv: hep-ph/9808304.

[305] S. Rakshit, G. Bhattacharyya and A. Raychaudhuri, *R-parity violating trilinear couplings and recent neutrino data*, Phys. Rev. D **59** (1999) 091701, arXiv: hep-ph/9811500.

[306] R. Adhikari and G. Omanovic, *LSND, solar and atmospheric neutrino oscillation experiments, and R-parity violating supersymmetry*, Phys. Rev. D **59** (1999) 073003.

[307] A. Abada and M. Losada, *Constraints on both bilinear and trilinear R-parity violating couplings from neutrino laboratories and astrophysics data*, Phys. Lett. B **492** (2000) 310, arXiv: hep-ph/0007041.

[308] J. Romao, M. Diaz, M. Hirsch, W. Porod and J. Valle,
A Supersymmetric solution to the solar and atmospheric neutrino problems,
Phys. Rev. D **61** (2000) 071703, arXiv: hep-ph/9907499.

[309] K.-m. Cheung and O. C. Kong, *Zee neutrino mass model in SUSY framework*,
Phys. Rev. D **61** (2000) 113012, arXiv: hep-ph/9912238.

[310] H. K. Dreiner, J. S. Kim, O. Lebedev and M. Thormeier,
Supersymmetric Jarlskog invariants: The Neutrino sector, Phys. Rev. D **76** (2007) 015006,
arXiv: hep-ph/0703074.

[311] H. K. Dreiner, M. Hanussek, J. S. Kim and S. Sarkar,
Gravitino cosmology with a very light neutralino, Phys. Rev. D **85** (2012) 065027,
arXiv: 1111.5715 [hep-ph].

[312] I. Esteban, M. Gonzalez-Garcia, M. Maltoni, T. Schwetz and A. Zhou,
The fate of hints: updated global analysis of three-flavor neutrino oscillations,
JHEP **09** (2020) 178, arXiv: 2007.14792 [hep-ph].

[313] J. Hosaka et al., *Solar neutrino measurements in super-Kamiokande-I*,
Phys. Rev. D **73** (2006) 112001, arXiv: hep-ex/0508053.

[314] Y. Ashie et al., *Evidence for an oscillatory signature in atmospheric neutrino oscillation*,
Phys. Rev. Lett. **93** (2004) 101801, arXiv: hep-ex/0404034.

[315] K. J. Kelly, P. A. N. Machado, S. J. Parke, Y. F. Perez-Gonzalez and R. Z. Funchal,
Neutrino mass ordering in light of recent data, Phys. Rev. D **103** (2021) 013004,
arXiv: 2007.08526 [hep-ph].

[316] P. F. Harrison, D. H. Perkins and W. G. Scott,
Tri-bimaximal mixing and the neutrino oscillation data, Phys. Lett. B **530** (2002) 167,
arXiv: hep-ph/0202074.

[317] F. James and M. Roos, *Minuit: A System for Function Minimization and Analysis of the Parameter Errors and Correlations*, Comput. Phys. Commun. **10** (1975) 343.

[318] A. Dedes, H. K. Dreiner and P. Richardson,
Attempts at explaining the NuTeV observation of dimuon events,
Phys. Rev. D **65** (2001) 015001, arXiv: hep-ph/0106199.

[319] P. Agrawal et al., *Feebly-interacting particles: FIPs 2020 workshop report*,
Eur. Phys. J. C **81** (2021) 1015, arXiv: 2102.12143 [hep-ph].

[320] J. L. Feng et al.,
"Planning the Future of U.S. Particle Physics (Snowmass 2013): Chapter 4: Cosmic Frontier",
Snowmass 2013: Snowmass on the Mississippi, 2014, arXiv: 1401.6085 [hep-ex].

[321] J. L. Hewett et al.,
"Planning the Future of U.S. Particle Physics (Snowmass 2013): Chapter 2: Intensity Frontier",
Snowmass 2013: Snowmass on the Mississippi, 2014, arXiv: 1401.6077 [hep-ex].

[322] J. Alexander et al., "Dark Sectors 2016 Workshop: Community Report", 2016,
arXiv: 1608.08632 [hep-ph].

[323] M. Battaglieri et al.,
"US Cosmic Visions: New Ideas in Dark Matter 2017: Community Report",
U.S. Cosmic Visions: New Ideas in Dark Matter, 2017, arXiv: 1707.04591 [hep-ph].

[324] J. Beacham et al.,
Physics Beyond Colliders at CERN: Beyond the Standard Model Working Group Report,
J. Phys. G **47** (2020) 010501, arXiv: 1901.09966 [hep-ex].

[325] C. A. Argüelles et al., *New opportunities at the next-generation neutrino experiments I: BSM neutrino physics and dark matter*, Rept. Prog. Phys. **83** (2020) 124201,
arXiv: 1907.08311 [hep-ph].

[326] R. K. Ellis et al.,
Physics Briefing Book: Input for the European Strategy for Particle Physics Update 2020,
(2019), arXiv: 1910.11775 [hep-ex].

[327] D. Curtin et al., *Long-Lived Particles at the Energy Frontier: The MATHUSLA Physics Case*,
Rept. Prog. Phys. **82** (2019) 116201, arXiv: 1806.07396 [hep-ph].

[328] S. Knapen and S. Lowette, *A guide to hunting long-lived particles at the LHC*, (2022),
arXiv: 2212.03883 [hep-ph].

[329] T. Asaka and M. Shaposhnikov,
The νMSM, dark matter and baryon asymmetry of the universe, Phys. Lett. B **620** (2005) 17,
arXiv: hep-ph/0505013.

[330] F. Capozzi et al., *Unfinished fabric of the three neutrino paradigm*,
Phys. Rev. D **104** (2021) 083031, arXiv: 2107.00532 [hep-ph].

[331] P. Minkowski, $\mu \to e\gamma$ *at a Rate of One Out of* 10^9 *Muon Decays?*,
Phys. Lett. B **67** (1977) 421.

[332] T. Yanagida, *Horizontal gauge symmetry and masses of neutrinos*,
Conf. Proc. C **7902131** (1979) 95, ed. by O. Sawada and A. Sugamoto.

[333] M. Gell-Mann, P. Ramond and R. Slansky, *Complex Spinors and Unified Theories*,
Conf. Proc. C **790927** (1979) 315, arXiv: 1306.4669 [hep-th].

[334] R. N. Mohapatra and G. Senjanovic, *Neutrino Mass and Spontaneous Parity Nonconservation*,
Phys. Rev. Lett. **44** (1980) 912.

[335] J. Schechter and J. W. F. Valle, *Neutrino Masses in SU(2) x U(1) Theories*,
Phys. Rev. D **22** (1980) 2227.

[336] E. K. Akhmedov, M. Lindner, E. Schnapka and J. W. F. Valle,
Left-right symmetry breaking in NJL approach, Phys. Lett. B **368** (1996) 270,
arXiv: hep-ph/9507275.

[337] E. K. Akhmedov, M. Lindner, E. Schnapka and J. W. F. Valle,
Dynamical left-right symmetry breaking, Phys. Rev. D **53** (1996) 2752,
arXiv: hep-ph/9509255.

[338] M. Malinsky, J. C. Romao and J. W. F. Valle,
Novel supersymmetric SO(10) seesaw mechanism, Phys. Rev. Lett. **95** (2005) 161801,
arXiv: hep-ph/0506296.

[339] R. N. Mohapatra and J. W. F. Valle,
Neutrino Mass and Baryon Number Nonconservation in Superstring Models,
Phys. Rev. D **34** (1986) 1642.

[340] M. C. Gonzalez-Garcia and J. W. F. Valle,
Fast Decaying Neutrinos and Observable Flavor Violation in a New Class of Majoron Models,
Phys. Lett. B **216** (1989) 360.

[341] HNL,
"Heavy Neutrino Limits: `https://github.com/mhostert/Heavy-Neutrino-Limits`".

[342] E. Fernández-Martínez, M. González-López, J. Hernández-García, M. Hostert and J. López-Pavón, *Effective portals to heavy neutral leptons*, (2023),
arXiv: 2304.06772 [hep-ph].

[343] G. Aad et al., *Search for long-lived charginos based on a disappearing-track signature using 136 fb^{-1} of pp collisions at $\sqrt{s} = 13$ TeV with the ATLAS detector*,
Eur. Phys. J. C **82** (2022) 606, arXiv: 2201.02472 [hep-ex].

[344] A. M. Sirunyan et al.,
Search for disappearing tracks in proton-proton collisions at $\sqrt{s} = 13$ TeV,
Phys. Lett. B **806** (2020) 135502, arXiv: 2004.05153 [hep-ex].

[345] S. Profumo, *Hunting the lightest lightest neutralinos*, Phys. Rev. D **78** (2008) 023507,
arXiv: 0806.2150 [hep-ph].

[346] I. Gogoladze, J. D. Lykken, C. Macesanu and S. Nandi,
Implications of a Massless Neutralino for Neutrino Physics, Phys. Rev. D **68** (2003) 073004,
arXiv: hep-ph/0211391.

[347] H. K. Dreiner et al., *Rare meson decays into very light neutralinos*,
Phys. Rev. D **80** (2009) 035018, arXiv: 0905.2051 [hep-ph].

[348] J. A. Grifols, E. Masso and S. Peris, *Photinos From Gravitational Collapse*,
Phys. Lett. B **220** (1989) 591.

[349] J. R. Ellis, K. A. Olive, S. Sarkar and D. W. Sciama,
Low Mass Photinos and Supernova SN1987A, Phys. Lett. B **215** (1988) 404.

[350] K. Lau, *Constraints on supersymmetry from SN1987A*, Phys. Rev. D **47** (1993) 1087.

[351] H. K. Dreiner, M. Kramer and B. O'Leary, *Bounds on R-parity violating supersymmetric couplings from leptonic and semi-leptonic meson decays*, Phys. Rev. D **75** (2007) 114016,
arXiv: hep-ph/0612278.

[352] P. Bechtle et al., *Killing the cMSSM softly*, Eur. Phys. J. C **76** (2016) 96,
arXiv: 1508.05951 [hep-ph].

[353] R. N. Mohapatra, *Supersymmetry and R-parity: an Overview*, Phys. Scripta **90** (2015) 088004,
arXiv: 1503.06478 [hep-ph].

[354] F. Domingo and H. K. Dreiner, *Decays of a bino-like particle in the low-mass regime*, (2022),
arXiv: 2205.08141 [hep-ph].

[355] H. K. Dreiner et al., *The ABC of RPV: Classification of R-Parity Violating Signatures at the LHC for Small Couplings*, (2023), arXiv: 2306.07317 [hep-ph].

[356] Q.-Y. Hu and L.-L. Huang,
Explaining $b \to s\ell^+\ell^-$ data by sneutrinos in the R -parity violating MSSM,
Phys. Rev. D **101** (2020) 035030, arXiv: 1912.03676 [hep-ph].

[357] M.-D. Zheng and H.-H. Zhang, *Studying the $b \to s\ell^+\ell^-$ Anomalies and $(g-2)_\mu$ in RPV-MSSM Framework with Inverse Seesaw*, (2021), arXiv: 2105.06954 [hep-ph].

[358] P. S. Bhupal Dev, A. Soni and F. Xu, *Hints of Natural Supersymmetry in Flavor Anomalies?*, (2021), arXiv: 2106.15647 [hep-ph].

[359] W. Altmannshofer, P. S. B. Dev, A. Soni and Y. Sui, *Addressing $R_{D^{(*)}}$, $R_{K^{(*)}}$, muon $g-2$ and ANITA anomalies in a minimal R-parity violating supersymmetric framework*,
Phys. Rev. D **102** (2020) 015031, arXiv: 2002.12910 [hep-ph].

[360] J. H. Collins, P. S. Bhupal Dev and Y. Sui,
R-parity Violating Supersymmetric Explanation of the Anomalous Events at ANITA,
Phys. Rev. D **99** (2019) 043009, arXiv: 1810.08479 [hep-ph].

[361] R. L. Workman et al., *Review of Particle Physics*, PTEP **2022** (2022) 083C01.

[362] H.-S. Lee, *Minimal gauge origin of baryon triality and flavorful signatures at the LHC*,
Phys. Lett. B **704** (2011) 316, arXiv: 1007.1040 [hep-ph].

[363] P. D. Bolton, F. F. Deppisch and P. S. B. Dev,
Neutrinoless double beta decay via light neutralinos in R-parity violating supersymmetry,
JHEP **03** (2022) 152, arXiv: 2112.12658 [hep-ph].

[364] S. Bansal, A. Delgado, C. Kolda and M. Quiros,
Limits on R-parity-violating couplings from Drell-Yan processes at the LHC,
Phys. Rev. D **99** (2019) 093008, arXiv: 1812.04232 [hep-ph].

[365] S. Bansal, A. Delgado, C. Kolda and M. Quiros, *Constraining R-parity-violating couplings in τ-processes at the LHC and in electroweak precision measurements*,
Phys. Rev. D **100** (2019) 093005, arXiv: 1906.01063 [hep-ph].

[366] J. L. Pinfold, *The MoEDAL Experiment at the LHC–A Progress Report*, Universe **5** (2019) 47.

[367] J. L. Pinfold, *The MoEDAL experiment: a new light on the high-energy frontier*,
Phil. Trans. Roy. Soc. Lond. A **377** (2019) 20190382, ed. by J. Dainton.

[368] J. P. Chou, D. Curtin and H. J. Lubatti, *New Detectors to Explore the Lifetime Frontier*,
Phys. Lett. B **767** (2017) 29, arXiv: 1606.06298 [hep-ph].

[369] C. Alpigiani et al., *An Update to the Letter of Intent for MATHUSLA: Search for Long-Lived Particles at the HL-LHC*, (2020), arXiv: 2009.01693 [physics.ins-det].

[370] M. Bauer, O. Brandt, L. Lee and C. Ohm,
ANUBIS: Proposal to search for long-lived neutral particles in CERN service shafts, (2019),
arXiv: 1909.13022 [physics.ins-det].

[371] K. Abe et al., *Letter of Intent: The Hyper-Kamiokande Experiment — Detector Design and Physics Potential —*, (2011), arXiv: 1109.3262 [hep-ex].

[372] E. Kearns et al., "Hyper-Kamiokande Physics Opportunities",
Snowmass 2013: Snowmass on the Mississippi, 2013, arXiv: 1309.0184 [hep-ex].

[373] H. K. Dreiner, H. E. Haber and S. P. Martin, *Two-component spinor techniques and Feynman rules for quantum field theory and supersymmetry*, Phys. Rept. **494** (2010) 1, arXiv: 0812.1594 [hep-ph].

[374] M. A. Diaz, "Bilinear R-parity violation", *International Workshop on Physics Beyond the Standard Model: From Theory to Experiment (Valencia 97)*, 1998 188, arXiv: hep-ph/9802407.

[375] A. Aguilar-Arevalo et al., *Improved search for heavy neutrinos in the decay $\pi \to e\nu$*, Phys. Rev. D **97** (2018) 072012, arXiv: 1712.03275 [hep-ex].

[376] W. Altmannshofer et al., "Testing Lepton Flavor Universality and CKM Unitarity with Rare Pion Decays in the PIONEER experiment", *Snowmass 2021*, 2022, arXiv: 2203.05505 [hep-ex].

[377] M. Daum et al., *Search for Admixtures of Massive Neutrinos in the Decay $\pi^+ \to \mu^+$ Neutrino*, Phys. Rev. D **36** (1987) 2624.

[378] E. Cortina Gil et al., *Search for heavy neutral lepton production in K^+ decays to positrons*, Phys. Lett. B **807** (2020) 135599, arXiv: 2005.09575 [hep-ex].

[379] E. Cortina Gil et al., *Search for K^+ decays to a muon and invisible particles*, Phys. Lett. B **816** (2021) 136259, arXiv: 2101.12304 [hep-ex].

[380] Y. Asano et al., *Search for a Heavy Neutrino Emitted in $K^+ \to \mu^+$ Neutrino Decay*, Phys. Lett. B **104** (1981) 84.

[381] R. S. Hayano et al., *HEAVY NEUTRINO SEARCH USING K(mu2) DECAY*, Phys. Rev. Lett. **49** (1982) 1305.

[382] P. Ballett, T. Boschi and S. Pascoli, *Heavy Neutral Leptons from low-scale seesaws at the DUNE Near Detector*, JHEP **03** (2020) 111, arXiv: 1905.00284 [hep-ph].

[383] K. Abe et al., *Search for heavy neutrinos with the T2K near detector ND280*, Phys. Rev. D **100** (2019) 052006, arXiv: 1902.07598 [hep-ex].

[384] F. Bergsma et al., *A Search for Decays of Heavy Neutrinos in the Mass Range 0.5-GeV to 2.8-GeV*, Phys. Lett. B **166** (1986) 473.

[385] P. Vilain et al., *Search for heavy isosinglet neutrinos*, Phys. Lett. B **343** (1995) 453.

[386] J. Orloff, A. N. Rozanov and C. Santoni, *Limits on the mixing of tau neutrino to heavy neutrinos*, Phys. Lett. B **550** (2002) 8, arXiv: hep-ph/0208075.

[387] A. Vaitaitis et al., *Search for neutral heavy leptons in a high-energy neutrino beam*, Phys. Rev. Lett. **83** (1999) 4943, arXiv: hep-ex/9908011.

[388] K. J. Kelly and P. A. N. Machado, *MicroBooNE experiment, NuMI absorber, and heavy neutral leptons*, Phys. Rev. D **104** (2021) 055015, arXiv: 2106.06548 [hep-ph].

[389] A. M. Cooper-Sarkar et al.,
Search for Heavy Neutrino Decays in the BEBC Beam Dump Experiment,
Phys. Lett. B **160** (1985) 207.

[390] R. Barouki, G. Marocco and S. Sarkar, *Blast from the past II: Constraints on heavy neutral leptons from the BEBC WA66 beam dump experiment*, SciPost Phys. **13** (2022) 118,
arXiv: 2208.00416 [hep-ph].

[391] P. Coloma, P. Hernández, V. Muñoz and I. M. Shoemaker,
New constraints on Heavy Neutral Leptons from Super-Kamiokande data,
Eur. Phys. J. C **80** (2020) 235, arXiv: 1911.09129 [hep-ph].

[392] F. Kling and S. Trojanowski, *Heavy Neutral Leptons at FASER*,
Phys. Rev. D **97** (2018) 095016, arXiv: 1801.08947 [hep-ph].

[393] J. De Vries, H. K. Dreiner, J. Y. Günther, Z. S. Wang and G. Zhou,
Long-lived Sterile Neutrinos at the LHC in Effective Field Theory, JHEP **03** (2021) 148,
arXiv: 2010.07305 [hep-ph].

[394] J. P. Lees et al., *Search for heavy neutral leptons using tau lepton decays at BaBaR*,
Phys. Rev. D **107** (2023) 052009, arXiv: 2207.09575 [hep-ex].

[395] E. Cortina Gil et al., *Search for π^0 decays to invisible particles*, JHEP **02** (2021) 201,
arXiv: 2010.07644 [hep-ex].

[396] J. P. Lees et al., *Improved Limits on B^0 Decays to Invisible Final States and to $\nu\bar{\nu}\gamma$*,
Phys. Rev. D **86** (2012) 051105, arXiv: 1206.2543 [hep-ex].

[397] A. Aguilar-Arevalo et al., *Search for heavy neutrinos in $\pi \to \mu\nu$ decay*,
Phys. Lett. B **798** (2019) 134980, arXiv: 1904.03269 [hep-ex].

[398] A. Aguilar-Arevalo et al., *Improved Measurement of the $\pi \to e\nu$ Branching Ratio*,
Phys. Rev. Lett. **115** (2015) 071801, arXiv: 1506.05845 [hep-ex].

[399] G. Marocco and S. Sarkar, *Blast from the past: Constraints on the dark sector from the BEBC WA66 beam dump experiment*, SciPost Phys. **10** (2021) 043, arXiv: 2011.08153 [hep-ph].

[400] R. Beltrán, G. Cottin, M. Hirsch, A. Titov and Z. S. Wang,
Reinterpretation of searches for long-lived particles from meson decays, JHEP **05** (2023) 031,
arXiv: 2302.03216 [hep-ph].

[401] V. V. Gligorov, S. Knapen, M. Papucci and D. J. Robinson,
Searching for Long-lived Particles: A Compact Detector for Exotics at LHCb,
Phys. Rev. D **97** (2018) 015023, arXiv: 1708.09395 [hep-ph].

[402] S. Cerci et al.,
FACET: A new long-lived particle detector in the very forward region of the CMS experiment,
JHEP **2022** (2022) 110, arXiv: 2201.00019 [hep-ex].

[403] A. M. Baldini et al., *Search for the lepton flavour violating decay $\mu^+ \to e^+\gamma$ with the full dataset of the MEG experiment*, Eur. Phys. J. C **76** (2016) 434,
arXiv: 1605.05081 [hep-ex].

[404] D. I. Britton et al., *Improved search for massive neutrinos in pi+ —> e+ neutrino decay*,
Phys. Rev. D **46** (1992) R885.

[405] G. Bellini et al.,
New limits on heavy sterile neutrino mixing in B8 decay obtained with the Borexino detector,
Phys. Rev. D **88** (2013) 072010, arXiv: 1311.5347 [hep-ex].

[406] R. Plestid, *Luminous solar neutrinos II: Mass-mixing portals*,
Phys. Rev. D **104** (2021) 075028, [Erratum: Phys.Rev.D 105, 099901 (2022), Erratum: Phys.Rev.D 105, 099901 (2022)], arXiv: 2010.09523 [hep-ph].

[407] M. Dentler et al., *Updated Global Analysis of Neutrino Oscillations in the Presence of eV-Scale Sterile Neutrinos*, JHEP **08** (2018) 010, arXiv: 1803.10661 [hep-ph].

[408] D. Gorbunov and M. Shaposhnikov, *How to find neutral leptons of the νMSM?*,
JHEP **10** (2007) 015, [Erratum: JHEP 11, 101 (2013)], arXiv: 0705.1729 [hep-ph].

[409] D. Gorbunov, I. Krasnov, Y. Kudenko and S. Suvorov,
Heavy Neutral Leptons from kaon decays in the SHiP experiment,
Phys. Lett. B **810** (2020) 135817, arXiv: 2004.07974 [hep-ph].

[410] K. Bondarenko, A. Boyarsky, D. Gorbunov and O. Ruchayskiy,
Phenomenology of GeV-scale Heavy Neutral Leptons, JHEP **11** (2018) 032,
arXiv: 1805.08567 [hep-ph].

[411] C. A. Argüelles, N. Foppiani and M. Hostert,
Heavy neutral leptons below the kaon mass at hodoscopic neutrino detectors,
Phys. Rev. D **105** (2022) 095006, arXiv: 2109.03831 [hep-ph].

[412] T. Abe et al., *Belle II Technical Design Report*, (2010),
arXiv: 1011.0352 [physics.ins-det].

[413] W. Altmannshofer et al., *The Belle II Physics Book*, PTEP **2019** (2019) 123C01, ed. by E. Kou and P. Urquijo, [Erratum: PTEP 2020, 029201 (2020)], arXiv: 1808.10567 [hep-ex].

[414] M. Hirsch and J. W. F. Valle,
Neutrinoless double beta decay in supersymmetry with bilinear R parity breaking,
Nucl. Phys. B **557** (1999) 60, arXiv: hep-ph/9812463.

[415] J. M. Berryman et al.,
Searches for Decays of New Particles in the DUNE Multi-Purpose Near Detector,
JHEP **02** (2020) 174, arXiv: 1912.07622 [hep-ph].

[416] P. Abratenko et al., *Search for long-lived heavy neutral leptons and Higgs portal scalars decaying in the MicroBooNE detector*, Phys. Rev. D **106** (2022) 092006,
arXiv: 2207.03840 [hep-ex].

[417] I. Boiarska, A. Boyarsky, O. Mikulenko and M. Ovchynnikov,
Constraints from the CHARM experiment on heavy neutral leptons with tau mixing,
Phys. Rev. D **104** (2021) 095019, arXiv: 2107.14685 [hep-ph].

[418] R. Acciarri et al.,
New Constraints on Tau-Coupled Heavy Neutral Leptons with Masses mN=280–970 MeV,
Phys. Rev. Lett. **127** (2021) 121801, arXiv: 2106.13684 [hep-ex].

[419] H. E. Haber and D. Wyler, *RADIATIVE NEUTRALINO DECAY*,
Nucl. Phys. B **323** (1989) 267.

[420] F. Capozzi et al., *Global constraints on absolute neutrino masses and their ordering*, Phys. Rev. D **95** (2017) 096014, [Addendum: Phys.Rev.D 101, 116013 (2020)], arXiv: 2003.08511 [hep-ph].

[421] G. Aad et al., *The ATLAS Experiment at the CERN Large Hadron Collider*, JINST **3** (2008) S08003.

[422] S. Chatrchyan et al., *The CMS Experiment at the CERN LHC*, JINST **3** (2008) S08004.

[423] G. F. Giudice and R. Rattazzi, *Theories with gauge mediated supersymmetry breaking*, Phys. Rept. **322** (1999) 419, arXiv: hep-ph/9801271.

[424] J. L. Feng, M. Kamionkowski and S. K. Lee, *Light Gravitinos at Colliders and Implications for Cosmology*, Phys. Rev. D **82** (2010) 015012, arXiv: 1004.4213 [hep-ph].

[425] S. Knapen and D. Redigolo, *Gauge mediation at the LHC: status and prospects*, JHEP **01** (2017) 135, arXiv: 1606.07501 [hep-ph].

[426] J. S. Kim, M. E. Krauss and V. Martin-Lozano, *Probing the Electroweakino Sector of General Gauge Mediation at the LHC*, Phys. Lett. B **783** (2018) 150, arXiv: 1705.06497 [hep-ph].

[427] J. S. Kim, S. Pokorski, K. Rolbiecki and K. Sakurai, *Gravitino vs Neutralino LSP at the LHC*, JHEP **09** (2019) 082, arXiv: 1905.05648 [hep-ph].

[428] V. M. Abazov et al., *Search for supersymmetry with gauge-mediated breaking in diphoton events at D0*, Phys. Rev. Lett. **94** (2005) 041801, arXiv: hep-ex/0408146.

[429] T. Aaltonen et al., *Signature-Based Search for Delayed Photons in Exclusive Photon Plus Missing Transverse Energy Events from $p\bar{p}$ Collisions with $\sqrt{s}$=1.96 TeV*, Phys. Rev. D **88** (2013) 031103, arXiv: 1307.0474 [hep-ex].

[430] M. Aaboud et al., *Search for photonic signatures of gauge-mediated supersymmetry in 13 TeV pp collisions with the ATLAS detector*, Phys. Rev. D **97** (2018) 092006, arXiv: 1802.03158 [hep-ex].

[431] A. M. Sirunyan et al., *Search for long-lived particles using delayed photons in proton-proton collisions at $\sqrt{s}$ = 13 TeV*, Phys. Rev. D **100** (2019) 112003, arXiv: 1909.06166 [hep-ex].

[432] T. Appelquist, H.-C. Cheng and B. A. Dobrescu, *Bounds on universal extra dimensions*, Phys. Rev. D **64** (2001) 035002, arXiv: hep-ph/0012100.

[433] A. Filimonova, R. Schäfer and S. Westhoff, *Probing dark sectors with long-lived particles at BELLE II*, Phys. Rev. D **101** (2020) 095006, arXiv: 1911.03490 [hep-ph].

[434] J. L. Feng et al., *The Forward Physics Facility at the High-Luminosity LHC*, (2022), arXiv: 2203.05090 [hep-ex].

[435] R. Schäfer, F. Tillinger and S. Westhoff, *Near or Far Detectors? Optimizing Long-Lived Particle Searches at Electron-Positron Colliders*, (2022), arXiv: 2202.11714 [hep-ph].

[436] V. Mitsou, *MoEDAL, MAPP and future endeavours*, PoS **DISCRETE2020-2021** (2022) 017.

[437] J. L. Feng, I. Galon, F. Kling and S. Trojanowski,
Axionlike particles at FASER: The LHC as a photon beam dump,
Phys. Rev. D **98** (2018) 055021, arXiv: 1806.02348 [hep-ph].

[438] A. Berlin and F. Kling, *Inelastic Dark Matter at the LHC Lifetime Frontier: ATLAS, CMS, LHCb, CODEX-b, FASER, and MATHUSLA*, Phys. Rev. D **99** (2019) 015021,
arXiv: 1810.01879 [hep-ph].

[439] L. A. Anchordoqui et al.,
The Forward Physics Facility: Sites, Experiments, and Physics Potential, (2021),
arXiv: 2109.10905 [hep-ph].

[440] S. Foroughi-Abari, F. Kling and Y.-D. Tsai,
Looking forward to millicharged dark sectors at the LHC, Phys. Rev. D **104** (2021) 035014,
arXiv: 2010.07941 [hep-ph].

[441] B. Batell, J. L. Feng and S. Trojanowski,
Detecting Dark Matter with Far-Forward Emulsion and Liquid Argon Detectors at the LHC,
Phys. Rev. D **103** (2021) 075023, arXiv: 2101.10338 [hep-ph].

[442] Z. S. Wang and K. Wang, *Long-lived light neutralinos at future Z−factories*,
Phys. Rev. D **101** (2020) 115018, arXiv: 1904.10661 [hep-ph].

[443] Z. S. Wang and K. Wang, *Physics with far detectors at future lepton colliders*,
Phys. Rev. D **101** (2020) 075046, arXiv: 1911.06576 [hep-ph].

[444] O. Fischer, Á. Hernández-Cabezudo and T. Schwetz, *Explaining the MiniBooNE excess by a decaying sterile neutrino with mass in the 250 MeV range*, Phys. Rev. D **101** (2020) 075045,
arXiv: 1909.09561 [hep-ph].

[445] V. Brdar, O. Fischer and A. Y. Smirnov,
Model-independent bounds on the nonoscillatory explanations of the MiniBooNE excess,
Phys. Rev. D **103** (2021) 075008, arXiv: 2007.14411 [hep-ph].

[446] P. Abratenko et al., *Search for an Excess of Electron Neutrino Interactions in MicroBooNE Using Multiple Final State Topologies*, (2021), arXiv: 2110.14054 [hep-ex].

[447] C. Giunti, A. Ioannisian and G. Ranucci, *A new analysis of the MiniBooNE low-energy excess*,
JHEP **11** (2020) 146, [Erratum: JHEP 02, 078 (2021)], arXiv: 1912.01524 [hep-ph].

[448] A. Ioannisian,
A Standard Model explanation for the excess of electron-like events in MiniBooNE, (2019),
arXiv: 1909.08571 [hep-ph].

[449] P. A. Zyla et al., *Review of Particle Physics*, PTEP **2020** (2020) 083C01.

[450] K. Desch, S. Fleischmann, P. Wienemann, H. K. Dreiner and S. Grab,
Stau as the Lightest Supersymmetric Particle in R-Parity Violating SUSY Models: Discovery Potential with Early LHC Data, Phys. Rev. D **83** (2011) 015013,
arXiv: 1008.1580 [hep-ph].

[451] G. Aad et al., *Search for trilepton resonances from chargino and neutralino pair production in $\sqrt{s} = 13$ TeV pp collisions with the ATLAS detector*, Phys. Rev. D **103** (2021) 112003,
arXiv: 2011.10543 [hep-ex].

[452] S. Dawson, *R-Parity Breaking in Supersymmetric Theories*, Nucl. Phys. B **261** (1985) 297.

[453] H. Abreu et al.,
Detecting and Studying High-Energy Collider Neutrinos with FASER at the LHC,
Eur. Phys. J. C **80** (2020) 61, arXiv: 1908.02310 [hep-ex].

[454] H. Abreu et al., *Technical Proposal: FASERnu*, (2020),
arXiv: 2001.03073 [physics.ins-det].

[455] K. Jod lowski and S. Trojanowski, *Neutrino beam-dump experiment with FASER at the LHC*,
JHEP **05** (2021) 191, arXiv: 2011.04751 [hep-ph].

[456] H. Abreu et al., *The trigger and data acquisition system of the FASER experiment*, (2021),
arXiv: 2110.15186 [physics.ins-det].

[457] J. Boyd, *The FASER W-Si High Precision Preshower Technical Proposal*, tech. rep.,
CERN, 2022, URL: https://cds.cern.ch/record/2803084.

[458] C. Athanassopoulos et al.,
The Liquid scintillator neutrino detector and LAMPF neutrino source,
Nucl. Instrum. Meth. A **388** (1997) 149, arXiv: nucl-ex/9605002.

[459] R. Ball et al., *The neutrino beam dump experiment at Fermilab (E613)*,
eConf **C801002** (1980) 172, ed. by V. Barger and D. Cline.

[460] A. A. Aguilar-Arevalo et al., *The Neutrino Flux prediction at MiniBooNE*,
Phys. Rev. D **79** (2009) 072002, arXiv: 0806.1449 [hep-ex].

[461] J. D. Bjorken et al.,
Search for Neutral Metastable Penetrating Particles Produced in the SLAC Beam Dump,
Phys. Rev. D **38** (1988) 3375.

[462] S. N. Gninenko, N. V. Krasnikov, M. M. Kirsanov and D. V. Kirpichnikov,
Missing energy signature from invisible decays of dark photons at the CERN SPS,
Phys. Rev. D **94** (2016) 095025, arXiv: 1604.08432 [hep-ph].

[463] S. N. Gninenko,
Search for MeV dark photons in a light-shining-through-walls experiment at CERN,
Phys. Rev. D **89** (2014) 075008, arXiv: 1308.6521 [hep-ph].

[464] D. Banerjee et al.,
Search for vector mediator of Dark Matter production in invisible decay mode,
Phys. Rev. D **97** (2018) 072002, arXiv: 1710.00971 [hep-ex].

[465] B. Aubert et al., *The BaBar detector*, Nucl. Instrum. Meth. A **479** (2002) 1,
arXiv: hep-ex/0105044.

[466] F. Kling and S. Trojanowski,
Forward experiment sensitivity estimator for the LHC and future hadron colliders,
Phys. Rev. D **104** (2021) 035012, arXiv: 2105.07077 [hep-ph].

[467] T. Yamazaki et al., *Search for Heavy Neutrinos in Kaon Decay*,
Conf. Proc. C **840719** (1984) 262, ed. by A. Meyer and E. Wieczorek.

List of Figures

List of Tables